University of Strathclyde

Department of Electronic and Electrical Engineering

A New Approach to Partial Discharge Measurements for Testing Electrical Insulation Systems

by
Alistair Reid
BEng(Hons) MIET AMIMechE

A thesis presented in fulfilment of the requirements for the degree of Doctor of Philosophy

2007

The copyright of this thesis belongs to the author under the terms of the United Kingdom Copyright Acts as qualified by University of Strathclyde Regulation 3.49. Due acknowledgement must always be made of the use of any material contained in, or derived from, this thesis.

Preface

This thesis is divided into 14 chapters:

Chapter 1 introduces partial discharge (PD) measurement as a diagnostic technique and describes the benefits of adopting a combined approach. The objectives of the study are defined.

Chapter 2 describes partial discharge processes, explaining common PD source topologies and PD pulse sequences.

Chapter 3 goes on to describe various PD measurement techniques, focusing on the IEC60270 standard and RF methods. Literature describing the RF method and its comparison with conventional measurements is reviewed.

Chapter 4 describes the calibration, testing and implementation of the experimental facility used for simultaneous partial discharge measurement.

Chapter 5 outlines the results of simultaneous RF/IEC measurements carried out on five common PD source geometries. Distinctive patterns specific to each PD source become apparent when RF energy is plotted against apparent charge for a large number of PD pulses.

Chapter 6 describes an investigation into the effect of test chamber geometry on the relationship between RF and IEC measurements. No direct relationship was apparent, with additional factors such as antenna orientation having a significant effect.

Chapter 7 presents phase-resolved partial discharge patterns obtained by capturing RF and IEC60270 PD measurements simultaneously along with phase position. Differences are apparent in the spread of PD magnitudes. Similarities in phase positions are attributed to the necessity to trigger on a single channel.

Chapter 8 proposes that the simultaneous measurement strategy can be enhanced by additionally calculating the relative spectral energies of the measured RF signals. Results indicate that the frequency distribution of RF energy could prove useful as an additional means of defect identification and characterisation.

Chapter 9 presents measurements of PD current pulses in SF_6 for a point-plane configuration using an extremely wide bandwidth (13GHz) measurement system. PD pulse shapes have been recorded with better resolution than has previously been possible. Results show a minimum rise time of 35 ps.

Chapter 10 expands on the outcomes reported in the previous chapter by investigating the effects of superposition of RF signals on the detected RF energy.

Chapter 11 presents the theoretical relationship between RF energy and apparent charge using an algorithm which can determine the complete response of a GIS chamber to a PD pulse of known parameters.

Chapter 12 discusses some of the questions that the research has so far answered as well as some questions it has raised.

Chapter 13 briefly summarises the findings of the research.

Chapter 14 outlines additional avenues of research which may be pursued to build upon the results outlined in this thesis.

Contents

Abstract

Partial discharge (PD) data has been recorded simultaneously using the conventional IEC60270 'apparent charge' measurement technique and the more recent Radio Frequency (RF) method. Due to the different responses of each system, combined measurement allows additional information on the nature of the PD source to be gained. PD was produced using a number of test cells containing PD sources typically encountered in practical insulation systems, such as free particles, floating electrodes and voids. When RF energy is plotted against apparent charge for a large number of discharges, characteristic patterns appear which may be used to distinguish between PD sources. Additionally, the combined technique has the ability to distinguish between simultaneously active PD sources by the appearance of multiple clusters. Additional work has been carried out to aid in the understanding and interpretation of these relationships. For example, an algorithm that models the complete response of a gas-insulated switchgear chamber has shown that PDs with a consistent pulse width produce correlation patterns that resemble a quadratic relationship. Additionally, direct PD current pulse measurement has shown a large variation in current pulse shape with faster rise times than previously expected (35 ps minimum). It is envisioned that the ability to relate RF measurements to the internationally accepted apparent charge level will aid in the general acceptance of the RF technique as a tool to quantify PD severity.

Chapter 1

Introduction

This chapter introduces partial discharge detection as a diagnostic tool, lists the strengths and weaknesses of the conventional IEC60270 technique and outlines the benefits of a combined RF/IEC system.

1.1 Motivation for the Present Study

1.1.1 The Requirement for On-line Diagnosis of Electrical Plant

Many transformers and other electrical plant items are approaching the end of their lifetimes, however it is only until recently that precise condition-based information on the current state of electrical plant is becoming an important factor. The financial consequences of a failure can easily exceed actual asset value, with some countries imposing severe regulatory fines for non-delivery. The lack of reliable diagnostic information on the condition of high voltage plant is therefore a matter of growing concern for electricity distribution companies [1].

Information on the current condition of the equipment can be gained using a number of techniques. These include integral methods such as $\tan\delta$ measurements, polarization measurements, dissolved gas analysis and transfer function analysis and often form the basis of standard evaluation or time-based maintenance procedures. However, the urgent requirement to optimise performance through higher availability is driving the need for more advanced asset evaluation. Partial discharge (PD) measurement is a popular condition monitoring technique which can reliably detect incipient faults and provide on-line diagnostic informa-

tion in real time.

1.1.2 Partial Discharge Detection as a Diagnostic Tool

When an electrical plant item such as a transformer or gas-insulated substation is first manufactured and assembled, PD detection is often used as a diagnostic tool to judge the condition of a component and the quality of its manufacture. For example, as a transformer ages, electrical and mechanical stresses can damage its internal components, including the windings and insulation. If the damage is not discovered and corrected, incipient faults can cause the transformer to operate outside its normal parameters, eventually leading to a catastrophic failure which will not only cause damage to surrounding equipment and facilities, but also incur severe regulatory fines as well as lost revenue and customer dissatisfaction.

Internal partial discharges such as those occurring in voids also involve acceleration and deceleration of electrons, producing signals with fast rise times. This rapid acceleration and deceleration produces electromagnetic radiation which is proportional to the rate of change of current for a given geometry. If the discharge source is sufficiently intense, as is the case with microsparks and large coronas, the discharge is followed by rapid expansion of the ionisation channel, generating an acoustic pressure wave. Partial discharge can also be observed by the emission of light from excited molecules and by the chemical detection of by products from any reaction initiated by the PD pulse.

Given the many observable effects of PD, a number of detection schemes have been developed over the years. Two effective techniques are the international IEC60270 Standard and the more recent Ultra High Frequency (UHF [1]) method which measures the energy radiated from the discharge site. Although the UHF and IEC60270 techniques have both proven effective and much expertise has developed in their application and interpretation, it is considered that a much more effective diagnostic tool could be realised by exploiting intrinsic complimentary attributes of the two approaches.

[1] Although measurement of PD by the radiated electromagnetic energy has been historically referred to as UHF measurement, RF (Radio Frequency) measurement is a more suitable definition since PD may produce signals containing frequencies outwith the UHF band. The two terms tend to be used interchangeably.

1.1.3 Strengths and Limitations of the IEC60270 Standard

The main strength of the IEC60270 standard relates to experience gained in its application. This has resulted in a test specification which is internationally accepted. An accepted standard for calibration of IEC60270 instruments, where pulses of a known charge are injected into the object under test, has meant that an upper limit on PD activity can be quantified in terms of apparent charge. Additionally, the conventional system is relatively simple to implement and can be fitted non-intrusively.

There are however, three major limitations pertaining to IEC60270 techniques:

1. Only *apparent* charge can be measured since there is no way of ascertaining the actual PD current directly.

2. A slowly damped output is produced in response to fast PD activity. This inhibits conventional systems from providing time-resolved information on multiple discharge variations or events that fall below the required resolution threshold. It has been previously shown that bursts of pulses which occur very close together (and hence contribute to a cumulative apparent charge) can be observed separately in the RF spectrum [2].

3. Most importantly, IEC60270 measurements do not account for pulse shape; the conventional technique can give the same apparent charge for two PD pulses that have quite different characteristics in the time domain. This is due to the limited bandwidth of the measurement system, which produces only a slowly damped response to fast PD activity. UHF measurements are, in contrast, capable of responding to variations in pulse shape and can therefore provide additional information about the discharge event which would otherwise be unavailable using conventional techniques.

1.1.4 The Benefits of a Combined System

Although the UHF method has the potential to overcome many of the shortcomings of the IEC60270 technique and has been successfully applied to GIS and transformer diagnostics for a number of years, it is unlikely to be accepted as a potential replacement for conventional measurements. The reasoning behind this

view is that UHF measurements cannot provide an absolute PD magnitude to replace the IEC60270 apparent charge.

While a certain magnitude of charge appears to offer a well defined upper limit on the acceptable level of partial discharge within an insulation system, it should be noted that this is *apparent* charge and is not equal to the actual charge displaced at the PD site. The relationship between real charge and apparent charge is equally as complex at that between apparent charge and UHF energy, however IEC measurements are favored when specifying transformer test requirements because of the many years of experience gained in their application.

Although neither the UHF or IEC60270 techniques possess the necessary attributes to be considered an ideal diagnostic tool, UHF measurements 'fill the gaps' as regards the aforementioned shortcomings. For example, UHF measurements can provide accurate information on PD location and exhibit a fast response to very short events within a PD pulse.

The benefits of a combined system are further exemplified when the fundamental differences in their response to PD events are considered. Essentially, conventional measurements are concerned with quantifying displaced charge in the test object under stress regardless of the stress mechanism, while UHF measurements respond to the dynamics of charge motion. Fundamentally, this is because electromagnetic radiation arises from charge acceleration. Since IEC60270 measurements are related to the integral of the PD current pulse and UHF measurements to its derivative, it is proposed that combining the two techniques will lead to a better physical understanding of unknown discharges taking place within the insulation system, and ultimately, better testing and diagnostic capabilities. Additionally, it is hoped that this study will contribute to the growing popularity of RF PD measurements as a diagnostic tool by providing an understanding of their relationship to conventional measurements, which have gained worldwide acceptance due to the experience gained in their application.

Chapter 2

Partial Discharges

Partial discharge is defined as a localised electrical discharge which only partially bridges the insulation between two conductors [3]. Because the breakdown is only local, it is described as partial.

The history of partial discharge detection is generally considered to stretch as far back as the eighteenth century to a publication by the experimental physicist, astronomer and mathematician Georg Christoph Lichtenberg who discovered what are now called 'Lichtenberg figures' in 1777 [4]. An example of such a pattern is shown in Figure 2.1. These are radial patterns, formed when a sharp electrode at a high potential is placed near an insulating surface. They remained a mystery for some 100 years until it was clarified that the figures are created by electrical discharges propagating along the dielectric surface. In some cases charge carriers are trapped on the highly insulating surface, creating latent invisible tracks and forming the circular and star-shaped figures.

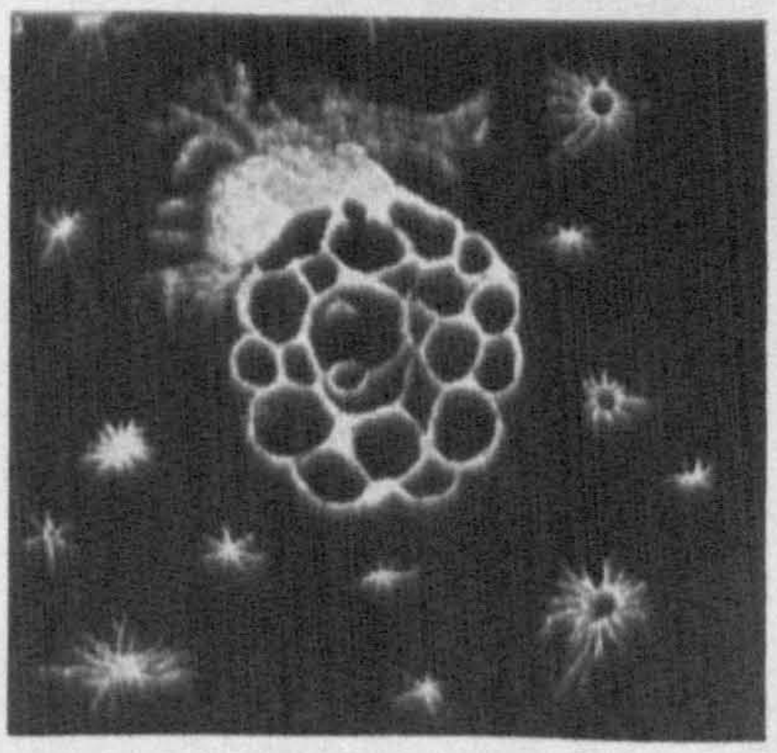

Figure 2.1: Lichtenberg's dust figures [4].

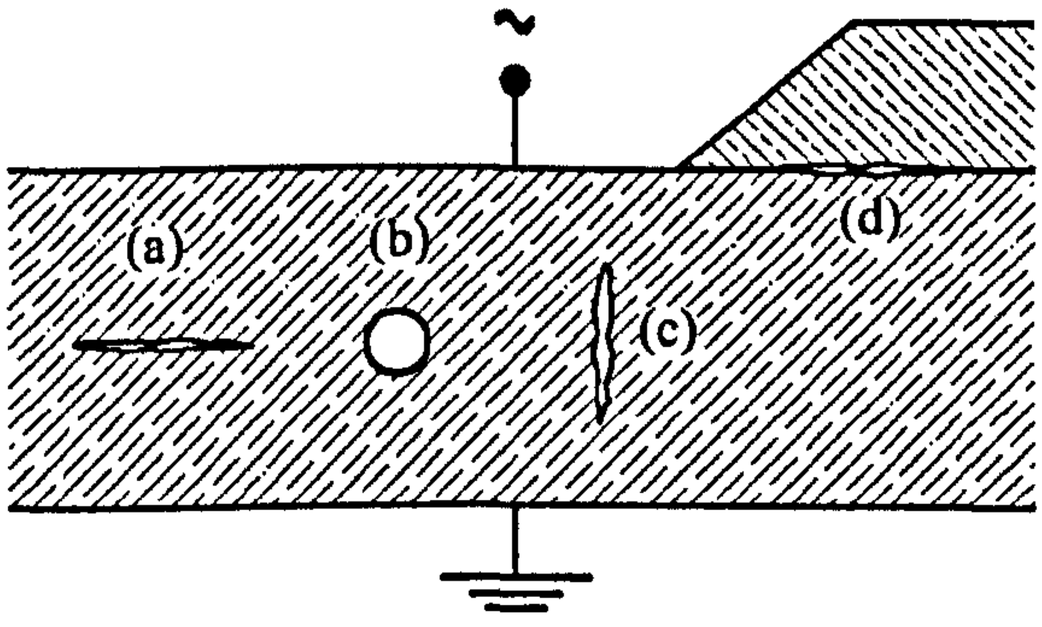

Figure 2.2: Voids in solid insulation.

2.1 Partial Discharge Source Topologies

2.1.1 Internal Discharges

Internal discharges can occur within solid insulation containing inclusions such as gas filled cavities. Such cavities often often occur in extruded plastics, cast resins and resin impregnated paper. The partial discharge inception voltage depends on the breakdown strength of the cavity. In some situations, it is possible to calculate the approximate electric field strength in the cavity. For example, in Figure 2.2 (a), where the cavity is situated perpendicular to the electric field, it is possible to approximate the electrical stress within the cavity by $E_c = \varepsilon E_d$, where E_c is the electric field in the cavity, ε is the dielectric constant of the insulating material and E_d is the electric field in the surrounding dielectric. For a spherical cavity as in Figure 2.2 (b), $E_c = 3\varepsilon \,/\, (1 + 2\varepsilon)\, E_d$. This tends to 1.5 as $\varepsilon \rightarrow \infty$. In situations where the cavity is parallel to the electric field, as shown in Figure 2.2 (c), $E_c = E_d$. When breakdown occurs in cavities of type (c) and (d), significant concentration of the electric field occurs. These types of cavities are therefore considered to be particularly dangerous [5].

The breakdown field strength of a cavity is given by the Paschen Curve shown in Figure 2.3 [1]. This is a graphical representation of Paschen's Law, which was first stated by Friedrich Paschen in 1889 [6]. Paschen's Law states that the breakdown characteristics of a gap are a non-linear function of the product of

[1] This figure is taken from the book 'Partial Discharge Detection in High Voltage Equipment', by F. H. Kreuger [5].

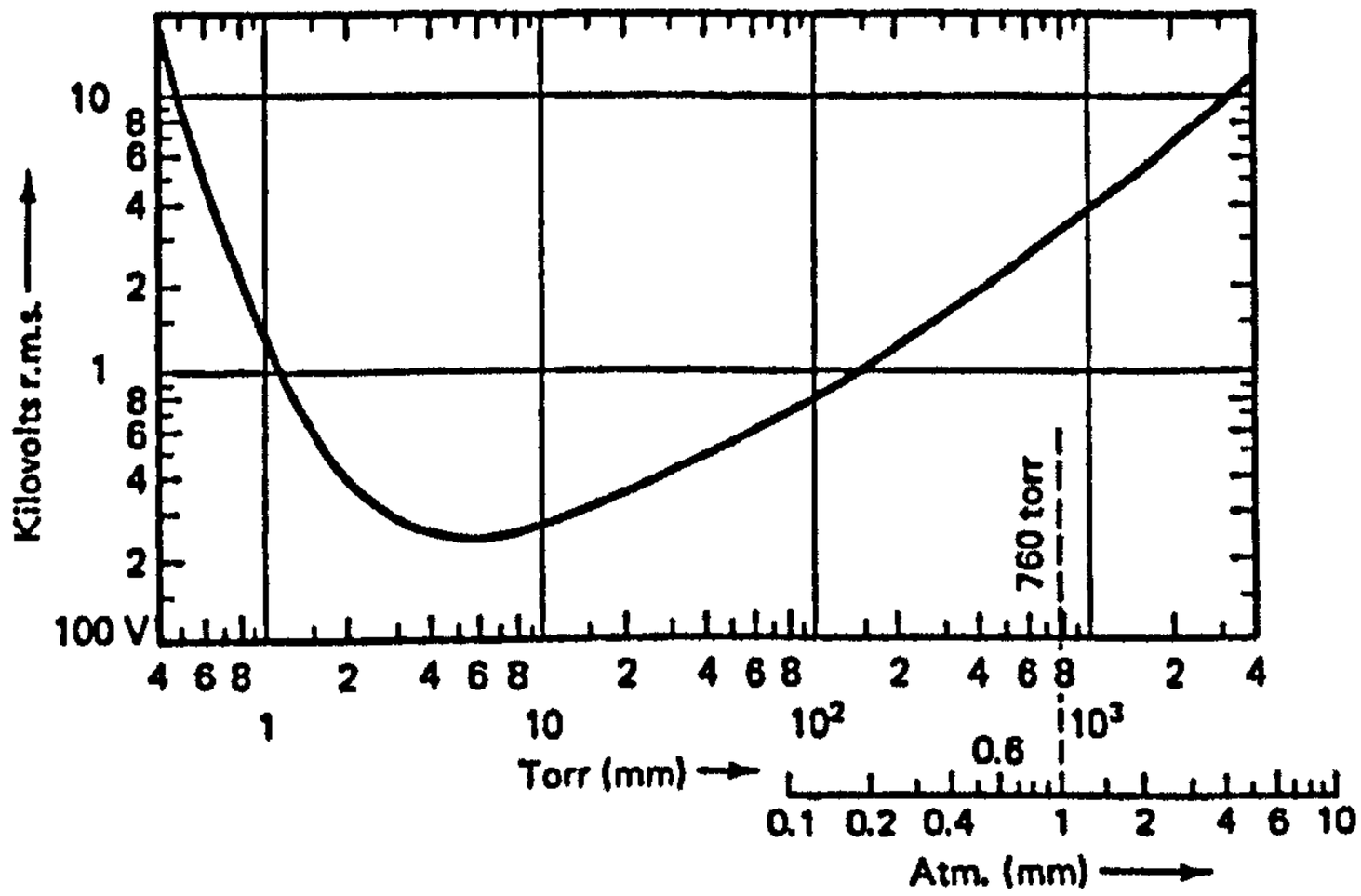

Figure 2.3: Paschen's curve, showing the breakdown voltage of air as a function of pressure times electrode spacing [5].

gap spacing and gas pressure:

$$V_s = Bpd / \ln\left(\frac{Apd}{\ln(1/\gamma)}\right) \tag{2.1.1}$$

The breakdown voltage also depends on a number of constants; γ represents the secondary ionisation coefficient, which describes the process in which positive ions generate electrons at the negative electrode through secondary emission. A and B are constants that depend on the gas properties and p and d represent pressure and gap spacing respectively. For air, $\gamma = 10^{-2}$, $A = 15\ cm^{-1}Torr^{-1}$ and $B = 365\ Vcm^{-1}Torr^{-1}$. In this case pressure in calculated in Torr, which as units of $mmHg$.

A second category of internal discharges are produced by inclusions within the insulating material. Inclusions can include dirt, fibres or other foreign particles. Inclusions will cause a breakdown to occur by stressing the electric field sufficiently, so as to reach the breakdown strength of the surrounding dielectric. When the initial breakdown occurs, a gas-filled cavity is formed.

Another family of internal discharges are those which occur in oil. Oil-filled cavities frequently occur between layers of oil-impregnated paper such as that used in transformer windings. The electric fields within these cavities can be calculated in a similar manner to the electric field in gas-filled cavities. See Chang et al. [7] for a more detailed discussion.

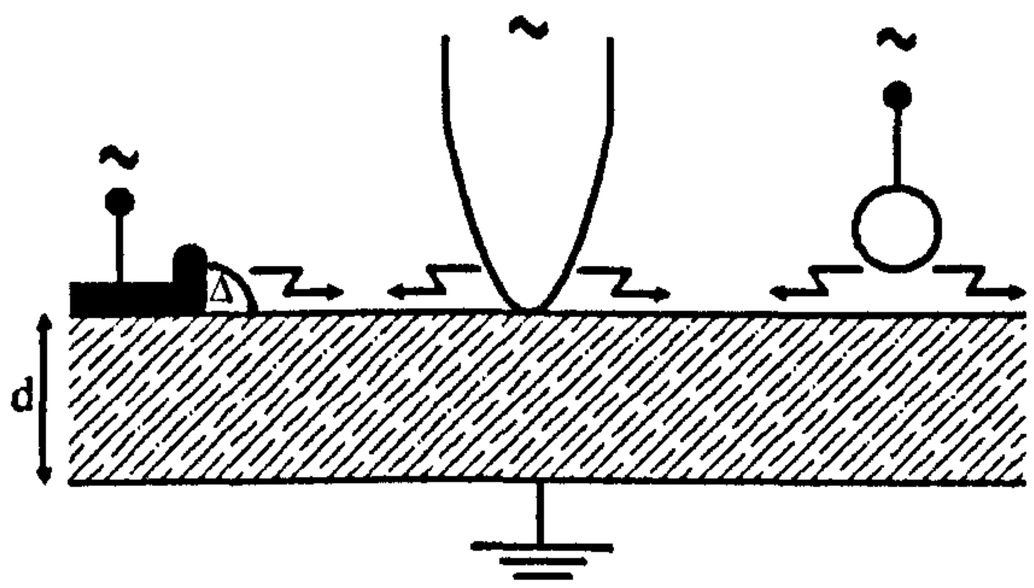

Figure 2.4: Surface discharges produced by various electrode configurations (after [5]).

2.1.2 Surface Discharges

Surface discharges may occur when there is a high electric field directed parallel to a dielectric surface. In practical terms, this can often occur in bushings, at the ends of cables and at the overhang of generator windings [5]. In general, surface discharges extend beyond the region where the electric field reached a sufficient magnitude to cause the onset of PD.

In a few cases it is possible to calculate the PD inception voltage for surface discharges in air. For example, the PD inception voltage for the first electrode configuration shown in Figure 2.4 is given by

$$V_i = \Delta E_i + d\frac{E_i}{\varepsilon} \tag{2.1.2}$$

where V_i is the applied voltage, Δ is the air gap and E_i is the breakdown field strength of the gap Δ. For simplicity, the inhomogeneity of the electric field has been neglected. A similar formula might be applied for surface discharges under oil, however the breakdown voltage U_i of an oil gap cannot be calculated using Paschen's Law. Additionally, calculation of the inception voltage based on empirical formulas does take into account the effects of contamination and moisture, which will have a significant influence.

2.1.3 Corona Discharges

Corona discharges are those which occur within a localised region near a sharp electrode as illustrated in Figure 2.5. If the electrode has a small radius of curvature, the electric field is enhanced above the local breakdown limit so that

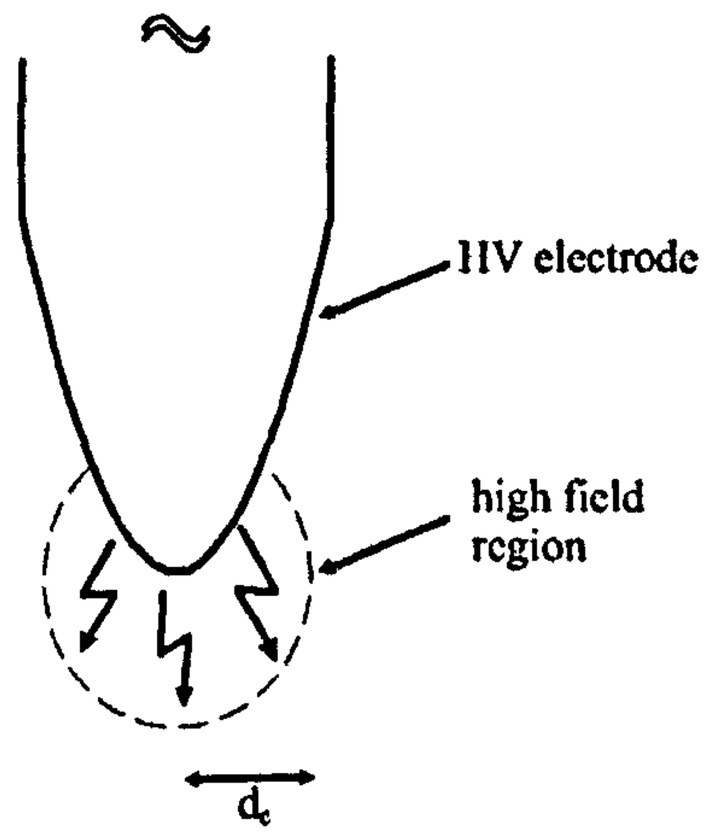

Figure 2.5: Corona discharges at a metallic point.

discharges occur but are confined within the enhanced region. The approximate condition for breakdown is given by

$$\overline{E}d_c \approx V_{s,min}\frac{(pd_c/(pd)_{min})}{\ln\left[2.72(pd_c/(pd)_{min})\right]} \tag{2.1.3}$$

where $\overline{E}$ is the average electric field, $V_{s,min}$ is the minimum breakdown voltage, which can be derived from Paschen's Law, d_c is the dimension of the corona region, and pd_{min} is the value of pd which corresponds to the minimum breakdown voltage. Current flows at a fairly constant rate, although the discharges within the corona region tend to extinguish and reform very rapidly. Equation (2.1.3) shows that as the electrode voltage is increaced, the size of the corona region increases accordingly.

2.1.4 Electrical Treeing

Electrical trees often stem from a defect within the insulation sample such as that shown in Figure 2.6 and consist of small cracks, forming a branch-like structure. They may also start where partial discharges occur in a void or from a raised point on the surface of an electrode, which, in practical terms, will never be perfectly flat. Treeing is particularly prevalent in organic materials such as polymers and is one of the major factors affecting the long term breakdown if such insulators. When a tree has grown for some time, considerable discharges occur in the hollow stem and the larger branches. These highly unstable discharge can cause the tree to grow rapidly, inducing breakdown within minutes or seconds.

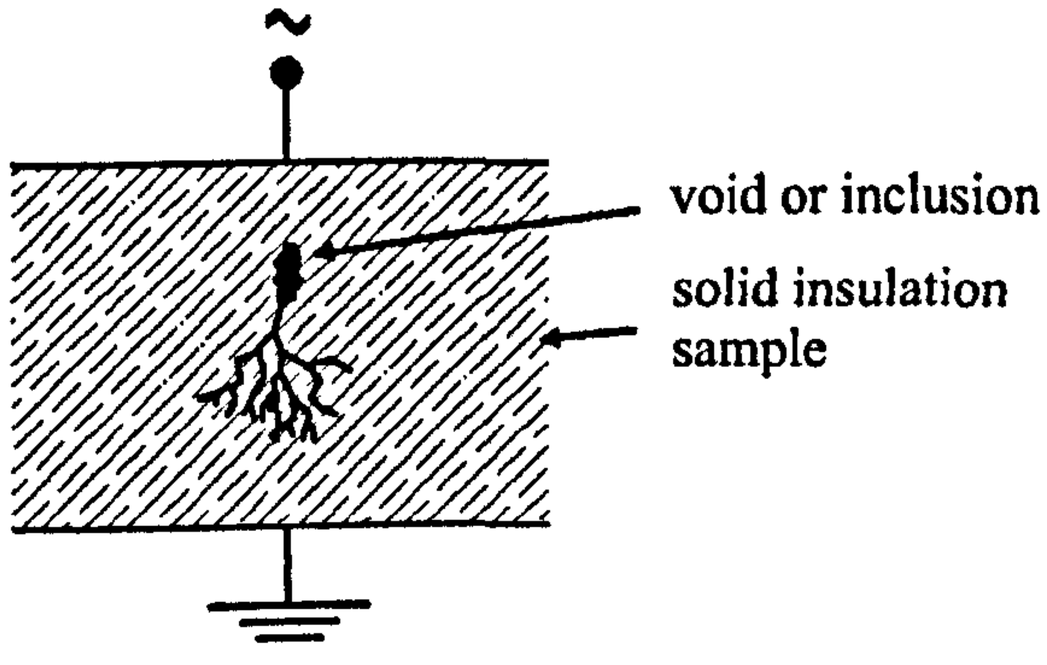

Figure 2.6: Electrical treeing in solid insulation.

2.1.5 Floating Components

A floating component is a conducting element which is not bonded to any other conductor. In GIS, the most common floating components are spacer inserts and corona shields [8]. Under certain conditions, a floating electrode will acquire an electric potential. The voltage and the amount of energy that the electrode acquires is a function of its area and its location within the gap. In other words, it is a function of the floating electrode capacitance.

The floating component will distort the electrostatic field between the upper and lower electrodes. The electric field will be enhanced at the high curvature points and the whole metallic body will acquire a certain voltage with respect to earth, although its net charge will be zero. When the critical electric field is reached for initiation of corona discharges on the sharp protrusions (see Figure 2.7), the floating electrode gains a charge of the opposite polarity to that of the corona source [9].

If the floating electrode has a vary small radius of curvature, the critical electric field will be reached with relatively low voltages being applied across the main gap. The critical electric field for corona onset can be calculated using the following equation, derived by Hilgarth [10]

$$E_a = \delta K_1 \left(1 + K_2/\sqrt{\delta r_k}\right) \tag{2.1.4}$$

where E_a is the maximum field on the sphere, δ is the relative air density, $K_1 = 30KV/cm$ for air, $K_2 = 0.47cm^{-1/2}$ and r_k is the radius of curvature.

A well-defined amount of energy is stored in the floating electrode. The maximum potential energy W stored in the gap can be calculated using

$$W = \frac{1}{2}CV^2 \tag{2.1.5}$$

where C is the floating electrode capacitance and V is the breakdown voltage of the secondary gap d_2. The breakdown voltage is given by the product of the breakdown electric field strength and the gap spacing

$$V = E_b d_2 \tag{2.1.6}$$

This can now be combined with equation 2.1.5 to obtain an expression for potential energy.

$$W = \frac{1}{2}Cd_2^2E_b^2 \tag{2.1.7}$$

It terms of the measured charge Q, the energy is given by

$$W = \frac{1}{2}Qd_2E_b \tag{2.1.8}$$

Due to their very high capacitance, it is common for floating electrodes to produce partial discharges in the order of 10,000 pC.

2.1.6 Free Particles

Free conducting particles are most likely to be encountered in GIS. These particles tend to bounce along the bottom of a GIS enclosure, with the amplitude of each bounce dependant on the size and shape of the particle, and on the voltage and phase of the conductor. A small discharge will be created between the free particle and the surrounding metal enclosure if the particle lands at a phase of the applied potential which is different from that at which it took off [8]. Therefore, upon landing there exists a potential difference between the particle and the metal sheath, causing a spark to occur. Statistics on GIS reliability [11, 12] show that the free particle is the most common cause of failure in such systems.

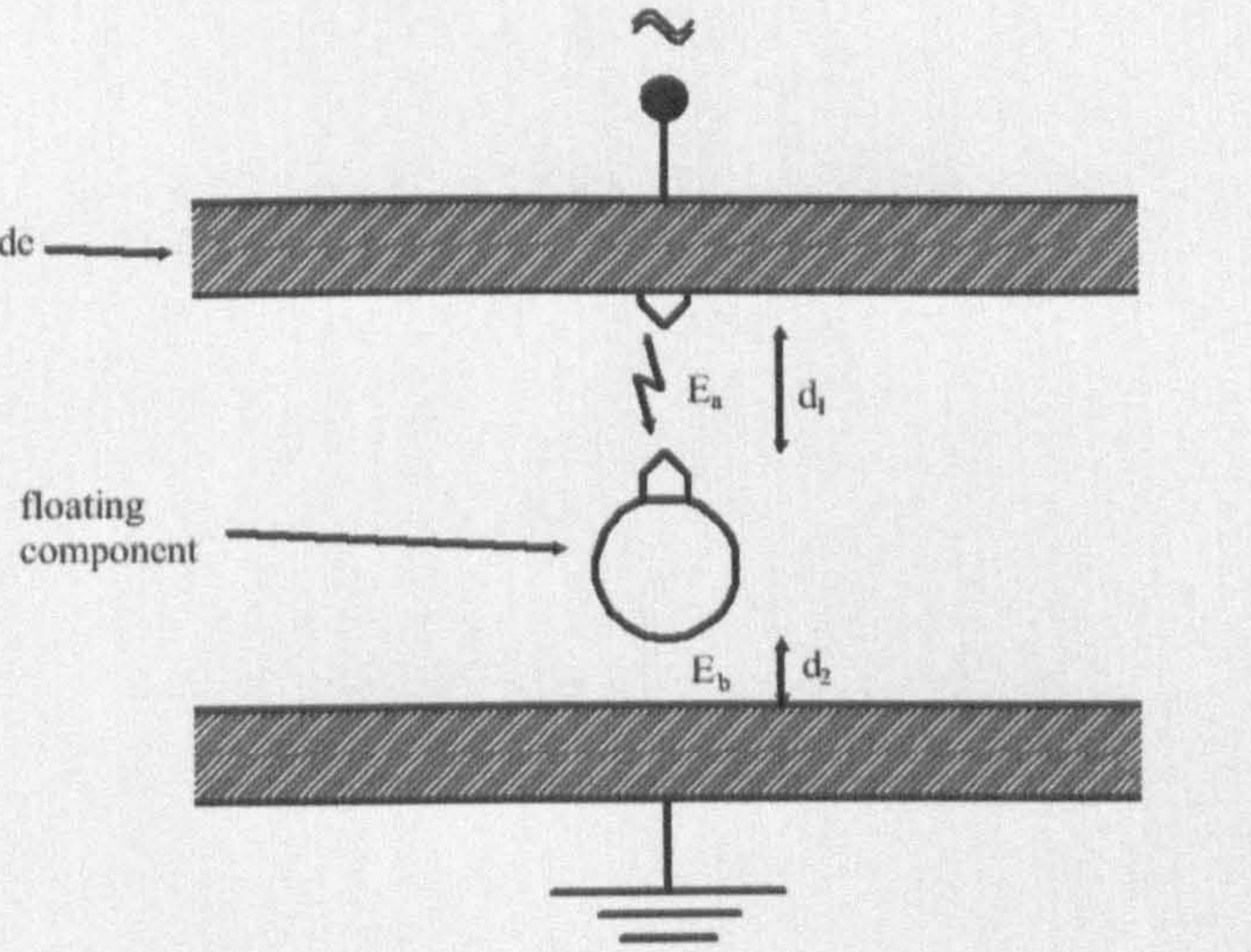

Figure 2.7: Corona from floating electrodes.

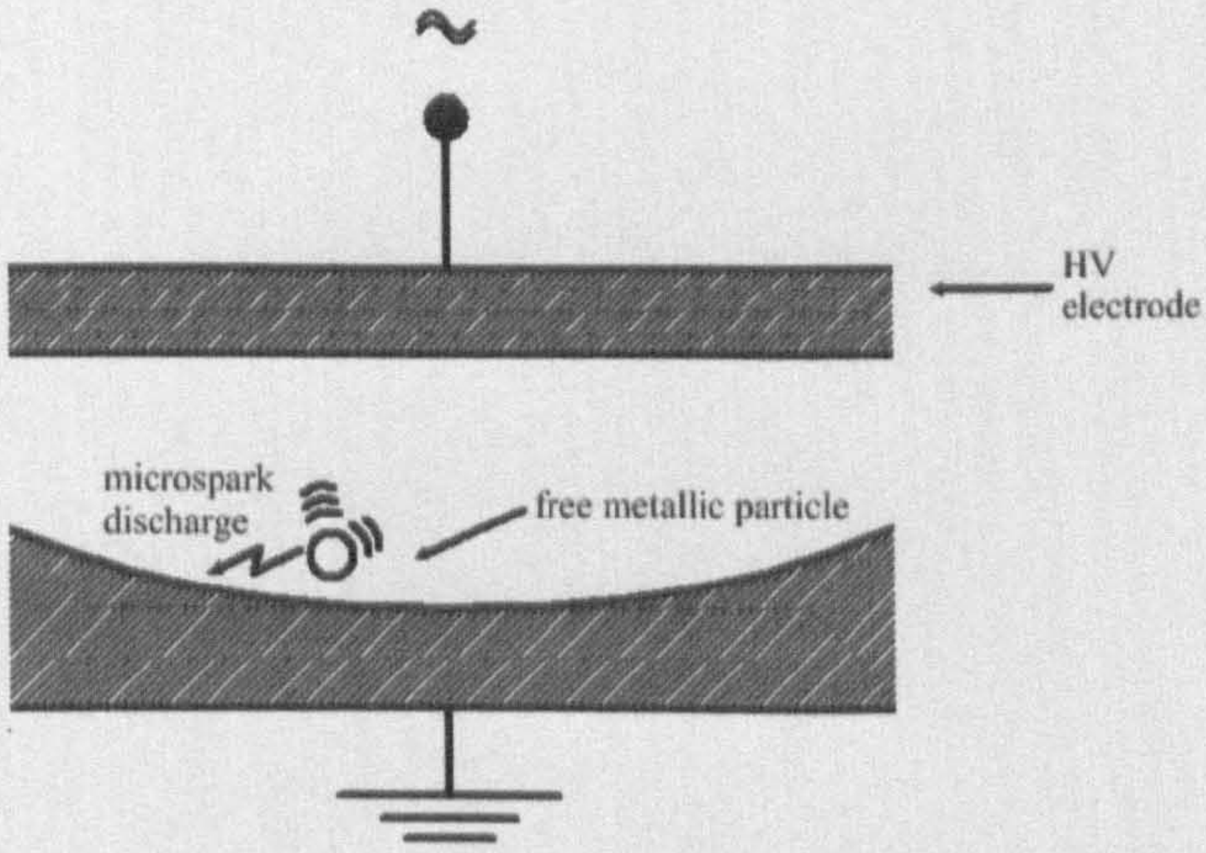

Figure 2.8: Microsparks from free metallic particles.

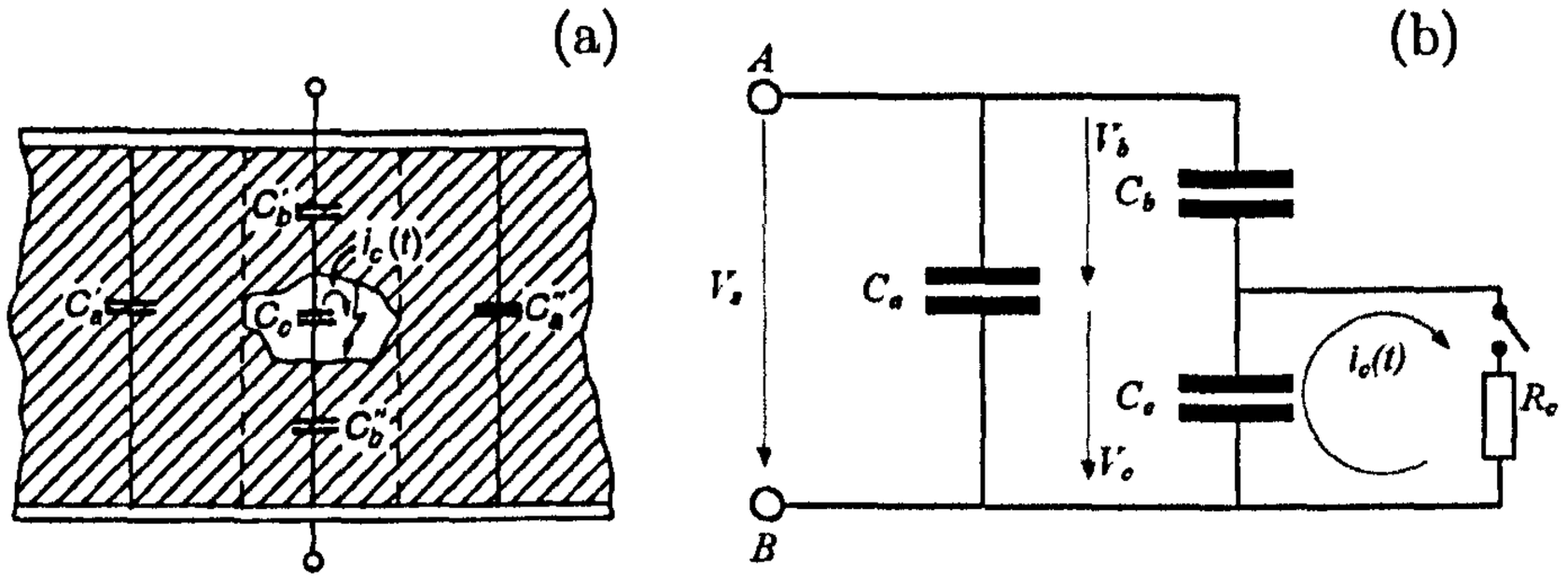

Figure 2.9: (a) Insulation system comprising of a cavity [13] and (b) its equivalent circuit. C_c represents the capacitance of the cavity, C_b represents the capacitance from the cavity walls to the outer electrodes and C_a represents the capacitance outside the cavity. $C_a = C_a' + C_a''$ and $C_b = C_b'C_b''/(C_b' + C_b'')$.

2.2 Partial Discharge Pulse Sequences Under Alternating Voltage

The recurring nature of PD pulses under sinusoidal a.c. voltage will be illustrated using internal discharges as a typical example. The equivalent circuit for a gas discharge cavity within an insulation sample such as those discussed in section 2.1 is given in Figure 2.9

As instanced by Figure 2.10 (a), when the voltage V_c causes the electric field in the cavity to reach inception E_{inc}, a discharge occurs [2] (in the figure, each vertical discontinuity represents a single partial discharge). The electric field within the cavity then drops to its residual value E_{res} and the discharge is extinguished. At this point the voltage across the cavity begins to increase once again. This voltage does not follow the envelope of the sine wave, but is offset by an amount proportional to $(E_{inc} - E_{res})$. This is due to the main electric field being counteracted by space charges within the cavity. When the electric field again reaches E_{inc}, a new discharge occurs and the process starts over. This will happen a number of times, depending on the values of E_{res} and E_{inc}. When the electric field across the void sample E_0 begins to decrease, the internal electric field E_i will also decrease until it reaches $-E_{inc}$. At this point a new discharge will occur. It is in this manner that patterns of discharges occur relative to the a.c reference wave. In this case void discharges have been considered and as shown in Figure 2.10, discharges tend to occur around the 1st and 3rd quadrants. Other partial

[2]The corresponding inception voltage can be calculated using Paschen's Law.

discharge sources will also produce phase-resolved patterns that are specific to their source topology. For example, corona discharges tend to occur initially on the negative peak of the reference cycle.

Today, the analysis of such phase-resolved patterns is one of the most commonly used diagnostic techniques to asses the condition of an insulation system and is employed by most commercially available PD measurement systems. It should be noted that analysis and interpretation of phase-resolved partial discharge (PRPD) patterns is a difficult task, especially if the discharge source is unknown or if multiple discharge sources occur simultaneously. For example, the complexity of accurately analysing such PRPD patterns is illustrated by Patsch and Berton [14], who show that there is a systematic phase shift in the PD sequence due to the build up or modification of local space charges. The authors claim that the discharge process is revealed to be highly deterministic when this effect is taken into account. Figure 2.10 (a) was produced using a simple mathematical model. A recent publication by Altenburger et al. [15] uses a newly developed stochastic theory of PD processes to make a statistical analysis of measured PRPD patterns. This allows for the interpretation of certain physical parameters related to the PD process such as first electron availability or decay time constants, giving a much more robust interpretation than traditional statistical parameters such as skewness and kurtosis, which may vary significantly even though the underlying mechanism remains the same.

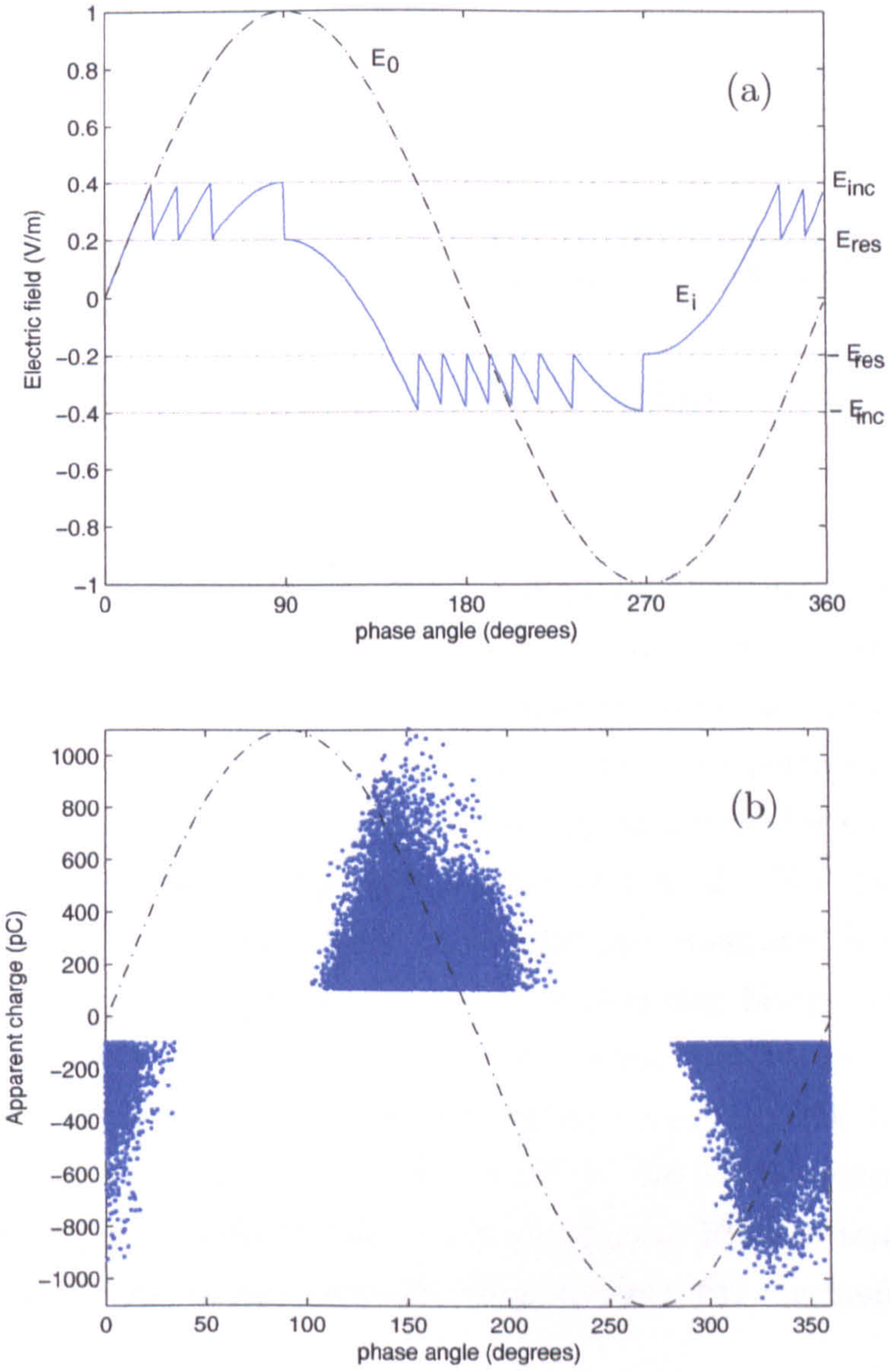

Figure 2.10: (a) A simulated PD pulse sequence. Each vertical discontinuity in the internal electric field E_i represents a partial discharge pulse. (b) A phase-resolved partial discharge pattern produced by an insulation sample containing a void, measured using the Lemke LDS-6 system. The equivalent circuit for such a source is shown in Figure 2.9

Chapter 3

The State of the Art in Partial Discharge Measurement

Kreuger [5] notes that the need for partial discharge detection arose in the early 1950s, when new high voltage dielectrics, including polyethylene and epoxy resin, were introduced. Production of these new insulators involved extruding and casting, which could easily leave a single cavity in an otherwise perfect dielectric. Previously, it was not considered that there was any real need for partial discharge detection since paper-based insulation was predominant. No special detection methods were needed for paper insulation since the integrated losses caused by the discharges could easily be measured using a Schering bridge [16].

The requirement for a tool to evaluate the integrity of these new insulation systems led to a vast increase in partial discharge research in the 1960s and early 1970s. Much of the research around this period [17–20] concentrated on the physical understanding of void discharges, but from the late 1970s onward, substantial progress was also made on the understanding of other PD mechanisms [21–29].

3.1 Partial Discharge Measurement Techniques

Partial discharges have many effects that in principle could be utilised to aid their detection. Each measurement technique relating to the many observable effects of PD has its own advantages and disadvantages ranging from practicality to sensitivity and noise immunity.

3.1.1 Optical Detection

Endeavour in this field of PD detection is largely academic because while optical detection is by far the most sensitive of all the measurement techniques (modern photo-multipliers can detect the emission of even a single photon), it is also one of the least practical. Optical radiation from a PD site is primarily in the ultraviolet band [30]. The energy of photons of this frequency means that they are absorbed strongly by SF_6, an insulator commonly used in gas insulated substations (GIS) and gas insulated lines (GIL). Difficulties are also encountered in transformer monitoring where the majority of systems are oil-filled. While new oil is relatively transparent and will allow light to propagate from the PD site, the opacity of transformer oil will increase over time [31]. Additionally, a clear optical path would be required between the sensor and PD source because, unlike radio waves, visible light will not deflect significantly round any obstacles due to its short wavelength. Despite these impracticalities, optical detection remains a powerful laboratory tool for finding the onset of PD activity from a known corona source.

3.1.2 Chemical Detection

Although chemical detection, or dissolved gas analysis (DGA), has been applied to various types of high voltage plant such as hydrogen-cooled generators and gas insulated substations [32, 33], it has been most successfully applied to oil-filled equipment.

Oil will tend to degrade under the continuous action of partial discharges and through bond scission, gases will be produced which are absorbed by the oil. These include: hydrogen (H–H), methane (CH_3–H), ethane (CH_3–CH_3), ethylene (CH_2=CH_2) and acetylene ($CH \equiv CH$). The combinations and relative quantities of the gases produced will give an indication of the nature, severity and associated temperature of the fault. In low energy PD, scission of the weak C–H bonds in the oil tends to dominate, resulting in the production of hydrogen gas. In the case of power transformers, where paper insulation (Cellose) is commonly used, byproducts from the reaction will also include carbon monoxide and carbon dioxide [31]. A range of commercially available equipment can be used for on-site measurements on large oil-filled transformers [34–36]. Gas chromatographs, infra-red spectrometers, semiconductor sensors and miniature fuel cells can all be used to analyse the dissolved gas. Interpretation and fault classification is based on the combination and relative quantities of dissolved gas in the measured

sample. The IEC60599 standard [37] uses a combination of the ratios C_2H_2/C_2H_4, CH_4/H_2 and C_2H_4/C_2H_6 to diagnose the cause of any fault, whether it be partial discharge, high or low energy discharge or thermal faults. Although this technique appears attractive because of its immunity to electrical interference, there are also disadvantages including the inability to locate the fault and the time required to obtain and analyse the oil sample. Removing oil from low volume items such as bushings may also deplete the insulation system itself. Some modern DGA systems such as those manufactured by Kelman, Severon and Hydran [34–36] are, however, able to analyse an oil sample on-line without depleting the oil volume.

Chemical detection in GIS is carried out using a similar technique, although it is not as widely accepted due to its low sensitivity. GIS are insulated by pressurised sulphur hexafluoride gas (SF_6). Under the action of continuous partial discharge, this will decompose to form sulphur tetrafluoride (SF_4). This reactive gas will in turn react with residual water vapor to form two more stable compounds; thionyl fluoride (SOF_2) and sulphuryl fluoride (SO_2F_2) [31]. Since these gases will be greatly diluted in a large volume of SF_6, detection of typical PD signals is insensitive. The disadvantages mentioned above rule out chemical detection as a singular solution for early partial discharge detection and location.

3.1.3 Acoustic Detection

Rapid expansion of the ionised gas channel caused by PD generates an acoustic pressure wave propagating in all directions from the site of the discharge. The detection of this mechanical energy is one of the oldest and simplest ways to detect the presence and location of partial discharges.

The main advantages associated with the technique are its immunity to electrical noise and the ability to provide information on the location of the PD through time-of-flight analysis. Such a system, however, is not immune to mechanical noise and can be affected by mechanical vibrations within the system, although it is possible to filter out these unwanted acoustic signals since they occur at a lower frequency (<100 kHz) than the PD signal itself (several MHz) [38]. An additional limitation is manifest in the complex nature of acoustic wave propagation. Due to the non-homogeneous nature of high voltage transformers and GIS, the acoustic signals do not travel in perfect spherical wavefronts. Reflections from internal components can lead to diminished signal strength and multi-path interference, requiring very sensitive detectors that are able to respond to small

changes in signal amplitude.

Disadvantages include the inability to apply the technique to an intrinsically noisy plant such as a motor or a generator, the requirement for the discharge source and sensor to have a relatively short spatial separation, which rules out any application to power cable monitoring, and the inability to quantify absolute discharge magnitude based on the acoustic signal.

3.1.4 Photography

Where discharges are external to the electrical plant, for example on overhead lines or busbars, it is possible to apply thermal imaging to their detection and measurement. Corona discharges produce UV radiation in the 230–405 nm range. It has recently been shown that it is possible to achieve high contrast daylight images of corona discharges using a UV video camera [39]. This technique exploits the fact that a region of this spectrum (240–280 nm) coincides with the UV solar blind band, in which there is no background radiation. Partial discharges which are of practical interest from a condition monitoring point of view are usually enclosed within either a metal clad exclosure or solid insulation, consequently thermal imaging is not widely employed by practical PD detection systems.

3.1.5 Electrical Detection - According to the IEC60270 Recommendations

The exact mechanisms and resulting signal properties of a partial discharge are not completely understood, though there are guidelines used by engineers when designing partial discharge detection systems. One such standard is the IEC60270 [3] which details test techniques for measuring the *apparent charge* of a PD pulse. It provides definitions and descriptions relating to measurement circuits and methods as well as calibration and test procedures for instrumentation. The standard defines partial discharge as follows:

> "Partial Discharge is a localized electrical discharge that only partially bridges the insulation between conductors and which may or may not occur adjacent to the conductor"

Measurement of the apparent charge q as a fundamental PD quantity is widely accepted and used today. The word *apparent* is used because this measured

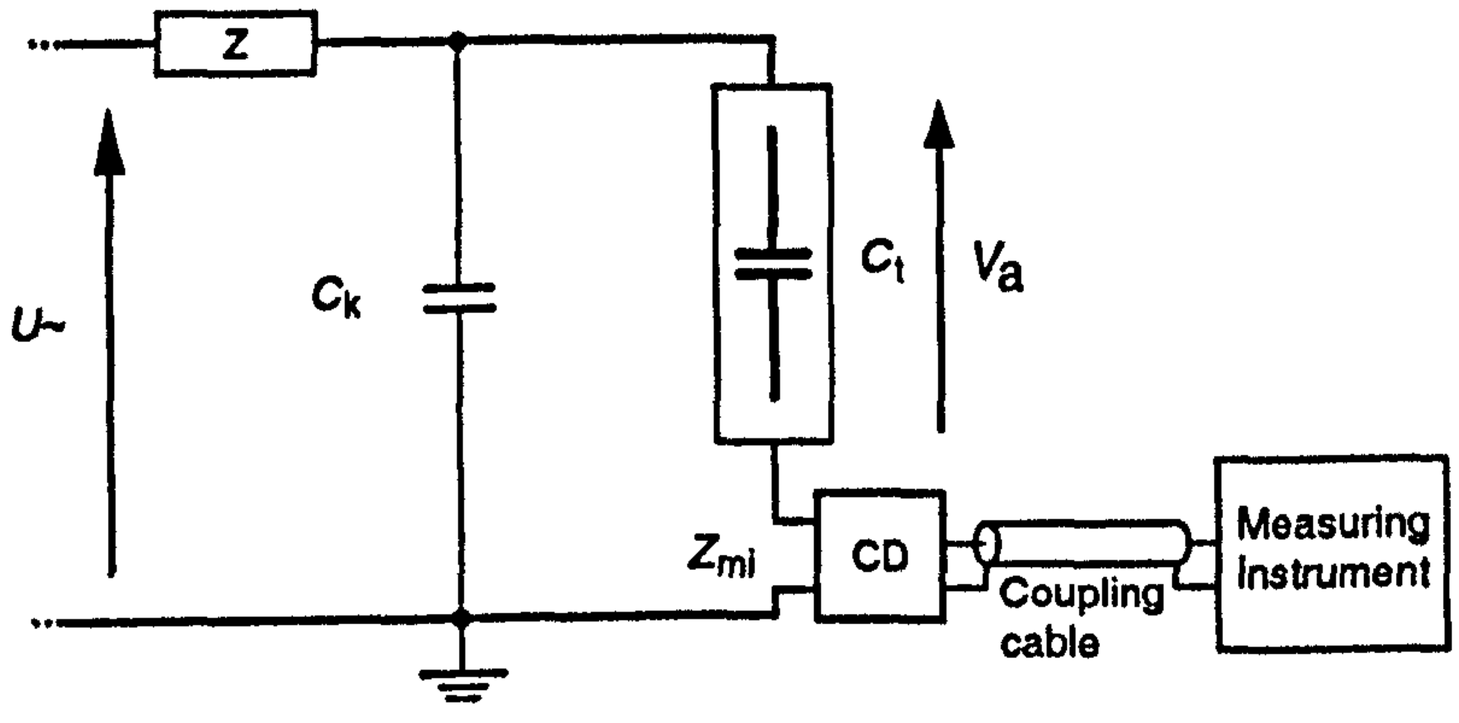

Figure 3.1: Conventional measurement as defined in the IEC60270 standard. Test object C_t within the basic PD test circuit. U is the supply voltage, Z_{mi} is the input impedance of the measurement system, C_k is the coupling capacitor, CD is the coupling device, Z serves to attenuate disturbances from the high voltage source [3].

quantity is not equal to the actual amount of charge locally involved at the site of the discharge, but rather the quantity which if injected between the terminals of the test object would give the same reading on the measurement system as the PD pulse itself [1].

The standard method for measuring partial discharges is based on the appearance of a current or voltage pulse at the terminals of a test object. The standard circuit for partial discharge measurement as defined in IEC60270 is shown in Figure 3.1. The test object can be anything from a simple dielectric specimen to a large HV apparatus undergoing a PD test. For now, let us assume that the test object is a simple capacitor containing a void in its dielectric that will produce partial discharges. Its equivalent circuit is shown in Figure 2.9

The test object is connected to a voltage source (usually an AC power supply). An impedance Z is connected between the voltage source and the parallel arrangement of the coupling capacitor and the test specimen to isolate these from the voltage source during the short duration of the partial discharge. During this short period, C_k acts as a storage capacitor (stable voltage source).

During the partial discharge, the storage capacitor C_k releases a charging current corresponding to the PD pulse $i(t)$ to cancel the voltage drop V_a across

[1] Pedersen and McAllister [40–43] argue that statements within the IEC60270 standard such as "the *amount* of charge locally involved at the discharge site" are misleading since the total net charge remains constant at any given time and what one can detect are the effects, in the form of electrostatic induction, of a change in charge distribution within the void.

C_t. Assuming $C_k \gg C_t$ [2], V_a is completely compensated and the charge transfer provided by the current pulse $i(t)$ is given by

$$q = \int i(t) = (C_t)\delta V_a$$

Again, assuming $C_k \gg C_t$ this becomes

$$q = \int i(t) = (C_a + C_b)\delta V_a \tag{3.1.1}$$

By comparison of the charges in the system before and after the discharge, the voltage drop across the terminal V_a can be found.

$$\delta V_a = \frac{C_b}{C_a + C_b}\delta V_c$$

Substituting this into (3.1.1) the apparent charge of a PD pulse can be obtained.

$$q = C_b \delta V_c$$

3.1.6 Electrical Detection - The UHF Technique

Before reviewing the development of the UHF technique from its embryonic stages in the early 1980s through to the present day, a summary of the basic principle behind its application will be given.

The current at the PD site has a sub nanosecond rise time [44] and, due to rapid acceleration of charge, gives rise to electromagnetic waves with energy spectra extending to frequencies of 200MHz and above [31]. The UHF band is defined as covering frequencies in the range 300–3000 MHz. Conveniently, high voltage plant inside which partial discharges often occur are in the form of a closed metallic chamber, for example a GIS chamber or a transformer tank. These will be excited into various modes of resonance which, along with their low loss, can allow the RF signal to persist from 50 ns to more than 500 ns.

Because RF signals radiating from the PD site are not greatly attenuated by electrical insulation, any signal measured by a UHF sensor will contain multiple reflections of the same pulse along with frequency components corresponding to the resonant modes of the GIS chamber or transformer. This gives the advantage

[2]This assumption is not always valid in practice since if C_k is made too large, more power will be drawn from the source. C_k is therefore often designed to be equal to C_t.

of high sensitivity and good signal to noise ratio but interpretation of the signal can be difficult. A useful analogy here is that of a ringing bell; the UHF signal can be likened to the acoustic ringing of the bell once struck, with the original PD pulse analogous to the hammer providing the initial mechanical excitation.

Although the electromagnetic effects of partial discharge have long been known [45], it was not until the early 1980s that significant effort was focused toward developing permanently installed PD monitoring systems based on the electromagnetic means of discharge detection and location. The need for such systems arose due to the relatively high failure rate of GIS at the time and the deficiencies of the acoustic location method. Since GIS are located at critical points within a distribution network, failures are to be avoided at all costs. Additionally, the acoustic method requires too many sensors for complete substation monitoring. The most significant publications on the development of the UHF technique will now be reviewed.

One of the earliest papers relating to UHF PD detection in GIS was by Boggs [8]. Invented in the early 1950s, gas insulated switchgear was still a relatively immature technology at the time of this article's writing. The author notes the unacceptably high failure rate of GIS at the time and mentions that partial discharge sources – particularly floating components – within the switchgear caused a number of forced outages and proved to be a substantial problem during commissioning. Some of the inadequacies of the acoustic location method are stated; specifically, that acoustic signals are substantially attenuated by spacers and that treeing within a solid dielectric is unlikely to produce a detectable acoustic signal. For these reasons, substantial effort was focused toward the development of the UHF technique for PD detection. The author then goes on to show three transient signals produced by three different partial discharge sources. One such signal is given in Figure 3.2. With hindsight it is clear that the fidelity of these signals was limited by the bandwidth of the measurement system (1 GHz) available at that time. The author also describes two discharge location techniques. The first uses the autocorrelation function to compare a pair of pulses received at either end of a gas insulated line (GIL) and the second applies the cross-correlation function to signals arriving at either end of a GIS, as this allows the system to ignore later reflections caused by the many junctions and impedance discontinuities within the substation.

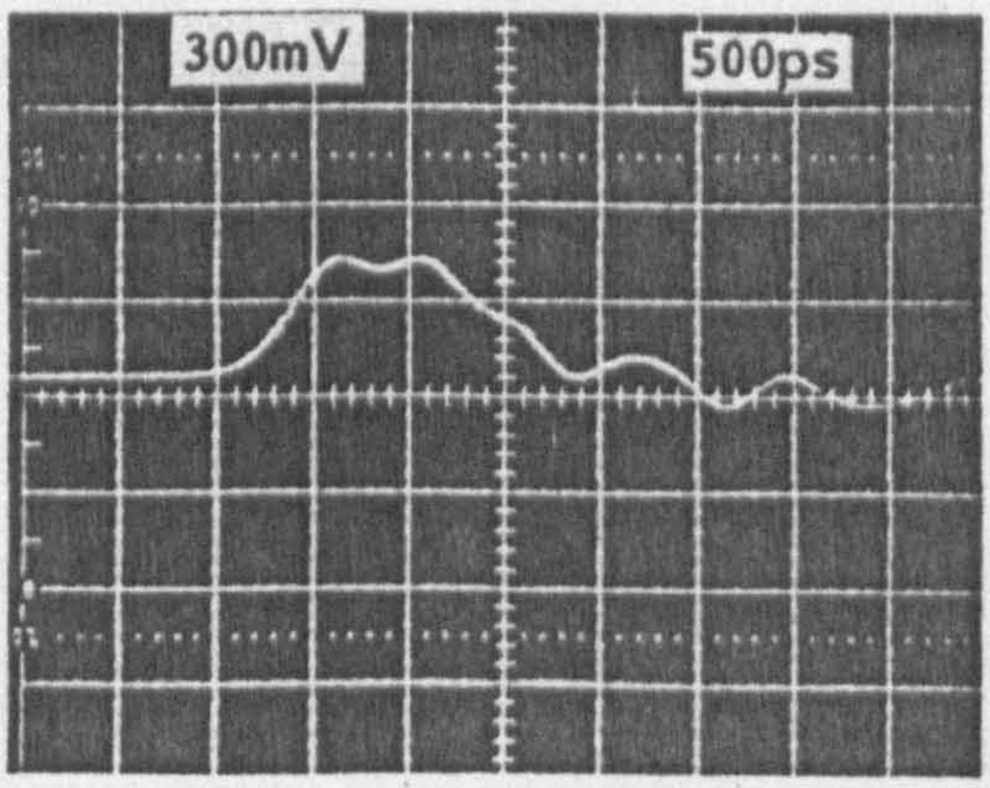

Figure 3.2: Transient electromagnetic signal generated by treeing in a solid dielectric spacer, as reported by Boggs [8]. Tests were carried out using a 20 m long GIS test chamber. Signal measured using an internal disk-type coupler.

Perhaps the most significant early study regarding the applicability of UHF signals as a diagnostic measurement for GIS is that of Hampton [46]. Several clear advantages of the UHF technique in relation to traditional methods are reported. Specifically, it is noted that while existing PD measurement techniques (which use acoustic or optical transducers) require very many sensors to be installed throughout the plant, the UHF method requires only one electrical coupler per phase due to the limited attenuation of the RF signal with distance along the GIS chamber. However, the authors report that under laboratory conditions, the PD source can be located to within ± 0.15 m by positioning a UHF sensor at either end of the GIS chamber and that in practice seven sets on each of the three phases give complete coverage of the GIS. A theoretical analysis of the resonant nature of GIS cavities is also made. In order to satisfy the boundary condition imposed by Maxwell's equations in the event of a PD pulse, many Transverse Electric (TE) and Transverse Magnetic (TM) modes are set up inside the GIS chamber [3]. For each of the many modes in a chamber, there is a cutoff wavelength which can be approximated by

$$\lambda_c = \pi(a+b) \tag{3.1.2}$$

[3]Excitation of a purely TEM mode signal would require symmetrical excitation of the waveguide, whereas the location of a PD current pulse is always asymmetrical with respect to the cross section

where a and b are the outer and inner radii of the conductor and chamber. For a 420 KV GIS, the cutoff frequency is approximately 250 MHz, above which higher order modes propagate with little loss. The peak frequencies of the resonant standing waves within the cavity were found to be very stable and reproducible for a well defined set of conditions, however, if the position of the PD source changed, a different set of resonant standing waves resulted. Three partial discharge test sources were used – rolling ball, floating screw and a corona point – to produce the required PD pulses in both the laboratory tests and field tests, where the PD sources were placed within an off-line substation. Several figures show the RF signals measured at the coupler outputs. Additionally, the authors used a spectrum analyser to identify PD sources in the frequency domain. The authors also report a disadvantage associated with UHF measurements stating that while the intensity of corona radiation in air falls off rapidly with increasing frequency, intense corona can produce interference with frequencies exceeding 1 GHz, enough to swamp the low levels of PD which need to be detected in GIS.

Pearson et al. [47] describe the implementation of a remote monitoring scheme for GIS, where the UHF signals are monitored continuously with the data being sent to an engineer through a modem. Additionally, the frequency spectra produced by three commonly occurring defects – corona, rolling ball and floating electrode – was measured using a spectrum analyser over a period of 20 - 30 seconds for each respective test sample. The article describes the architecture and operation of the continuous monitoring system. As one would expect, the system was rather primitive by today's standards but nonetheless an outstanding achievement for the time. Diagnostic information comprised of a phase-resolved PD pattern in the form of a histogram. Each histogram spanned one cycle of the 50 Hz supply. In this early incarnation, the system relied on an engineer to provide a diagnosis based on visual inspection of the data.

A comprehensive review of the state of the art in GIS monitoring is also given by Pearson et al. [30], with the authors concentrating particularly on the UHF technique. The main objectives of GIS diagnostics were specified as follows: firstly, to detect whether a defect is present; secondly to identify it as a free particle, floating electrode and so on and thirdly to locate the fault so that it may be corrected. It was noted that much experience had been gained through testing both on site and during commissioning, and this highlighted the need for

the following developments:

1. A better understanding of the physical processed leading to breakdown is needed due to the complex and intermittent discharges often seen in GIS systems.

2. Continuous monitoring systems tend to produce vast quantities of data, therefore the task of interpreting this data needs to be carried out by expert systems to avoid overburdening the engineer.

3. PD monitoring systems should be expanded to other equipment such as circuit breakers and transformers to provide a complete diagnostic system.

It was shown that the complete transfer function, from PD source to coupler output, can be modeled when the PD is represented as a current source within a coaxial waveguide. This made it possible to define the sensitivity required for a UHF coupler or even an entire monitoring system. As can be seen from Figure 3.3 the results showed reasonable agreement between measured and simulated signals at the UHF coupler output. The signals both show a peak amplitude of around 0.5 mV occurring at 39 ns as well as a comparable resonance pattern. It was also noted that UHF coupler design is largely dictated by 'high-voltage' requirements, in other words, the coupler should be designed primarily so as to not to cause any enhancement of the local electric field. So whereas a radial monopole would have excellent sensitivity, it would also invite breakdown and would therefore be unacceptable.

More recently it has been shown that using a minimum of three UHF sensors, PD sources inside a transformer can be accurately located using time-difference-of-arrival measurements [48–50]. Figure 3.4 shows three UHF sensors, used as part of a system which implements this location method, installed on a 275-33kV 120MVA transformer.

3.1.7 Quantifying UHF Measurements

UHF partial discharge signals contain complex features. Each signal contains frequency components that are dictated by the original PD current pulse shape as well as multiple reflections and resonant components produced by the test environment. A need therefore arises to reduce the UHF measurement to a single quantifiable parameter. Using the peak amplitude [51] is flawed since much of

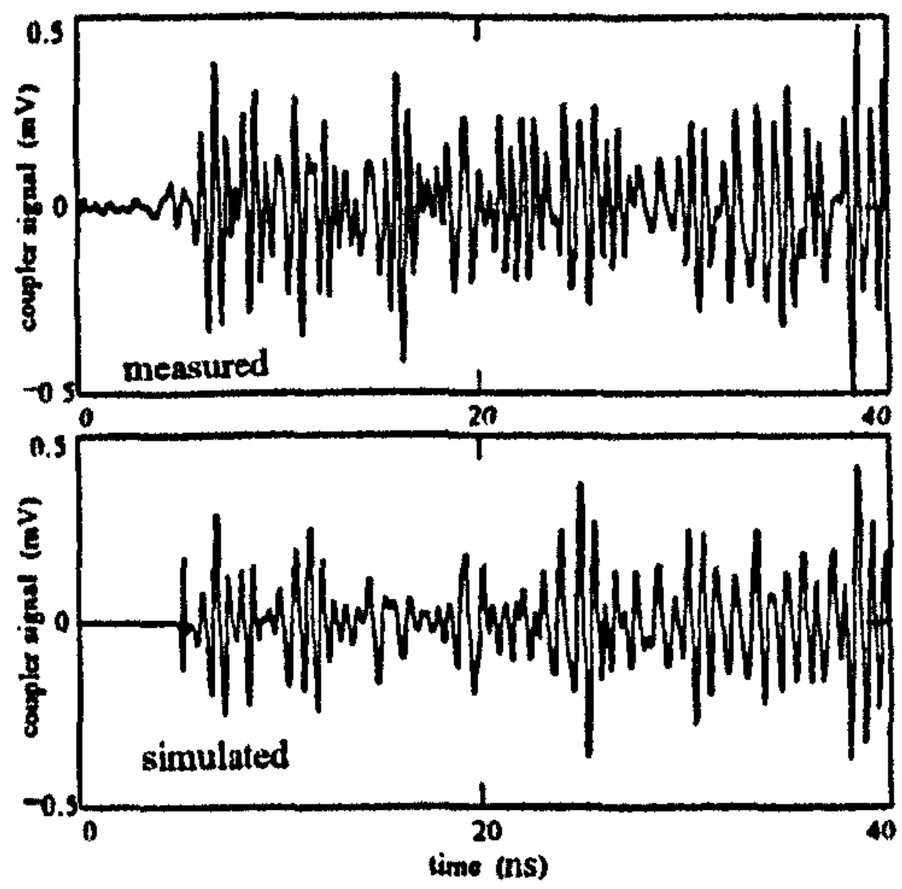

Figure 3.3: Measured and simulated coupler output signals in response to a 0.5 pC PD pulse, as reported by Pearson et al. [30]

the additional information contained within the signal is ignored. The cumulative energy [52] is a more suitable measurement since all sampled points on the trace are takin into account. This is calculated by effectively taking the discrete time integral of the PD signal by summing the energy at each data point using the formula

$$U_i = U_{i-1} + \Delta T \sum_{i=1}^{n} \frac{V_i^2}{R} \tag{3.1.3}$$

where U_i is the energy of the discretised signal at point i, U_{i-1} is the total energy at the previous data point, ΔT is the time between samples, V is the voltage output from the UHF sensor, and R is the input impedance of the oscilloscope.

3.2 The Combined Measurement Strategy

Does a combined measurement strategy, which harnesses the unique and complementary aspects of both the IEC60270 and UHF techniques have the potential to provide a better physical understanding and interpretation of unknown discharges taking place within an insulation system? This is a question which has not been previously addressed. Throughout the course of this research the potential of the combined measurement strategy will be investigated. By simultaneously measuring partial discharge using both techniques, the usefulness of an integrated measurement system as a diagnostic tool will be assessed, thereby making a unique

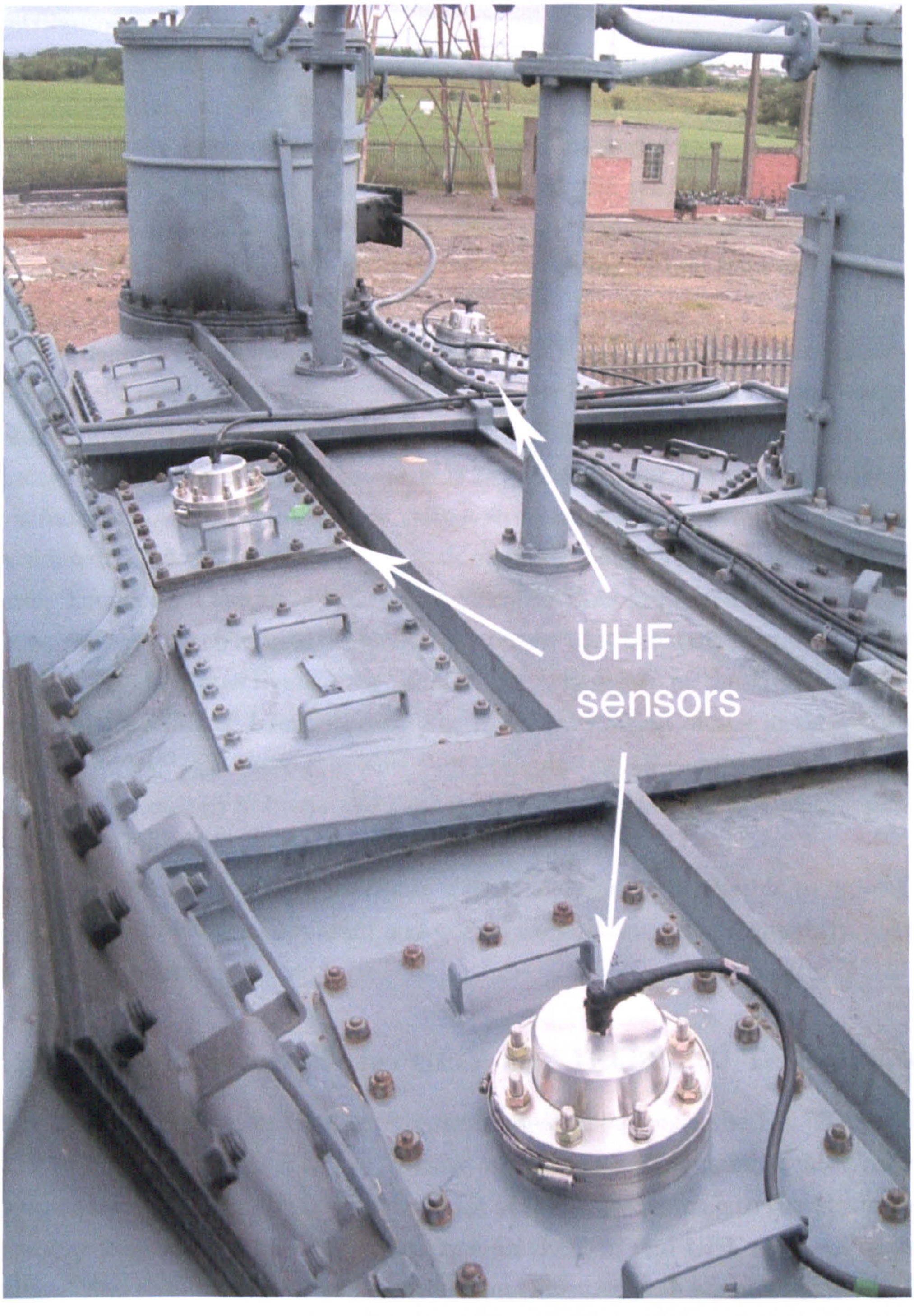

Figure 3.4: An array of three UHF sensors installed on a 275-33kV 120MVA transformer at Motherwell. Arrays of UHF sensors can be used to locate internal defects using time-difference-of-arrival measurements. Figure courtesy of I. B. B. Hunter, Scottish Power.

contribution to knowledge.

Since both systems respond differently to the same PD pulse, it is postulated that information on the PD pulse shape and therefore the type and severity of a defect can be obtained through simultaneous measurement. This has been suggested by Cleary et al. [53], who predict that the relationship between RF energy U and apparent charge q of a PD pulse will be quadratic in form, provided the pulses have a consistent width, i.e. only vary in amplitude from one pulse to the next.

V is defined as the output voltage from a UHF sensor, E as the propagating electric field incident on the sensor and i as the PD current. The relationship between V and q can be established through the following three logical arguments: Firstly, $V \propto E$ since the UHF sensor is a passive, linear device. Secondly, E is a function of di/dt. Since only pulses that are scaled in amplitude will be considered, di/dt will be directly proportional to the peak amplitude of the current pulse. Therefore, if the amplitude of the PD pulse doubles, so will the magnitude of the radiated electric field. Thirdly, for pulses of a constant shape, the peak amplitude I_p is proportional to q. Finally, the energy U of the UHF signal at the coupler output is determined by numerical integration of the instantaneous output power V^2/R, where R is 50Ω. Since calculating RF energy involves taking square of the output voltage, the relationship between energy and charge for a repeatable, single PD source becomes: $U \propto q^2$ [53].

Therefore for a single PD source in a fixed location, it is possible to quantify the relationship between apparent charge and radiated energy, provided the pulse shape is consistent.

3.2.1 Comparison of the UHF and IEC60270 Techniques

As mentioned earlier, simultaneous measurement using both the IEC60270 and UHF techniques is a novel and innovative way of potentially gaining more information about the PD source, hence the lack of literature relating to this study. So before making a more detailed comparison on the IEC and UHF methods, some publications that compare both measurement strategies in some way — either by comparing their sensitivity of their phase-resolved characteristics — will be examined briefly.

In order that an unequivocal comparison be made between the various PD measurement techniques, CIGRE Working Group 15-03 [54] arranged for the

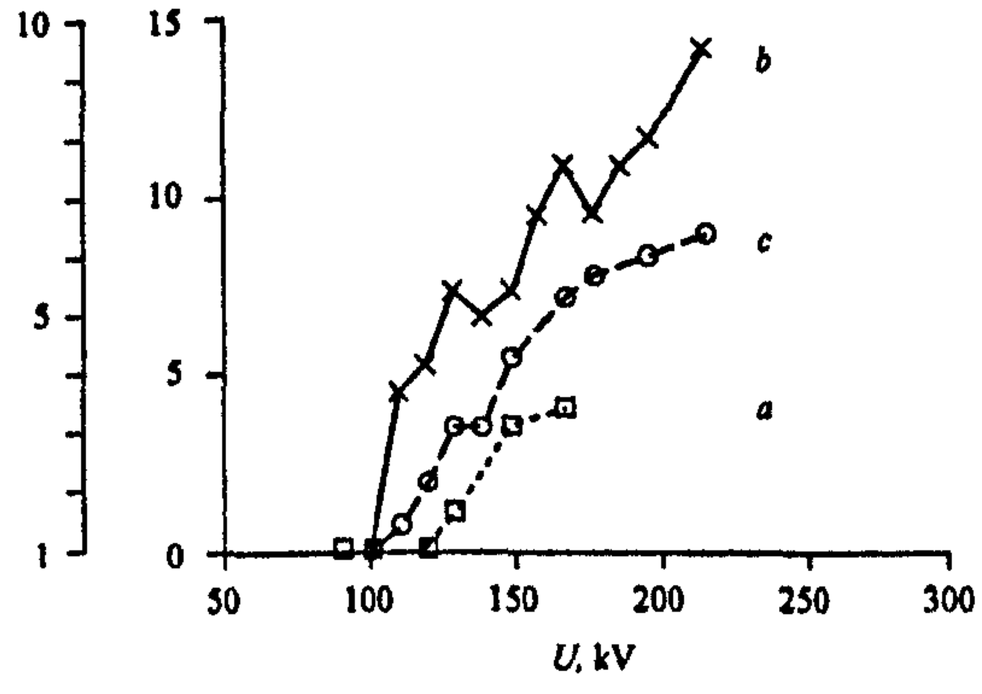

Figure 3.5: The results of tests comparing the sensitivity of three measurement systems in their response to PD from a protrusion on a GIS busbar, as reported in [54]. SNR is plotted against applied voltage for (a) IEC60270 (pC/pC) (b) UHF (dB) and (c) acoustic (mV/mV).

sensitivity of the IEC60270, UHF, acoustic and chemical methods to be compared simultaneously by testing the response of each system to a range of artificial PD sources. The data from the various techniques is expressed as signal to noise ratios so that the results may be compared. The results of tests on a protrusion attached to a 6m long busbar are shown on Figure 3.5. The general conclusions of this and other studies are summarised by Pearson et al. [30]:

- The acoustic, conventional (IEC60270) and UHF techniques all show good sensitivity.
- Acoustic measurements are nonintrusive but attenuation of the signal is high across barriers within the GIS and along the GIS chamber.
- Conventional PD measurements require an external coupling capacitor and therefore cannot be used on GIS in service.
- The UHF technique is suitable for in-service monitoring but for maximum sensitivity couplers need to be fitted inside the GIS [4].

A brief comparison of the sensitivity of the UHF method in relation to conventional IEC60270 measurements was made by Kock et al. [56]. It was shown that the conventional technique is susceptible to external electrical disturbances

[4]More recent results by Judd et al. [55] have shown that if the external coupler is properly designed, it can achieve better sensitivity than an internal UHF coupler

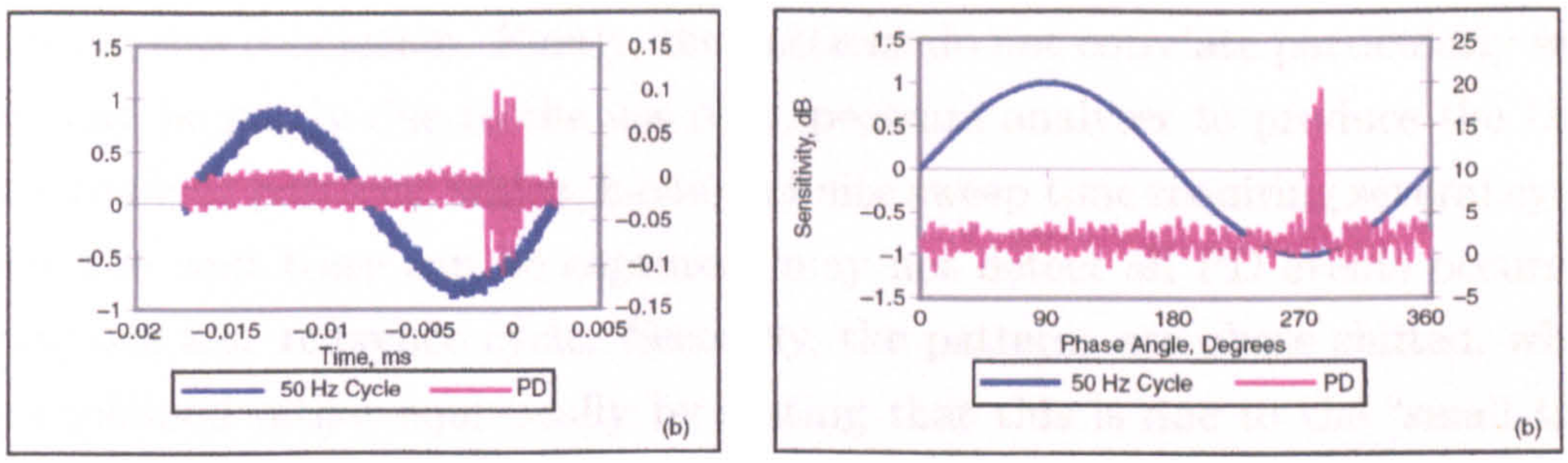

Figure 3.6: Comparing phase-resolved partial discharge patterns produced by IEC and UHF measurement systems for a corona discharges in air [57].

such as corona from overhead lines when applied to continuous on-line monitoring of Gas Insulated Switchgear (GIS). The authors noted that UHF techniques are better suited to on-line monitoring because corona discharges do not create signals with appreciable energy in the UHF range. During on-site testing, external corona measured at a level of 30,000 pC using the conventional system could be completely suppressed during UHF measurement by the addition of a 500 MHz high-pass filter. It was also shown that UHF television transmissions, mobile phone services and a nearby radar tower proved significant sources of interference, making identification of individual UHF spectral features difficult using a narrow band detection system. A comparison was made between phase-resolved patterns using the conventional, broadband UHF and narrowband UHF methods, however, no quantitative information was given respecting the similarity of these patterns, with the authors only using the phrase "the structure of both fingerprints is very similar" [5]. The paper concludes that the UHF method is "slightly less sensitive than the conventional method", however, this is not quantified in any way.

Phase-resolved PD patterns obtained using both conventional and UHF methods for a number of different discharge sources are compared in [57]. An example is shown in Figure 3.6. The authors concluded that a good phase correlation exists between each of the respective patterns, stating that a "visual study of the figures confirms this". There are, however, several points that must be raised

[5]It is important to note here that even if a quantitative comparison were made, there is no guarantee that it would be fair unless the individual PD pulses were measured simultaneously using both techniques and each pulse pair could be distinguished individually on the phase resolved plots.

regarding this conclusion. Firstly, the patterns do not correlate particularly well. This may be partly due to the use of a spectrum analyser to produce the UHF phase resolved patterns, which, having a finite sweep time requiring several cycles before the next trace can be captured, may not detect all PD events occurring during one a.c. reference cycle. Secondly, the patterns are phase shifted, which was explained rather equivocally by stating that this is due to the "small time difference between measurements and the duration of each recording".

Kurrer and Feser [58] made some interesting measurements regarding the sensitivity of the UHF method in comparison with conventional PD measurements. The authors compared the sensitivity of both techniques using a variety of PD sources including protrusions, free particles and fixed particles located inside a GIS chamber. An interesting observation was that the increase in UHF signal level is not necessarily proportional to that of the IEC60270 signal and depends on the type of defect. Only one PD source produced a good correlation between the amplitudes of both signals. The UHF technique was said to provide sensitive on-site PD measurements because of its noise immunity. On the other hand, it was observed that conventional IEC60270 measurements cannot achieve the same sensitivity on site as in the laboratory because of susceptibility to external interference. The authors made an interesting assertion regarding the need to adopt a new procedure for UHF calibration in comparison with traditional measurements. Whereas the IEC60270 technique quantifies the PD magnitude in terms of apparent charge , the UHF method cannot be calibrated in the same manner due to fundamental differences in the response of both systems to the same PD event.

3.2.2 Comparing the Responses of the UHF and IEC Systems to a PD Pulse

Published results comparing UHF and conventional PD measurements are fairly sparse. In order to compare these techniques in more detail it is important to understand how each system responds to a PD event. To this end Figure 3.7 serves two purposes. Firstly, the very different time scales on which the two systems respond to the same PD event are illustrated. A UHF pulse has a very fast response to the initial PD event and, due to multiple refections within the

enclosure, can persist for anything up to 1 μs. Secondly, it can be seen that IEC60270 pulses provide only a slow damped oscillatory response to fast PD activity. Figures 3.7 (b) and (c) show the response of two narrowband IEC60270 instruments to the same PD event.

IEC60270 instruments are classified as either wideband or narrowband depending on their frequency response. A wideband instrument consists of a wideband amplifier followed by an integrator, which is characterised by the time constant of its integrating capacitor and resistor network and has a typical bandwidth of $100 \leq \Delta f \leq 400$ kHz. The final amplitude of the signal is proportional to the total charge. Wideband instruments are capable of providing PD pulse resolution times of less than 10 μs. A narrowband instrument is defined in IEC standard 60270 as having a bandwidth of $\Delta f \approx 10$ kHz and a midband frequency of $9 \leq f_m \leq 30$ kHz.

It has been shown that UHF and IEC instruments respond to the same PD event on very different timescales and that while the IEC60270 technique attempts to quantify displaced charge, or integral of PD current, the UHF method responds to the time-derivative of PD current; two quantities that are not necessarily proportional. This is illustrated by Figure 3.8, which shows two partial discharge pulses, approximated using a Gaussian equation:

$$I_0 e^{-t^2/2\sigma^2} \tag{3.2.1}$$

where I_0 is the peak current and σ is a parameter that determines the rise time. It can be seen on examination of Figure 3.8 (a) that pulse 2 contains almost three times the quantity of charge in pulse 1 and since conventional measurement are concerned with quantifying displaced charge, pulse 2 would produce a higher apparent charge measurement on a conventional system. Although pulse 1 contains a small quantity of charge, due to its fast rise time it would produce a larger RF signal as shown in Figure 3.8 (b). This fundamental difference lies at the heart of the programme of research to be carried out.

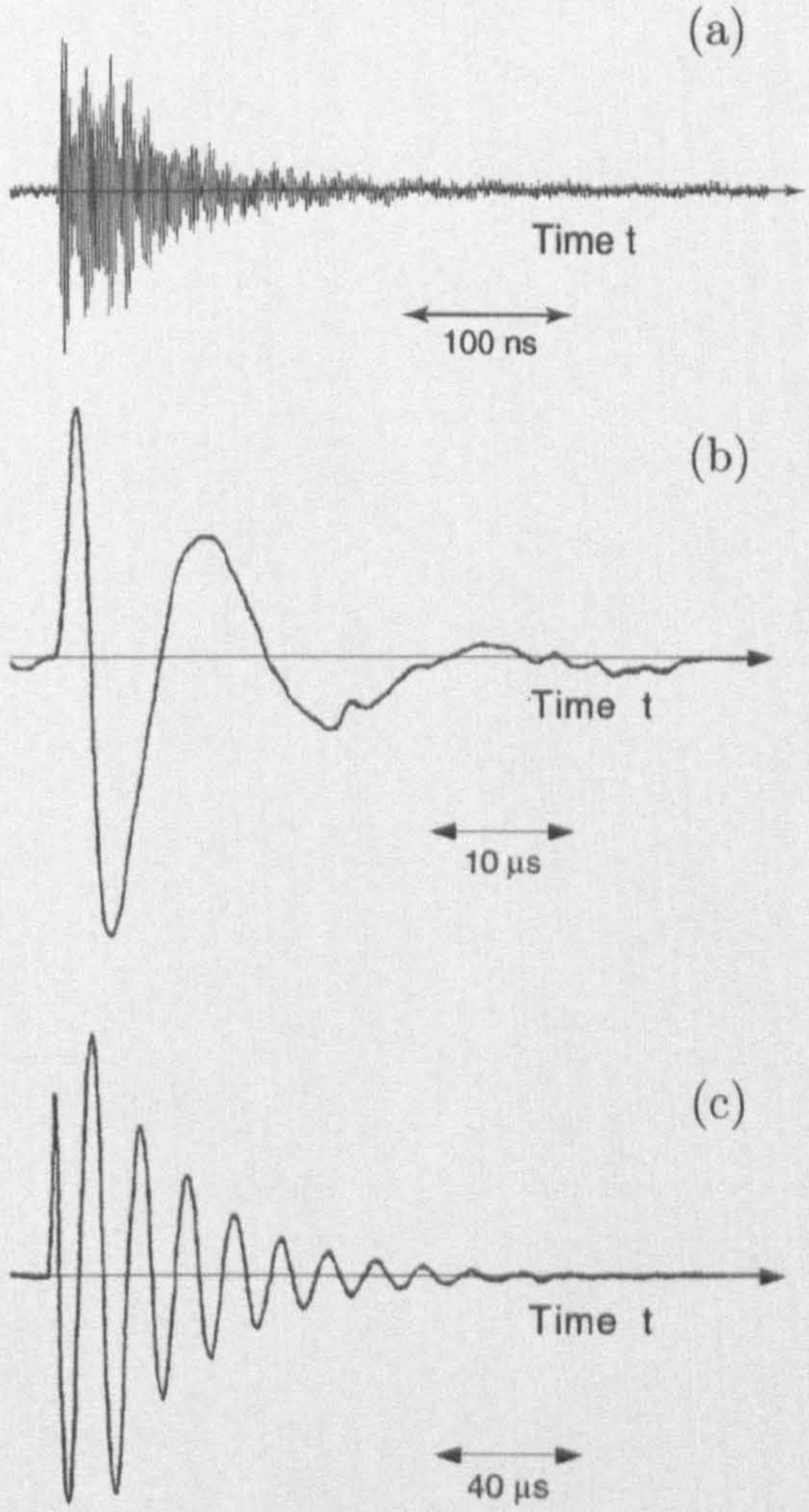

Figure 3.7: (a) A typical UHF signal produced by a void in solid insulation, (b) response of a $440kHz$ narrowband IEC60270 instrument to a PD pulse [3], (c) response of a $10kHz$ narrowband IEC60270 system to the same pulse [3].

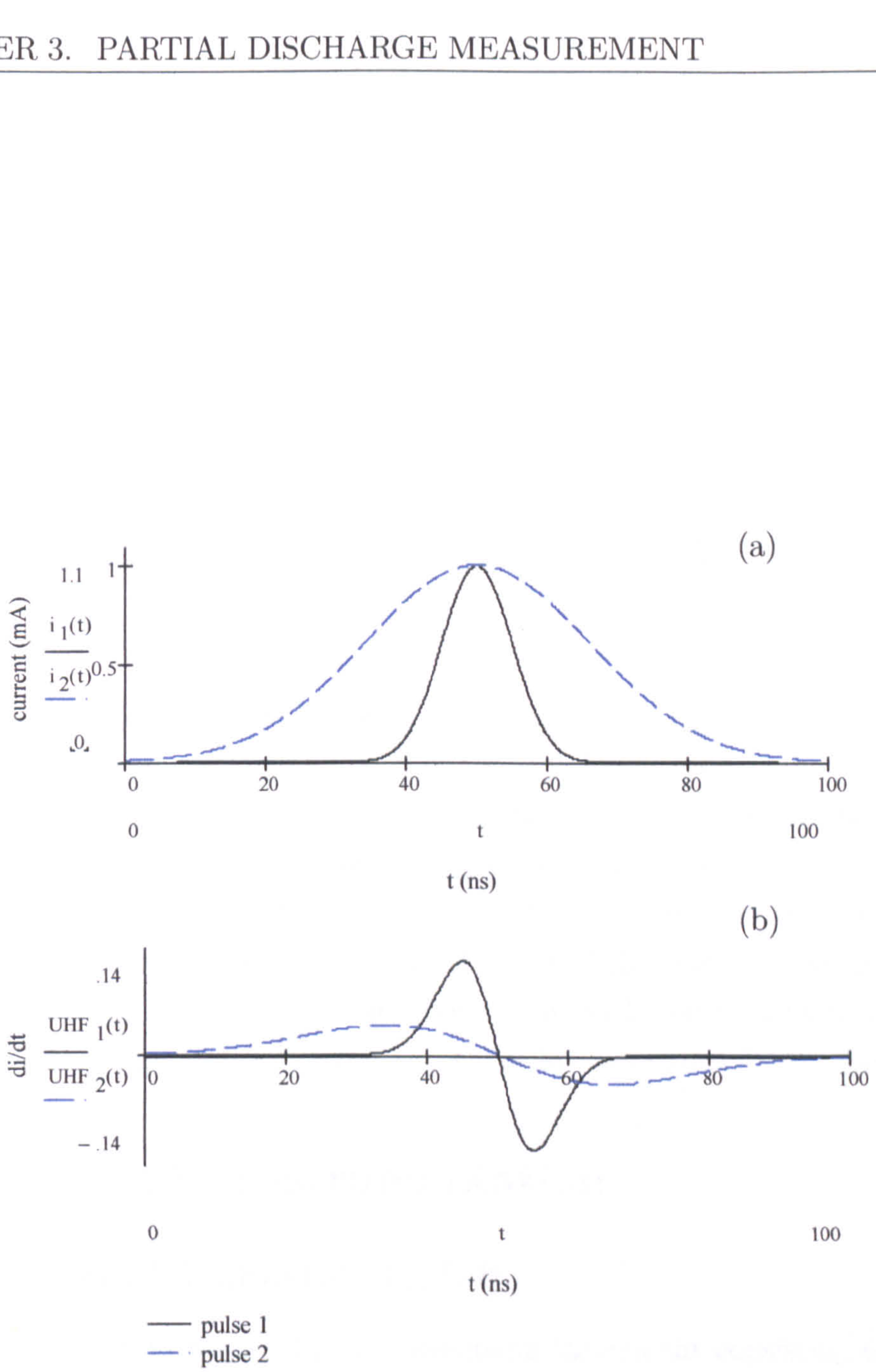

Figure 3.8: (a) Two partial discharge current pulses represented using a Gaussian function. (b) Time-derivative of the current pulses.

Chapter 4

Test Unit and Calibration

This chapter describes the calibration, testing and implementation of an experimental facility used for simultaneous partial discharge measurement applying both UHF and IEC60270 techniques. It outlines the basic principle behind the IEC60270 technique as well as describing its associated hardware. Evaluation of the test unit, including UHF sensors, is made by taking measurements on a number of well-defined PD test objects. Testing of the combined measurement system in its completed form is also reported on, with correlations being made between UHF energy and IEC apparent charge for two industrial components.

4.1 IEC60270 Instrumentation

4.1.1 Lemke Diagnostics LDS-6

The LDS-6, shown in Figure 4.1, is a wideband instrument consisting of an adjustable wideband preamplifier followed by an active integrator. The response of the integrator to a PD pulse is a voltage signal increasing with the instantaneous sum of charge. The final amplitude of the signal is proportional to the total charge.

Although the system contains many analytical and statistical features such as the ability to store and recall frequency distributions, phase-resolved distributions and impulse-impulse correlations, our main interest only concerns the output from the active integrator, the signal from which is proportional to the calibrated apparent charge of the PD pulse.

The measurement system also allows the user to store point-on-wave (phase-resolved) partial discharge data for later analysis. The system was tested using

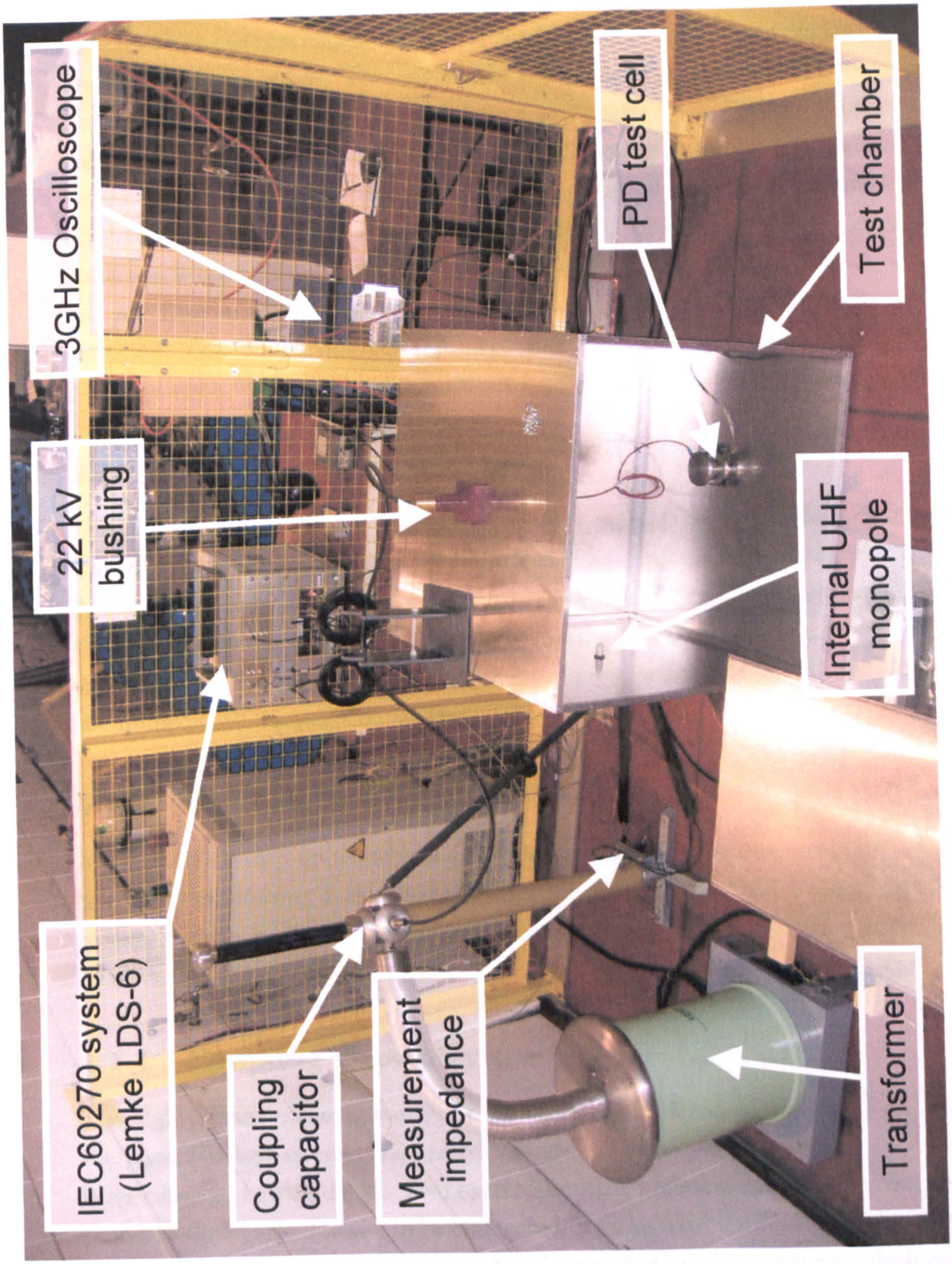

Figure 4.1: Experimental arrangement.

the PD test cells described in section 4.4.2. Phase-resolved partial discharge data can be saved in ASCII format. MATLAB is used to convert the data into a matrix of elements corresponding to the number of PD pulses occurring at a given charge and phase angle. The results are shown in Figure 4.2. PRPD patterns are as expected for the PD sources geometries under test. For the point-plane configuration, discharges are shown to initially occur on the positive half-cycle rather than the negative half-cycle of the reference wave, as would normally be expected. This is due to electrode configuration, since in this case the plane electrode is connected to the HV supply and the point electrode is connected to ground. Discharges from the void test cell occur in the first and third quadrants as expected. The free particle cell produces discharges that occur at random phase positions while their maximum amplitude is enveloped by the a.c. reference wave.

4.1.2 Regulating Transformer

The regulating transformer provides a variable output voltage of 0-380 V. The Unit consists of a single phase variable transformer with three-phase motor drive. A manually controlled 'kill' switch and under voltage coil with magnetic and thermal release are provided at the input. The unit also provides a phase reference signal to the LDS-6 PD measurement system, which can be utilised for the simultaneous PD acquisition system.

4.1.3 HV Test Transformer

A 0.38/100 kV step-up transformer, provides a high potential to an object under test. The transformer is oil-filled and uses the Oil Natural Air Natural (ONAN) cooling technique. The transformer is rated at 10 kVA for continuous usage and 20 kVA for up to 10 hours on.

4.1.4 Coupling Capacitor

The high voltage coupling capacitor shown in Figure 4.1 is represented by C_k in the basic PD test circuit. The rated voltage is 100 kV AC and the capacitance is specified at 1 nF $\pm$ 10 %. Two current-limiting high-voltage resistors are also shown in the figure. These can be connected in series with the coupling capacitor, providing an additional safety precaution in any test situation where a flashover

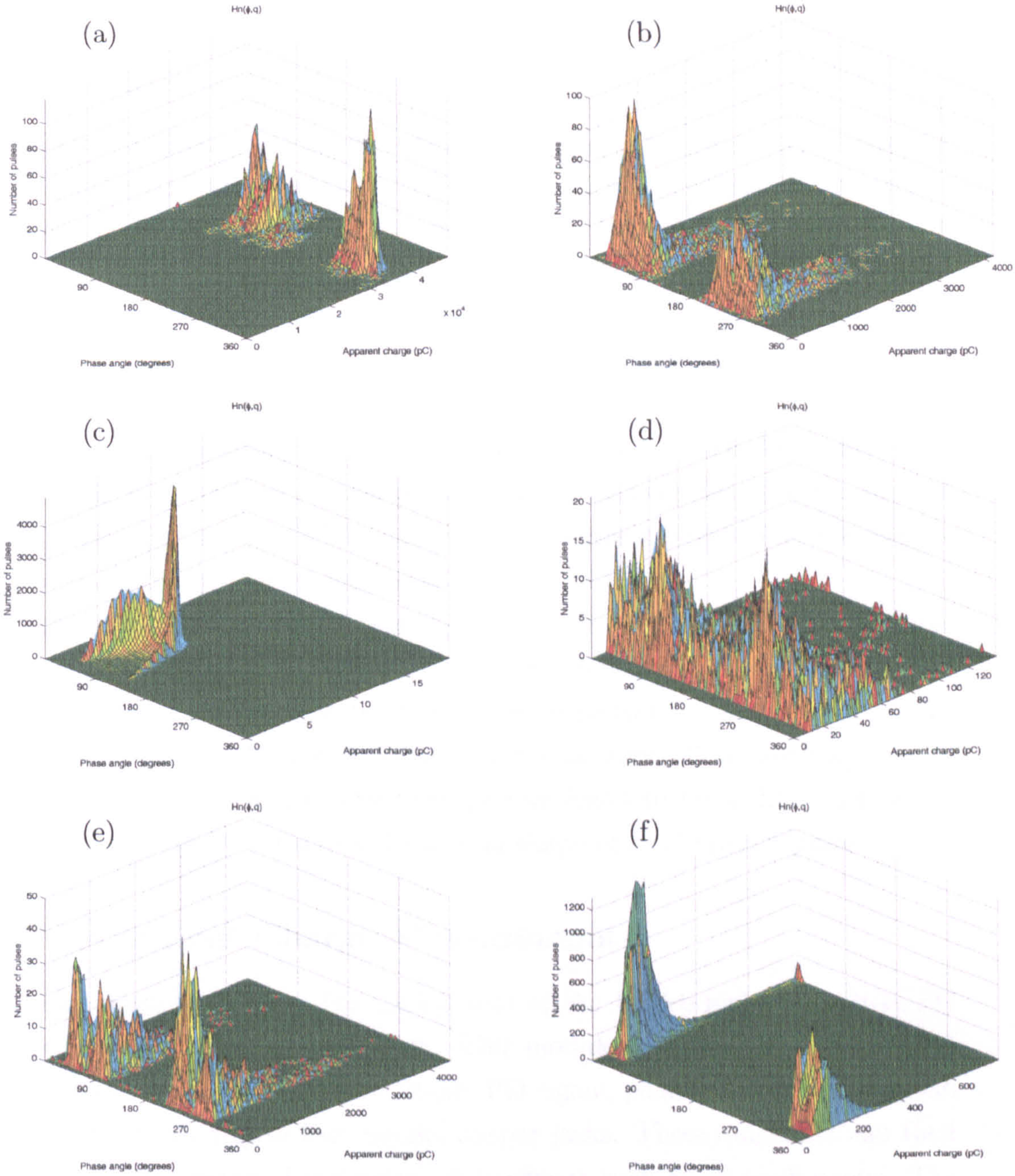

Figure 4.2: Initial testing of the IEC60270 measurement system. Phase-resolved PD patterns for (a) floating electrode in SF_6, 2 bar, (b) 0.6 mm diameter void in resin, (c) point-plane in SF_6, 14 mm tungsten needle, 25μ tip, HV applied to plane electrode, (d) free aluminium particle in SF_6, 2 bar, (e) 0.8 mm diameter void in resin, (f) surface discharge on perspex.

is likely to occur. Each resistor is rated at 1 MΩ. The HV resistors can be seen connected to the top of the coupling capacitor in Figure 4.1.

4.1.5 Calibration

The object of calibration is to verify that the system will be able to measure the specified PD magnitude correctly. Calibration of a measurement system in the complete test circuit is made to determine the scale factor k for the measurement of apparent charge. Since the capacitance of a test object C_t will affect the circuit characteristics, the IEC standard specifies that calibration should be made with each new test object unless capacitance values vary within ±10 %.

Calibration of the IEC60270 test system is achieved by injecting current pulses of known charge magnitude into the terminals of the test object. This calibration is performed in the relevant range of the magnitudes expected. For the present investigation, the Lemke LDC-5 is used to inject current pulses of known charge. Calibration of the system is automated by the LDS-6.

To check the repeatability of current pulses produced by the LDC-5 calibrator, a number of performance tests were carried out. For each calibration setting, rise time and charge magnitude were checked for consistency. The rise time varies from 3 to 10 ns, which is well within the 60 ns upper limit specified in the IEC60270 standard. The measured charge was found to be within ±6% of the specified value. Figure 4.3 shows the typical shape of a calibration pulse.

4.1.6 Apparent Charge Measurement

The main interface between the analog part of the LDS-6 and the built-in PC is known as the Digital Control Unit. This module facilitates measurement of the integrated apparent charge, wideband PD signal, peak test voltage and peak apparent charge by way of four coaxial output jacks. These quantities can then be analysed using external measurement hardware such as an oscilloscope. The output impedance from all four terminals is 1 kΩ.

Since our combined measurement strategy specifies simultaneous acquisition of both apparent charge and UHF energy, the integrated response of the input unit, shown in Figure 4.4 (b), is fed directly into the oscilloscope along with the phase reference voltage and signals from one or two RF sensors. However, before apparent charge can be calculated, the relationship between the peak output

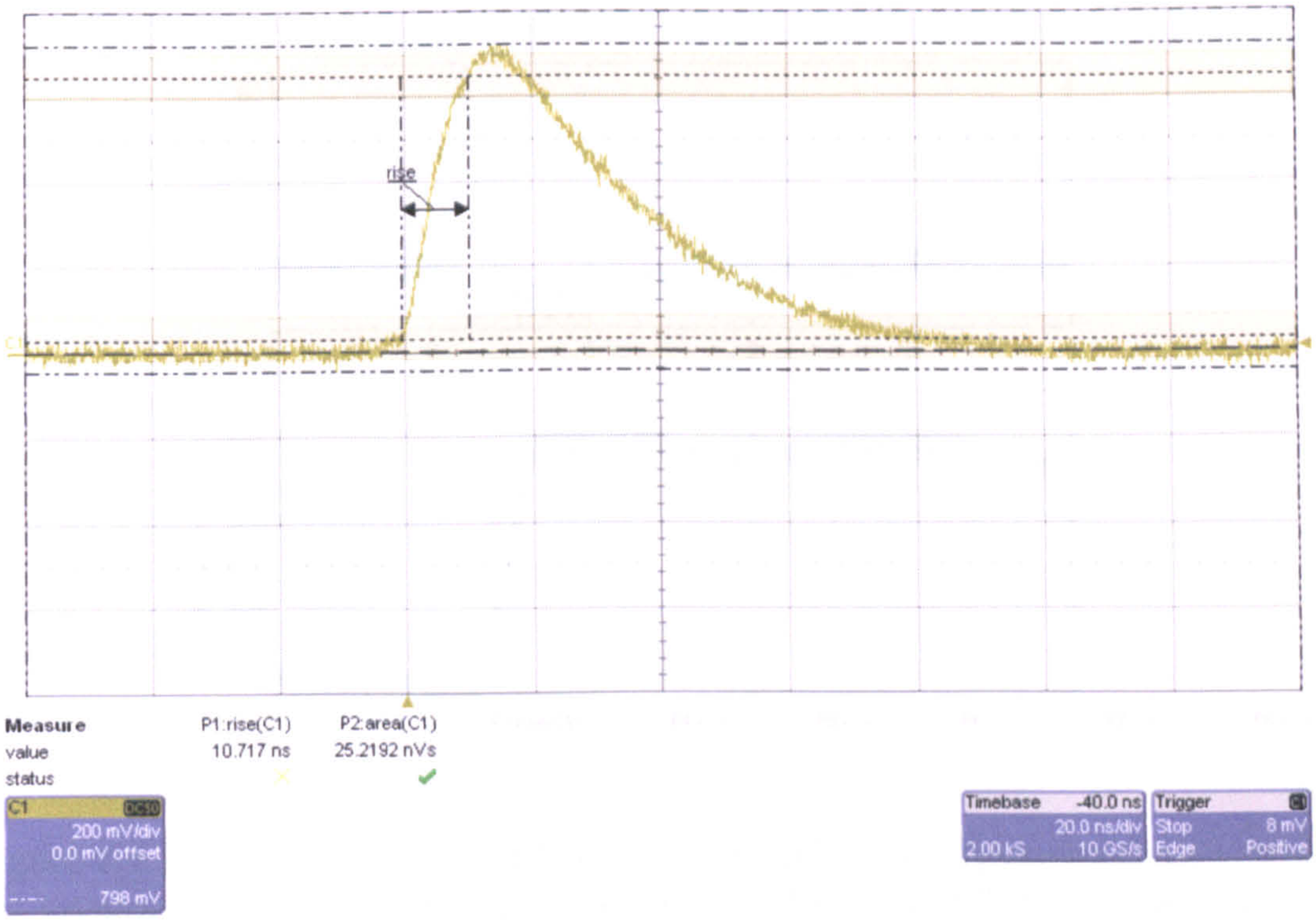

Figure 4.3: A 500 pc calibration pulse from the LDC-5.

voltage from the LSD-6 Digital Control Unit and apparent charge must be quantified for a given PD source. This is achieved by injecting artificial PD pulses of known magnitude and plotting these against their corresponding output voltage measured on the oscilloscope. An example is given in Figure 4.5. It should be noted that the output voltage never actually reaches 140 V as shown on the y-axis. Rather, these voltages result from factoring out the attenuation applied internally by the LDS-6. It is also noted that this relationship will change whenever a new calibration is made. Re-calibration is most likely to be implemented when the PD test object is replaced by one whose capacitance is judged to fall outwith ± 10 % of the previous value.

4.2 RF Measurement

Many diverse forms of UHF couplers exist [30, 59–61] for GIS monitoring applications, planar couplers are preferred since they cause minimal distortion of the electric field. Disk couplers, spiral couplers and dipoles have all shown good sensitivity, however, due to the required mounting arrangements on real electrical

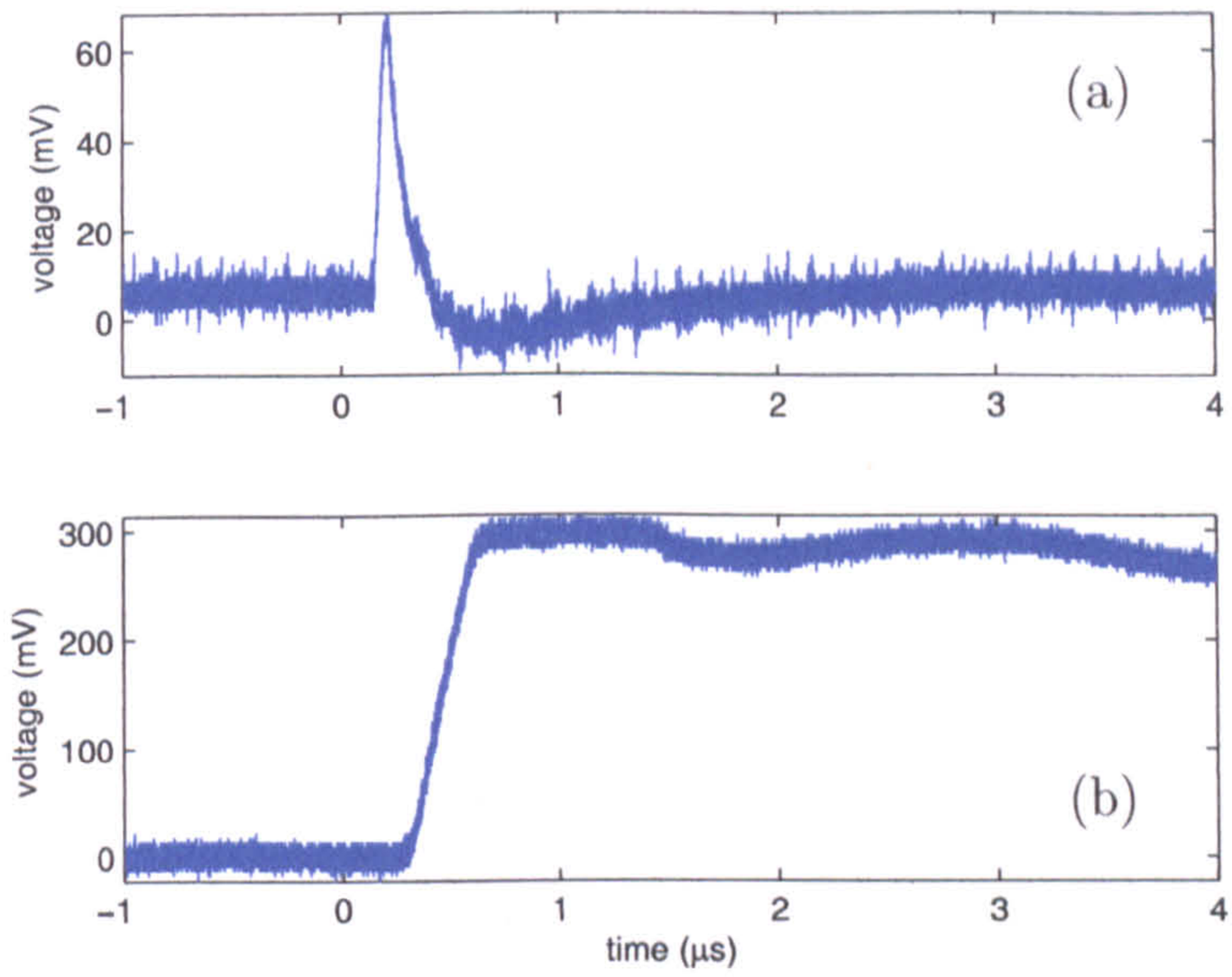

Figure 4.4: The response of the LDS-6 to a PD pulse. (a) Apparent charge signal. (b) Integral of the apparent charge signal taken from the 'CHARGE' terminal on the Digital Control Unit - the peak value is directly proportional to apparent charge.

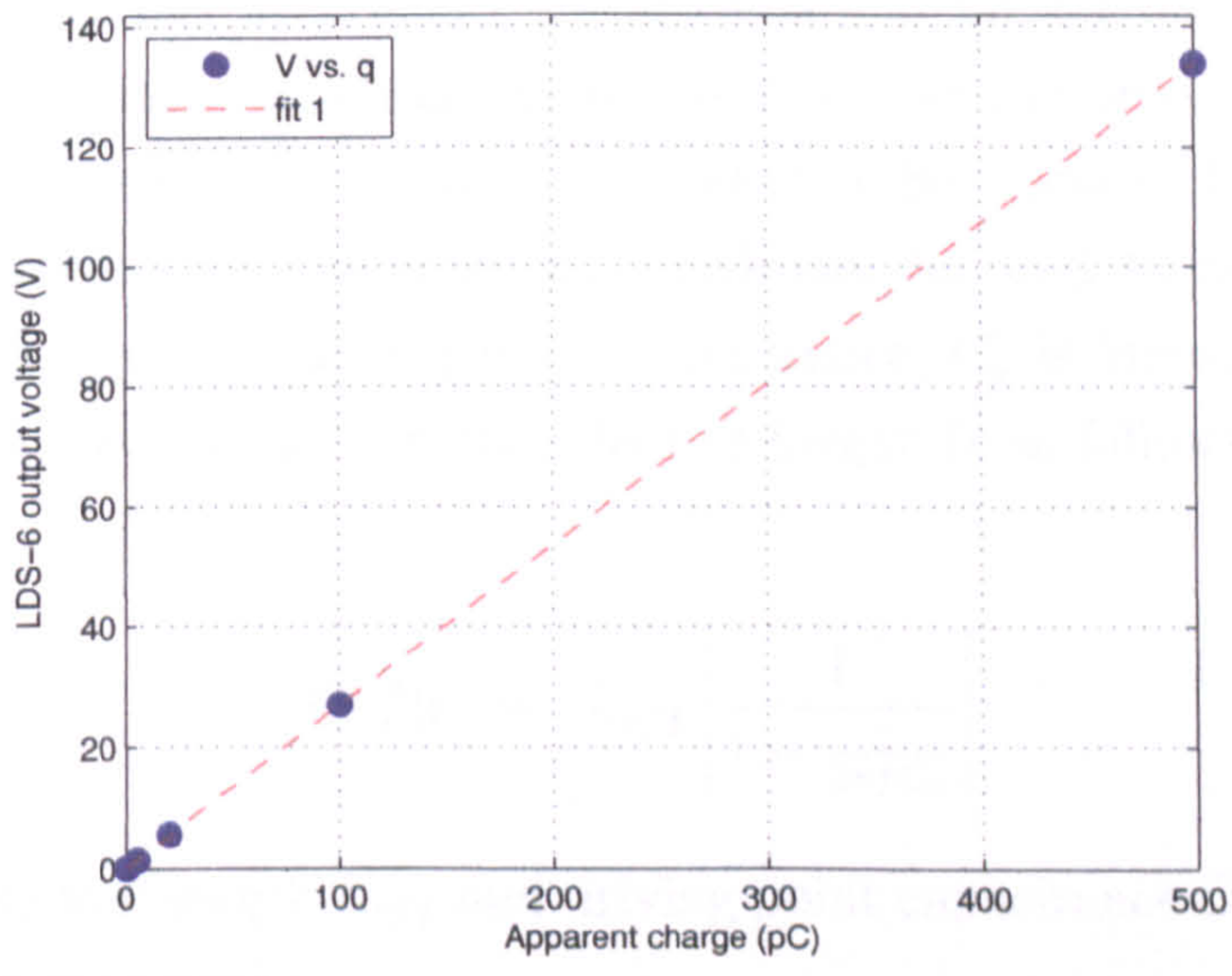

Figure 4.5: Calibrating the LDS-6. The graph shows an example of the relationship between the magnitude of the injected charge and the corresponding peak output voltage from the LDS-6 'CHARGE' output terminal for a particular test configuration. The relationship varies depending on the impedance of the test object but remains linear.

plant, the response of these couplers can be complex. For the purposes of this investigation, all aspects of the transfer function will be kept as simple as possible. RF monopole antennas were therefore manufactured and fitted so as to intrude minimally into the test volume. The couplers were designed to cause minimal distortion of the electric field. The simplicity of a monopole antenna is advantageous firstly in that construction is fast and relatively cheap – a monopole need only consist of a wire and a microwave coaxial connector – secondly in that their frequency response is well understood and thirdly in that the sensor couples with the electric field normal to the chamber wall in a simple manner.

4.2.1 RF Sensor Calibration

Calibration is performed on all RF sensors using a pulsed gigahertz transverse electromagnetic (GTEM) cell. The transient calibration system [62, 63], is able to provide the frequency response of the sensor in the range 0.2 - 2 GHz by subjecting it to a step electric field with a rise time of less than 100 ps.

Four monopoles antennas were manufactured initially. The monopole antenna was chosen because of its simplicity; a monopole is easy to mount on a ground plane and can be constructed using only an SMA connector and a wire. Because the frequency response of a monopole antenna can be derived empirically, its complex-valued transfer function can be used to find the original electric field. The monopole can therefore be used as an electric field probe. Figure 4.6 shows the equivalent circuit for the antenna, which can be used to derive the transfer function provided the driving point capacitance, C_a is known. The transfer function is expressed in terms of the effective height H as follows [64]

$$|H(f)| = L_{eff}\left|\frac{1}{1-\frac{j}{2\pi f C_a}}\right| \tag{4.2.1}$$

The effective half length L_{eff} and driving point capacitance C_a of a monopole antenna can be expressed as

$$L_{eff} = \frac{L}{2}\cdot\frac{2\ln\frac{2L}{r}-1}{2\ln\frac{2L}{r}-2+\ln 4} \tag{4.2.2}$$

$$C_a = \frac{4\pi\epsilon_0 L}{2\ln\frac{2L}{r}-2-\ln 4} \tag{4.2.3}$$

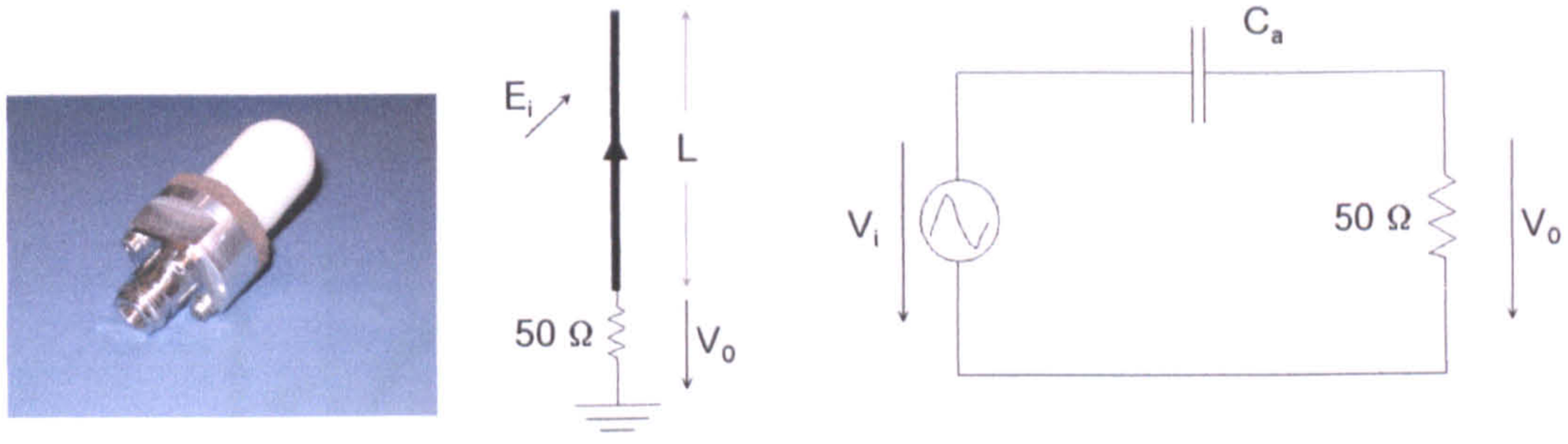

Figure 4.6: A monopole antenna with its equivalent circuit.

[64] where L is the physical length of the antenna (35 mm) and r is its radius (0.5 mm). According to Equations (4.2.3) and (4.2.2), the coupler has a driving point capacitance $C_a = 2.058$ pF and an effective half length of $L_{eff} = 16.1$ mm. Figure 4.7 shows the transfer function for the monopole, plotted using Equation (11.2.6), is in close agreement with that obtained using the GTEM calibration cell. Because the transfer function is complex-valued as shown in Figure 4.8, it can be used to reconstruct the incident signal.

4.2.2 Reconstruction of the Incident Electric Field

Reconstruction of the incident signal is achieved firstly by zero-padding the measured signal with a base 2 number of data points. Zero padding allows the number of points on the time domain record to be increased, producing a decreased frequency spacing in the discreet fourier transform, allowing more accurate visual comparisons between frequency spectra [65]. The signal is then transformed into the frequency domain and truncated to eliminate frequencies below 10 MHz. This is because calibration in the time domain using a transient cell is only accurate at higher frequencies [1].The resultant frequency spectrum is then divided by the RF sensor transfer function. The real part of the inverse FFT is then computed for the resultant signal, giving the incident electric field as shown in Figure 4.9.

[1]See IEEE Standard 1309 [66]

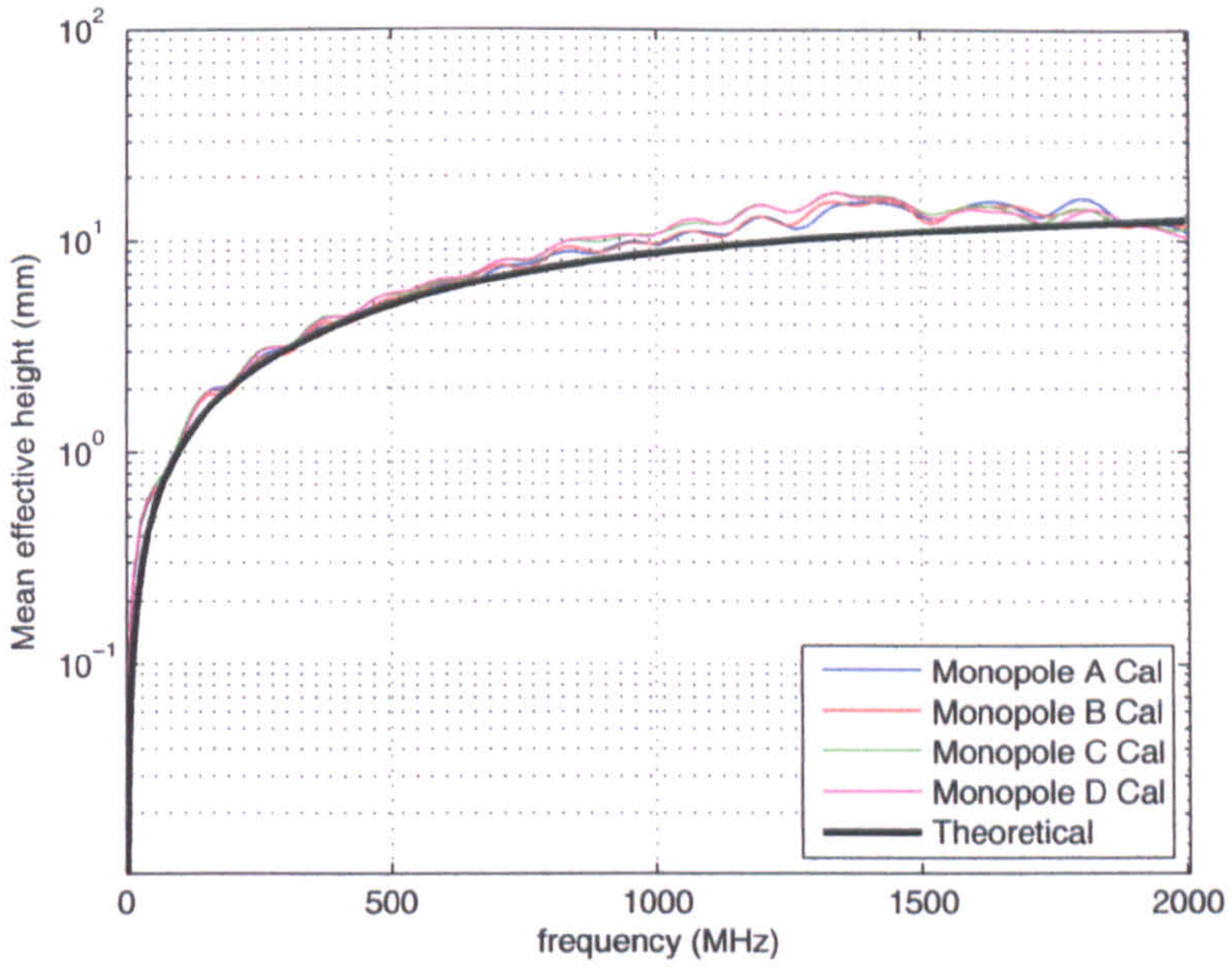

Figure 4.7: The transfer functions of four identical monopole antennas are shown along with the response of an ideal monopole having the same dimensions. Measured transfer functions were found using a pulsed GTEM calibration cell. Theoretical response was plotted using values of $C_a = 2.058$ pF and $L_{eff} = 16.1$ mm.

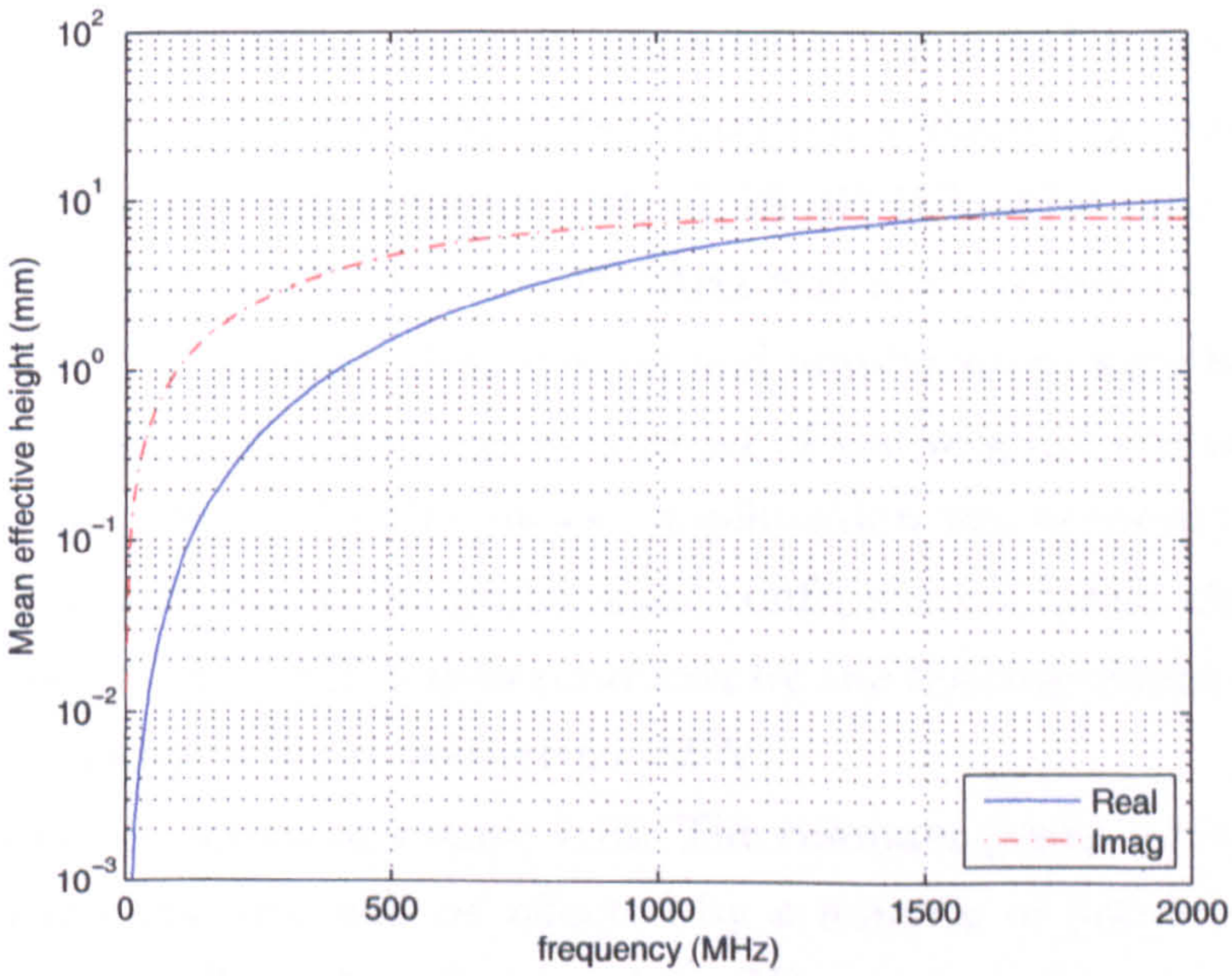

Figure 4.8: Real and imaginary parts of the complex monopole transfer function (shown as the black line in Figure 4.7).

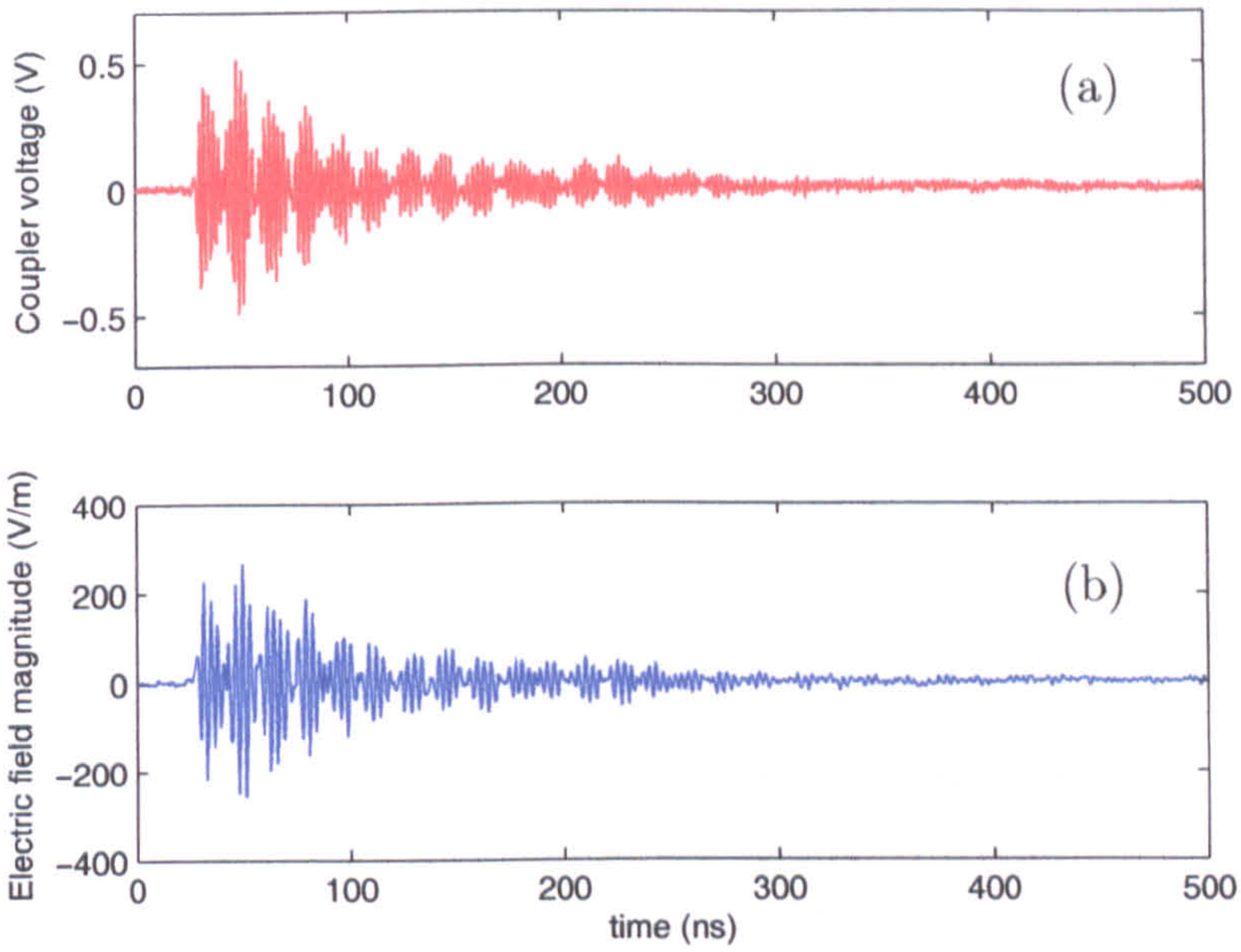

Figure 4.9: (a) Output voltage from RF sensor. (b) Incident electric field reconstructed using the RF sensor transfer function.

4.2.3 RF Sensor Response to Selected PD Sources

The RF part of the measurement system was evaluated by capturing selected PD signals produced using the test geometries mentioned previously. It was necessary to either attenuate or amplify the output voltage from the UHF coupler depending on the PD source under test. A 25 dB HP8447D dual channel UHF amplifier with a bandwidth of 0.1–1300 MHz was used as well as HP8491A 12.4 GHz bandwidth attenuators. Attenuation and amplification were factored out in post-processing to give a true representation of the original signal. Due to the respective amplitudes of the PD pulses, amplification was necessary for detection of RF signals produced by the point-plane configuration, while attenuation was required for detection of RF pulses produced by the floating electrode in order to limit the oscilloscope's input voltage to <5 V.

The signals are shown in Figure 4.10. The resonant peaks, which can be seen in the frequency spectra, will be affected by a number of parameters including the location of the PD within the chamber, PD current pulse shape, RF coupler response and external interference. Resonant peaks at 225 MHz are common to all defects. The surface discharge contains three other main frequency components of 325, 475 and 775 MHz. RF signals from the free particle test cell are less resonant,

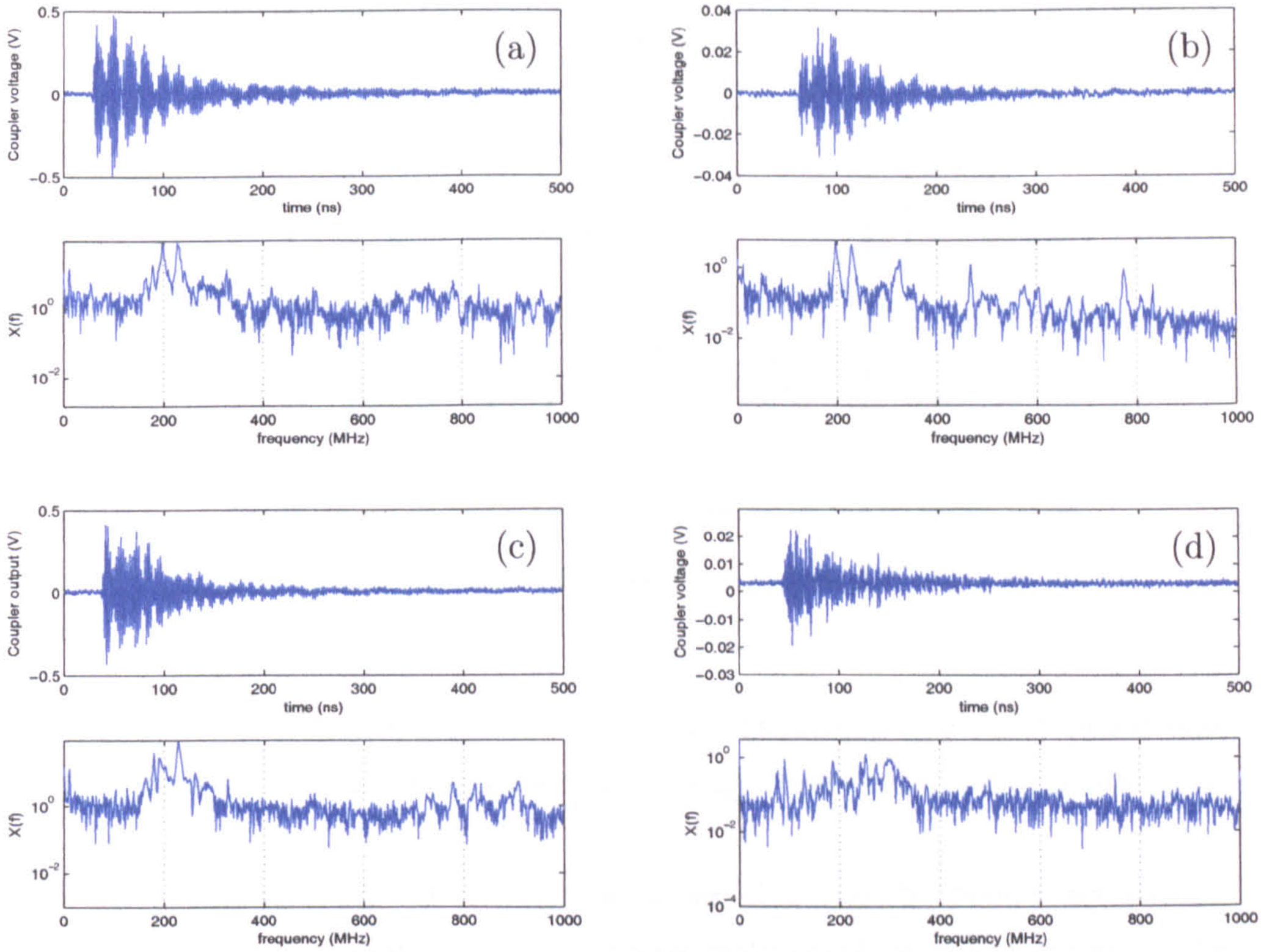

Figure 4.10: RF signals and corresponding frequency spectra produced by a (a) floating electrode, (b) surface discharge, (c) void in resin and (d) free particle in SF_6.

containing a wider spread of frequency components at a lower amplitude.

4.3 Phase Angle Measurement

4.3.1 Phase Reference Circuit

In order to accurately determine the phase position at which each PD occurs, a phase reference circuit, which produces an output voltage that is proportional to phase angle, was constructed. Using a BNC connection, it is possible to obtain the 50 Hz reference wave directly from the HV power supply used to energise the PD test cell. Unfortunately, since it is necessary to capture both RF and IEC pulses using a short timebase, the point at which each pulse occurs becomes ambiguous. This is because the same voltage levels occur on both the rising and

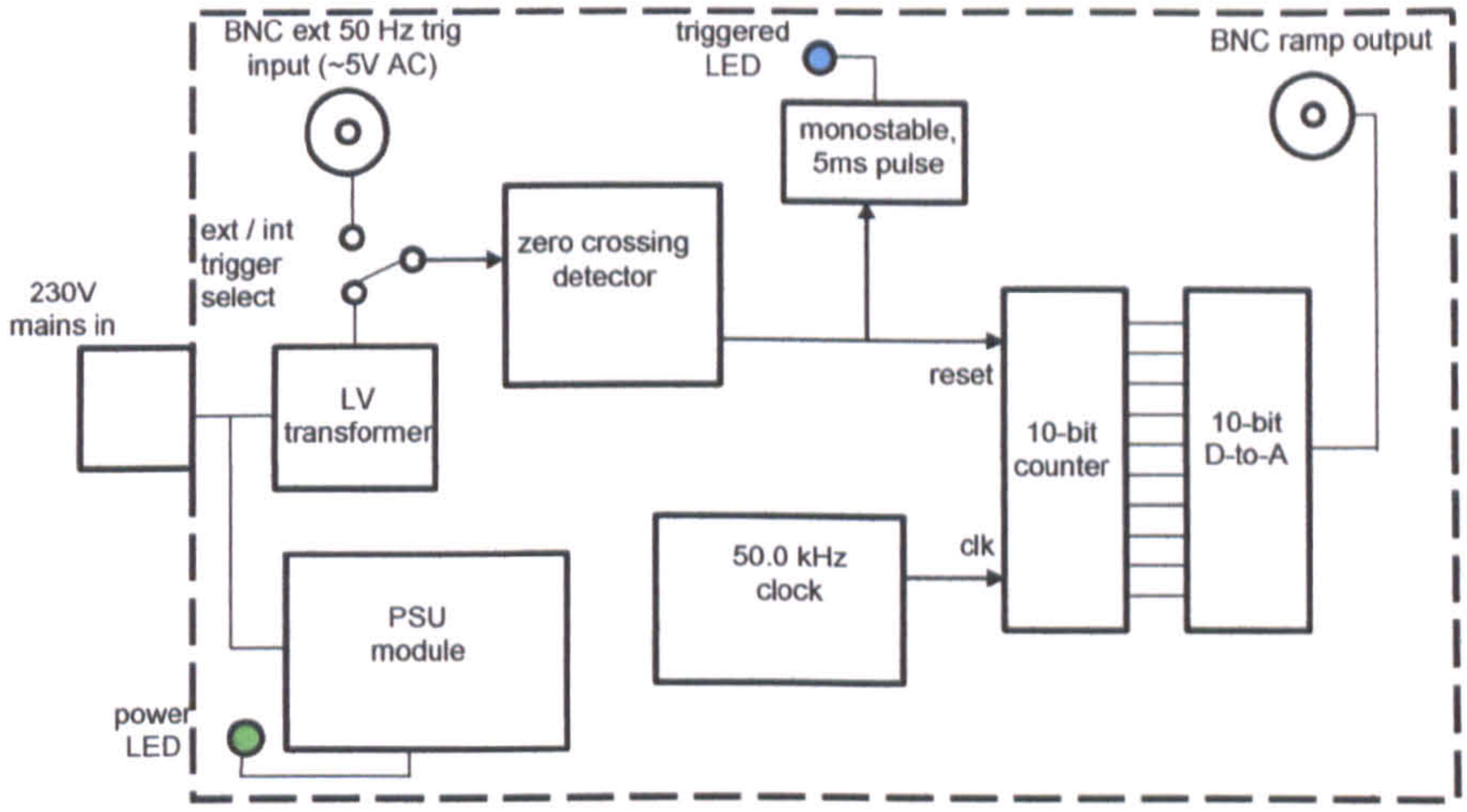

Figure 4.11: Phase reference circuit.

falling edges of the reference sine wave and when examined in a short timeframe, it is impossible to determine whether the voltage corresponds to the rising or falling edge.

The phase-reference circuit (PRC) overcomes this issue by producing a ramp output voltage that is proportional to the phase position of the reference wave. An additional advantage is the ability to overcome any phase ambiguity introduced by the presence of harmonics or voltage spikes in the a.c. supply. Figure 4.11 shows the circuit layout. A circuit schematic is provided in Appendix B.

4.3.2 Phase Reference Software

High-level software, developed using Matlab, has been used to produce the phase resolved patterns from data which has been previously captured and saved using the oscilloscope. Since the PRC produces a voltage ramp at its output where 0 V corresponds to 0^0 and 2.56 V corresponds to 360^0, calculating the phase position is simply a matter of multiplying the voltage level by 360/2.56. As with simultaneous RF/IEC measurement, the software calculates the energy of the captured RF pulses by taking the discrete integral of the trace. The peak value of the IEC pulse is proportional to apparent charge and is dependent on the IEC calibration factor for the PD source under test as well as any attenuation on the channel. Due to the large quantity of data recorded (around 6000 traces), it can take around 15 min to process the data for a single experiment. The software therefore produces a small data file containing phase-resolved information so that

the program only requires to be run once in order to produce the PRPD patterns.

4.4 Construction of Test Unit Incorporating Both Techniques

4.4.1 Test Chamber

The test chamber consists of the 1 m^3 aluminium box shown in Figure 4.1. The chamber was designed so as to provide a defined geometry for consistency of measurement. The chamber is also sealed to provide shielding from extraneous signals and to maximise the total energy of any measured RF signals. One side panel can be removed to allow quick access to any test objects located inside the chamber. A bushing is used to connect the HV supply to the object under test. The bushing is PD-free up to 20 kV, which is greater than the inception voltage for all test objects.

Connection to the HV supply is made by means of an RG213 coaxial cable with both the inner and outer conductors connected to the supply. Connections to the bushing and coupling capacitor are made using specially manufactured PD-free brass connectors which can be observed in Figure 4.1.

4.4.2 PD Sources

A number of PD sources have been manufactured to recreate various defects typically encountered in insulation systems. Most cells consist of a small pressure vessel formed by a Perspex cylinder between aluminium end plates clamped together with insulating tie rods and containing one of the defects.

Figure 4.12 shows a void discharge test cell. Between the upper and lower electrodes is a resin sample containing voids. Figure 4.13 shows a surface discharge test cell. Tracking on the outer surface of the perspex casing was caused by a flashover and has now been utilised to produce a repeatable surface discharge source. Figure 4.14 shows a point-plane test cell which is used to produce corona discharge. The test cell also facilitates direct PD current pulse measurement by means of a 50 Ω coaxial connection to the needle electrode. Figure 4.15 shows a floating electrode test cell containing pressurised sulphur hexafluoride (SF_6) gas. The cell produces large discharges (in the order of 10,000 pC). Figure 4.16 shows a free particle test cell, also containing pressurised SF_6 gas. The test cell is based

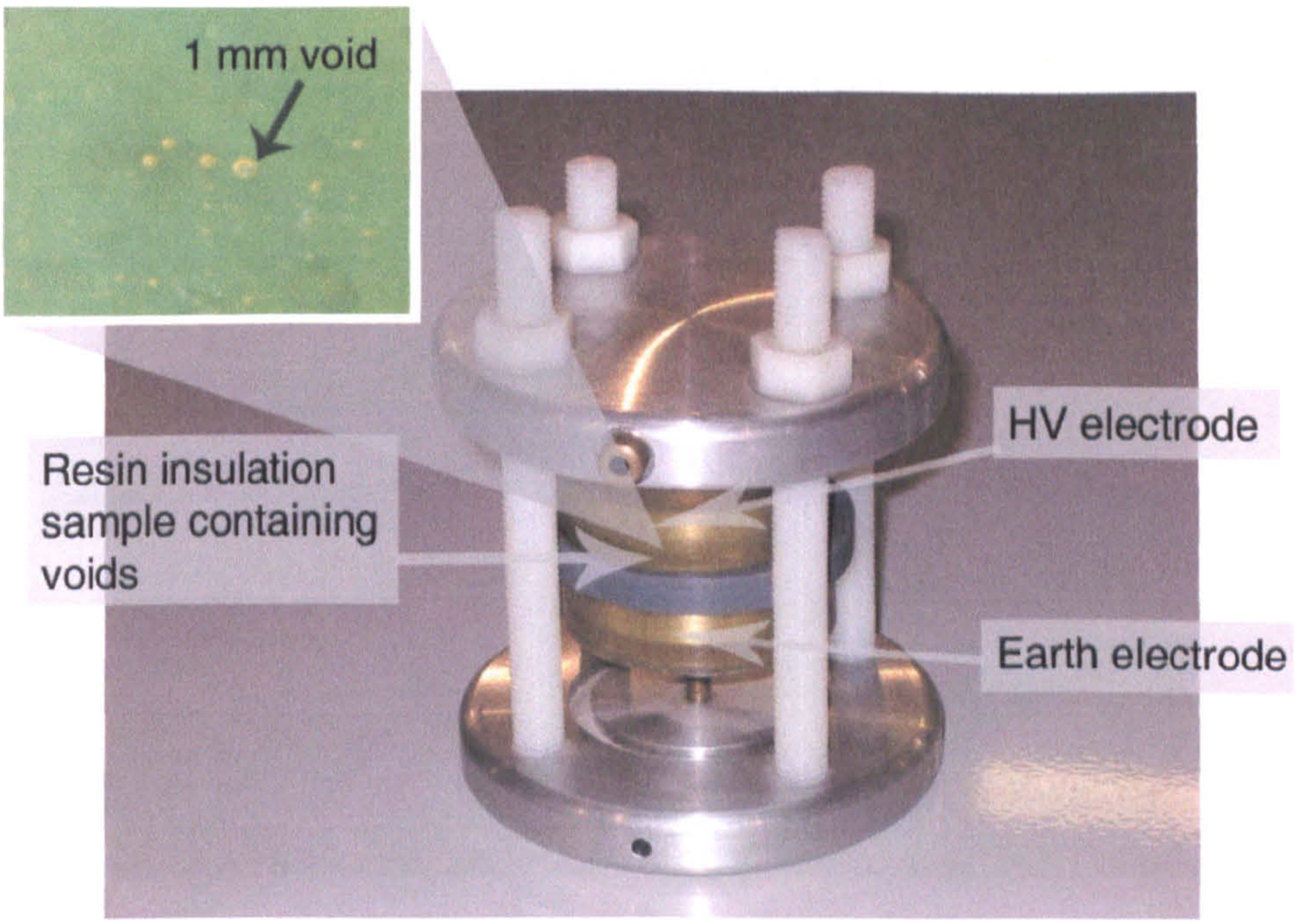

Figure 4.12: Void discharge test cell.

on a design by Hampton et al. [46] containing an aluminium sphere that can move freely in a concave dish.

4.4.3 Data Acquisition and Analysis

Simultaneous acquisition of RF, IEC and phase reference data is achieved using a single oscilloscope (LeCroy WavePRO 7300). Using a single oscilloscope is advantageous as it facilitates the use of 'sequencing mode' to store 20 to 500 waveforms in the oscilloscope's acquisition memory. This allows dead time between trigger events to be limited. Complicated sequences of PD events can be captured in fine detail while ignoring uninteresting periods. Figure 4.18 shows the LeCroy 7300 oscilloscope operating in sequence mode. It should be noted that since RF and IEC pulses are acquired simultaneously, each pulse pair [2] in the figure can be traced back to a single PD event. Around 4000 PD events are recorded for each test configuration. Due to the large volume of data (around 70 MB), calculation of RF energy and peak apparent charge cannot be performed in real time.

[2] RF and IEC60270 pulses

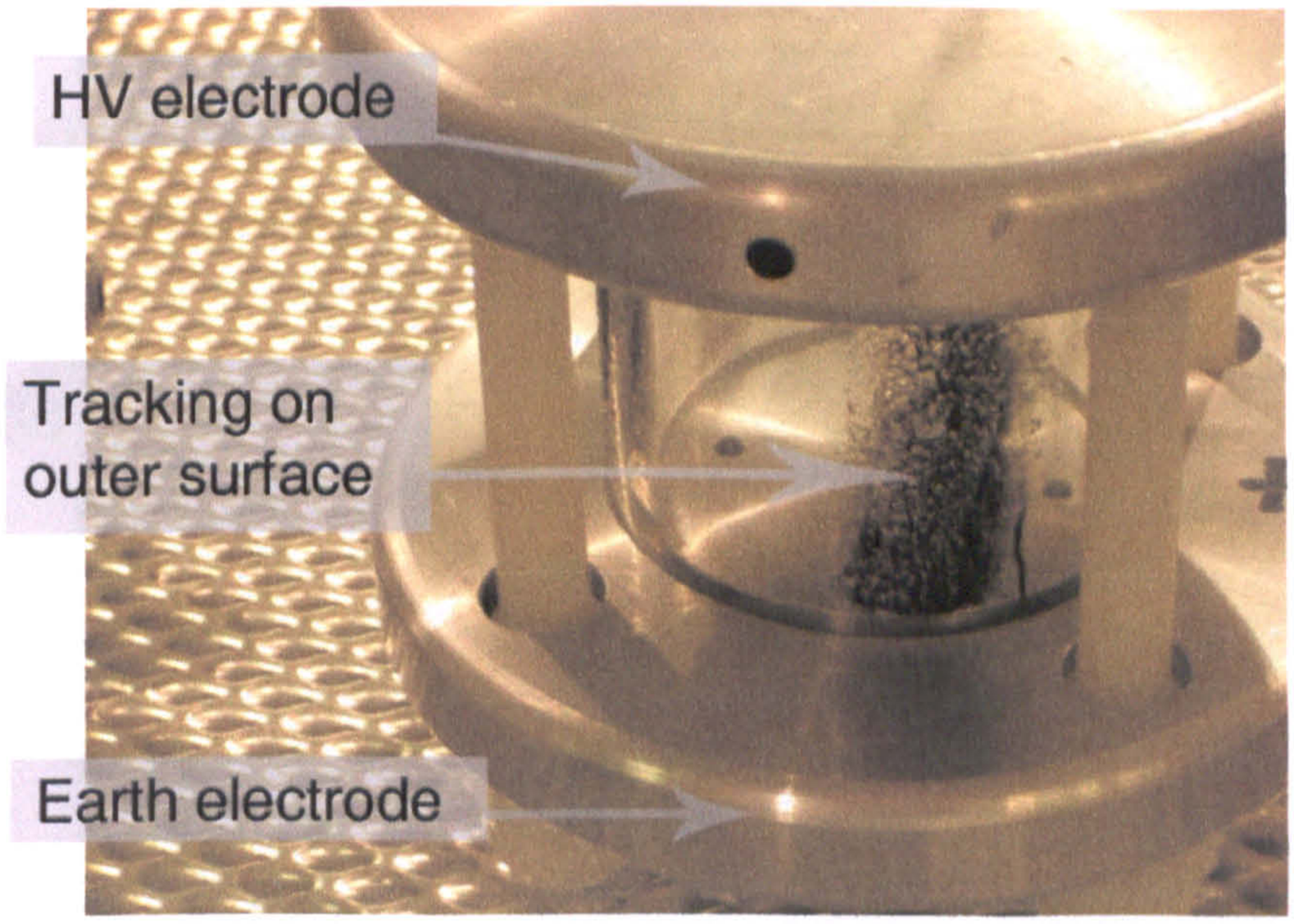

Figure 4.13: Surface discharge test cell.

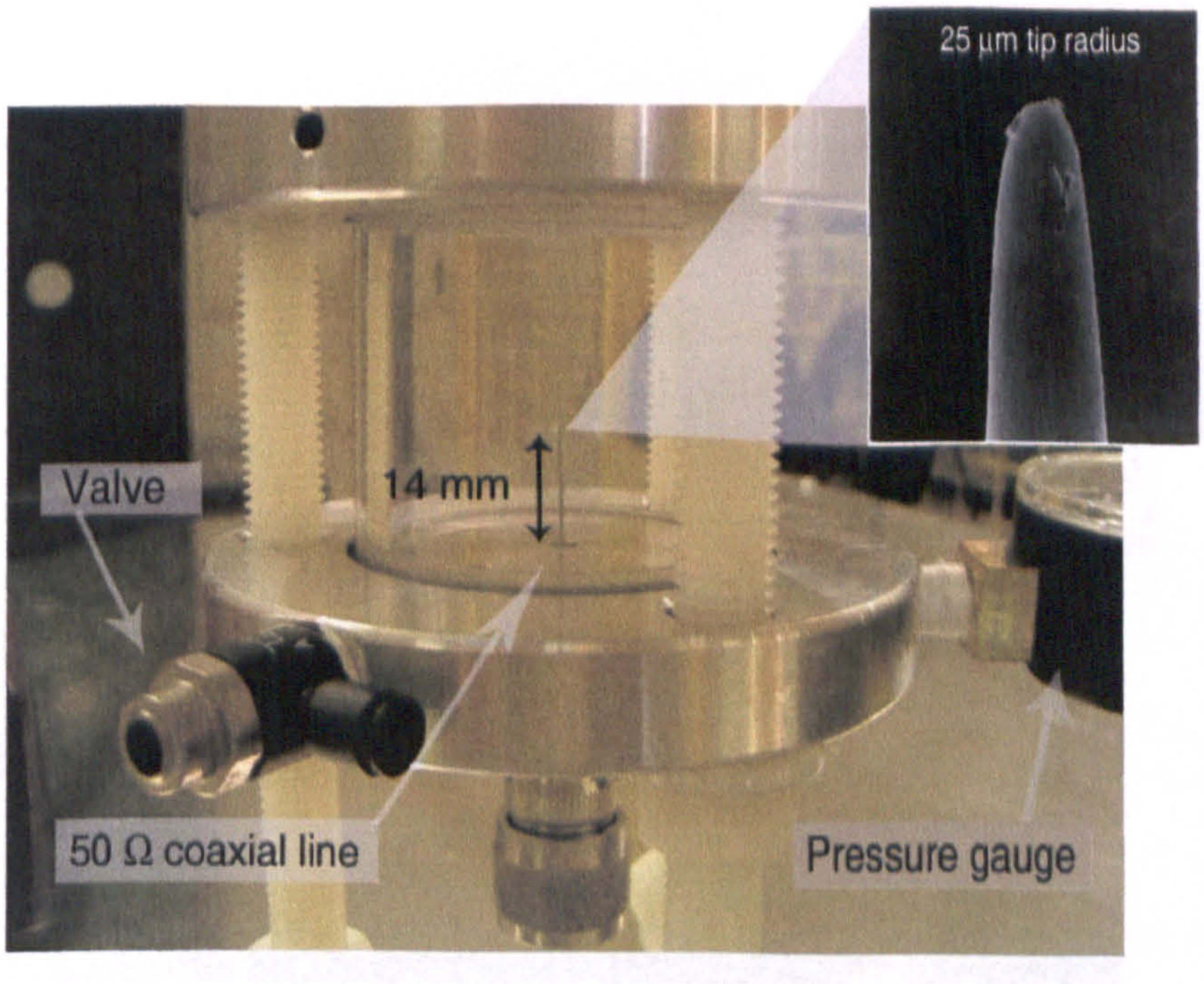

Figure 4.14: Point-plane test cell.

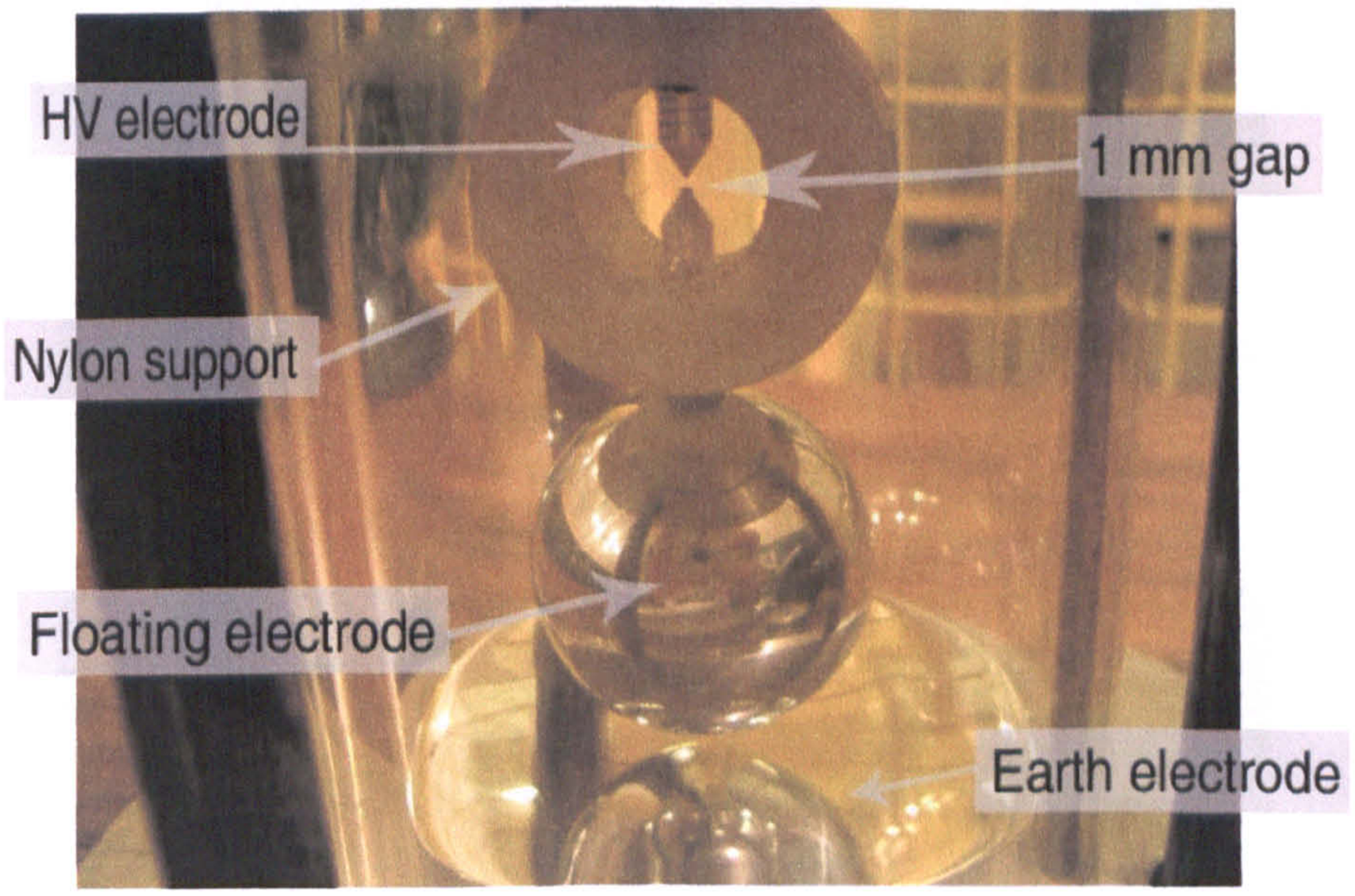

Figure 4.15: Floating electrode test cell.

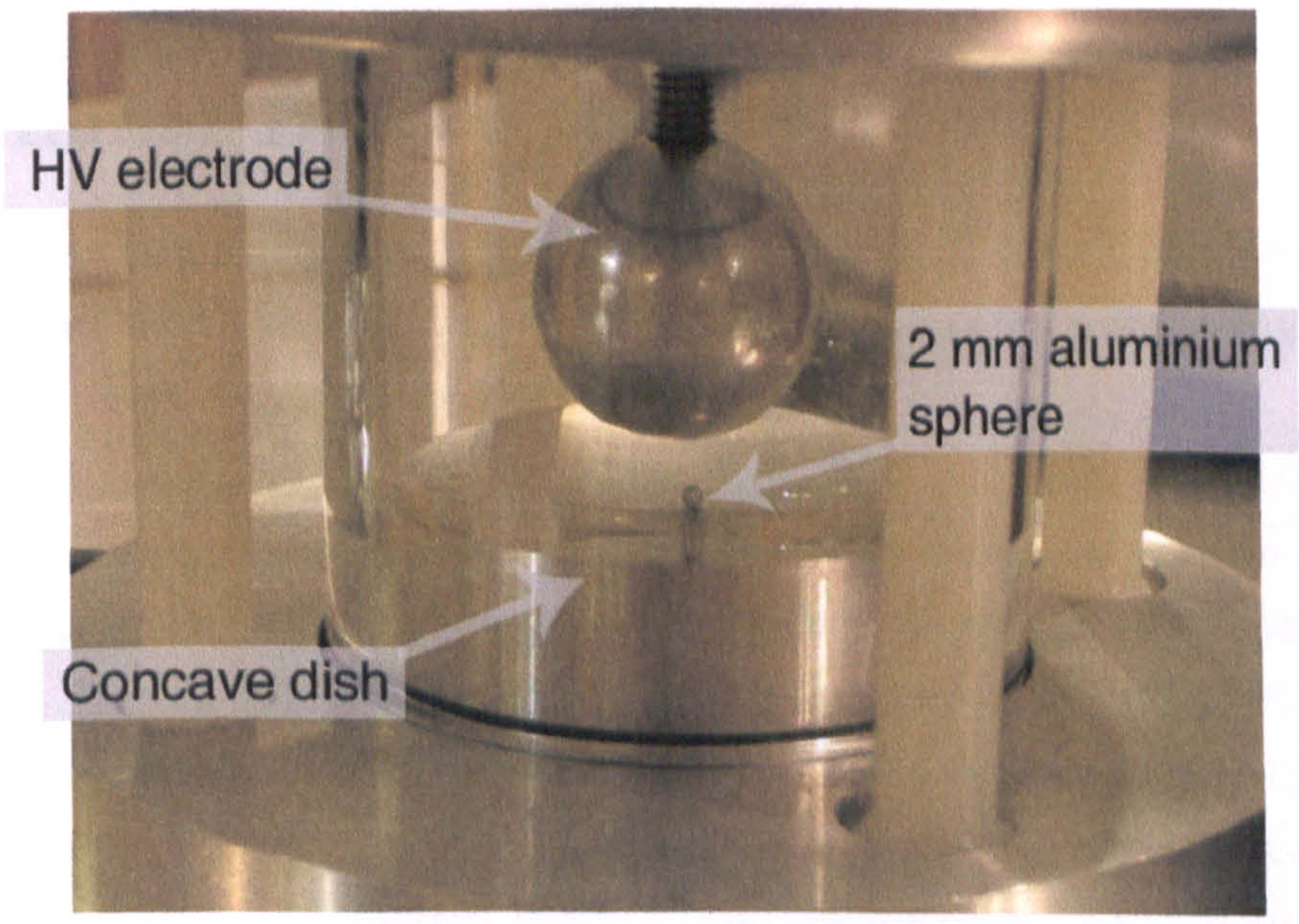

Figure 4.16: Free particle in SF_6.

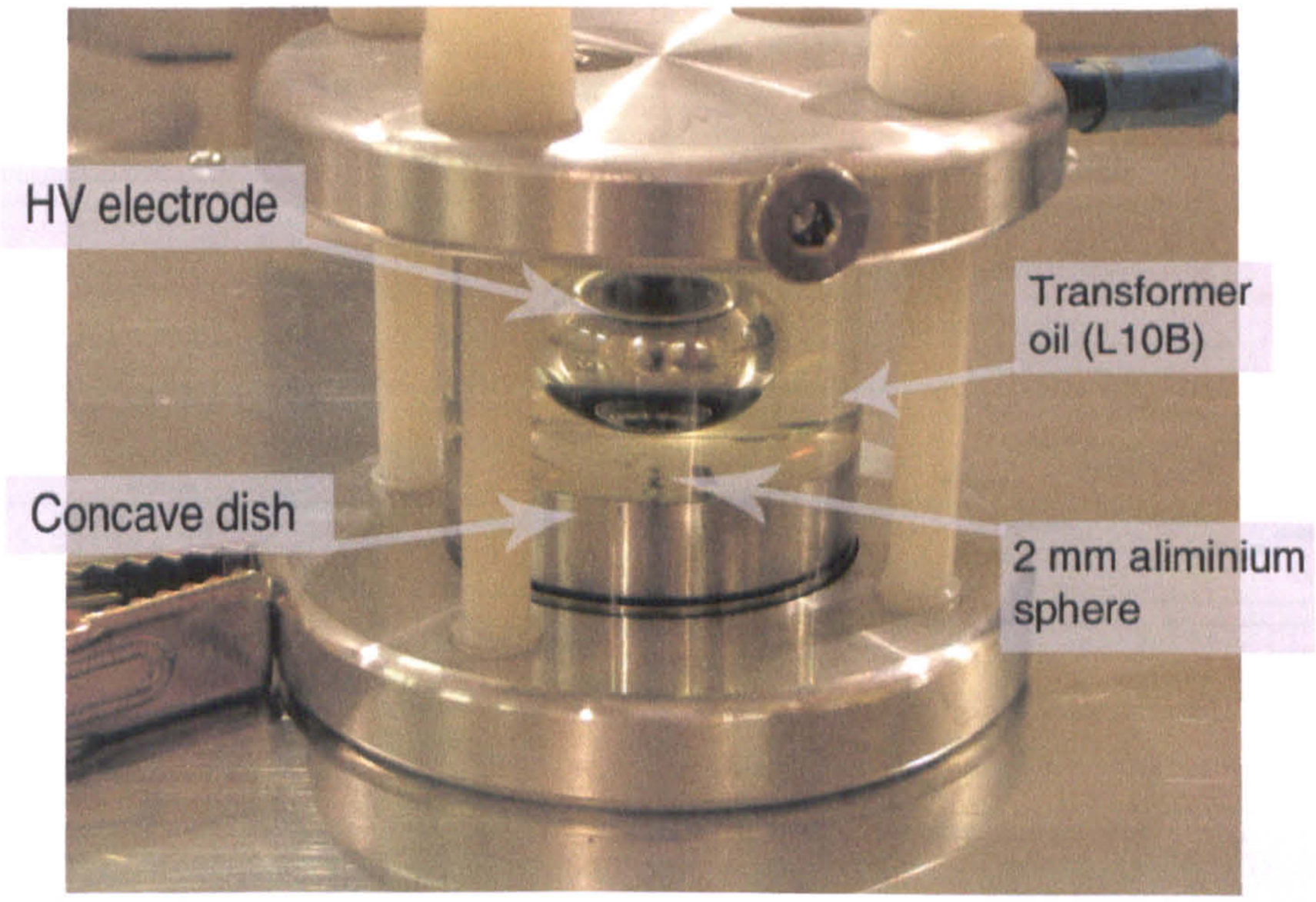

Figure 4.17: Free particle in oil.

High level software was therefore developed using MATLAB in order to read the recorded data and plot it in the required format. Due to the large number of traces recorded, the process can take up to half an hour for a single experiment.

4.5 Initial Trials

To ascertain the feasibility of a combined measurement strategy utilising both the UHF and IEC60270 techniques, testing was undertaken on a tap changer section and a small resin-impregnated transformer.

The tap changer is shown is Figure 4.19 and had been found to produce partial discharge during on-site testing [67]. Recreation of on-site conditions involved immersing the tap changer in mineral oil and placing it within a metallic enclosure. Two broadband UHF sensors can be seen mounted on either side of the test chamber to the left and to the right of the tap changer. Simultaneous measurement of both the RF and IEC60270 signals was implemented over a range of voltages. Figure 4.21 shows the relationship between UHF energy and IEC apparent charge for partial discharges produced by the tap changer.

Secondly, RF energy and IEC apparent charge were correlated for PD produced by a small resin-impregnated transformer, shown in Figure 4.20. The

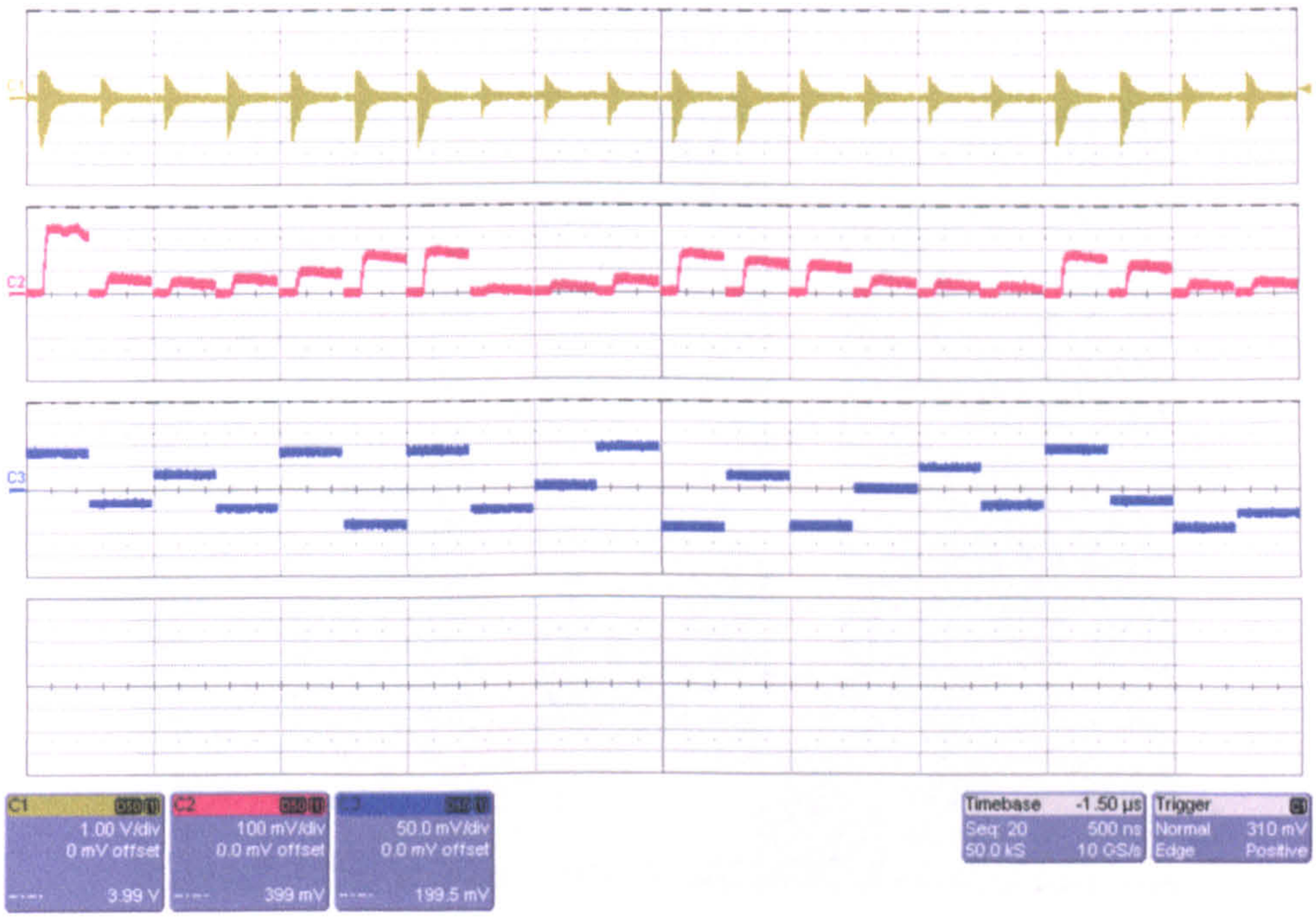

Figure 4.18: Screenshot from the LeCroy 7300 oscilloscope showing simultaneous acquisition of RF (Ch1), IEC (Ch2) and phase reference (Ch3) signals.

transformer is suspected of producing both void discharges and surface discharges simultaneously. The results are shown in Figure 4.21. At inception, one cluster is visible consisting of PDs of around 5000 pC. As the voltage is increased to 5.4 kV a second cluster becomes visible with an average apparent charge of around 9000 pC. A further increase in the applied voltage of 0.4 kV produces discharges having higher magnitude in terms of both apparent charge and RF energy, with cluster separation becoming less defined. It is hypothesised that each cluster is caused by a separate PD mechanism. Techniques such as k-means and c-means clustering could be used to determine the number of clusters in the correlation plot analytically [68].

In order to gain a better understanding of unknown discharges taking place within an insulation system testing has been undertaken on a range of well-defined PD geometries in order to characterise the correlations in terms of the relationship between UHF energy and IEC apparent charge. This will be described in the following chapter. It would be expected that the correlations are also affected by a number of factors, including some what are unrelated to the PD source. The effect of chamber geometry will be discussed in Chapter 6.

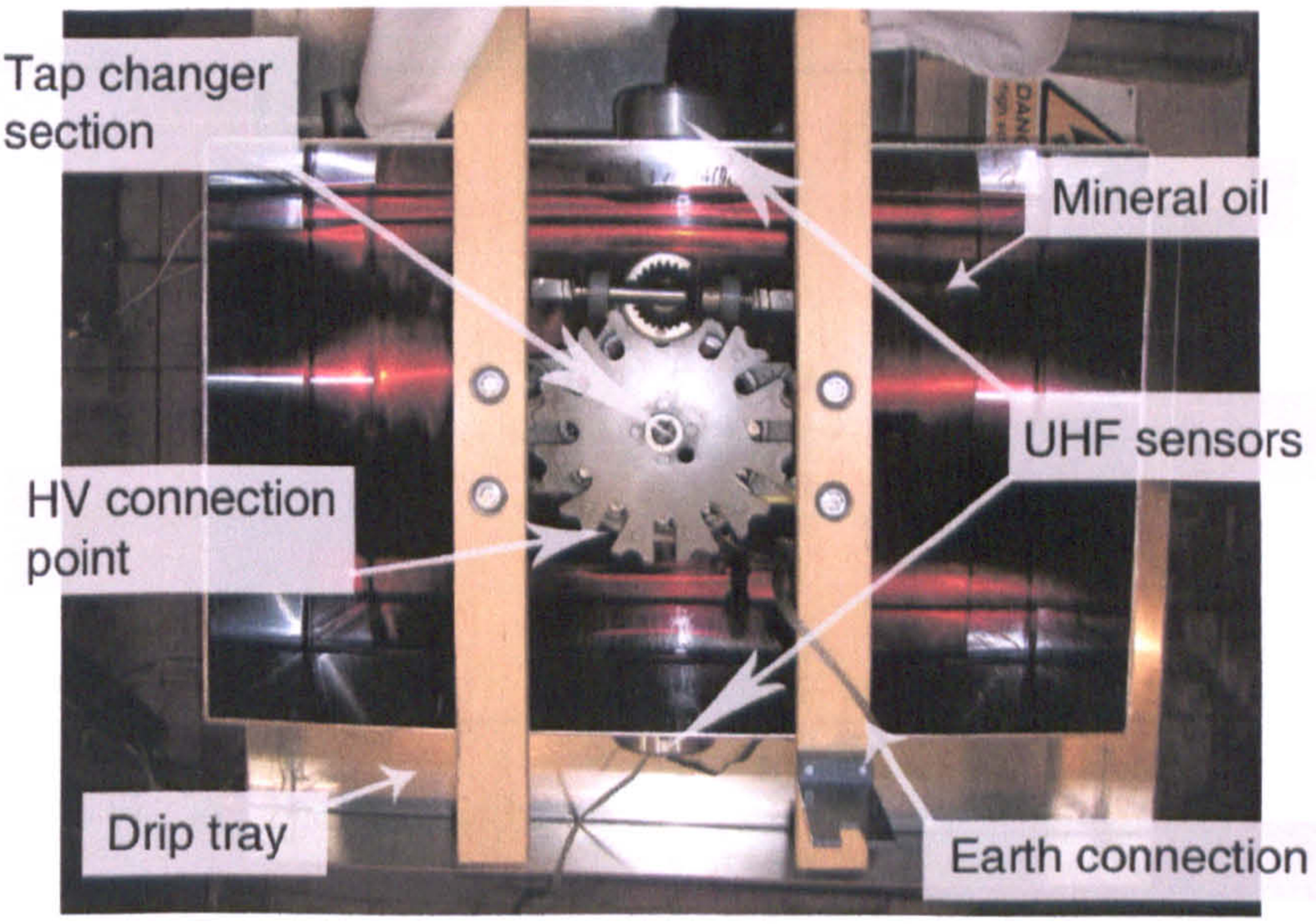

Figure 4.19: A tap changer section immersed in oil. Two broadband UHF sensors can be seen to the left and to the right of the tap changer, which is located within a partially enclosed metallic chamber.

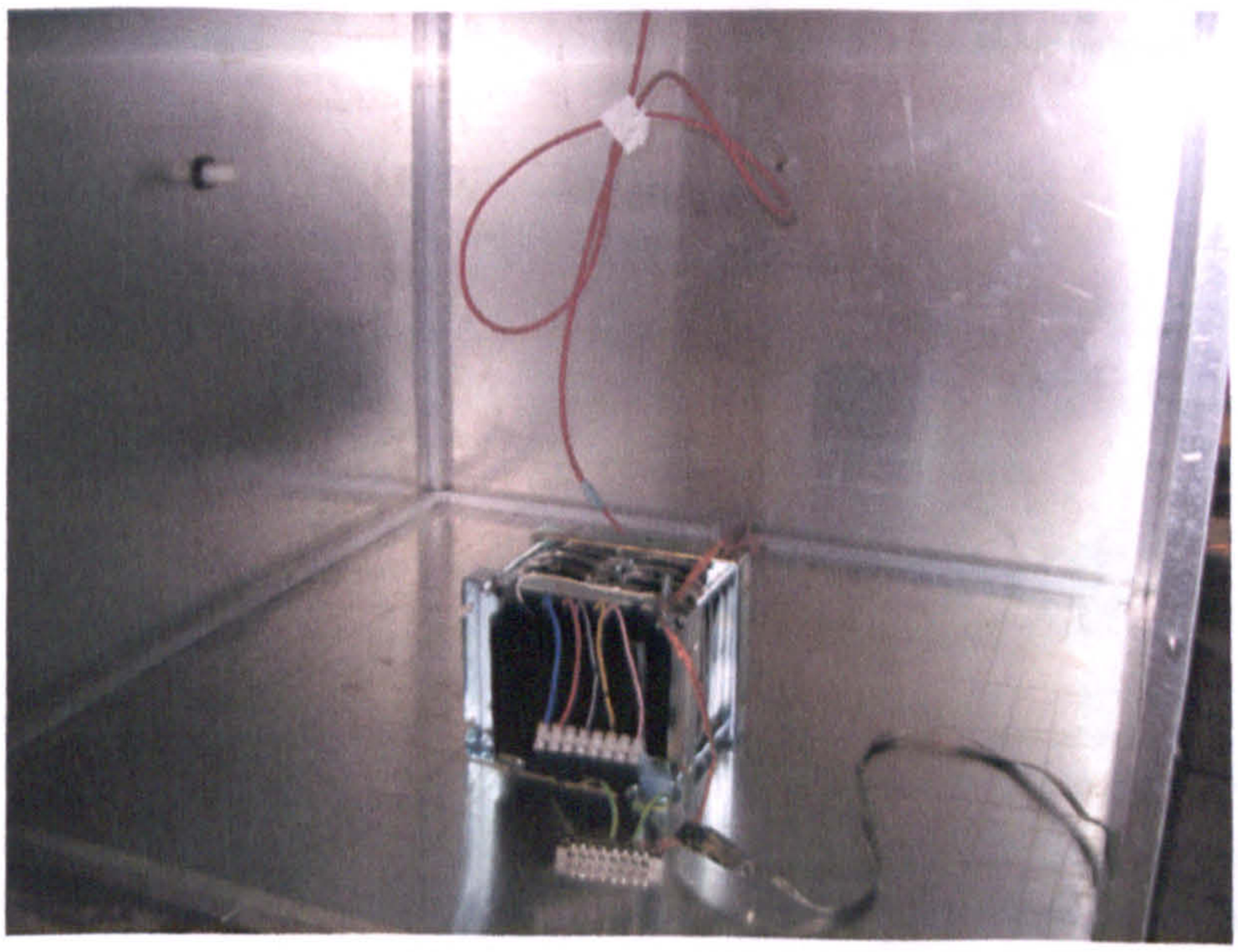

Figure 4.20: Experimental set up for simultaneous PD measurement on a small resin-impregnated transformer.

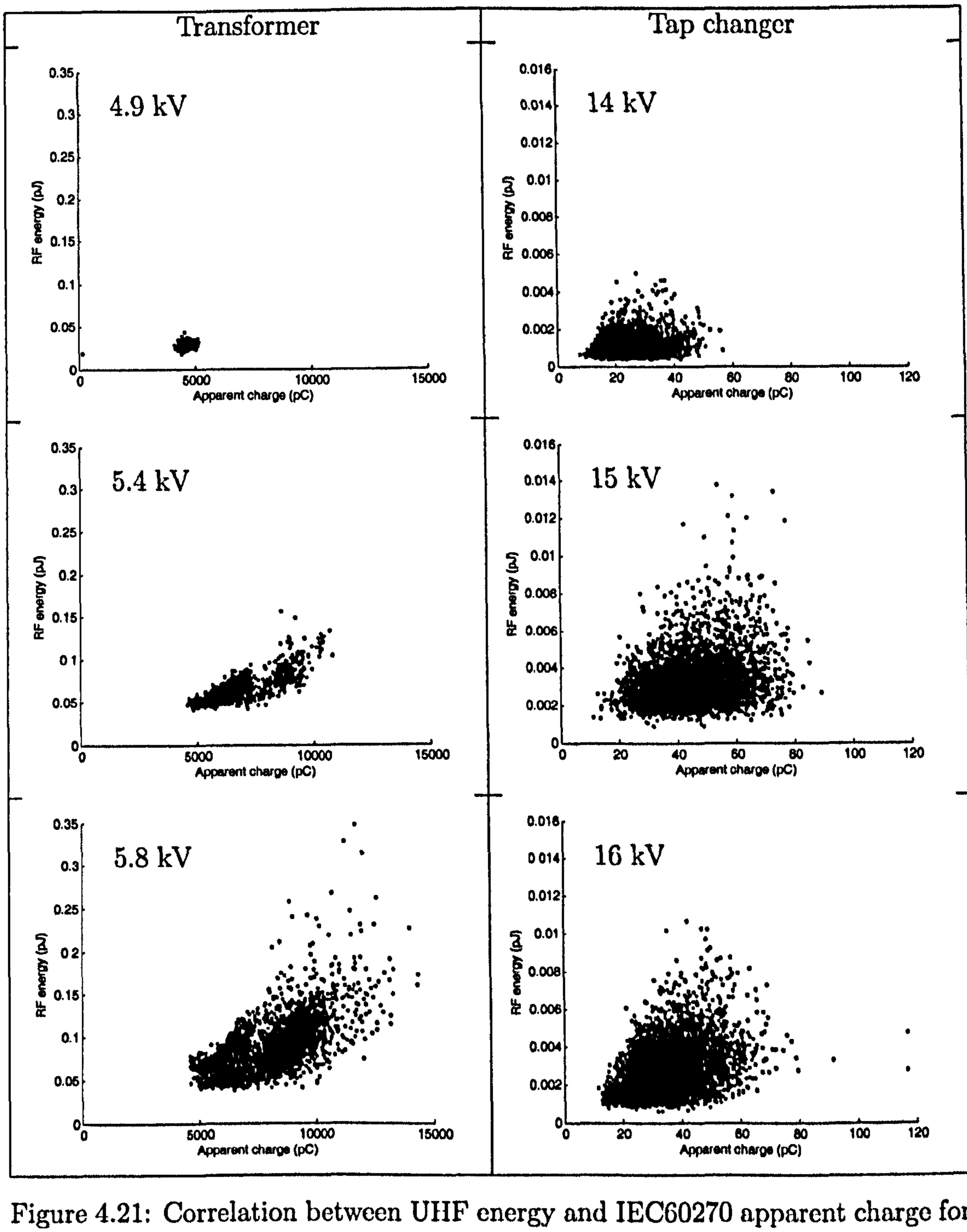

Figure 4.21: Correlation between UHF energy and IEC60270 apparent charge for partial discharges produced by a small resin-impregnated transformer and a tap changer section.

4.6 Conclusions

This chapter has described calibration, testing and implementation of the experimental facility used for simultaneous partial discharge measurement applying both UHF and IEC60270 techniques. It has outlined the basic principles behind the IEC60270 technique as well as describing the associated hardware. Design options have been reviewed and construction of the complete facility had been implemented based on these considerations. Test objects with defined topologies have been manufactured, including floating electrodes, free metallic particles, voids in solid insulation and sharp protrusions, and have been tested separately using RF electric field sensors and the IEC60270 measurement system. The combined measurement system in its completed form has been tested on two industrial components; a tap changer and a small resin-impregnated transformer. High-level software has been developed to process both data sets. The results seem promising, as features within the initial correlations such a multiple clusters would be unidentifiable using either of the measurement systems individually.

Chapter 5

Key Features of Correlations

The purpose of this chapter is to summarise results from a number of experiments carried out on a range of PD geometries. For each source geometry, PD measurements have been made simultaneously using both IEC and RF techniques. Five common PD source topologies have been re-created under laboratory conditions using the test cells described in section 4.4.2. Variations in the correlation between apparent charge and RF energy with a number of parameters related to each source configuration (pressure, voltage, insulation medium etc.) will be quantified by plotting apparent charge against RF energy for a number of PD signals (around 2000 per channel).

5.1 Selection of Geometries

Factors affecting the relationship between RF and IEC measurements on a given PD source are numerous. These include variables related to the source itself and variables related to the measurement system. Examples of the latter include trigger source (RF or IEC), accommodating the dynamic range of the acquired signal, choice of trigger level, system re-arm rate and measurement frequency range. Factors directly related to the source geometry include the topology of the defect, structures in contact with the PD source, external environment (enclosed or open) and source orientation.

In order that experimental design was focused on the most valuable aspects of testing within the available time frame, and to ensure that efforts are not spread too thinly, a 'matrix' of test geometries was defined. This matrix will additionally serve as a useful platform on which to extend the current work once the research

project is completed.

Summarising the outcome of various discussions related to this matter, it was firstly agreed that, due to their relevance in GIS, extensive testing would be undertaken on free metallic particles. Statistics on GIS reliability [11, 12] show that free metallic particles were the most common cause of failure in the first generation of GIS systems [1]. Testing on solid insulation was also deemed essential. It is proposed that simultaneous measurement could prove useful on components such as bushings, where metallic inclusions and voids can occasionally occur in oil-impregnated and resin impregnated bushings respectively. Metallic inclusions may not be evident using conventional PD testing but can cause puncture of the bushing during impulse testing. Finally, the point-plane configuration will be considered. Partial discharge mechanisms in air and SF_6 are well understood in terms of the point-plane geometry and have been extensively reported upon over the past century.

A variety of insulating media was also utilised, partly due to, but not limited to the fact that each has significant relevance to practical insulation systems. For instance, mineral oil is used extensively in power transformers and SF_6 is prevalent in GIS. A diagram of the test configuration is shown in Figure 5.1.

5.2 Results

5.2.1 Free Metallic Particles in SF_6

Single Particle

For the single aluminium sphere, Figure 5.2, correlations are characterised by a large spread of apparent charge for a given value of RF energy. The spread in apparent charge is non linear with the discharge density increasing near the envelope of the correlation curve. The most obvious feature of these correlations is a well defined upper limit on the maximum RF energy produced by the PD source. This is characterised by the hyperbolic envelope of the PD pattern and can be quantified for a given apparent charge. The gradient of the envelope has been shown to be dependant on the surface area of the particle under test. Any variations are, however, negligible in comparison with the order-of-magnitude variations between defect sources. The envelope of the correlation curve does not

[1] Floating shields tend to be the most common cause of failure in the new generation of GIS.

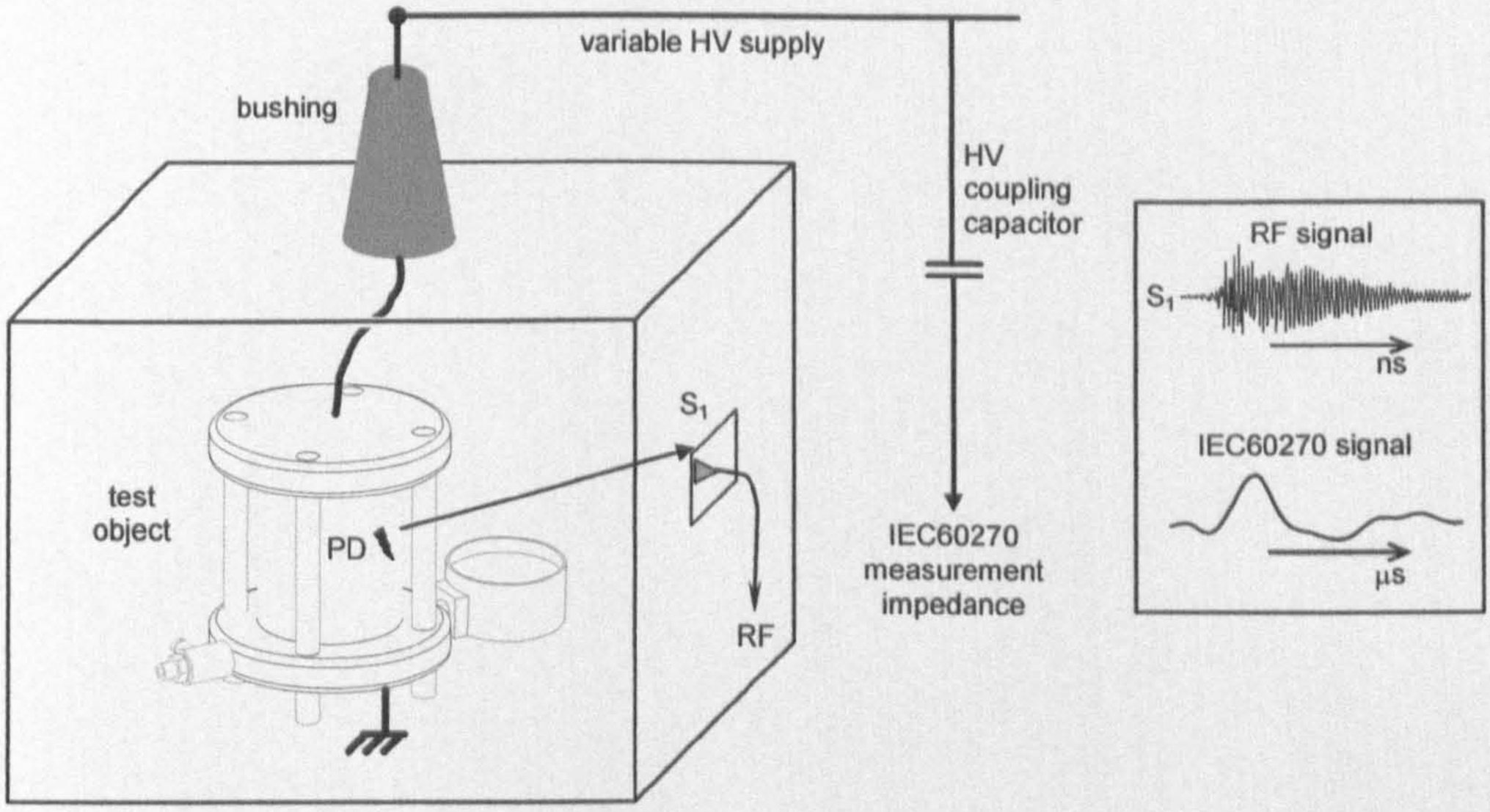

Figure 5.1: Experimental set-up. Test cells are positioned within a $1m^3$ aluminium test chamber and are energised through a HV bushing which is PD-free up to 25 kV.

vary over the pressure range tested. A 2.5 mm diameter (medium sized) particle consistently produces the highest gradient.

Double Particles

When multiple particles are present, the number of particles producing discharges cannot be identified by examination of the correlation plot alone. Correlation patterns have similar features to those produced by single free particles. Certain combinations of particles radiate more effectively than others, for example, the combination of a 3 mm and a 2 mm particle produces the largest initial gradient on the correlation graph. Again, there is no significant variation in the RF/IEC correlation over the pressure range 1–3 bar.

5.2.2 Free Particles in Oil

Single Particle

Particles in oil radiate lower RF energy levels to those in SF_6. The apparent charge is also around two orders of magnitude lower. The correlation, Figure 5.3, resembles a quadratic curve, indicating a fairly constant pulse shape. Both

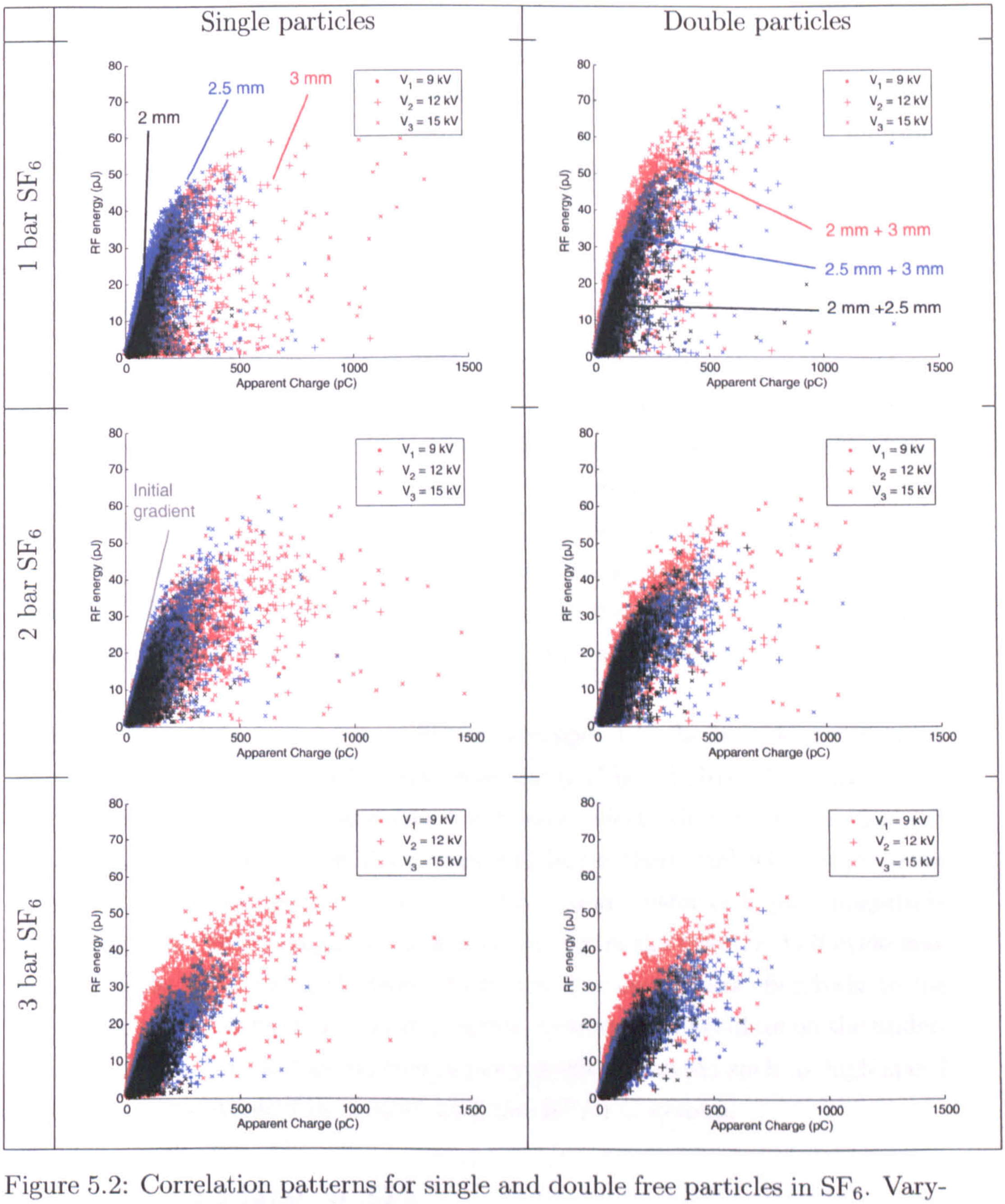

Figure 5.2: Correlation patterns for single and double free particles in SF_6. Varying voltage, particle size and pressure.

apparent charge and RF energy increase with applied voltage. As in SF_6, the 2.5 mm particle radiates most effectively.

Double Particles

Again, since correlation curves are similar for single and multiple free particles, it is only possible to say that at least one particle is present. As with multiple free particle s in SF_6, 2 mm and 3 mm particles radiate more effectively than any other combination.

5.2.3 Floating Electrode in SF_6

The correlation plot, Figure 5.4, is characterised by two distinct clusters that are separated on the basis of apparent charge. Clusters become distinct at pressures of 4 bar and above. The floating electrode configuration produces high amplitude discharges both in terms of RF energy and apparent charge. Once discharge inception has been reached, PD magnitude does not vary with applied voltage. It has been shown that both IEC and RF discharge magnitudes increase with increasing SF_6 pressure (Fig. 5.4 (a)). It has also been demonstrated that cluster separation, RF energy and apparent charge increase with gap spacing over the range $x = 0.25 \ldots 1$ mm, see Figure 5.5.

The two clusters have been shown to correspond to discharges occurring on the negative and positive half-cycles respectively (Fig 5.4 (b)). When high voltage is applied to the protrusion (see the floating electrode test cell photograph in Fig 4.15), it is likely that discharges will begin there and will couple more effectively to the IEC system, producing the second cluster of higher magnitude IEC pulses. The lower magnitude pulses occurring on the negative half cycle may originate from the floating electrode itself and thus couple less effectively to the IEC measurement system. It is only possible, however, to speculate on the underlying PD mechanism unless another measurement technique such as high-speed photography was applied in parallel with the RF/IEC system.

5.2.4 Point-plane in SF_6

Tests carried out just above inception on the point-plane cell produce correlation patterns resembling a quadratic envelope as shown in Figure 5.6. An increase in voltage produces a corresponding increase in RF and IEC discharge levels. The

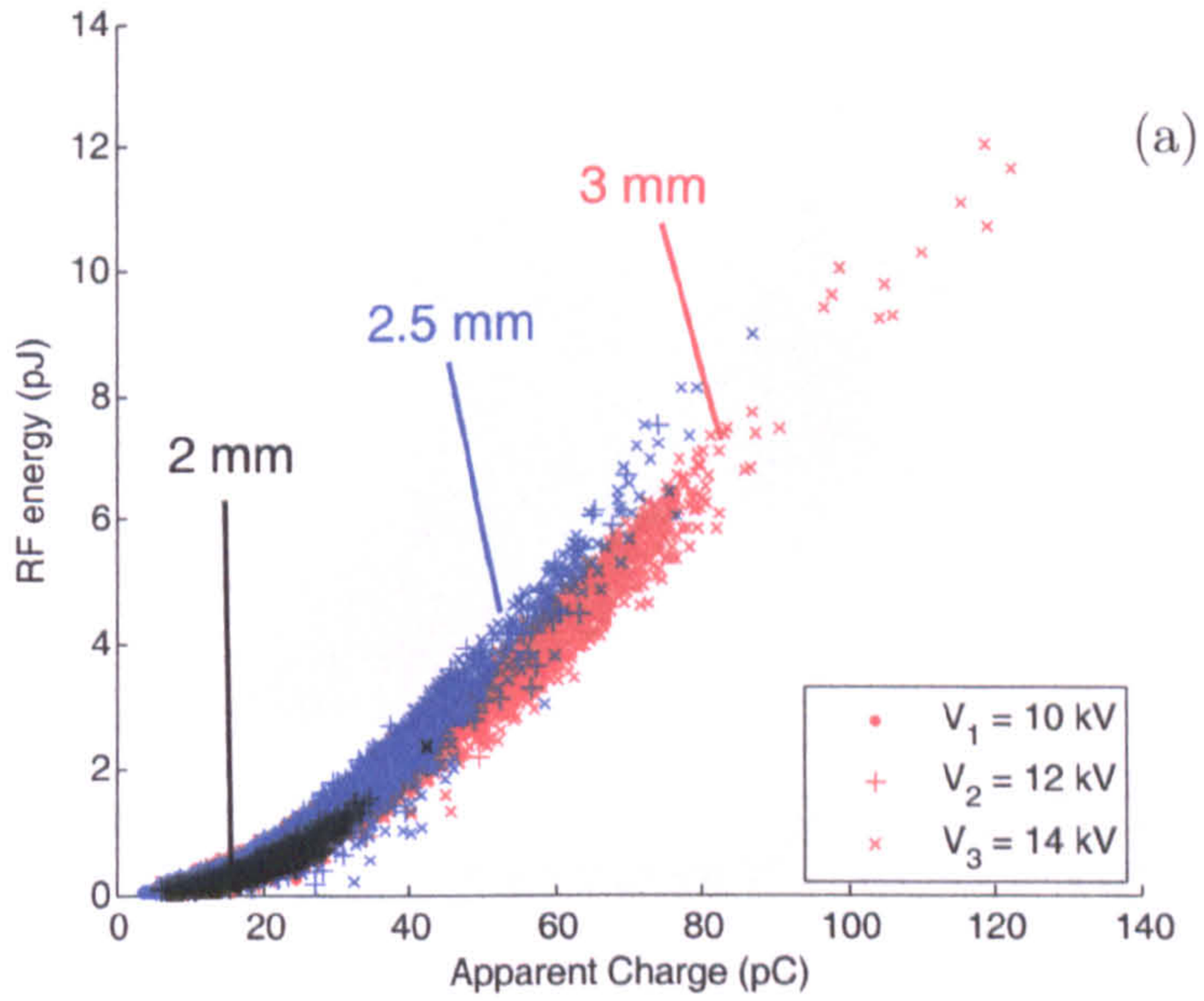

Figure 5.3: Correlation patterns for (a) single and (b) double free particles in oil, showing the effect of voltage and particle size.

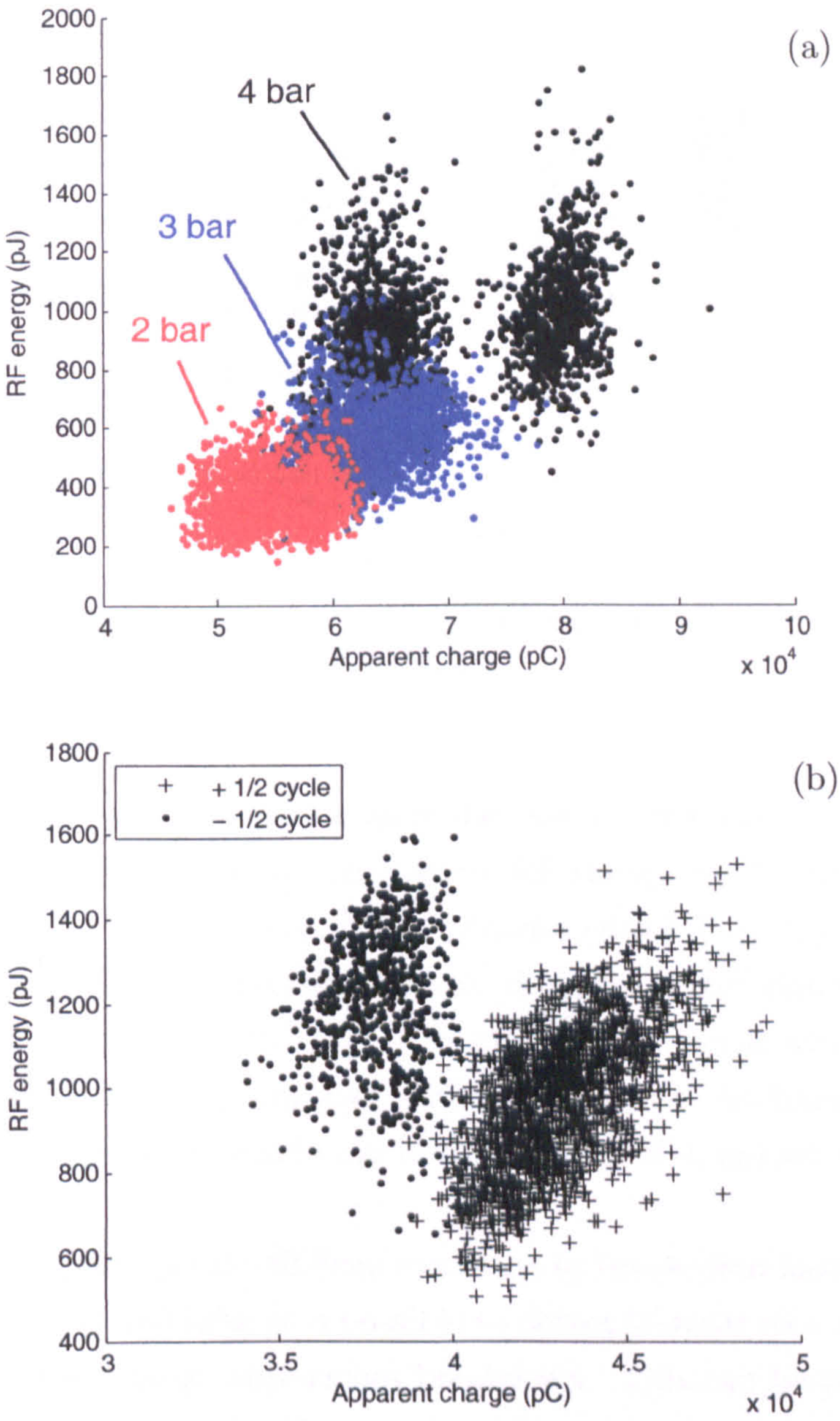

Figure 5.4: Correlation pattern for a floating electrode in SF_6. (a) The effect of SF_6 pressure. $V_1 = 16kV$, $V_2 = 17kV$, $V_3 = 18kV$. (b) Simultaneous measurement of RF and IEC signals along with phase reference shows that the clusters correspond to discharges occurring in the positive and negative half cycles. 4 bar, 16 kV applied voltage.

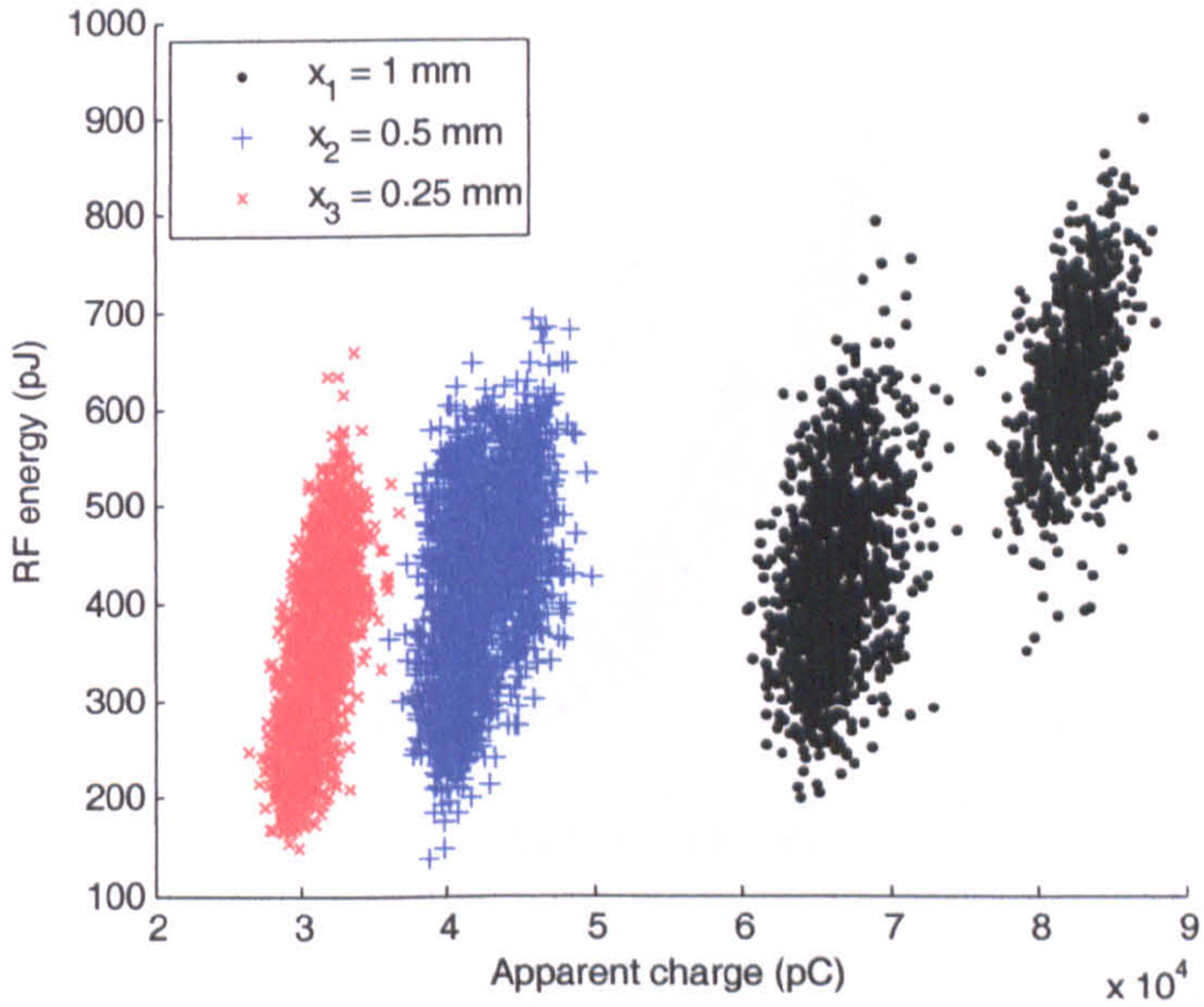

Figure 5.5: Correlation pattern for a floating electrode in SF_6. The effect of gap separation x. 4 bar, 14 kV applied voltage.

quadratic correlation is not as clear as in the case of a free particle in oil, having a larger spread of apparent charge for a given RF energy value. All measurements on the point-plane cell show low PD amplitudes with RF energy in the order of fJ. The UHF amplifier is thus necessary for detection of RF signals.

There is no significant variation in the correlation trend with SF_6 pressure. A decrease in gap spacing increases the severity of the discharge, producing a corresponding increase in amplitude both in terms of apparent charge and RF energy.

Tests on the point-plane cell from inception to breakdown have shown that at lower pressures (50–150 kPa) it is possible to detect transfer to a more severe PD mechanism as the voltage approaches breakdown. This can be observed in Fig. 5.7. The correlation pattern shows a transition from the previously described quadratic correlation to a high-amplitude PD cluster. As the cell approaches breakdown, the cluster shifts position towards the origin, showing a decrease in both RF and IEC discharge amplitude.

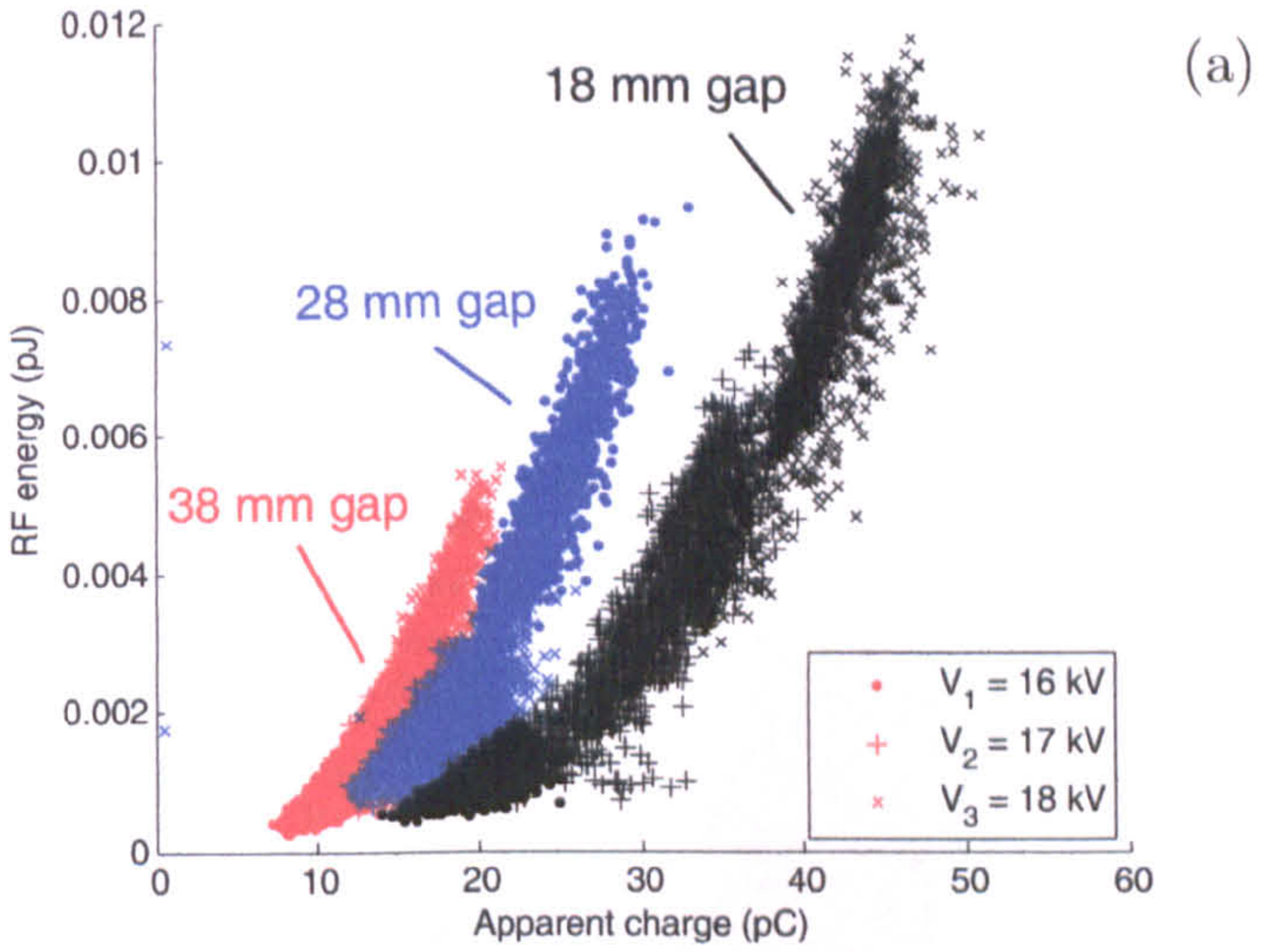

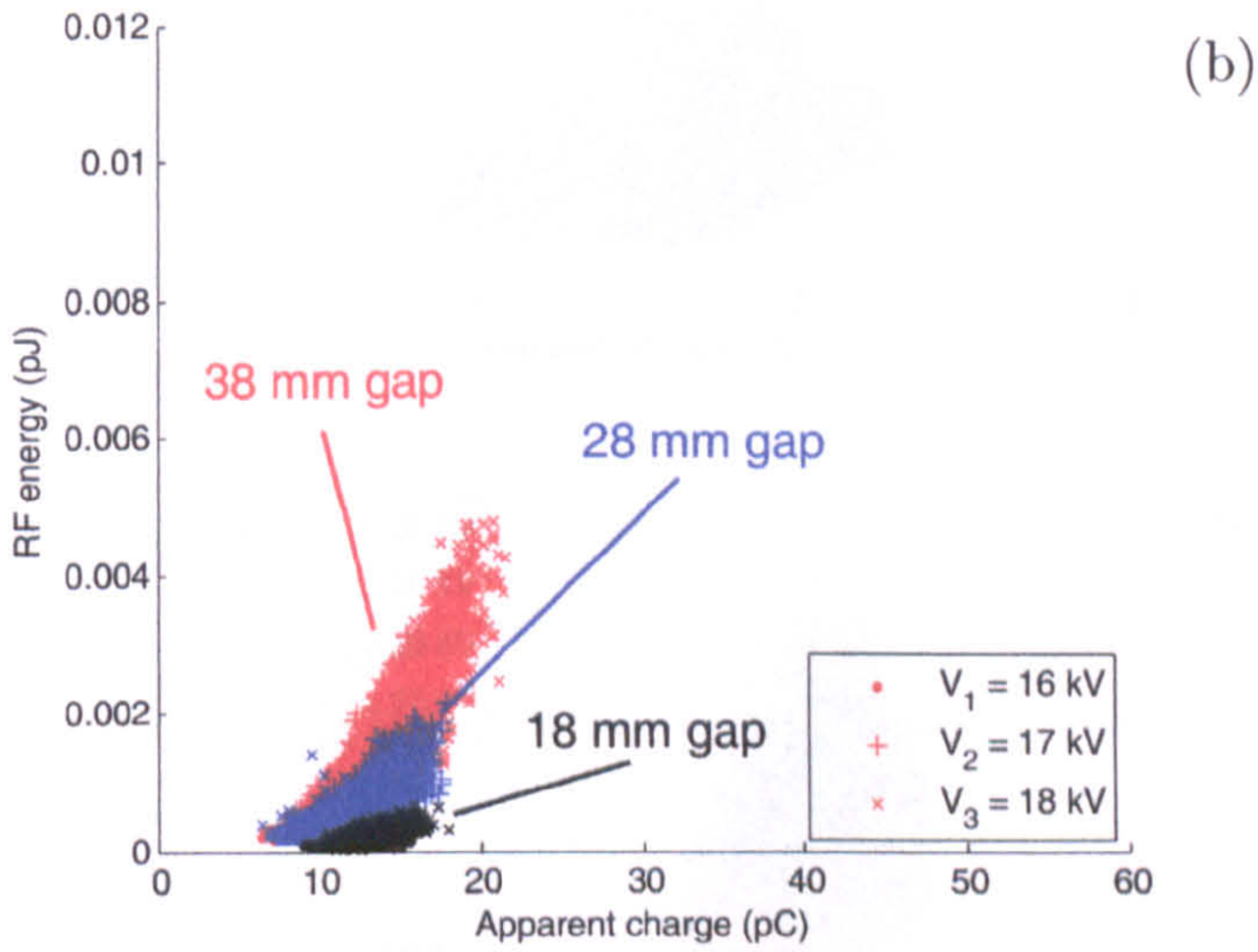

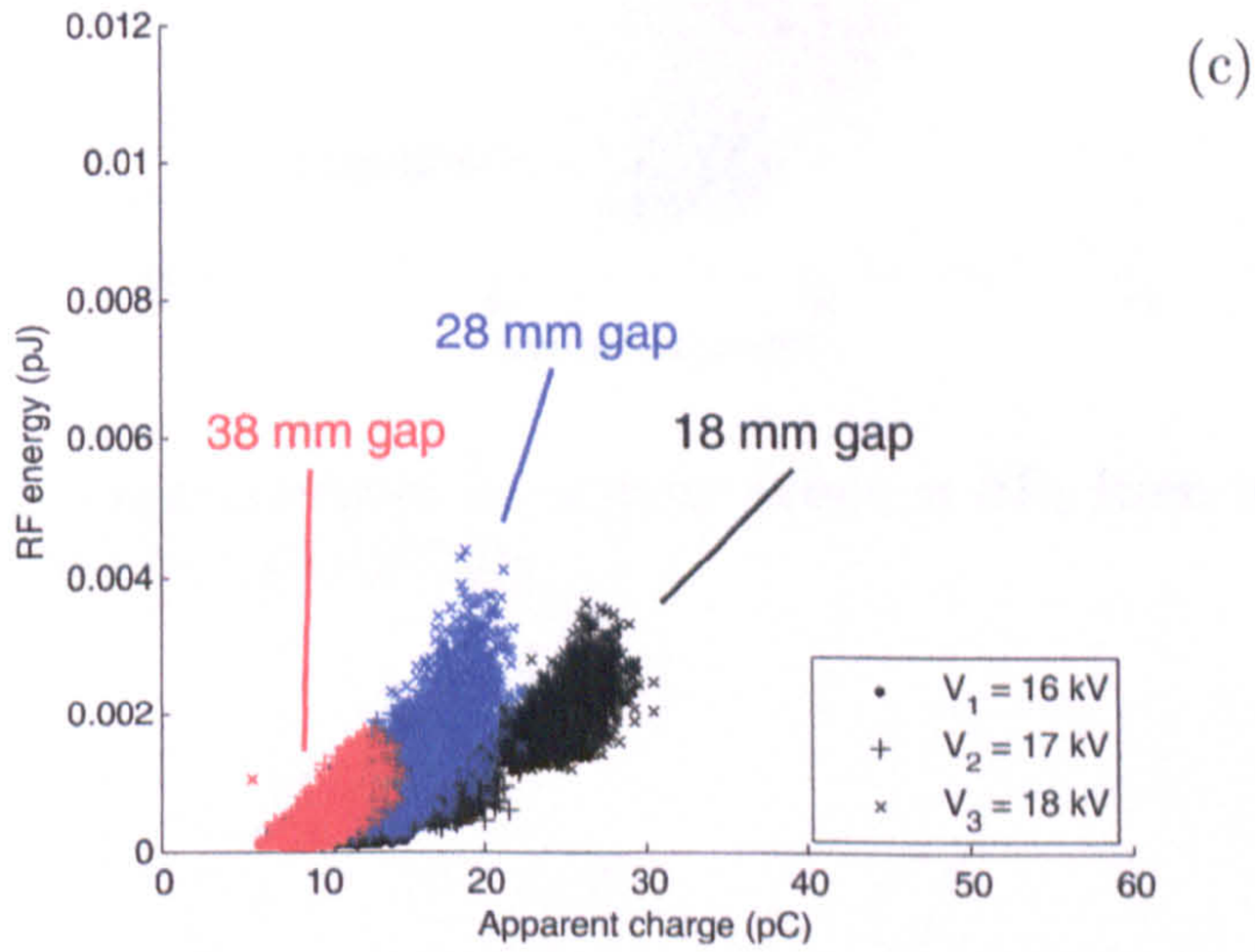

Figure 5.6: Correlation patterns for a point-plane configuration in SF_6. (a) 1 bar, (b) 2 bar, (c) 3 bar.

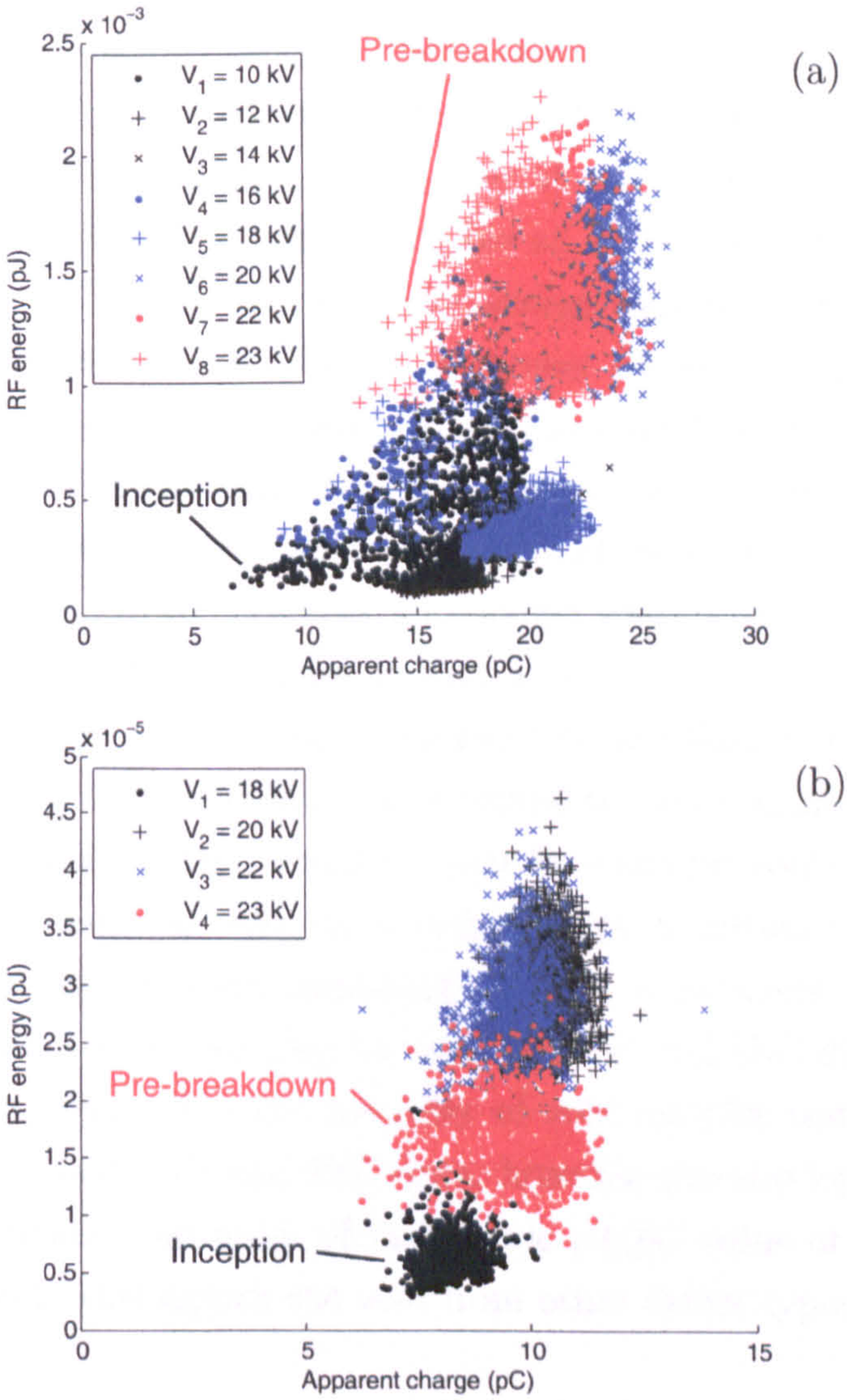

Figure 5.7: Correlation patterns for a point-plane in SF_6 from inception to pre-breakdown. (a) 50 kPa, (b) 150 kPa.

5.2.5 Voids in Resin

This is perhaps the most interesting and the most difficult to describe in a concise manner since large variations in PD pulse characteristics occur between void samples. For example, the correlation characteristic for a void sample in resin manufactured at Strathclyde University is shown in Fig 5.8. Although the number of voids in the sample is unknown, it is hypothesized that the two visible clusters (labeled 1 and 2 in 5.8) correspond to two simultaneously active voids sources within the sample. On examination of the plot it can be seen that three clusters are present. Two clusters are initially visible at 13 kV, with the third cluster, containing similar IEC levels but higher RF energy, becoming visible as the voltage is increased to 16 kV. The third cluster may either correspond to a third void or a more severe PD mechanism. It has since been shown that is possible to discriminate between two simultaneously active void sources using combined RF/IEC measurement. This was achieved by simultaneously activating two resin samples that were known to each contain a single void. The correlation plot for this particular configuration is shown in Fig. 5.11.

Tests on additional void samples manufactured at Glasgow Caledonian University show that the correlation has the potential to vary significantly over time. For example, Fig 5.9 shows the correlation plot for a sample containing five voids. It is apparent that discharge activity is only present in certain voids within the sample, with additional clusters appearing after the experiment has run for approximately 30 minutes. It can also be seen that RF and IEC discharge magnitudes decrease over time. For the majority of void samples tested, there is no clear correlation between RF and IEC data, however the envelope of the correlations consistently show an order of magnitude pJ/pC value of $R = 1 \times 10^{-9}$, which can be used to distinguish the void from other defect types.

5.3 Discussion

Simultaneous measurement of apparent charge and RF energy yields more information about a PD source than each system individually. In some ways this is an intuitive result since it is not possible for a combined system to give any less information than each system on its own.

An important concept is in regard to the *order-of-magnitude pJ/pC level*, or the order-of-magnitude gradient of the correlation plots. This quantity may

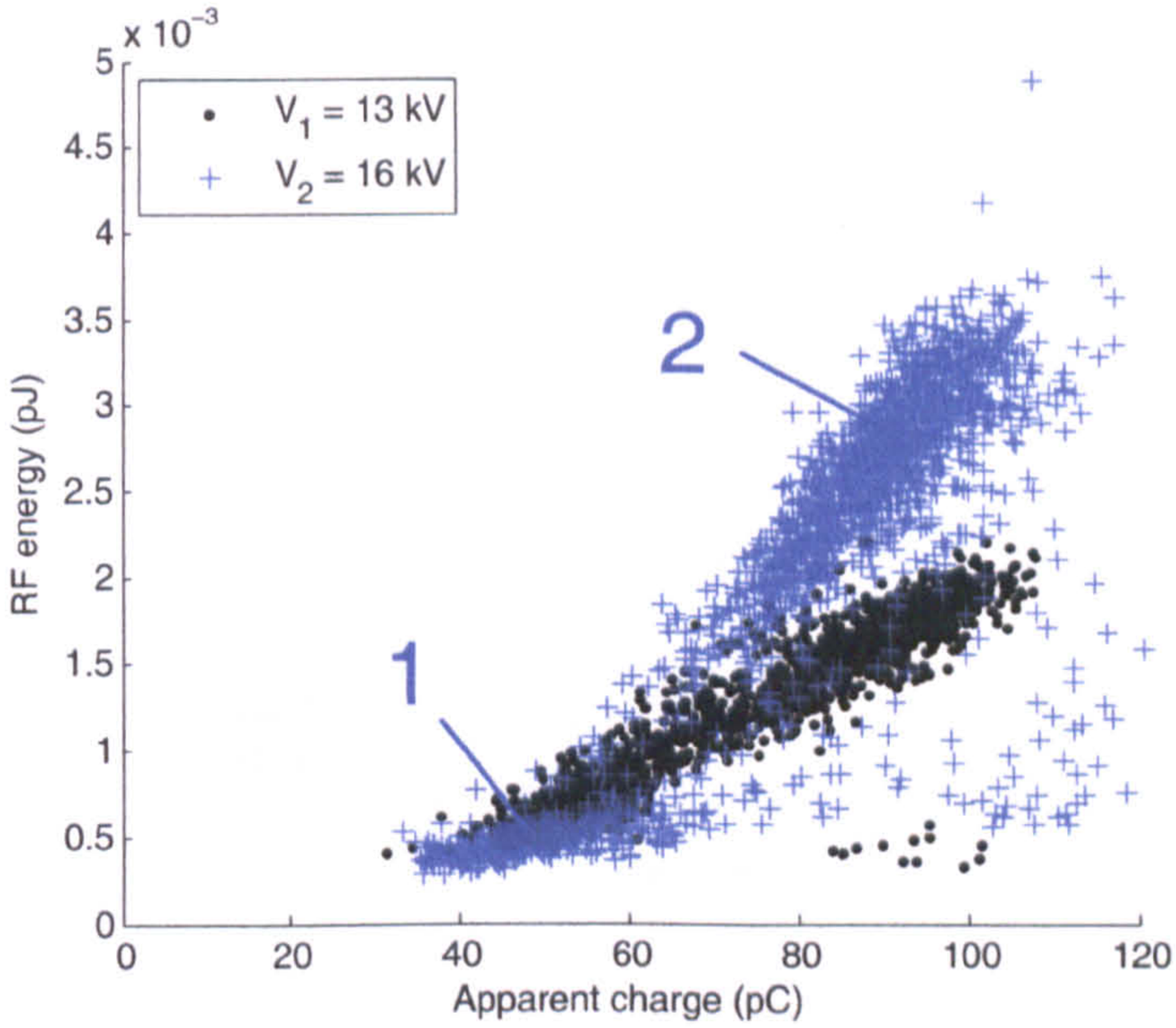

Figure 5.8: Correlation pattern for a resin sample manufactured at Strathclyde University containing an unknown number of voids. The correlation illustrates the ability of a combined system to identify multiple discharge sources within the sample, with two cluster becoming visible at 16 kV.

be calculated using either of two methods since there is no significant difference between the results in each case. Firstly, the 'average gradient' can be taken, where the sum of the gradient of each individual point on the correlation graph is computed and divided by the total number of the points on the plot (Eqn. (5.3.1)). Secondly, the 'gradient of averages' may be used (Eqn. (5.3.2)), where the mean q and U values are taken to produce a single point on the correlation graph. The gradient of this point is equal to the pJ/pC level.

$$\sum_{i=1}^{N} \frac{(U_i/q_i)}{N} \tag{5.3.1}$$

$$\frac{\sum_{i=1}^{N} (U_i/N)}{\sum_{i=1}^{N} (q_i/N)} \tag{5.3.2}$$

pJ/pC levels for the defects under test are summarised in Table 5.1. It has been shown that using a combined system it is possible to identify multiple voids within an insulation sample. An additional advantage involves the ability to remove any spurious signals from the IEC channel by utilising the insusceptibility of RF measurements to corona interference.

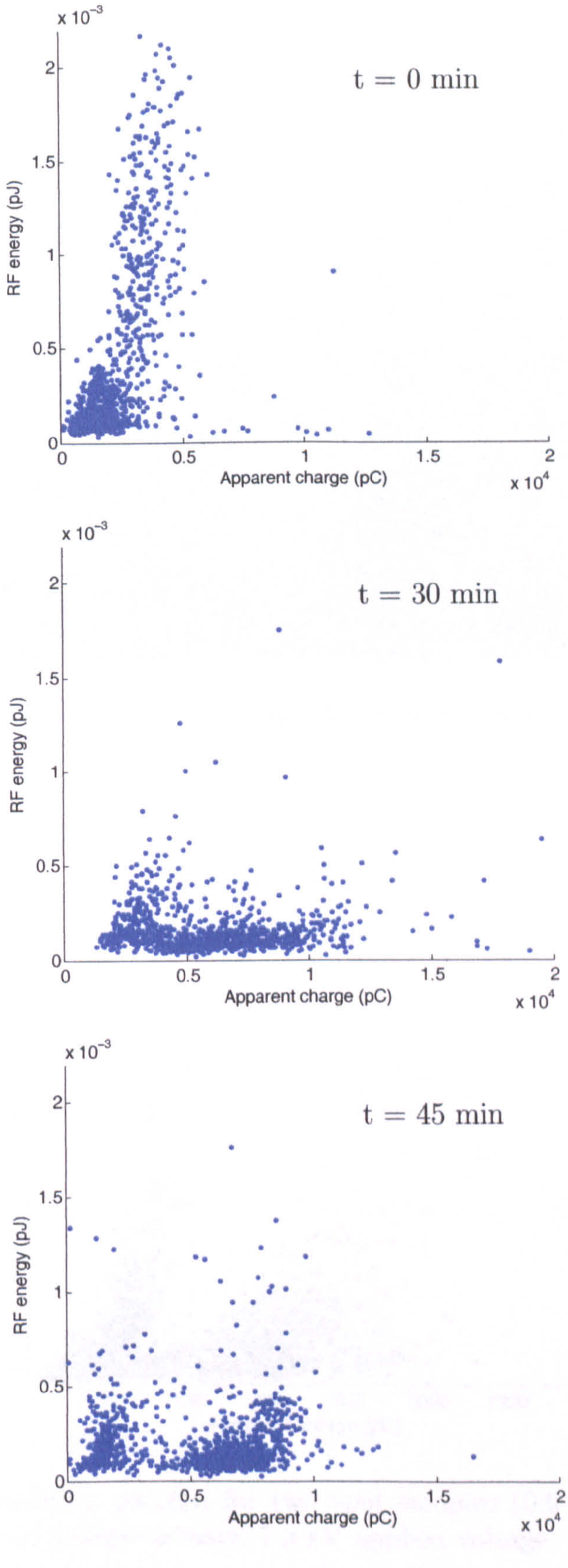

Figure 5.9: Correlation pattern for a resin sample containing 5 voids. The plot shows the variation in the discharge pattern over a period of 45 minutes. 12 kV applied voltage.

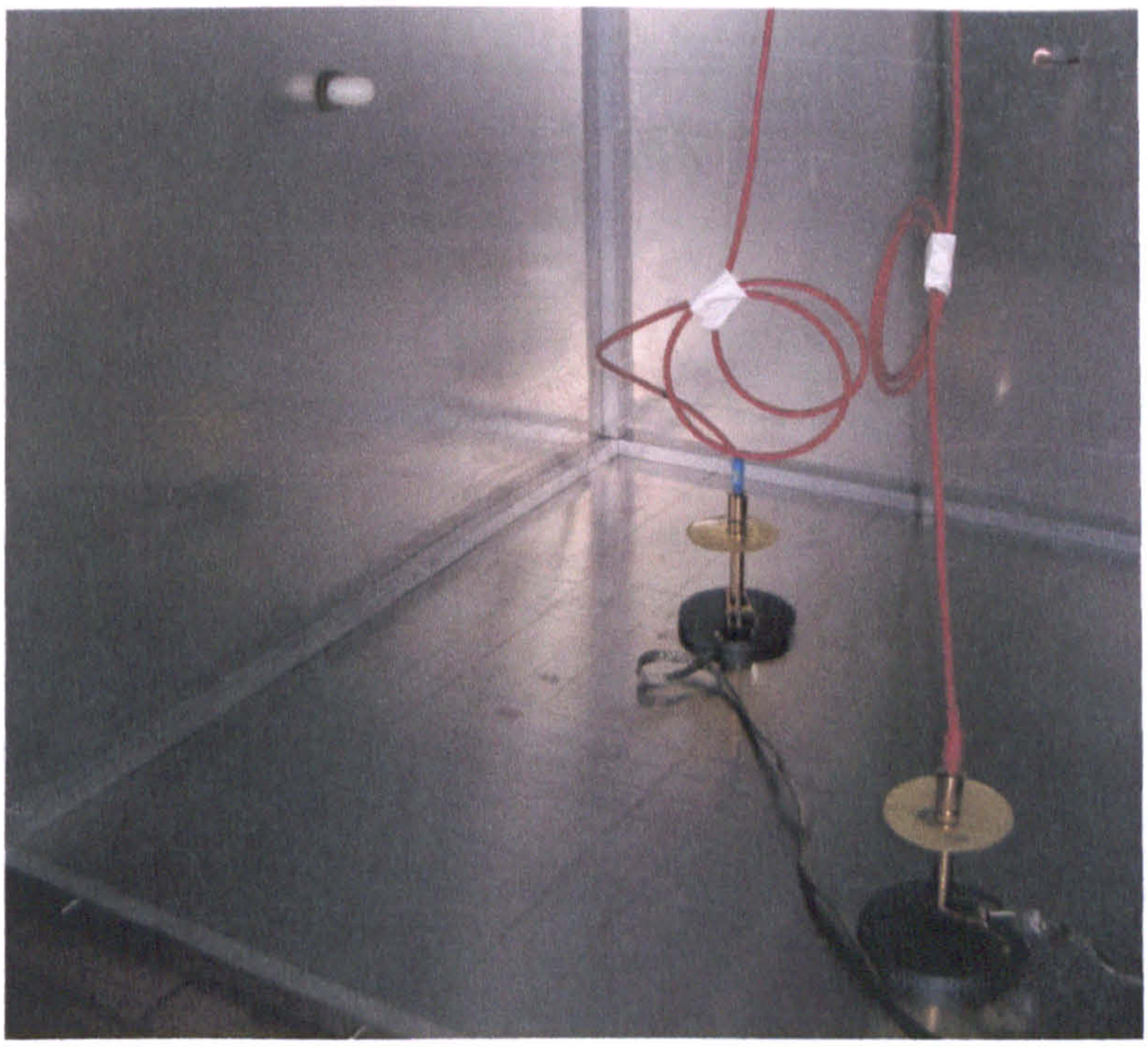

Figure 5.10: 0.6 mm and 1.39 mm diameter void samples activated simultaneously.

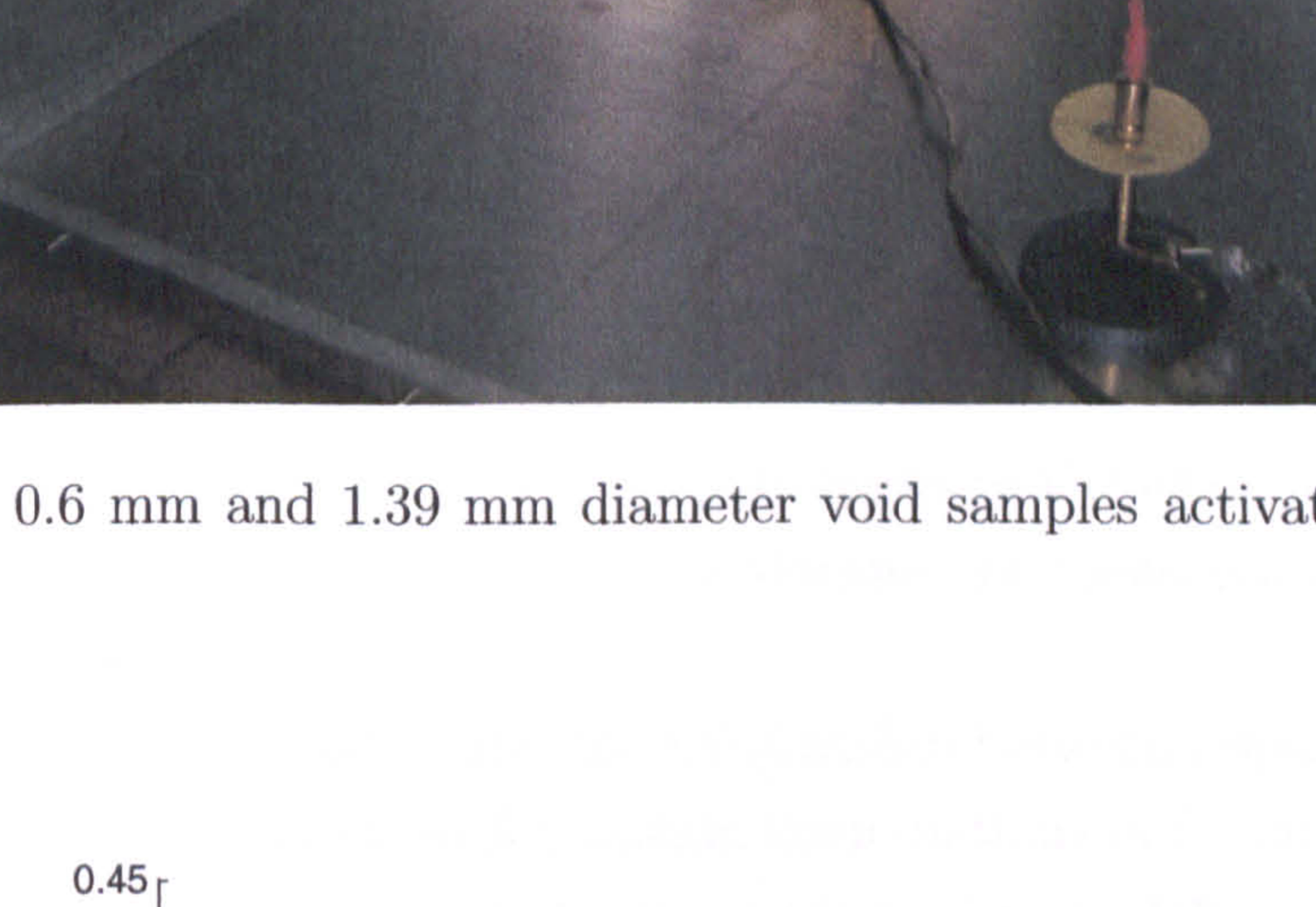

Figure 5.11: Correlation pattern for two void samples (0.6 mm and 1.39 mm diameters) activated simultaneously. 7.3 kV applied voltage.

Table 5.1: Order-of-magnitude pJ/pC levels for various PD source configurations.

Defect	pJ/pC level
Floating electrode in SF_6	$1*10^{-3}$
Free particles in oil	$2*10^{-2}$
Free particle in SF_6	$5*10^{-2}$
Point-plane in SF_6	$3*10^{-4}$
Void in resin	$3*10^{-5}$

Although PD can be identified by phase-resolved measurements, certain complications arise when applying diagnoses of laboratory-acquired data to the diagnosis of field measurements. For example, harmonic distortion of the HV sinusoid can produce unreliable phase-resolved measurements. The combined strategy overcomes this problem since no phase reference is needed for defect identification.

The results presented represent a step towards standardisation of RF measurements. The RF technique is mentioned briefly in section 4.6 of the IEC60270 standard under the heading 'Ultra-wide-band instruments for PD detection'. The standard only mentions that it is possible to measure PD using ultra wide bandwidth equipment but gives no recommendations for measurement methods or bandwidth requirements.

From the data obtained so far, the relationship between apparent charge and RF energy has been quantified for certain combinations of factors related to the PD source. Although the results do not conflict with the RF section of the IEC standard, it may be possible to draft an improved section based on the information gained thus far.

5.4 Conclusions

A measurement system has been constructed which allows simultaneous acquisition of RF and IEC60270 traces produced by a PD pulse. A number of defects have been characterised in terms of the relationship between RF energy and IEC apparent charge. This has been achieved by plotting RF energy against apparent charge on a 2D scatter plot, defined as the 'correlation plot'.

It has been shown that, due to the different responses of each system to the same PD event, correlation between each measurement reveals additional information on the shape of the underlying PD current pulse, allowing identification of PD source topologies and in some cases, simultaneously occurring defects or

mechanisms. The order-of-magnitude relationship between RF energy and apparent charge (pJ/pC level) has been introduced. This was found to vary significantly between defects. Since PD quantification in terms of apparent charge has become well accepted over a number of decades, characterisation of the pJ/pC relationships for a given test configuration may allow RF measurements to be used with as greater degree of confidence when determining PD severity.

Chapter 6

The Influence of Chamber Geometry on RF/IEC Correlations

It has been shown that by simultaneous measurement of RF energy and IEC apparent charge, it is possible to identify certain PD sources (Chapter 5) as well as give some indication of the shape of the underlying PD pulse (Chapter 3). In this chapter the effect of test chamber geometry on the relationship between the two measured quantities is investigated. Experiments on various PD source topologies have been carried out using three different test chambers. In most cases, the nature of the correlation pattern was found to be consistent. However variations were found in the order-of-magnitude relationship between the RF energy and apparent charge. Variations in the order-of-magnitude pJ/pC level are complex and do not scale linearly across the various chamber volumes. Additionally, variations in the pJ/pC level with chamber geometry are dependent on defect type. It is likely that additional factors, namely coupler orientation and distance relative to the PD source, have a significant effect on the correlations.

6.1 Introduction

During the course of the present investigation, simultaneous measurement using both RF and conventional PD measurement techniques has been extensively undertaken using a range of PD sources, such voids in resin, free particles and floating electrodes. It has been shown that when RF energy is plotted against

apparent charge, distinctive characteristic patterns appear which are depending on the defect under test. It has also been found that the order-of-magnitude relationship between the two measured quantities is dependent on the defect. However, all experiment thus far have been carried out using the same test chamber (an aluminium box of side 1 m). The purpose of the test chamber is provide an environment that allows the measured UHF PD pulses to persist, mimicking the response that would normally be observed in a transformer or GIS chamber. It is hypothesised that the geometry of the test chamber will have an effect on the correlation plots and it is necessary to understand the nature of such an effect if results on simultaneous measurement obtained in the laboratory are to be used as a basis for identification of the type or severity of a defect occurring in a real plant item such as a power transformer, the internal dimensions of which are significantly greater than those of the laboratory test chamber.

Simultaneous measurement was therefore carried out on test cells within two additional test chambers; a large aluminium box, shown in Fig. 6.1 and an aluminium cylinder shown in Fig. 6.2. Details of the experimental set up are described in the next section.

6.2 Experimental Procedure

For each test chamber, PD produced by a range of test cells was measured simultaneously using both RF and IEC techniques. Three test chambers were used, having volumes of 3.91 m^3, 1 m^3 and 0.24 m^3 respectively. Monopole antennas have been fitted internally to each chamber to detect the radiated energy produced by each discharge. Each monopole has an effective length of 16.1 mm. PD was also measured using a conventional IEC60270 system (Lemke LDS-6). Signals from both the conventional system and the RF antenna were fed simultaneously into a 3 GHz bandwidth digital oscilloscope with a sampling rate of 20 GS/s and recorded. Around 2000 PD signals have been recorded for each test configuration.

RF and IEC PD data is correlated in post-processing using high-level software, since, due to the complexity of the calculations it is not possible to achieve this in real-time. Due to the complex resonant nature of RF PD pulses, the peak amplitude is an ambiguous measure. Calculating the energy of the pulse takes into account all points on the signal and is therefore a measure which is more proportional to the energy radiated by the original PD current pulse.

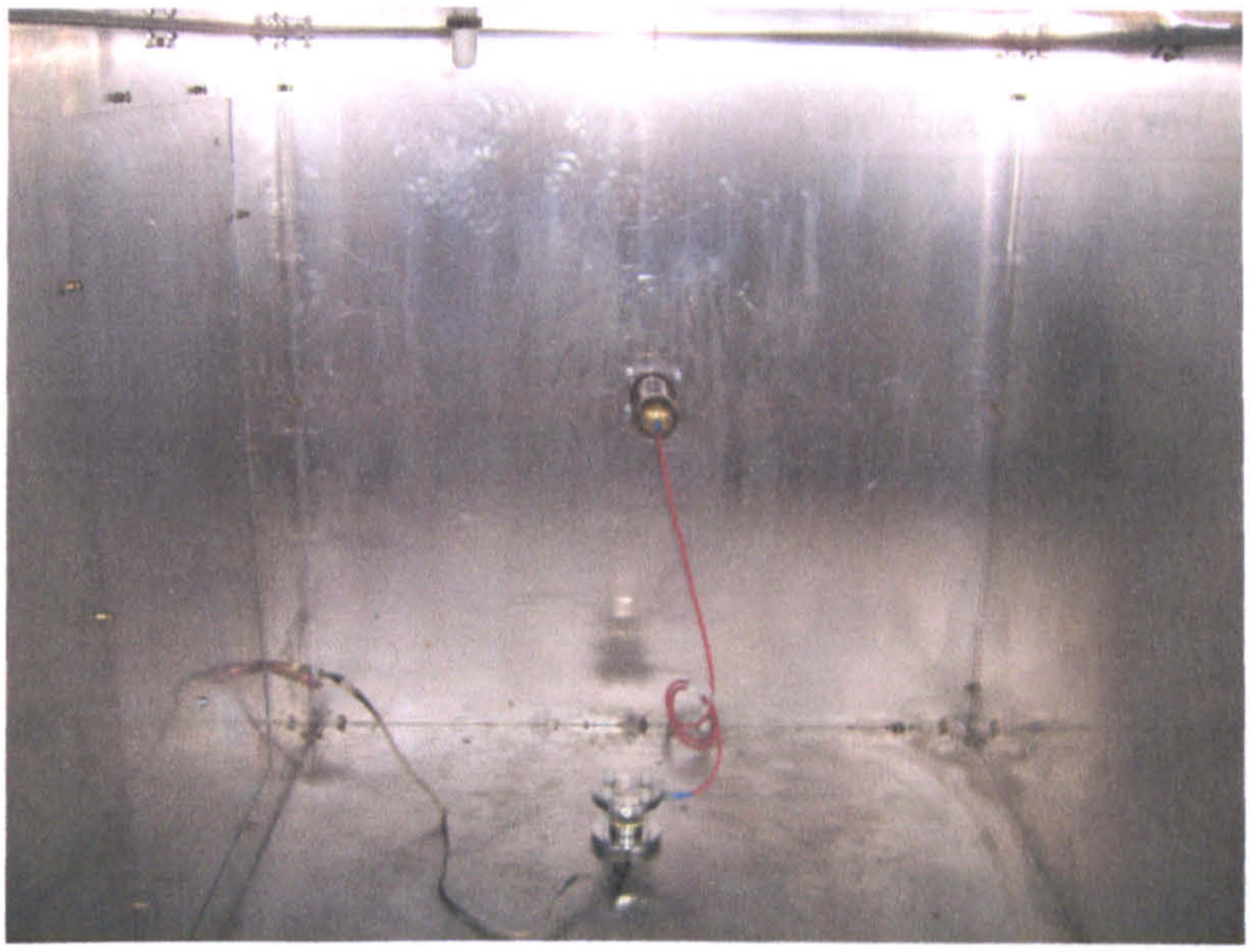

Figure 6.1: An aluminium test chamber of dimensions 2.5 m * 1.25 m * 1.25 m (v=3.91 m^3). The test cell is connected to the HV supply through a 20 kV bushing. A UHF monopole antenna (top) detects radiated electromagnetic pulses from the test cell.

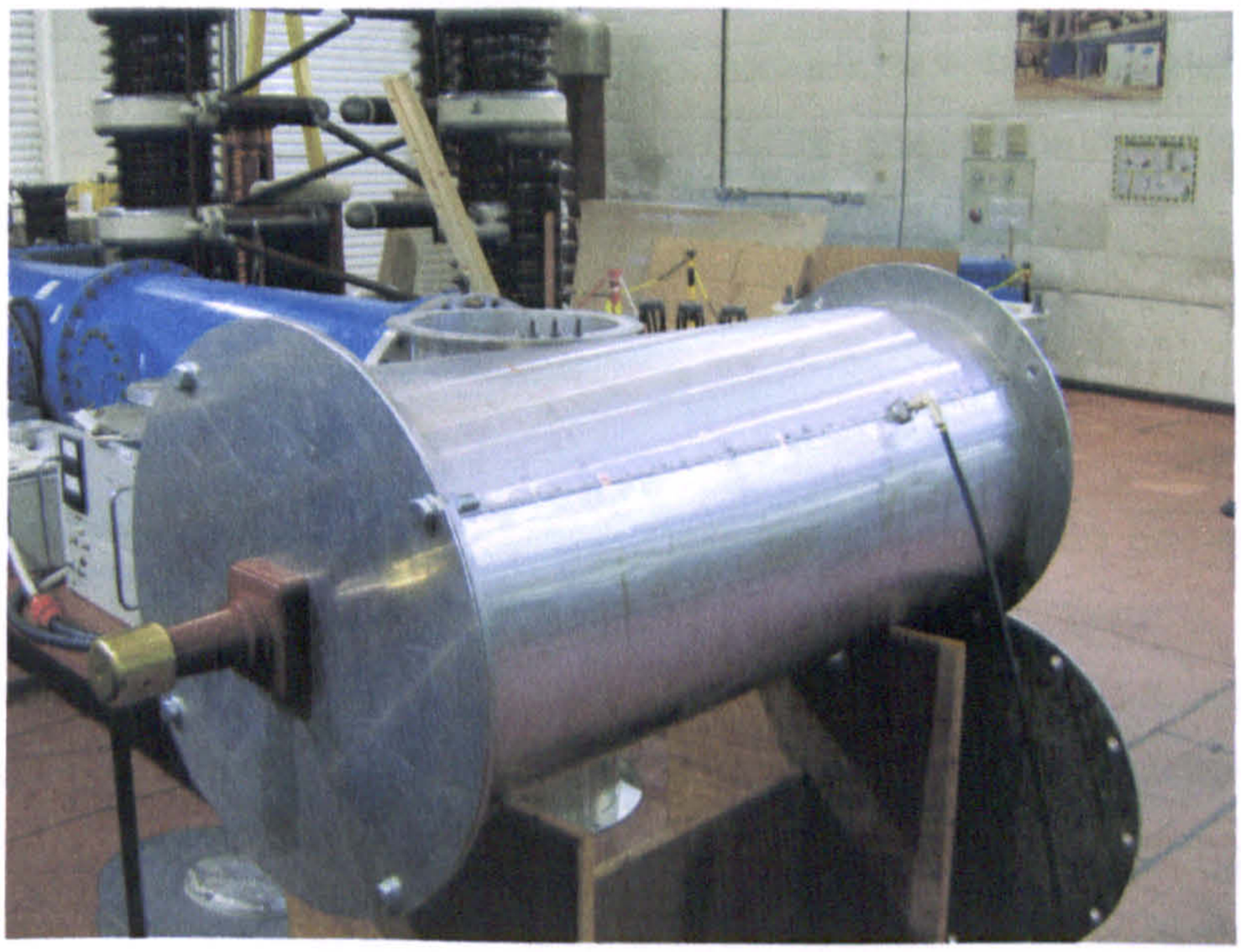

Figure 6.2: An aluminum cylinder of diameter 0.5 m and length 1.2 m is used to emulate a GIS chamber. The HV bushing can be seen at the near end. The test chamber has a volume of 0.24 m^3

Table 6.1: Order-of-magnitude pJ/pC levels for defects in varying sizes of test chamber.

Defect	3.91 m^3 box	1 m^3 box	0.24 m^3 cylinder
Floating electrode in SF_6	$1*10^{-3}$	$1*10^{-3}$	$1*10^{-2}$
Free particles in oil	$2*10^{-3}$	$2*10^{-2}$	$1*10^{-2}$
Free particle in SF_6	$7*10^{-4}$	$5*10^{-2}$	$3*10^{-2}$
Point-plane in SF_6	$1*10^{-6}$	$3*10^{-4}$	$4*10^{-5}$
Void in resin	$4*10^{-6}$	$3*10^{-5}$	$5*10^{-4}$

6.3 Results

Figs. 6.3 to 6.7 compare correlation patterns for five PD sources placed within two separate test chambers. Results for the 1 m^3 test chamber have been shown previously. During testing, it was necessary to re-calibrate the IEC system several times using the same test cell. In most cases this resulted in only a slight variation in the calibration factor for results on the same test cell, the maximum variation in the calibration factor was 30% for two separate experiments on the point-plane cell. In the case of the free particles, it is possible to identify two correlation clusters, produced by the respective 2.5 mm and 3 mm particles within the test cell, for tests on the GIS cylinder. Since the clusters are separated on the basis of UHF energy, it is possible that in this case the clusters can be separated due to a favorable antenna orientation. Another exception is the void sample. In this case variation in the appearance of the correlation pattern is due to degradation of the sample due to electrical stressing.

6.4 Discussion

It can be seen from the results that apparent charge values do not vary by more than would be expected due to re-calibration of the IEC system. One would expect UHF energy to decrease with a larger tank size, however it can be seen on examination on Fig. 6.8 that, although the largest tank does produce the lowest pJ/pC levels, in general, the medium tank (1 m^3) produces the highest levels. The two exceptions are the floating electrode and the void. It appears unlikely that pJ/pC levels obtained in the laboratory can be applied to plant diagnosis in the field using a simple scaling factor related to tank size. There are other factors which must be considered. Antenna position and orientation relative to the PD source may also have an effect on the RF/IEC relationship. The shape of the

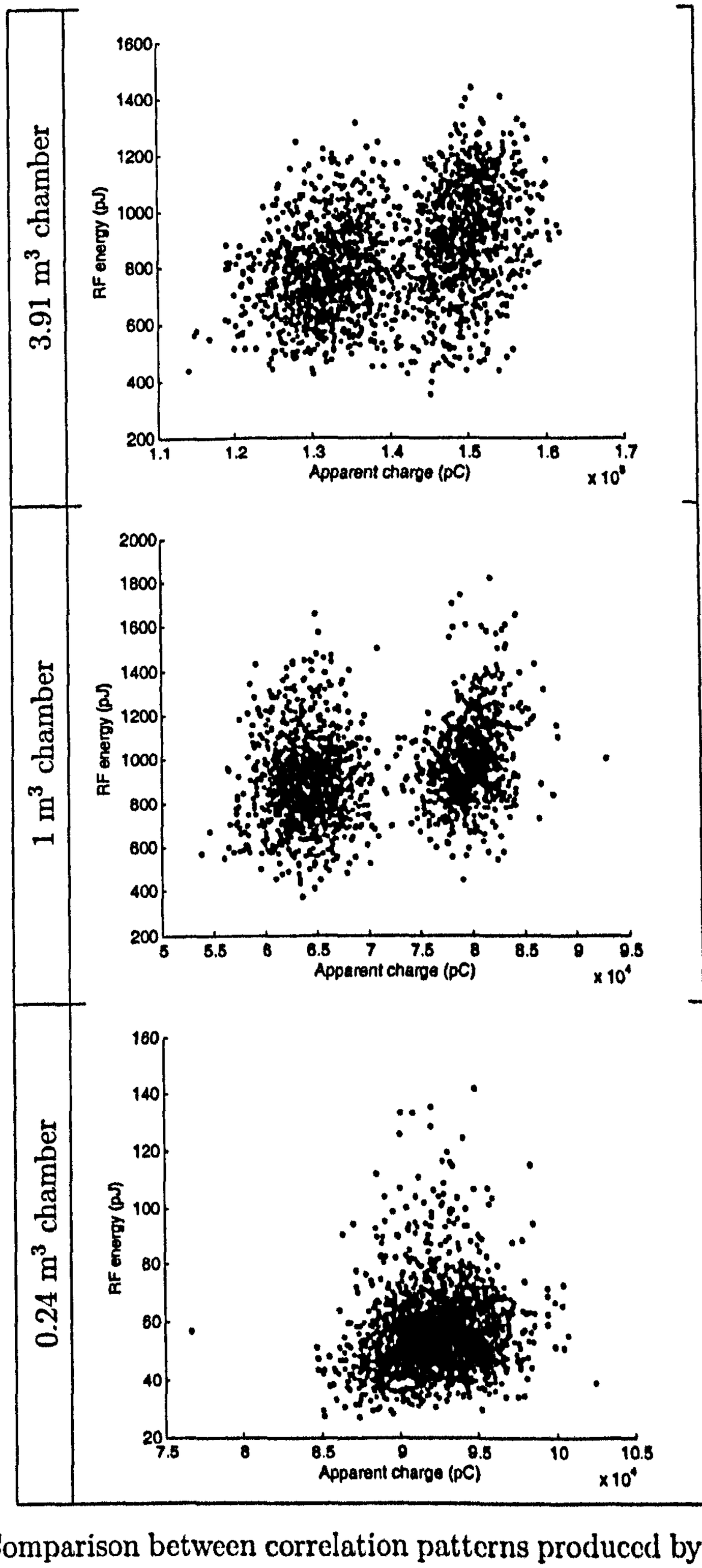

Figure 6.3: Comparison between correlation patterns produced by a floating electrode using three different chamber geometries. 4 bar gauge pressure, 18 kV applied voltage.

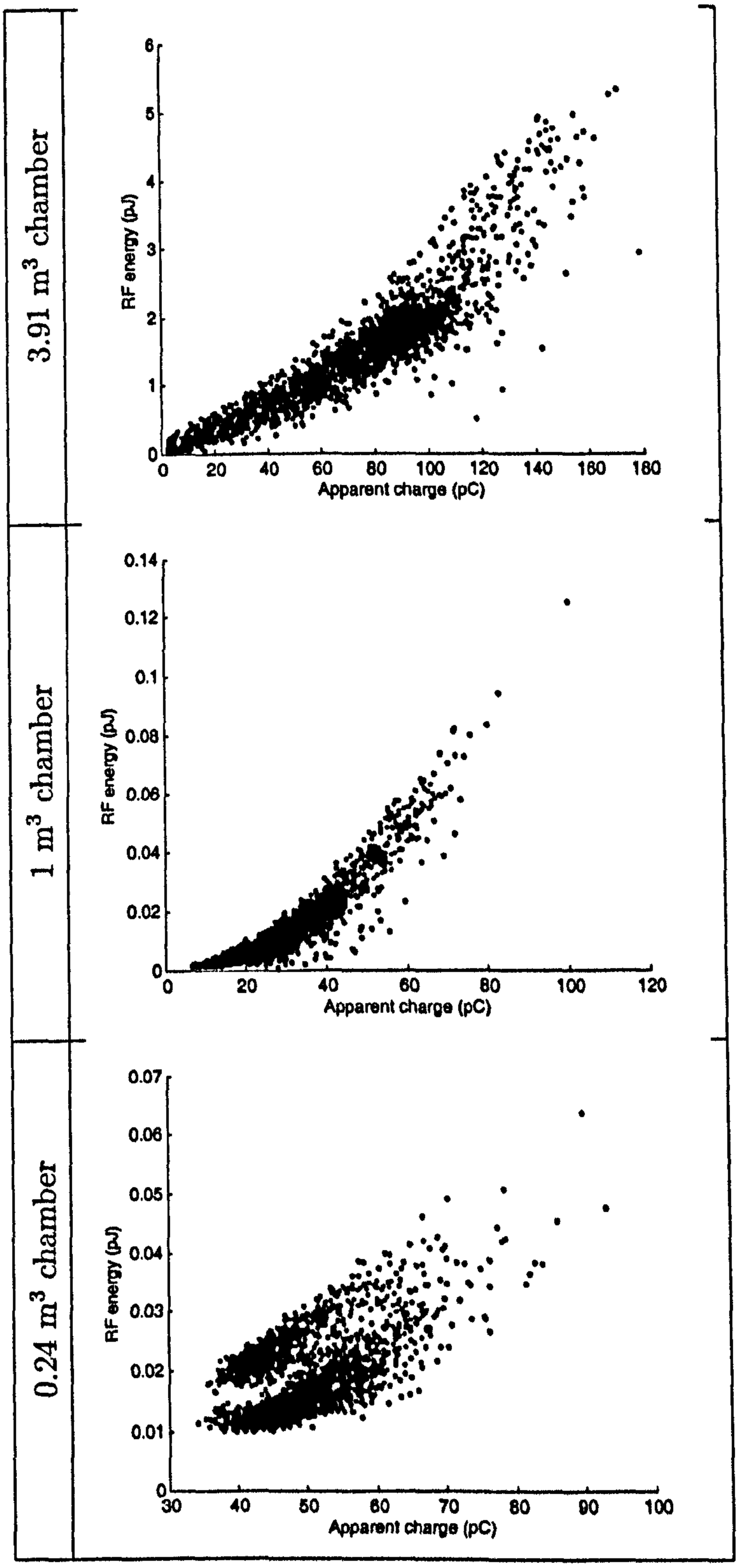

Figure 6.4: Comparison between correlation patterns produced by a double free particle in oil (2.5 mm + 3 mm diameters) using three different chamber geometries. 15 kV applied voltage.

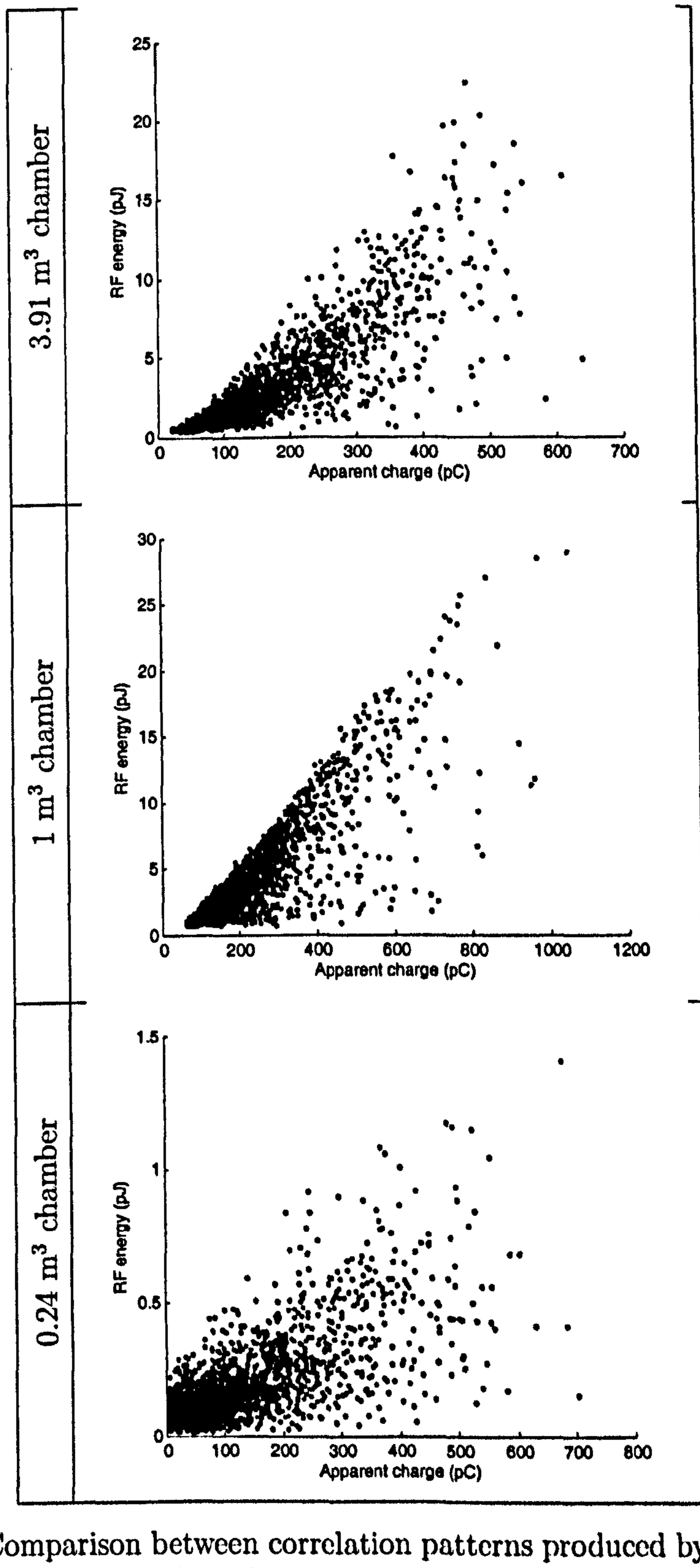

Figure 6.5: Comparison between correlation patterns produced by a 2 mm diameter aluminium free particle in SF_6 using three different chamber geometries. 10 kV applied voltage.

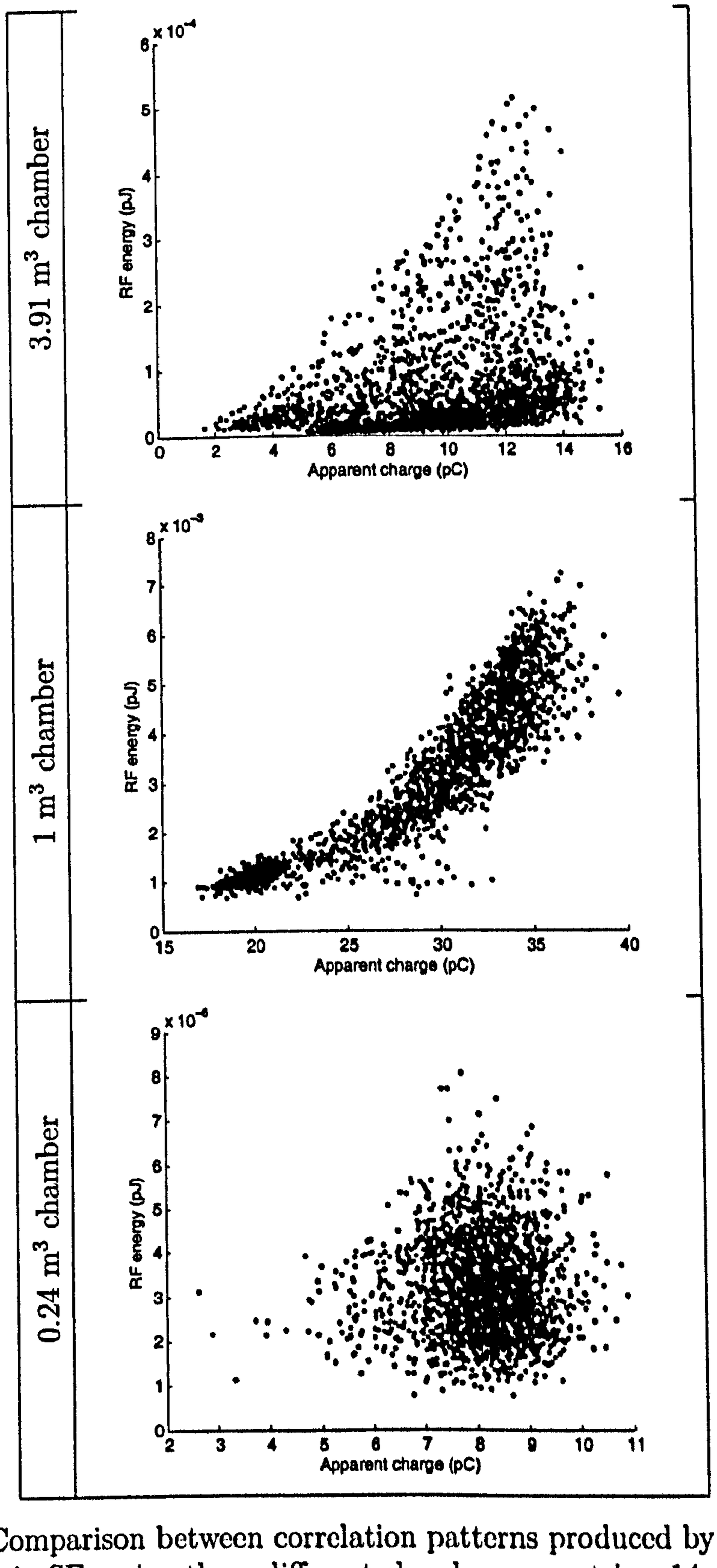

Figure 6.6: Comparison between correlation patterns produced by a point-plane configuration in SF_6 using three different chamber geometries. 14 mm needle, 25 μm tip radius, 18 mm gap, 14 kV applied voltage, 1 bar gauge pressure.

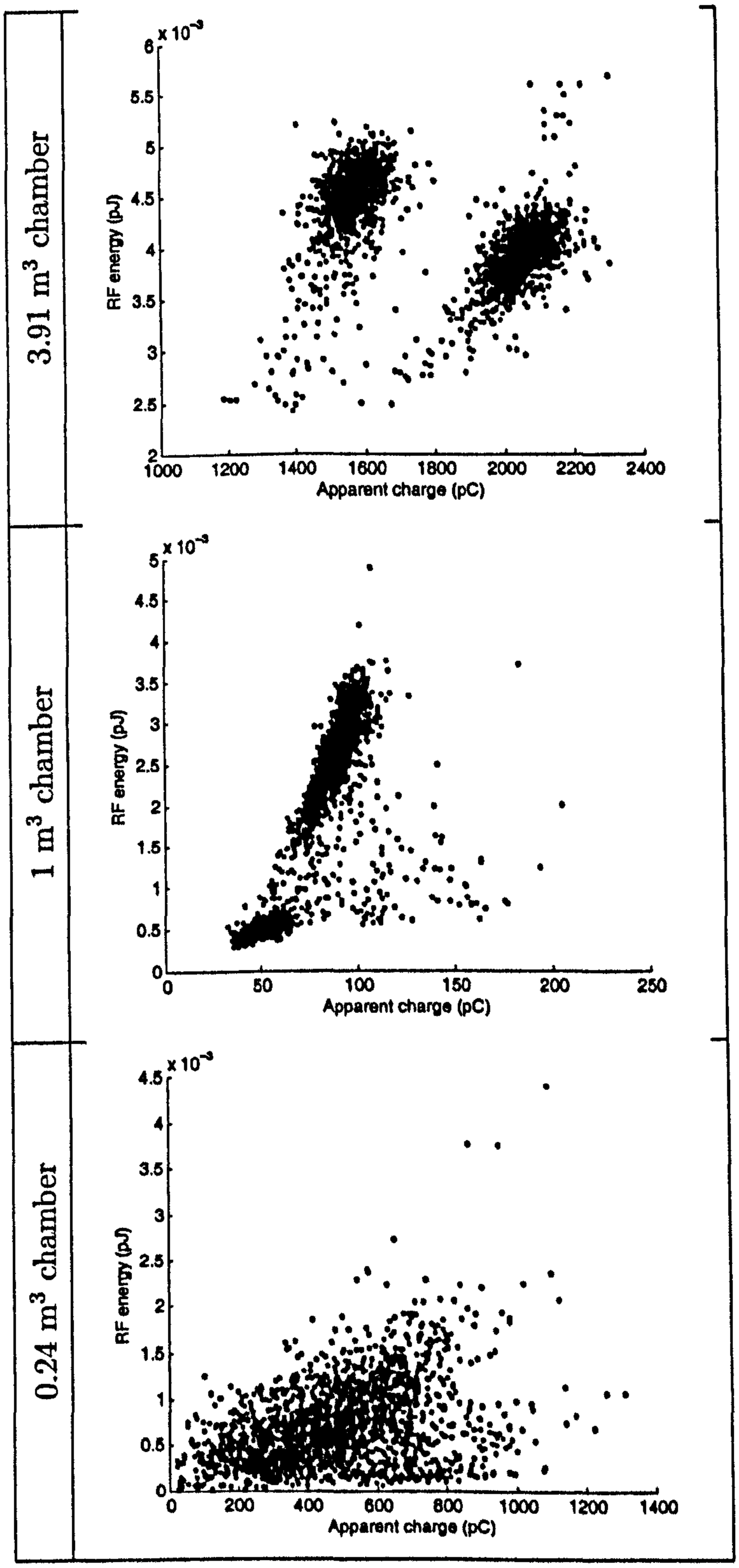

Figure 6.7: Comparison between correlation patterns produced by a void in resin using three different chamber geometries. 16 kV applied voltage.

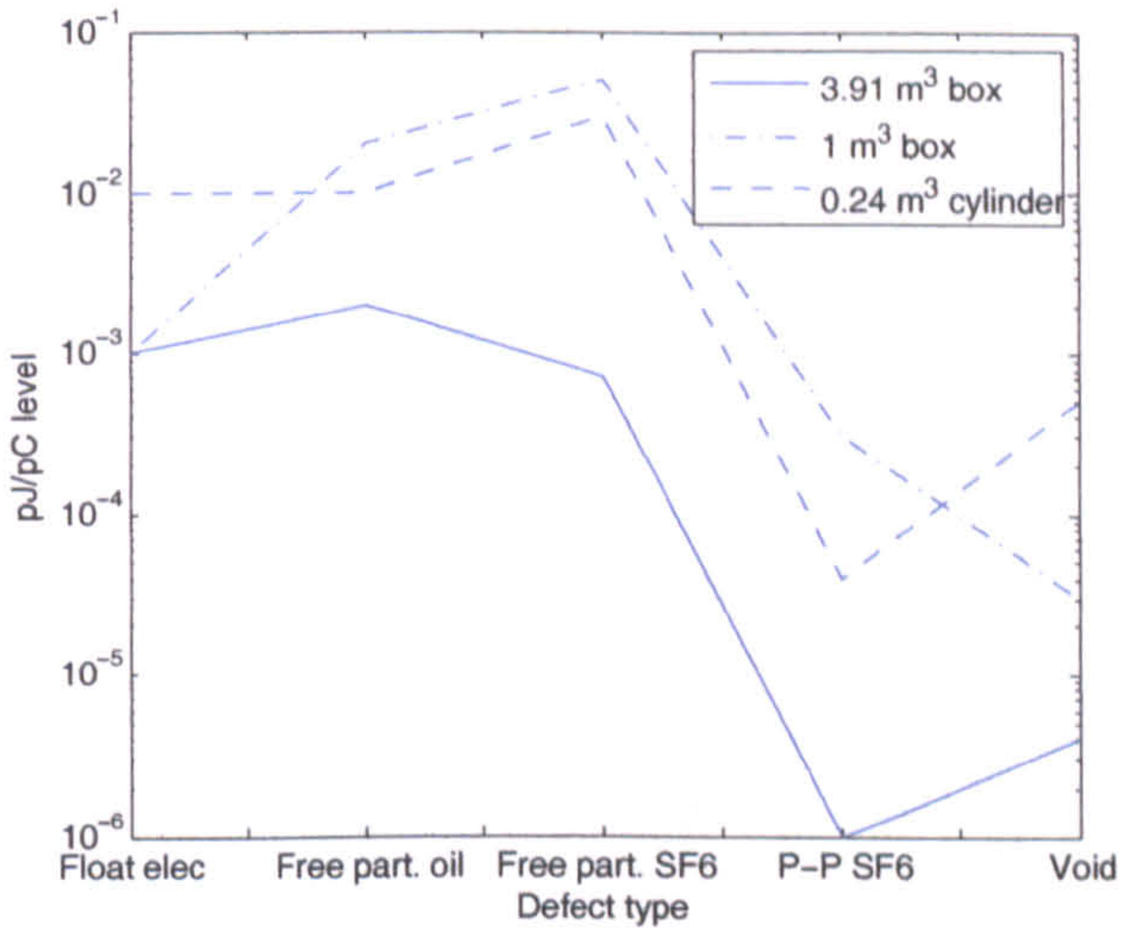

Figure 6.8: Variation in the order-of-magnitude relationship (pJ/pC) between UHF energy and apparent charge between PD sources for three different tank geometries.

tank will influence the TE and TM modes and will therefore affect the measured RF energy for a given source configuration. Clearly, the 0.24 m^3 chamber differs from the larger two in that it is cylindrical. Only test chambers that were readily available in the HV laboratory were used, with any influence of the shape of the tank assumed to be negligible.

Fig. 6.9 shows the variation in UHF levels with the surface area and volume of the test chambers. The average, maximum and minimum UHF energy levels were obtained by observing the value corresponding to a constant level of apparent charge on each of the three correlation plots corresponding to a particular defect type. It would be expected that for larger chamber geometries, the amplitude of the UHF signal would be lower and the signal would persist for longer. For the floating electrode and the void, UHF levels decrease with increasing tank volume and surface area, however for all other defects, UHF levels peak at the 1 m^3 box. Again, it is possible that this is a result of both the orientation of the antenna and its position relative to the defect. Although every attempt was made to seal the test chambers, EM leakage from the chamber may also be a factor. In order to eliminate these factors, it would be necessary to install an array of equally-spaced couplers throughout each chamber and determine the average UHF energy produced over the array. Even if this were feasible, producing a repeatable coupler position relative to the defect would still be a challenge.

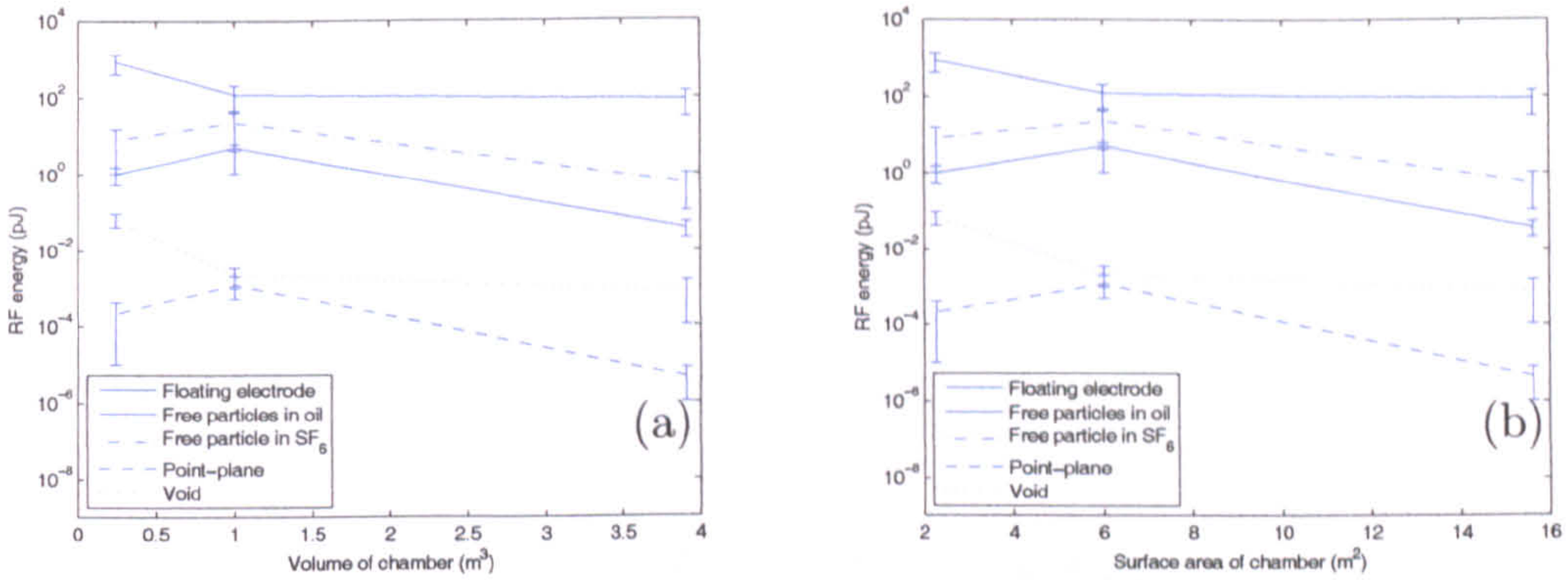

Figure 6.9: The relationship between (a) UHF energy and chamber volume, (b) UHF energy and chamber surface area. UHF energy levels are acquired from the correlation plots by reading the maximum, minimum and average value corresponding to a given level of apparent charge.

6.5 Conclusion

The order-of-magnitude relationship between RF energy and apparent charge varies depending on the geometry of the test chamber. This variation is not a simple linear relationship, with results indicating that, in general, the 1 m^3 chamber produces the highest pJ/pC levels. The relationship between pJ/pC level and chamber geometry also depends on the PD source, with a void sample in resin showing the highest order-of-magnitude relationship for the smallest test chamber – a result which would perhaps be expected intuitively since RF amplitudes would be expected to be higher for a smaller geometry. This leads to the conclusion that a number of other factors may have a more significant effect on the pJ/pC level than chamber geometry, namely coupler orientation and distance relative to the PD source. As far as the implications for any potential diagnostic tool are concerned, it is unlikely that pJ/pC relationships obtained in the laboratory can be applied directly to the diagnosis of unknown defects in the field. It is however, recommended that simultaneous measurement is applied to the plant item under test in order that the order-of-magnitude pJ/pC relationship can be calibrated for the given test environment.

Chapter 7

Simultaneous IEC60270 and RF Phase-Resolved PD Measurement

This chapter presents phase-resolved partial discharge patterns obtained using RF and IEC techniques for a number of different defects sources. Results indicate that due to the different responses of each system, clear differences exist in the phase-resolved data, implying that more accurate defect classification should be achieved if a measurement system is trained exclusively using either IEC or RF data. Combining both outcomes may also provide additional diagnostic information.

7.1 Introduction

Defect classification has historically been achieved by representing the data in phase-resolved form. The phase-resolved partial discharge (PRPD) pattern consists of PD data recorded over a period of time plotted on a 3-dimensional graph.

Today, the analysis of such PRPD patterns is one of the most commonly used diagnostic techniques for assessing the condition of an insulation system and is employed by most commercially available PD measurement systems. Attempts have been made to automatically classify PD sources based on statistical techniques. Such classification is often based on conventional PD measurements. However, given the increasing popularity of RF PD measurements for fault diagnosis on large electrical plant items such as power transformers [49,50,52,67,69], which respond to the dynamics of charge motion, questions arise as to whether the same classification techniques can be applied, or whether a system trained using IEC data can classify a PD source using RF data. Since both the RF and IEC

techniques in principle respond differently to the same PD pulse, phase-resolved data from each system has the potential to vary for measurements on the same PD source geometry. Phase-resolved plots produced using conventional measurements are defined as 'ϕ-q-n plots', where the number of discharges n is plotted against phase angle and apparent charge. Phase-resolved plots produced using RF measurements are defined as 'ϕ-U-n plots', where U is the energy of the RF signal as defined by Equation (3.1.3).

7.2 Background

Very few studies have been undertaken which compare the UHF and IEC techniques [56, 58, 70] and to the author's knowledge no publications compare phase resolved patterns obtained simultaneously on a pulse by pulse basis using the two measurement systems. By capturing RF, IEC and phase data simultaneously using a 3GHz bandwidth oscilloscope, it is possible to achieve a fair comparison between the two measurement methods. In other words, each pulse-pair on the respective PRPD plots can be distinguished individually and related back to the original PD current pulse. The results presented therefore represent the first true simultaneous phase-resolved measurement. The use of a high bandwidth oscilloscope rather than the conventional spectrum analyser ensures that all events occurring on one a.c. reference cycle are captured.

7.3 Experimental set up

The experimental set up is similar to that used in combined RF/IEC measurements with the addition of the phase reference signal measured on one of the oscilloscope's spare channels.

7.4 Results

Figures 7.1 to 7.5 compare PRPD patterns produced using PD data measured simultaneously using both RF and IEC techniques. For patterns produced using a floating electrode, shown in Figure 7.1, both apparent charge and UHF energy levels are high as would be expected. Clear differences exist in the two sets of patterns. A large spread exists in the magnitude of the measured UHF pulses,

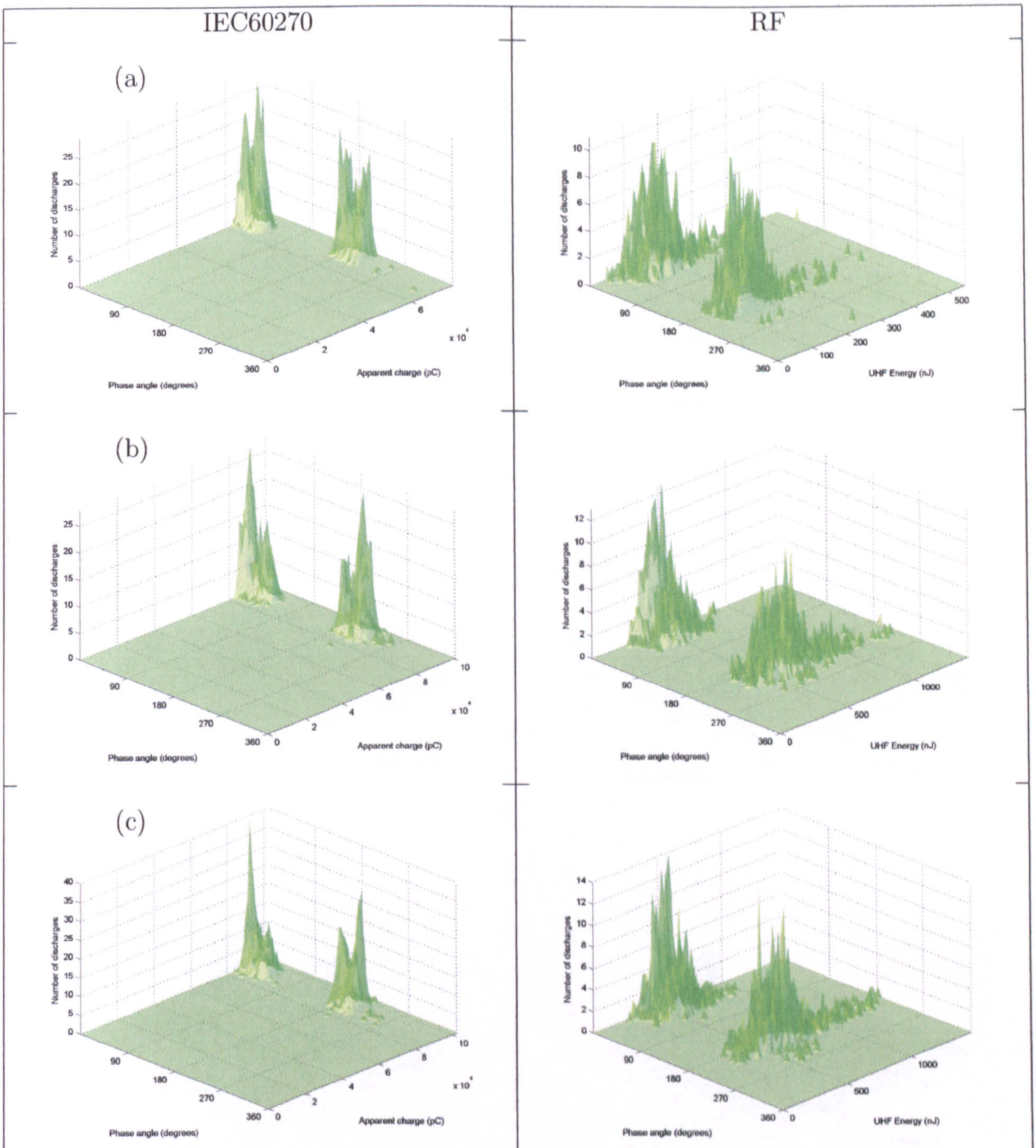

Figure 7.1: Phase resolved patterns for PD measured simultaneously using IEC and RF techniques. IEC and RF patterns for a floating electrode-type defect in SF_6. (a) 2 bar gauge pressure, 15 kV applied to upper electrode, (b) 4 bar, 18 kV, (c) 4 bar, 20 kV.

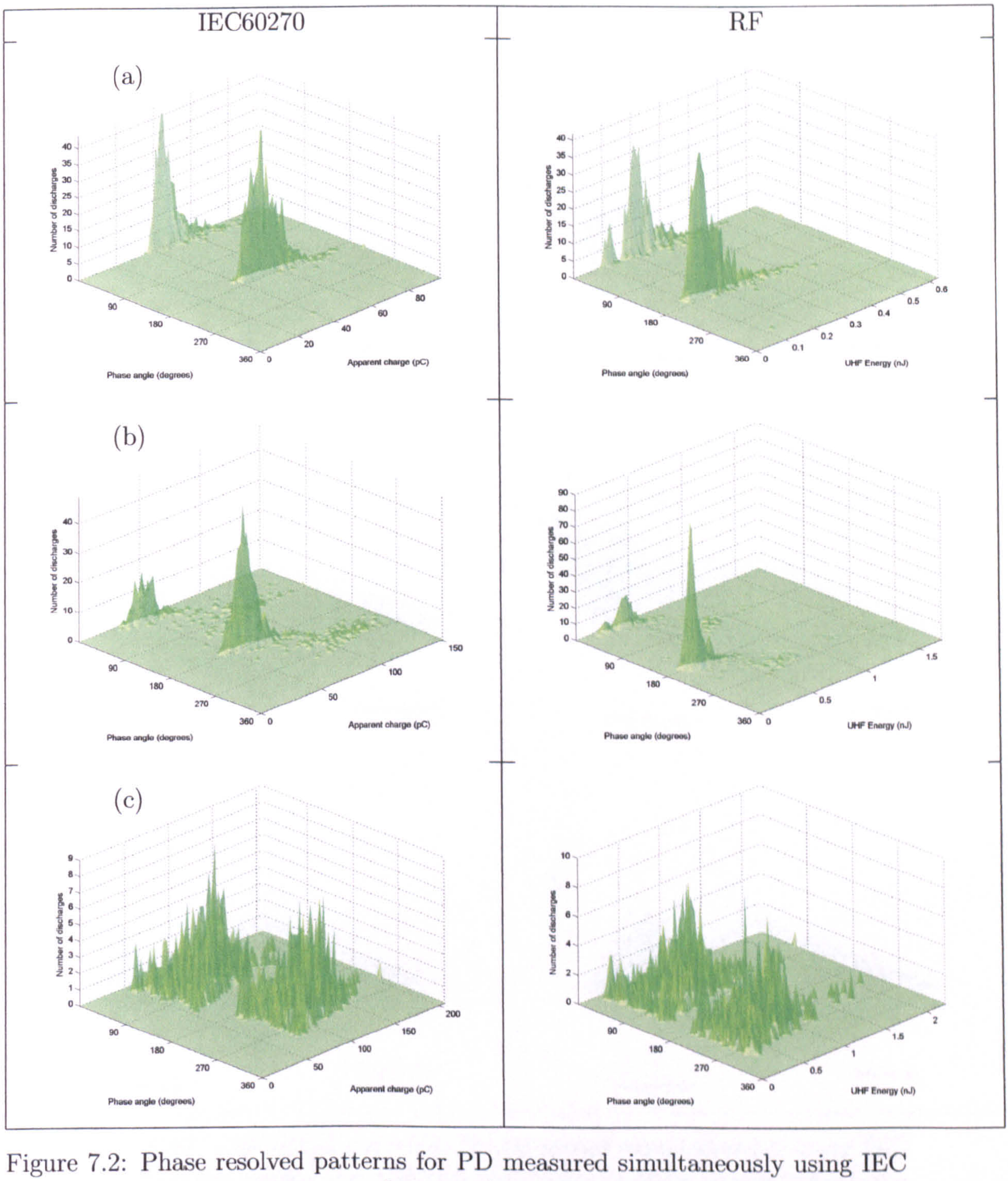

Figure 7.2: Phase resolved patterns for PD measured simultaneously using IEC and RF techniques. 2.5 mm and 3 mm free spherical aluminium particles in transformer oil. (a) 13 kV applied to upper electrode, (b) 14 kV, (c) 15 kV.

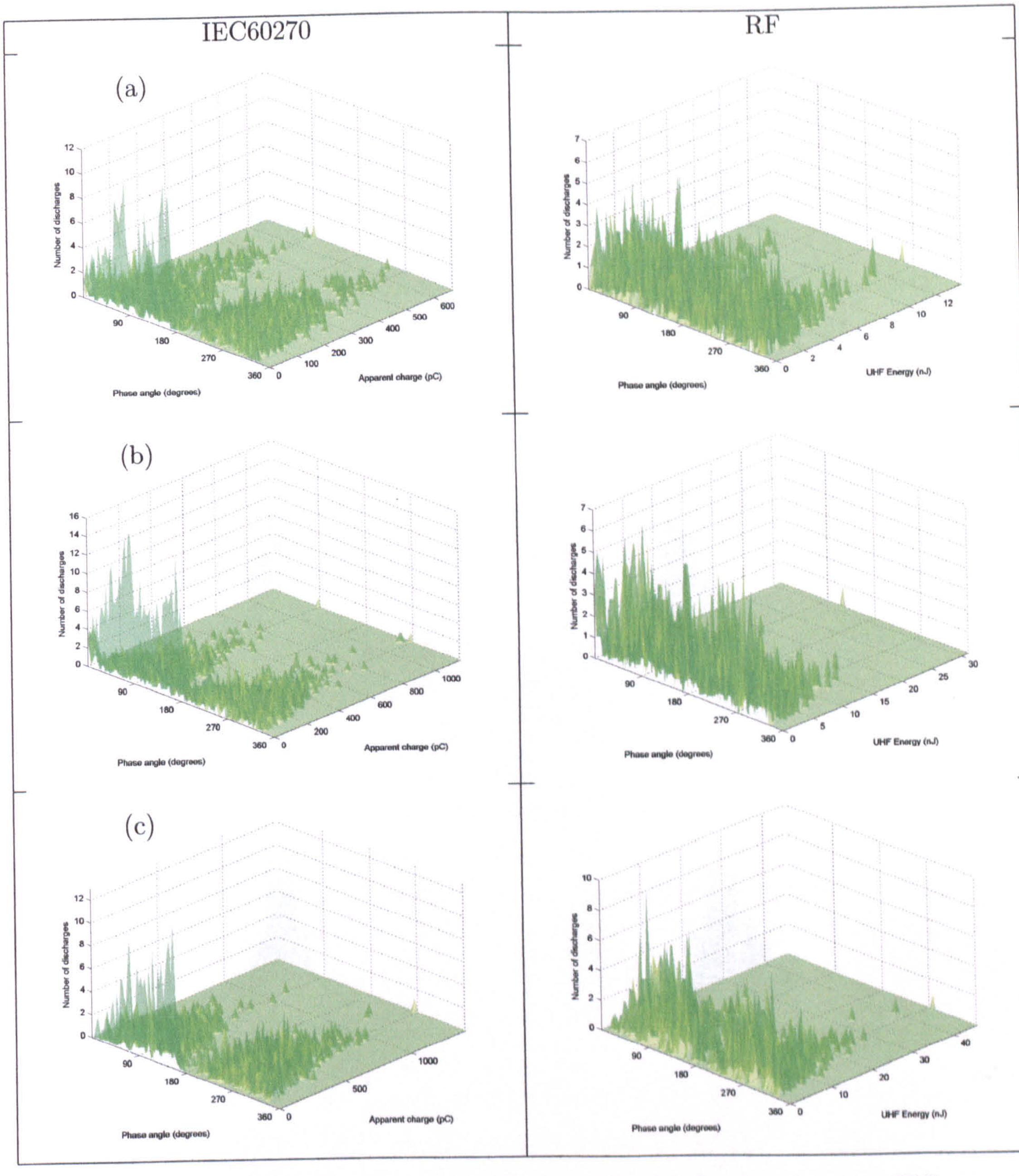

Figure 7.3: Phase resolved patterns for PD measured simultaneously using IEC and RF techniques. 2 mm free spherical aluminium particle in pressurised SF_6 gas. 2 bar gauge pressure. (a) 10 kV applied to upper electrode, (b) 14 kV, (c) 15 kV.

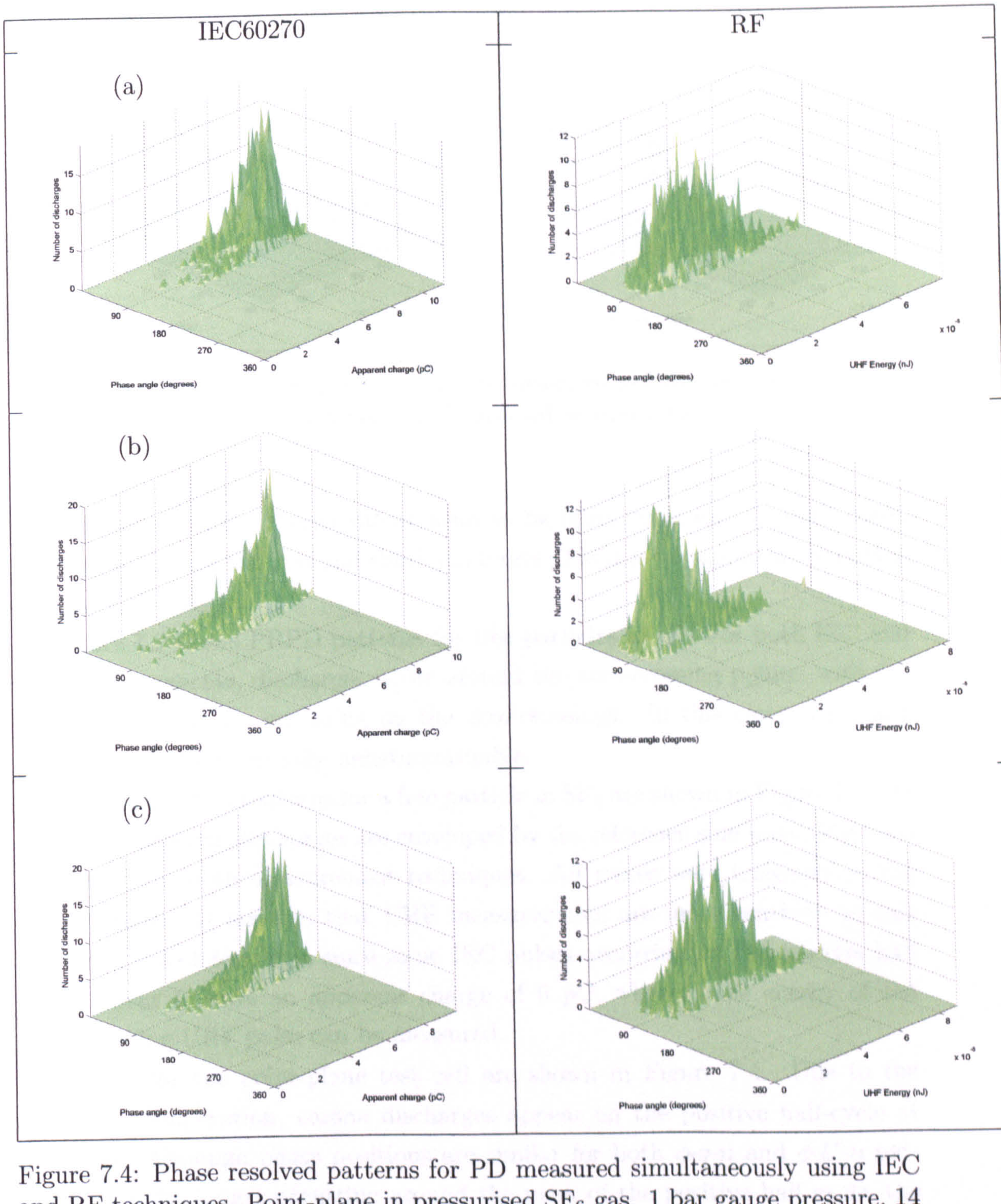

Figure 7.4: Phase resolved patterns for PD measured simultaneously using IEC and RF techniques. Point-plane in pressurised SF_6 gas. 1 bar gauge pressure, 14 mm tungsten needle, 25μ tip radius. (a) 14 kV applied to upper electrode, (b) 16 kV, (c) 17 kV.

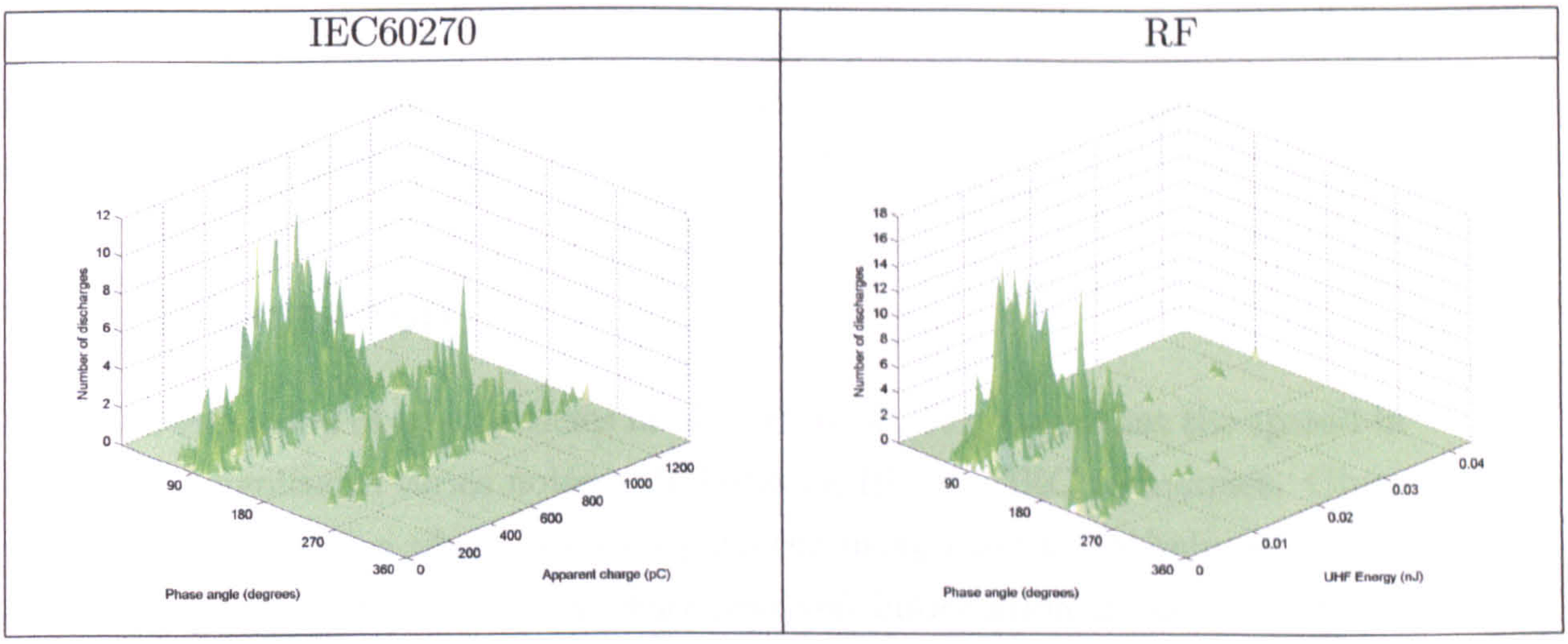

Figure 7.5: Phase resolved patterns for PD measured simultaneously using IEC and RF techniques. Void in resin. 15 kV applied to upper electrode.

whereas the apparent charge values seem to be fairly constant. In both cases, discharges occur in the first and third quadrants. There is no significant variation with applied voltage.

Figure 7.2 shows PRPD patterns for free particles in oil. For both IEC and UHF measurements, discharges occur around the zero-crossing points, with the highest pulse density occurring on the zero-crossings. In this case, ϕ-q-n and ϕ-U-n patterns are virtually indistinguishable.

ϕ-q-n and ϕ-U-n patterns for a free particle in SF_6 are shown in Figure 7.3. As would be expected, discharges are enveloped by the reference sine wave. Patterns are similar for both measurement techniques. All traces were triggered on the UHF channel. It appears that UHF measurements are more sensitive to this particular defect topology, since some IEC pulses occurring on the positive half cycle appear to have an apparent charge of 0 pC, whereas the energy of the corresponding UHF pulse can be measured.

Results for the point-plane test cell are shown in Figure 7.4. Due to the electrode configuration, corona discharges appear on the positive half-cycle at inception. Although phase positions are similar for both ϕ-q-n and ϕ-U-n patterns, with discharges occurring around the peak of the positive half cycle, the discharge cluster is skewed toward the upper end of the apparent charge scale for conventional measurements, whereas the maximum number of discharges seems to correspond to the mean UHF energy value in the ϕ-U-n graph.

Figure 7.5 shows ϕ-q-n and ϕ-U-n patterns for a resin sample containing an

unknown number of voids. As expected, discharges occur mainly in the first and third quadrants. For the ϕ-U-n pattern, a larger pulse density occurs at the lower end of the UHF energy scale.

7.5 Discussion

With the exception of free particles in oil and in SF_6 it is clear that the spread in discharge magnitudes varies noticeably between RF and IEC techniques. Given the difference between phase resolved patterns using the two techniques, classification algorithms which rely on phase-resolved information to identify defects may prove more accurate if trained exclusively on either IEC of RF data.

On examination of the results, there is apparently no significant variation in phase position between ϕ-q-n and ϕ-U-n patterns. This may be due in part to the manner in which the PD signals are triggered. Signals from both IEC and UHF channels are captured when the UHF channel is triggered, as would be expected on any oscilloscope. Although it can be seen that the spread in discharge amplitude varies noticeably for both data sets, the phase positions are very similar and is likely a result of triggering both channels on the UHF pulses. This is an inevitable consequence of a practical system that can only trigger on one data source. Therefore in order to achieve a more rigorous comparison, it may be necessary to use an oscilloscope that has the capability of triggering on either the UHF *or* the IEC channel. Whether it is possible to implement an 'OR' triggering function will be explored further in future.

7.6 Conclusions

Phase-resolved patterns have been obtained for PD measured simultaneously using RF and IEC techniques for a number of different defects sources including free particles, protrusions, floating electrodes and voids. Oil, SF_6 and resin were used as insulating media. Simultaneous measurement allows points on the respective patterns to be related back to the same original PD current pulse. Results have shown that due to the different responses of each system, a more accurate defect classification should be achieved if a measurement system is trained exclusively using either IEC or RF data. It has been noted that similarity in phase positions between the respective PRPD plots may be partly due to the necessity to trigger

all data on a single channel. It may be possible to overcome this issue by using an oscilloscope that is capable of triggering all traces on either the IEC or the RF channel.

Chapter 8

Frequency Distribution of RF Energy from PD Sources and its Application in Combined RF and IEC60270 Measurements

It has been shown that correlation between RF energy and apparent charge can yield important information regarding the shape of the underlying PD pulse. It is proposed that this new measurement strategy can be further enhanced by additionally calculating the relative spectral energies of the measured RF signals. The spectral energies of radiated RF PD pulses vary depending of the topology of the defect source and therefore may serve to enhance the quality of diagnostic information. Results indicate that the frequency distribution of RF energy measured simultaneously along with apparent charge could prove useful as an additional means of defect identification and characterisation.

8.1 Combining RF and IEC60270 Measurements

Although neither the RF or IEC techniques possess the necessary attributes to be considered an ideal diagnostic tool, RF measurements overcome some of the the shortcomings regarding the IEC technique. For example, RF measurements can provide accurate information on PD location and exhibit a fast response to very short events within a PD pulse. Figure 8.1 (a) shows the correlation between IEC apparent charge and RF energy for partial discharges produced by a free metallic

particle in oil. Figure 8.1 (b) shows a correlation pattern for PD produced by a point-plane configuration in SF_6.

The benefits of a combined system are exemplified when the fundamental differences in the response of the respective measurement systems is considered. Essentially, conventional measurements are concerned with quantifying displaced charge in the test object under stress regardless of the stress mechanism, while RF measurements respond to the dynamics of charge motion. Fundamentally, this is because electromagnetic radiation arises from charge acceleration. Since IEC60270 measurements are related to the integral of the PD current pulse and RF measurements to its derivative, combining the two techniques will lead to a better physical understanding of unknown discharges taking place within the insulation system, and ultimately, better testing and diagnostic capabilities.

8.2 Frequency Distribution of RF Energy

Two RF signals produced by two separate defects are presented along with their respective fourier transforms in Figure 8.2. It is noted that the shape of these signals, or their 'signature', is affected by three factors. Firstly, by excitation of resonances within the chamber which are governed by the shape of the original current pulse and by the dimensions of the chamber. Secondly, by propagation effects such as reflection, dispersion and attenuation and finally, by the efficiency and bandwidth of the RF coupler, or antenna. Therefore, assuming all other factors remain constant – dimensions of the chamber, defect location, antenna response, etc – it is possible to identify a specific fault type by the characteristics of the measured RF signal. This has been shown previously by Meijer [71] and has been employed to distinguish between different PD sites [72]. It is proposed that this additional knowledge can be used to enhance the combined measurement strategy. In the study presented here, the frequency spectrum was split into five bands, with the energy contained within each band plotted against the corresponding apparent charge for a given PD pulse. The proposed method aims to facilitate automatic defect classification for large sets of data.

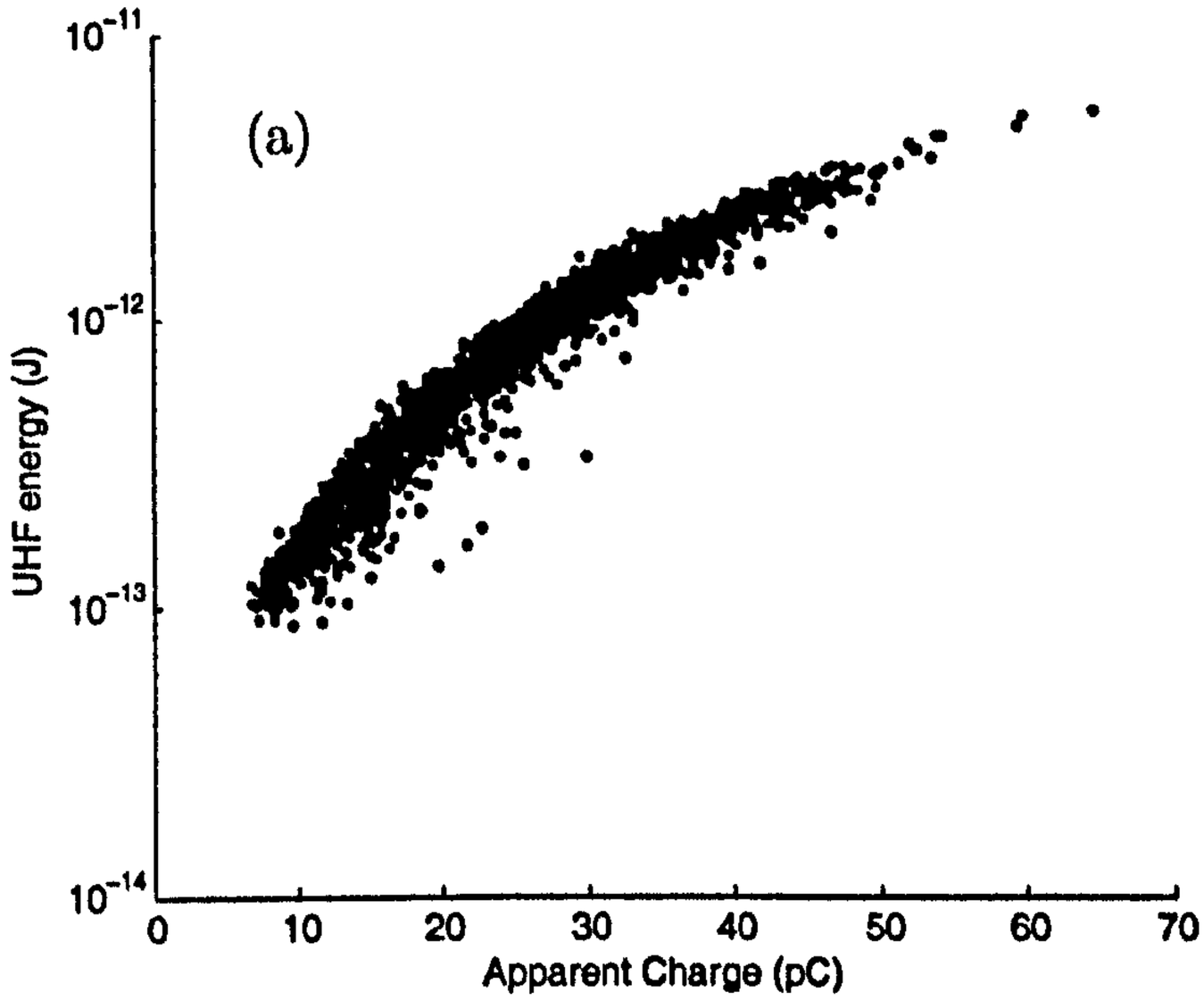

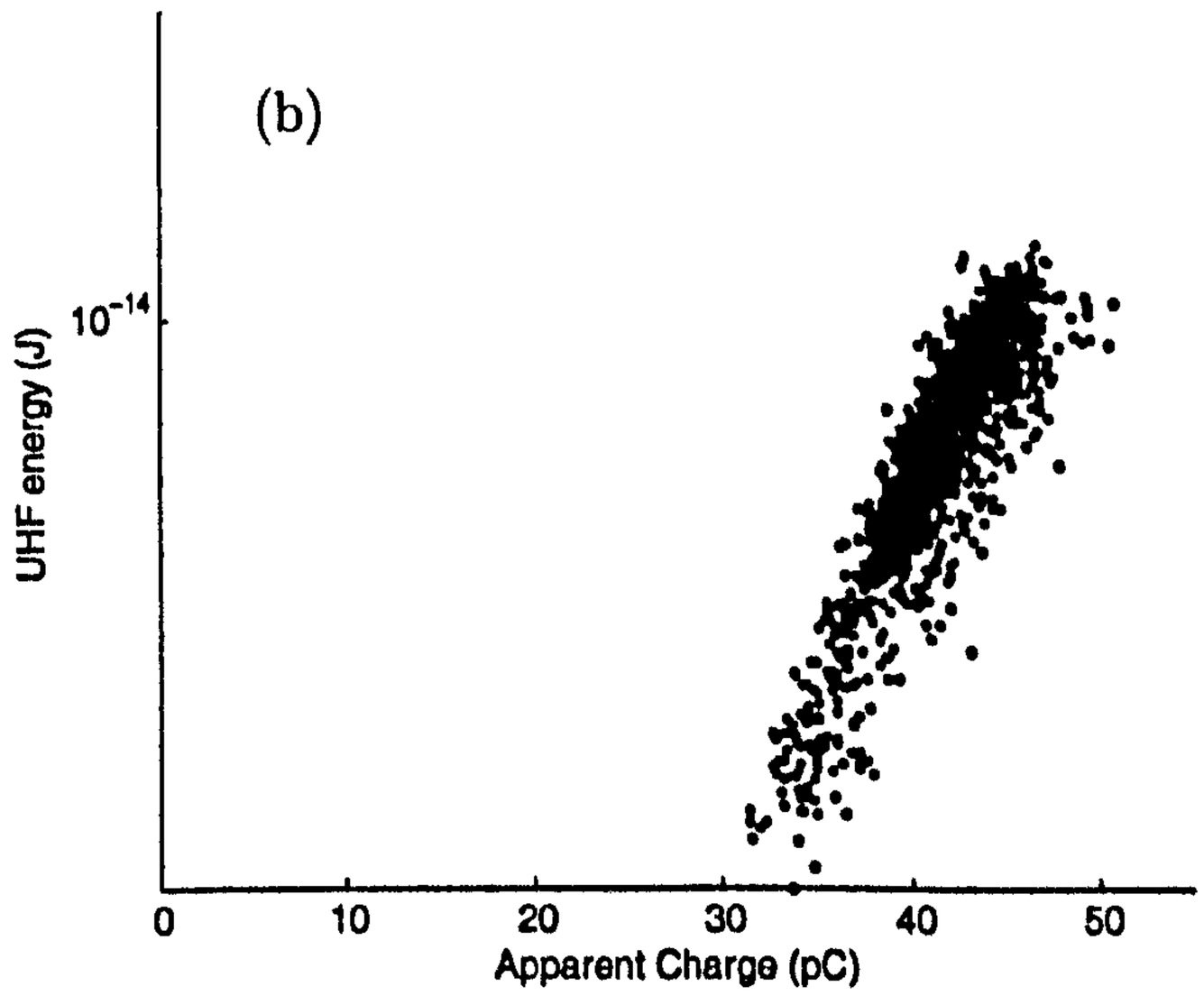

Figure 8.1: (a) Correlation between RF energy and IEC60270 apparent charge for PD produced by a 2mm aluminium sphere in reclaimed transformer oil (L10B) at an applied voltage of 10 kV. (b) Correlation between RF energy and IEC60270 apparent charge for a point-plane configuration in SF_6. 12 kV applied to plane electrode, 150 kPa SF_6 pressure, 18 mm gap spacing, 25 micron tip radius.

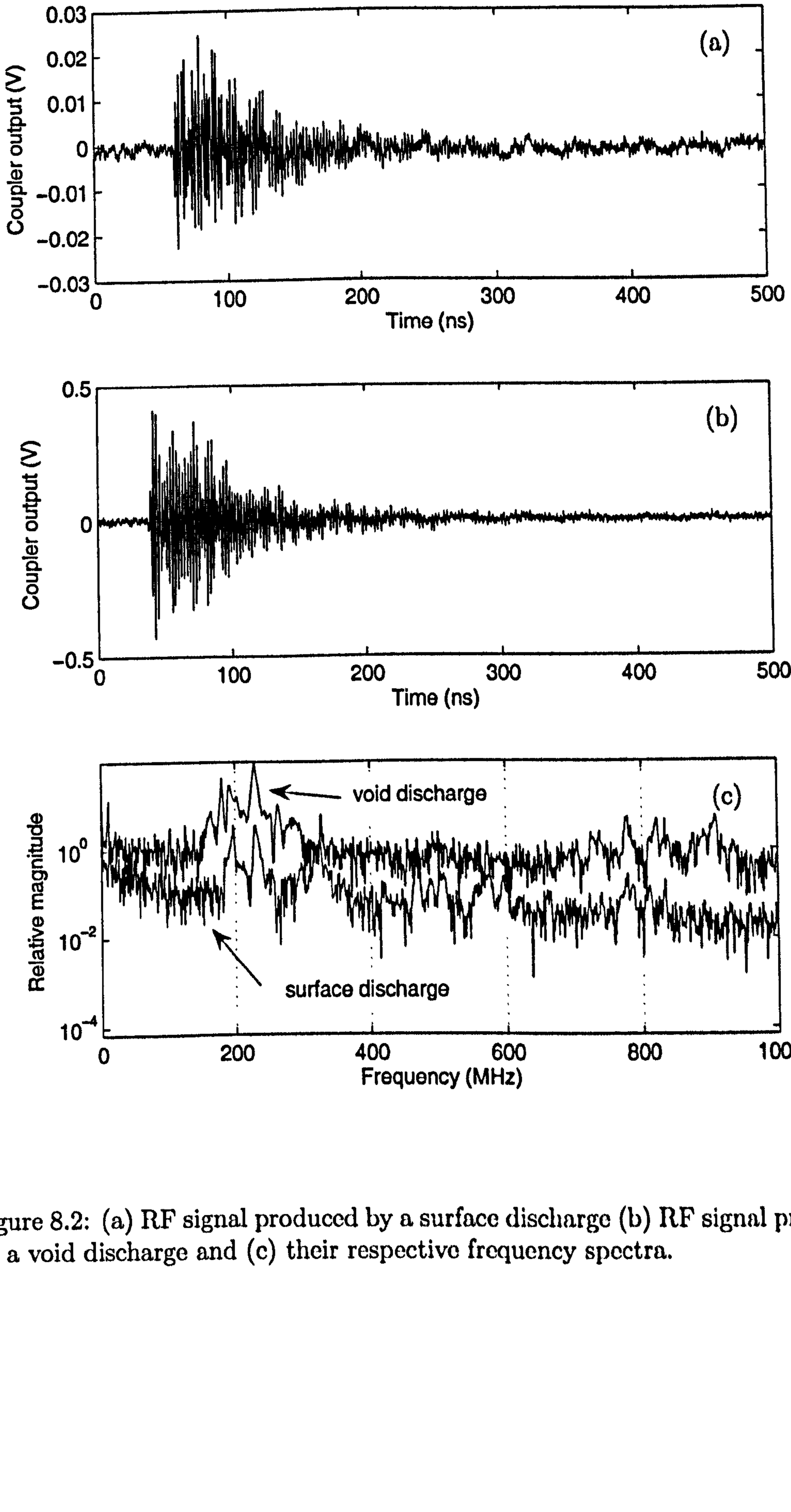

Figure 8.2: (a) RF signal produced by a surface discharge (b) RF signal produced by a void discharge and (c) their respective frequency spectra.

8.3 Applying Frequency-Selective Techniques to Combined Measurements

Similar correlations patterns exist for certain defects, for example, free particles in oil and protrusions in SF_6 both exhibit pulse shapes conducive to a quadratic relationship between apparent charge and RF energy. Such defects can however be separated by the order-of magnitude relationship between RF energy and apparent charge, which will of course be specific to the particular tank geometry and PD source location. Additionally, it is possible to gain information on the frequency characteristics of RF signals using the technique described previously.

Figures 8.1 (a) and 8.1 (b) show the respective correlations between IEC apparent charge and RF energy for a free particle in oil and a point-plane in SF_6. For each data set, RF signals have been filtered into 5 frequency bands using a finite impulse response (FIR) filter. This is achieved in post-processing where high-order filters can be implemented. In this case a 1000th-order filter was used. The resulting 5 sets of RF signatures have been plotted against apparent charge to produce Figures 8.3 (a) and 8.3 (b). This is a useful method for presenting frequency characteristics of a given PD source while simultaneously showing the correlation between RF energy and apparent charge. Comparing the two figures, it is clear that while their respective correlation patterns appear similar, RF signals produced by the free metallic particle contain a relatively high proportion of energy in the 400–600MHz band compared to the 600–800MHz band. The defects can therefore be separated on this basis.

8.4 Conclusions

Combining IEC60270 and RF PD measurement techniques has a number of potential advantages. Correlating apparent charge with RF energy for a number of PD pulses could allow better identification of the type and severity of defect in the the object under stress. It has been shown that this technique could be further enhanced by additionally calculating the spectral energies of the measured RF pulses. This allows for automatic extraction of frequency-domain characteristics, thus allowing effective defect identification in cases where correlation between apparent charge and RF energy alone is insufficient.

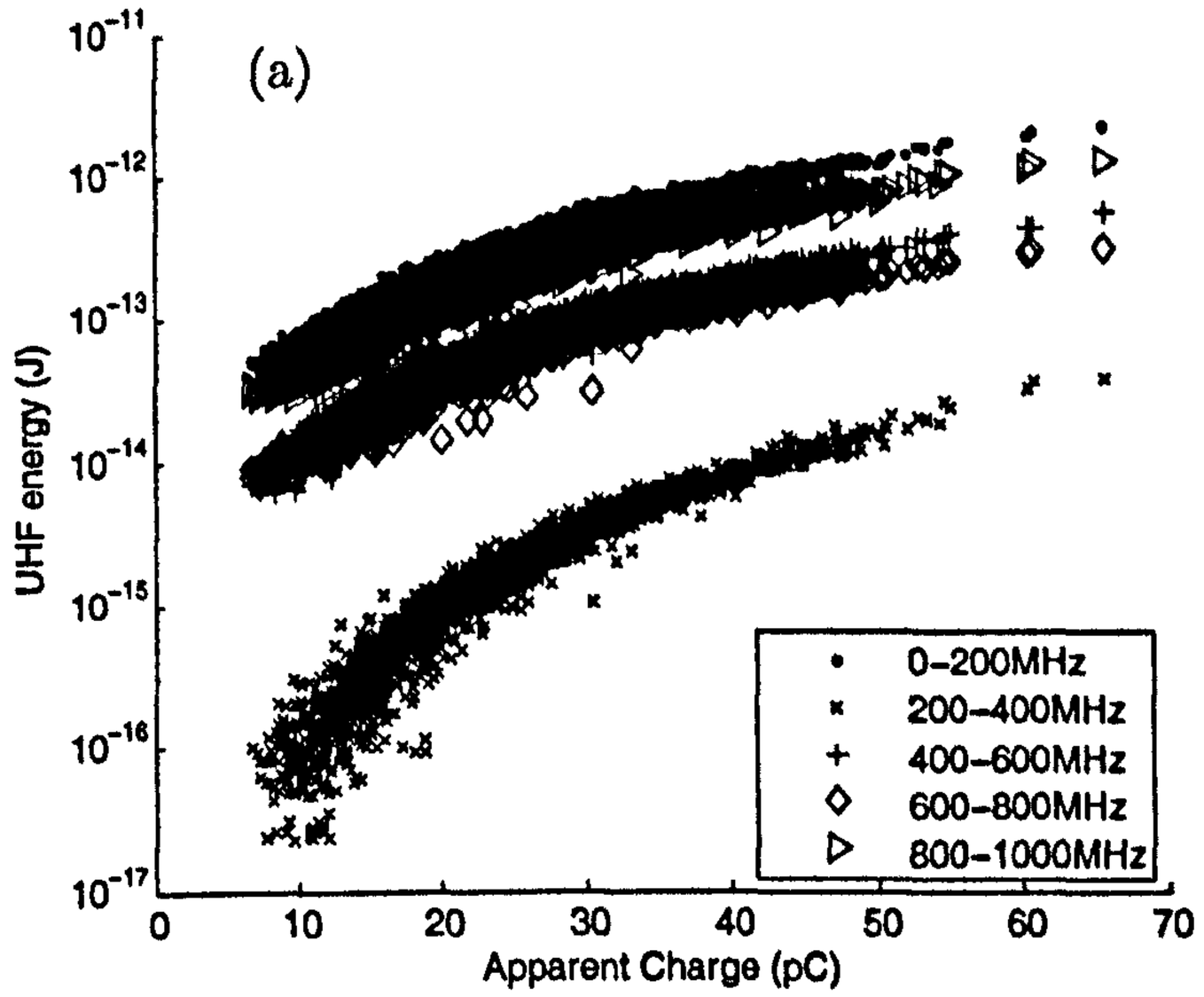

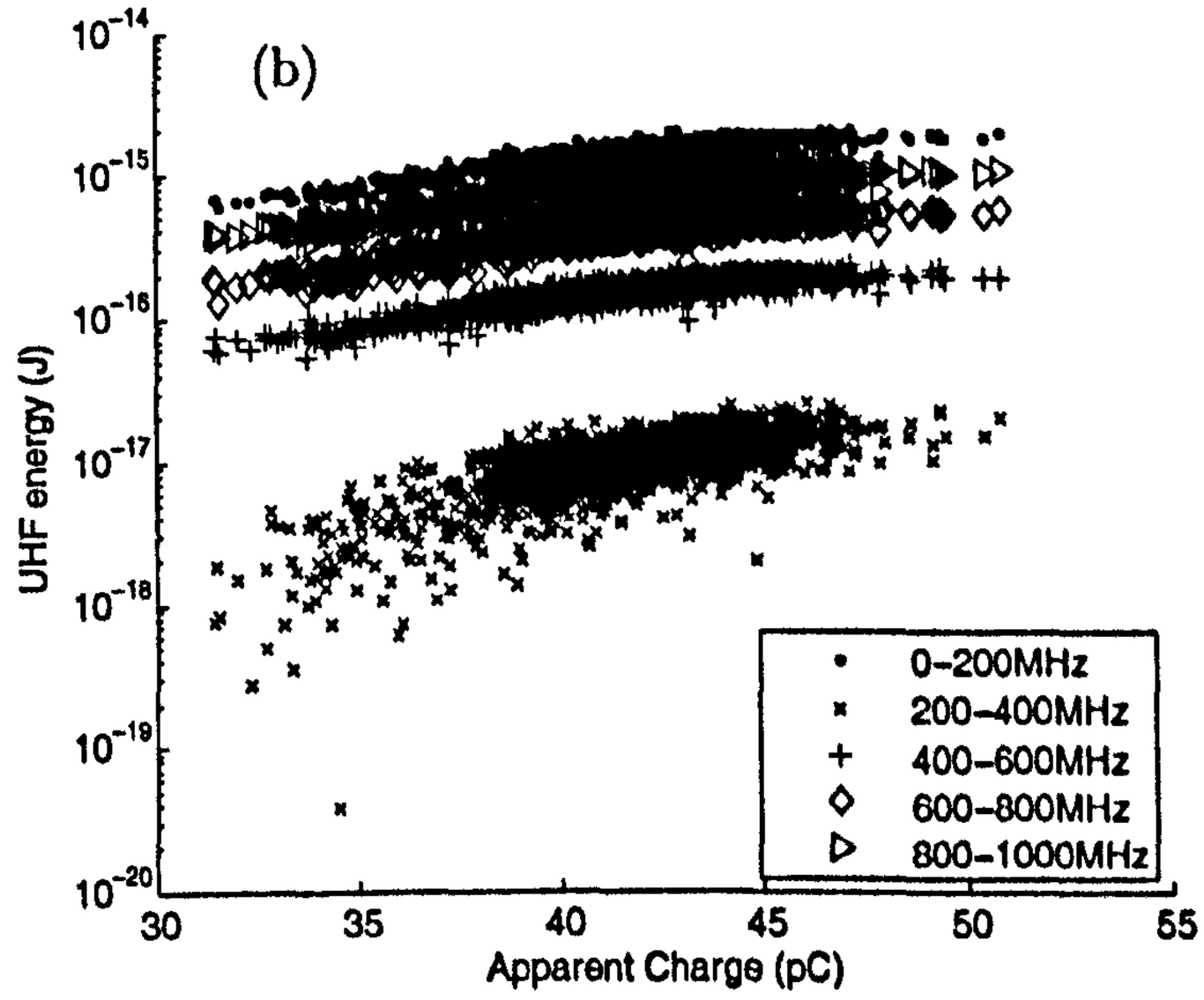

Figure 8.3: (a) Filtered RF-IEC correlation for PD produced by a 2mm aluminium sphere in reclaimed transformer oil (L10B) at an applied voltage of 10 kV. (b) Filtered RF-IEC correlation for a point-plane configuration in SF_6. 12 kV applied to plane electrode, 150 kPa SF_6 pressure, 18 mm gap spacing, 25 micron tip radius.

Chapter 9

Partial Discharge Current Pulses in SF_6

The practical advantages of employing non-contact radio frequency (RF) methods for detecting partial discharges (PD) in high voltage equipment have led to significant effort being focused on the diagnosis of electrical plant using RF techniques. This has particularly been the case for gas insulated substations, which use sulphur hexafluoride (SF_6) as an insulating medium. One of the most important challenges facing RF diagnostics is the problem of relating the RF emissions to some measure of severity of the PD. Previous work has established that the amplitude or energy of RF signals radiated from a PD source is strongly dependent on the rate of change of current in the PD pulse. In this chapter, measurements of PD current pulses in SF_6 are presented for a point-plane configuration using an extremely wide bandwidth (13GHz) measurement system. By this means, PD pulse shapes have been recorded with better resolution than has previously been possible and rise times have been measured with a high degree of accuracy. The results show a considerable variation of the pulse shape, with the minimum rise time measured being 35 ps. With this high time-domain resolution, it is possible to distinguish features within the PD pulses that will affect the energy of the radiated RF signal. In particular, the current pulses tend to occur in bursts of up to ten individual pulses in as little as 1 ns, which will excite multiple RF signals in rapid succession.

9.1 Introduction

Direct measurement of PD current pulses provides valuable data that can be used to more accurately define the excitation function for analytical studies and numerical modeling of PD and associated phenomena. For example, in his fundamental studies of corona mechanisms in SF_6, Morrow [73–75] solved the continuity equations governing the onset of corona pulses in SF6 from which he was able to compute the current pulse in the external circuit. Morrow's plot of the current pulse in [75] shows a risetime in the region of 100 ps, but could only be compared with experimental data in the form of a pulse measured with equipment having a limiting risetime of 0.5 ns. More rigorous validation of PD models will become possible using the data reported in the present chapter.

Another area of increasing importance in which accurate measurements of PD current pulses will find application is numerical modeling of PD [76–79], in which the aim is to better understand the radiated electromagnetic fields and develop new means of coupling efficiently with them using diagnostic RF sensors.

In this chapter a point-plane configuration is used in an experimental study of partial discharge pulses in SF_6 gas. This configuration has been widely used to study PD phenomena [54, 80, 81] because it represents a convenient way of generating sufficient electrical stress to initiate PD. The small tip radius of the needle leads to an enhancement of the electric field at the tip. In this region the physical processes are governed by the local electric field stress which is a function of the overall electrode configuration and the applied voltage. By conducting experiments at voltages just above PD inception the field at the needle tip will be of the level required to induce typical PD in a practical engineering system.

Historically, what was generally considered to be the lower limit on the rise time of a PD pulse was actually governed by the bandwidth of the measurement system. Thus as measurement technology has advanced and oscilloscope bandwidths have increased, so has the perceived upper frequency content of partial discharge current pulses. In the mid 1900's this was considered to be in the order of 100MHz, whereas the results presented show that the upper frequencies extend into the GHz range. The results presented in this chapter show that pulse rise times can be as low as 35 ps, as measured using a system with bandwidth of 13 GHz.

Related work in this field [82–85] has involved wideband measurement of the conducted partial discharge current pulses generated by free, or hopping metallic

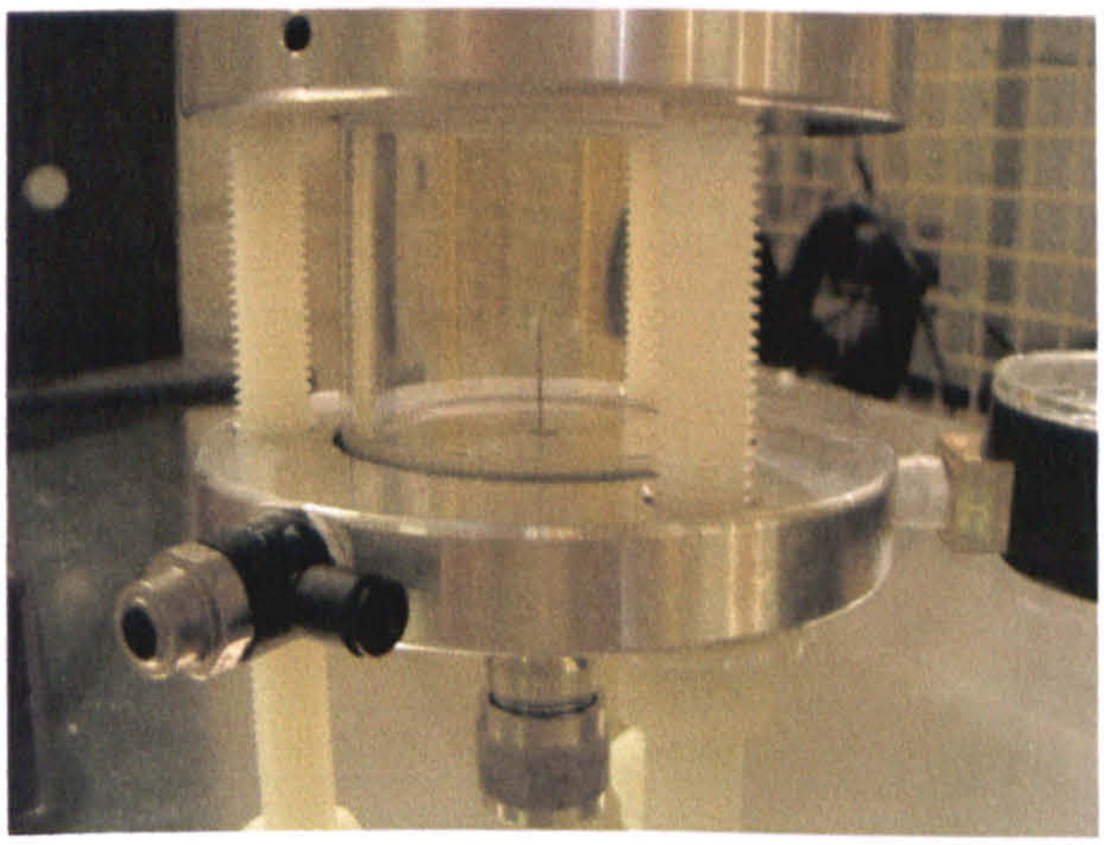

Figure 9.1: Matched-impedance point-plane test cell to facilitate direct measurement of partial discharge current pulses

particles commonly encountered in GIS, and of corona discharges. Although the microsparks created by such particles do not strictly conform to the definition of partial discharge, their characteristics are very similar.

The present investigation differs from the referenced work in that the bandwidths of the measurement system is at best three times that used previous investigations. To state this qualitatively, Judd [82] reported in 1998, the most accurate direct PD measurements up until that date using a bandwidth of 4 GHz and Okubo et al. [86] make direct partial discharge measurements using a point-plane electrode configuration, again using a bandwidth of 4 GHz. However, in the following sections it will be shown that a 13 GHz bandwidth is able to resolve features of the PD pulse shape to well under 100 ps and quantify the current pulse rise time.

9.2 High Bandwidth Measurement of PD Pulses

9.2.1 Test cell

A point-plane test cell containing pressurised sulphur hexafluoride (SF_6) was specially manufactured to enable direct measurement of corona discharge occurring around the needle tip. The test cell facilitates variation of needle length and gas pressure, change in PD pulse shape with these parameters to be quantified. The test cell is also designed to contain SF_6 gas which can be varied in pressure from 0–400 kPa. SF_6 is used because of its insulating properties, reducing the risk of

flashover in the point-plane gap, as well as its relevance to electrical equipment.

Due to the electrode configuration, with the needle at ground potential, pulses first appear at the peak of the positive half-period. Assuming the electrode configuration remains the same, a further increase in the applied voltage will give rise to additional pulses, which appear on the negative half-period and are more irregular. The following section shows clear differences in the time-domain characteristics of both positive and negative corona.

An important aspect to consider is impedance matching of the needle with the transmission line. To ensure that the impedance of the system remained as close as possible to 50Ω the connection from the needle to the base of the test cell was designed as a 50Ω transmission line using the equation

$$Z_0 = \frac{138}{\sqrt{\varepsilon_r}} \log \frac{b}{a} \tag{9.2.1}$$

where, ε_r is the relative permittivity of the dielectric, $b = 2$ mm (the radius of the outer conductor) and $a = 0.87$ mm (the radius of the inner conductor) [87]. In this case the dielectric is SF_6 for which $\varepsilon_r = 1$ gives sufficient accuracy.

Discharge Mechanisms in SF_6

Electric field enhancement around the tungsten needle tip causes a localised breakdown of the gas, leading to corona discharges. This typically occurs when the local electric field exceeds 90×10^5 V/(Pa m) [81]. PD mechanisms for a point-plane in SF_6 can be divided into three main stages. The physical appearance of the corona varies over these stages, as does the observed current pulse. Firstly, at low pressures ($\sim$ 50 kPa) a diffuse glow corona is observed. Current pulses have amplitudes of $\sim$ 10 μA and occur in burst at $\sim$ 2 μs intervals. Secondly, filamentary discharges appear as the gas pressure is increased. The formation of each streamer produces a burst of sub-nanosecond current pulses, typically varying in amplitude from 0.1 to 1 mA. Thirdly, longer filamentary discharges, or leaders begin to appear with increasing gas pressure. Leader discharges consist of a number of steps, beginning with a large formation pulse [81].

9.2.2 Measurement Equipment

The test cell was connected to a high sampling rate oscilloscope (40GS/s, 13GHz bandwidth) by a matched, low loss transmission line. The transmission line was

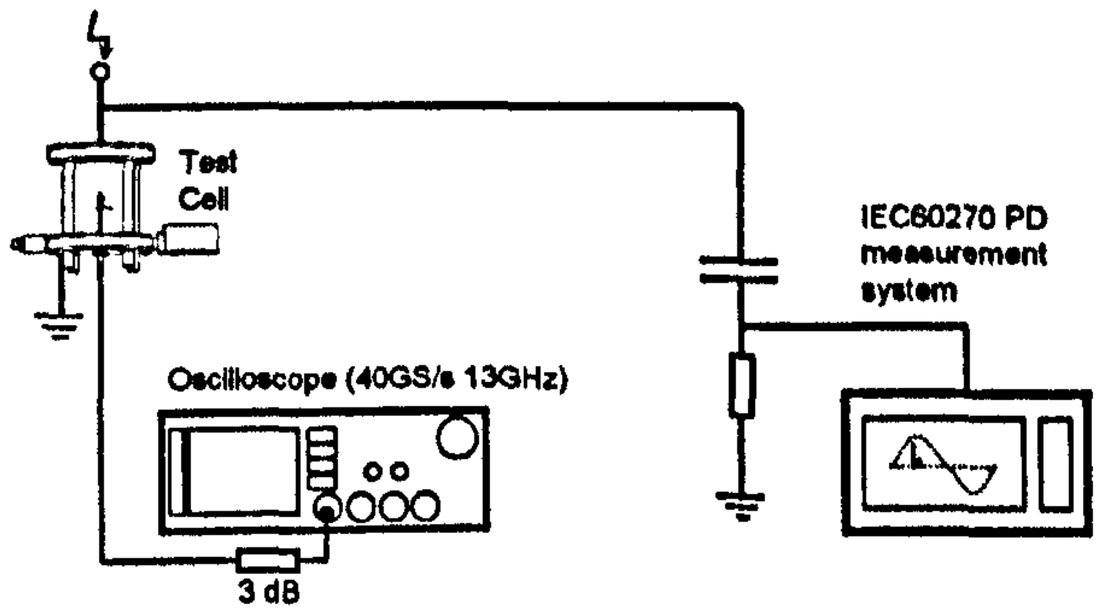

Figure 9.2: Experimental set-up. PD current pulses are measured by connecting a matched-impedance point-plane test cell directly to the oscilloscope. A conventional measurement system monitors the severity of PD activity while controlling the applied voltage.

connected to the base of the test cell via an hermetically sealed SMA connector, which was in turn connected to the needle by a brass cylinder specifically designed as a 50Ω coaxial line, matching the input impedance of the oscilloscope. The test cell was connected directly to the oscilloscope through a 3dB attenuator (calibrated up to 12.4 GHz), providing a DC path to ground and preventing capacitive charging of the cable. Finally, all PD signals were recorded only at or slightly above inception voltage to avoid the risk of flashover, which would damage the measurement system.

Although by far the majority of PD pulses can be accurately measured, the accuracy obtained for the shortest pulses must be questioned when their rise times approach that of the measurement system. Since conventional analogue oscilloscopes have a Gaussian frequency response, it is possible to determine the actual rise time of a measured signal from the inverse RMS relationship between measured rise time, signal rise time and system rise time. However, modern digital oscilloscopes tend to have a flat frequency response making it necessary to rely on empirical formulas supplied by the manufacturer to determine measurement accuracy. From the data available on the Agilent Infiniium 8000 Series it is possible to calculate that a measured rise time of 40 ps is accurate to within ±5 %, 48 ps to within ±2.5 % and 56 ps to within ±1.5 %.

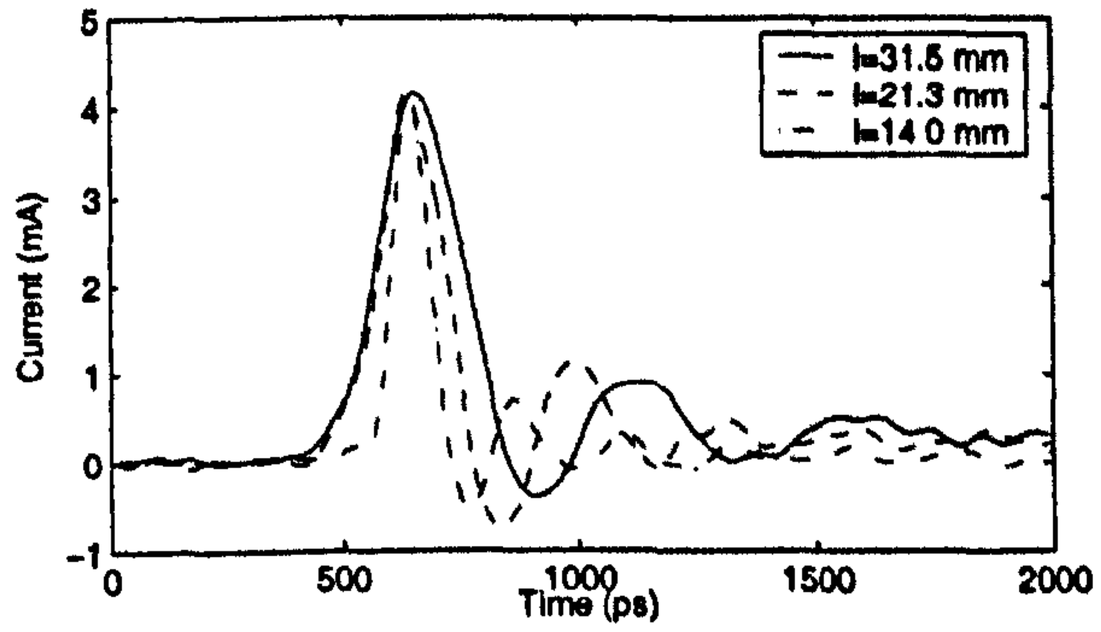

Figure 9.3: Three PD current pulses produced using three different needle lengths l. The ringing frequency is inversely proportional to needle length.

9.2.3 Evaluating the Effect of Needle Length on Current Pulses

Previous experiments showed a damped oscillatory PD current pulse [82], thought to be due to either ringing of the measurement system, caused by insufficient bandwidth or by oscillating PD current on the needle cause by impedance mismatch. In order to determine the cause of this damped oscillatory pulse, the effect of varying the needle length was investigated. It was hypothesised that the oscillation period of the reflected pulses would be proportional to the transient time along the needle and hence to needle length. To substantiate this possibility the needle was shortened from its maximum length of 31.5 mm to 21.3 mm and finally to 14.3 mm. To avoid ambiguity all other variables were kept constant. For instance, if the needle is shortened by a pre-defined amount, the plate separation is reduced accordingly, thus keeping a constant gap between point and plane.

Figure 9.3 shows three current pulses corresponding to the three respective needle lengths. If the needle is regarded as a high-impedance transmission line, some of the PD current will be reflected back along the high impedance needle after it reaches the low impedance coaxial connector. Since the pulse is moving from a high to a low impedance, the reflected pulse will be of the opposite polarity. The reflected pulse travels back to the needle tip, where it is reflected by an effective open-circuit, which does not cause polarity reversal. The pulse then returns to the coaxial interface. Thus, the measured transit time between two positive peaks in the waveforms shown in Figure 9.3 is four times the transit time of the needle. If this hypothesis is correct, it would be expected that a straight line with a gradient equal to 1/4 of the speed of light would be obtained when the

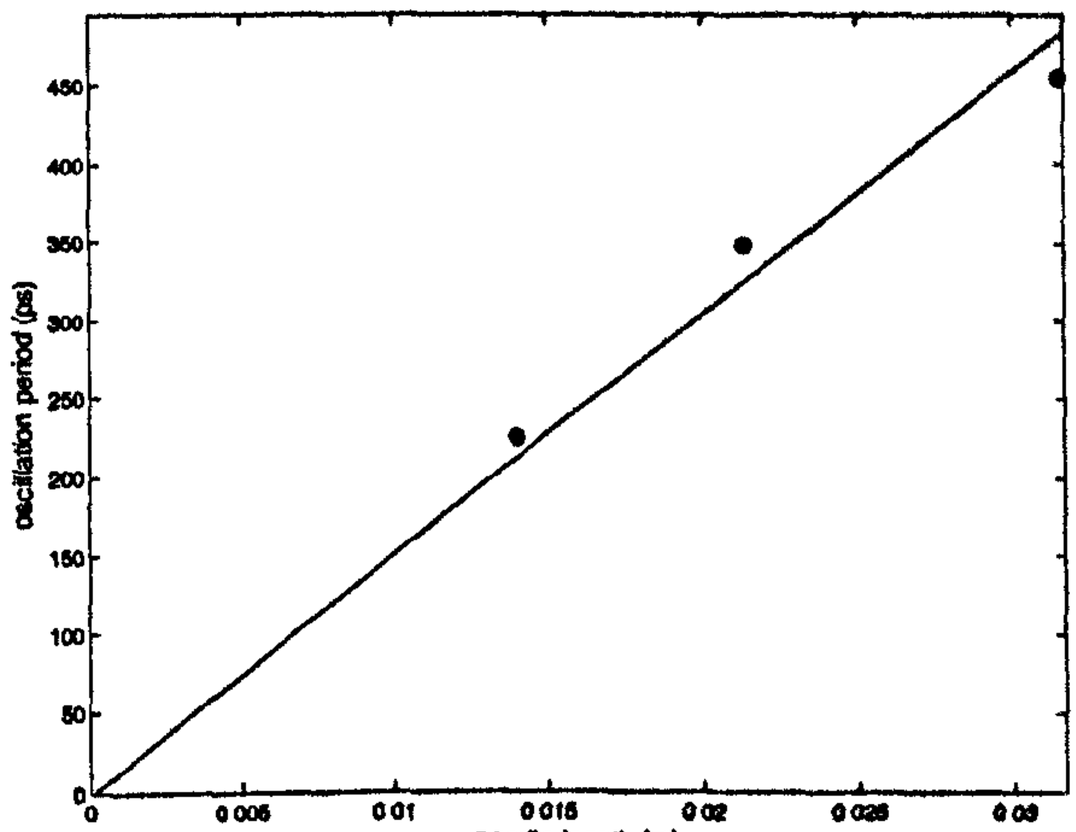

Figure 9.4: Variation of the oscillation period with needle length. The best-fit straight line was found using linear regression.

oscillation period of the current pulses, shown in Figure 9.3, is plotted against their respective needle lengths. The gradient of the best-fit straight line shown in Figure 9.4 is $v = 77.46 \times 10^{-6}\ ms^{-1}$ which, taking into account measurement error, is sufficiently close to 1/4 of the speed of light ($c/4 = 74.95 \times 10^{6}\ ms^{-1}$) [88] to support the hypothesis.

It is therefore certain that parasitic effects produce an unwanted impedance mismatch and it cannot be guaranteed that our observed signal is a true representation of the original current pulse occurring at the tip. These effects can however be mitigated by reducing the length of the needle. The study shows that the short pulses are easily affected by the test geometry, therefore current pulse measurements taken at the plane rather than the point [86] cannot be considered accurate representations of the pulse shape.

9.2.4 Measurements

With the effect of needle length having been considered, this section goes on to describe measurements of PD current pulses, showing the variation in pulse shape and rise time with pressure.

Four tests were carried out, with the results summarised in Table 9.1. Here that rise time is defined as the time taken for the PD signal to rise from 10 % to 90 % of its peak amplitude. Another important note regards the polarity of the PD current pulses. Conventionally, positive (anode) corona is measured using a point-plane gap in which high voltage is applied to the point electrode. Hence

for a positive applied voltage, electrons in the high field region will be drawn to the anode giving a positive pulse, conversely, for a negative applied voltage, electrons in the high field region will be repelled from the cathode, and a negative pulse will be produced. Our test arrangement differs from the conventional setup in that the high voltage supply is connected to the plane electrode, with the point electrode connected to the inner conductor on a coaxial line to facilitate direct current pulse measurement. Therefore at positive voltages electrons will be repelled into the low field region, producing a negative pulse on the oscilloscope. The reverse will of course be true for negative voltages. Consequently, 'positive corona', in the conventional sense, will appear as a negative pulse and 'negative corona' as a positive pulse.

Positive Corona

The use of a 13 GHz bandwidth system allows us to observe features of the pulse shape not previously discernable. Examining Figures 9.5 to 9.7, it is clear that each waveform contains complex features. Whether these complex pulse shapes are a result of multiple PD events occurring simultaneously at the PD tip, or of the physical motion of charge for a single PD event is an interesting question that is beyond the scope of this thesis.

A rise time of 35 picoseconds was measured at 210 kPa using the shortest needle. This is the fastest PD rise time measured to date, suggesting that a system bandwidth in excess of 10 GHz is needed for accurate direct measurement of partial discharge.

Negative Corona

Negative corona pulses are also shown in Figs. 9.5 to 9.7. It is interesting to note that at higher pressures (> 200 kPa) multiple PD pulses begin to appear, with each pulse train lasting for around 800 ps. At lower pressures, current pulses tend to conform more closely to a Gaussian shape.

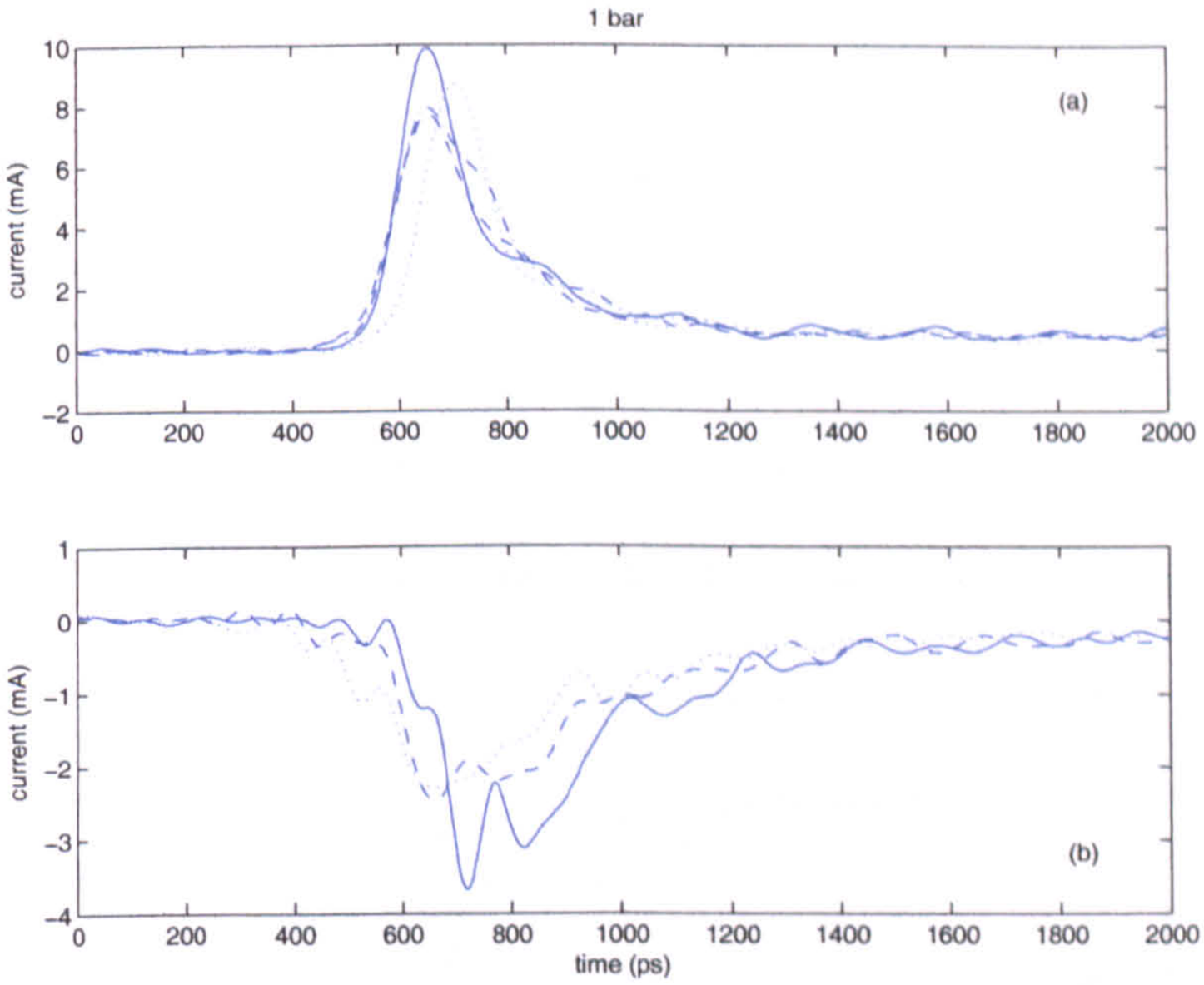

Figure 9.5: Typical examples of (a) negative and (b) positive corona pulses in SF_6. $P = 100$ kPa, $V = 11.3$ kV. 14 mm needle length.

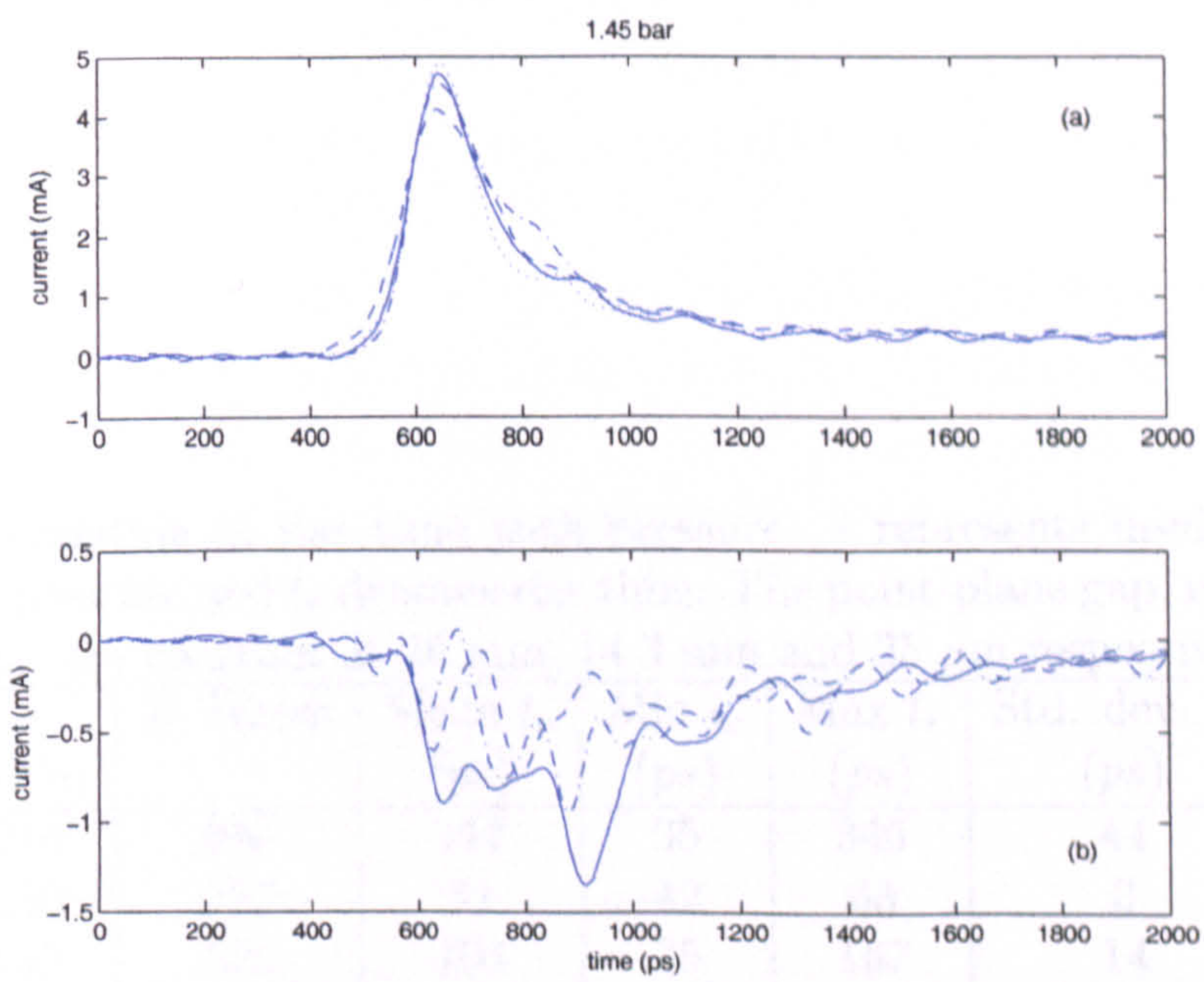

Figure 9.6: Typical examples of (a) negative and (b) positive corona pulses in SF_6. $P = 145$ kPa, $V = 11.0$ kV. 14 mm needle length.

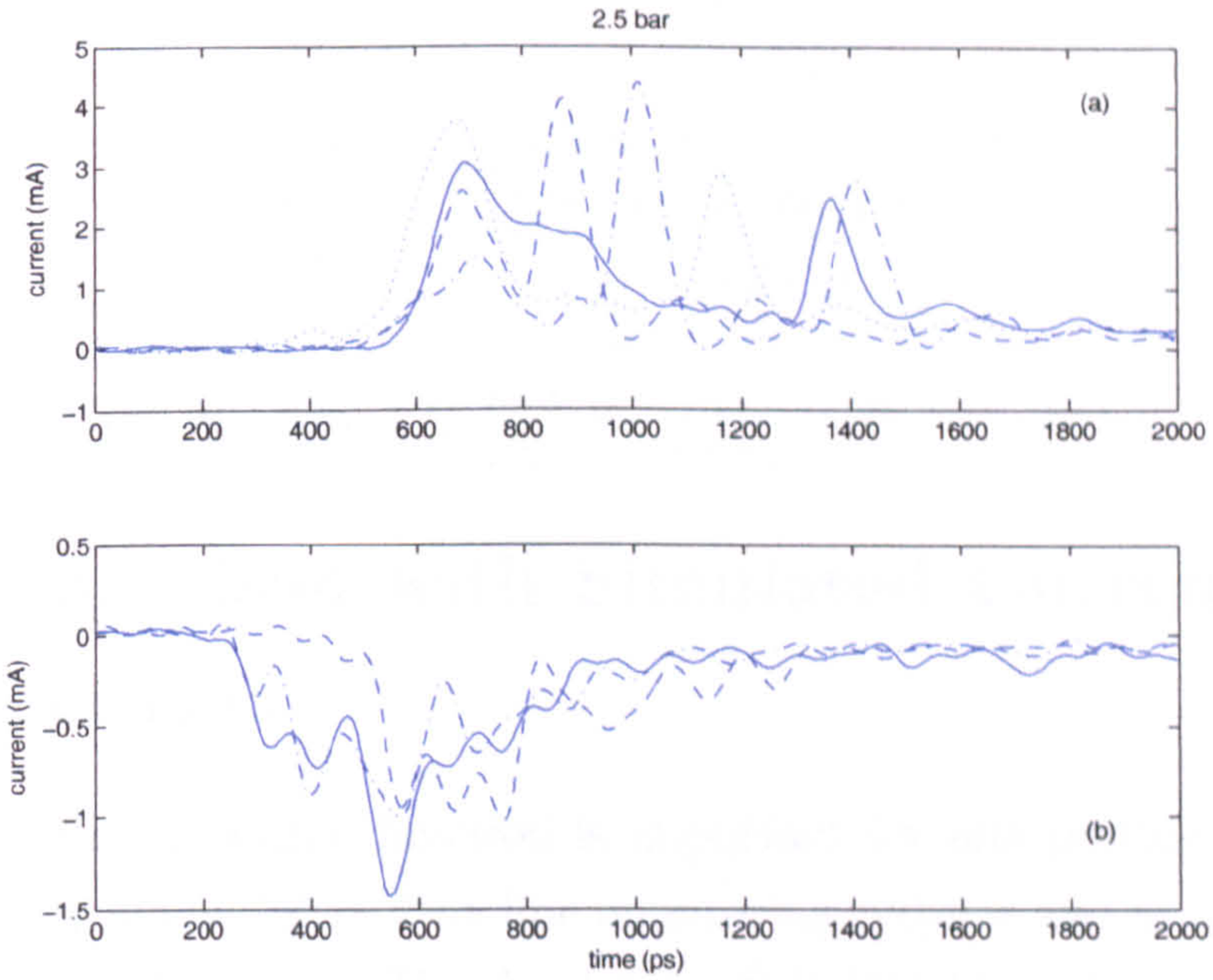

Figure 9.7: Typical examples of (a) negative and (b) positive corona pulses in SF_6. $P = 250$ kPa, $V = 14.9$ kV. 14 mm needle length.

Table 9.1: Variation in rise time with pressure. l represents needle length, p denotes SF_6 pressure and t_r denotes rise time. The point-plane gap, needle length and tip radius are constant at 26 mm, 14.3 mm and 25 μm respectively.

p (kPa)	# Traces	Mean t_r (ps)	Min t_r (ps)	Max t_r (ps)	Std. dev. t_r (ps)
210	540	117	35	346	44
250	727	51	42	63	3
145	515	104	75	167	14
100	512	95	64	173	16

Table 9.2: Simulated PD current pulse equations in the time and frequency domains.

Equation	Time domain $i(t)$
Wanninger	$\frac{I_1}{T_1} t e^{1-t/T_1}$
Gaussian	$I_0 e^{-t^2/2\sigma^2}$
Double Exp.	$I_m \left[(1+\alpha t)e^{-\alpha t} - (1+\beta t)e^{-\beta t}\right]$
	Frequency domain $I(\omega)$
Wanninger	$\frac{q}{(1+j\omega T_1)^2}$
Gaussian	$I_0 \sigma \sqrt{2\pi} e^{-\frac{1}{2}\omega^2\sigma^2}$
Double Exp.	$I_m \left[\frac{1}{\alpha+j\omega} - \frac{1}{\beta+j\omega} + \frac{\alpha}{\alpha+j\omega} - \frac{\beta}{\beta+j\omega}\right]$

9.3 Comparison with Simulated Current Pulse Equations

Knowledge of the excitation function is important for interpreting the PD signals detected by many different on-line monitoring systems and in modeling and analysis of their performance. The simulation of electrical transients using electromagnetic modeling software requires a time-domain model for the current pulse. One option is to use the Gaussian equation [89] as an approximation to the excitation function. Approximation of electrical discharge pulses can also be achieved through the use of two more equations; Wanninger's equation [83] and the Double Exponential equation [90]. These are presented along with their respective Fourier transforms in Table 9.2.

In Wanninger's equation, I_1 is the peak amplitude, T_1 governs the rise time, and the total charge in the current pulse is given by $q = eI_1T_1$. In the Gaussian equation, I_0 is the peak current and σ is chosen for best matching of the pulse shape with measured pulses. In the Double Exponential equation, I_m defines the amplitude and α and β define the pulse shape.

It was noted previously that at lower pressures signals which approximate more closely to the Gaussian equation can be observed. In addition, the distorting effects of the needle can be mitigated by shortening its length as much as possible. To ascertain how closely our measured pulses approximate to the ideal PD equations, iterative curve fitting was applied. The Wanninger and double exponential equation impose a specific shape, whereas the Gaussian equation is more flexible and can be fitted to real PD data more easily. Curve fitting was therefore applied using a Gaussian function.

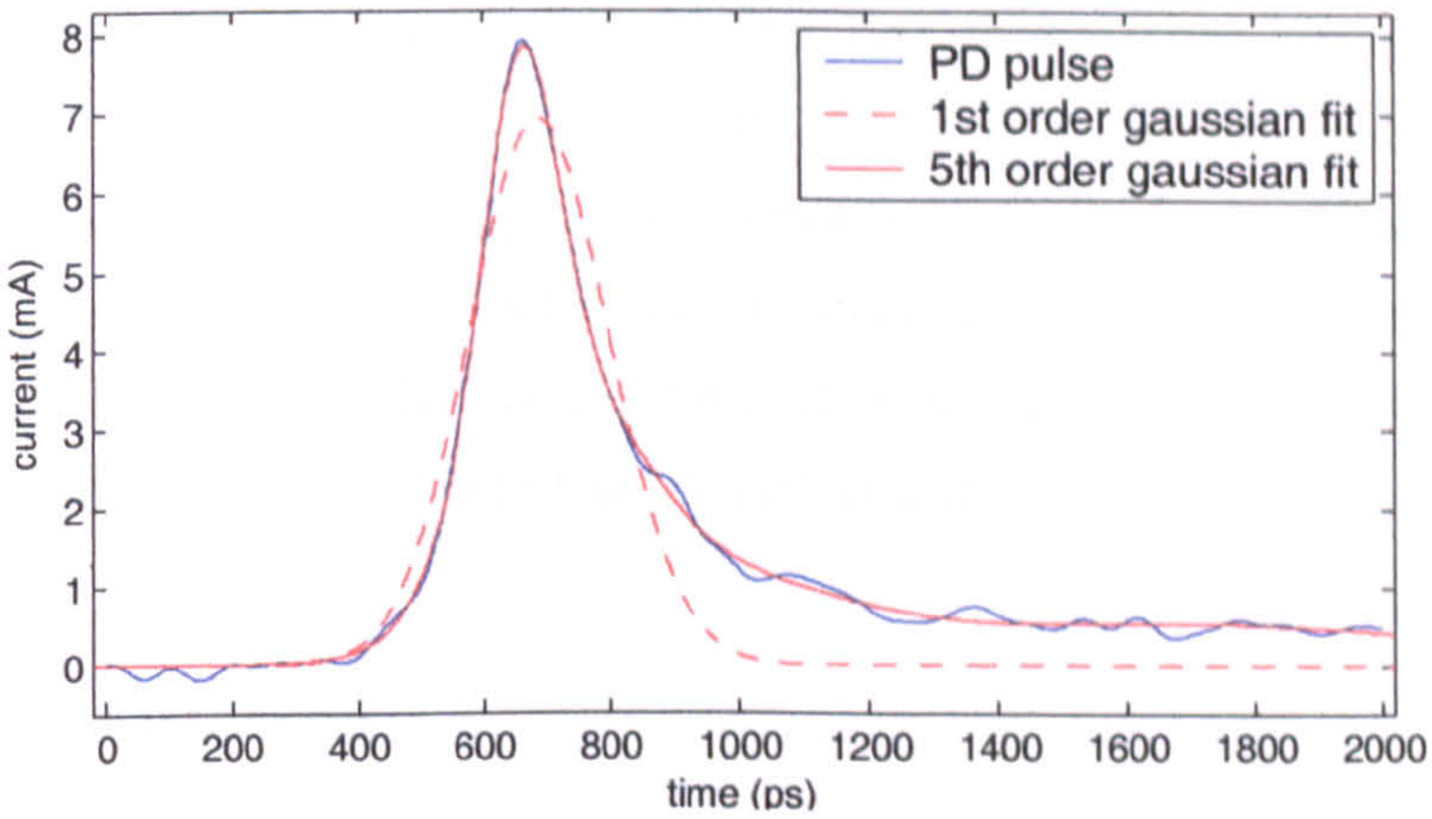

Figure 9.8: Iterative curve fitting shows that a higher-order Gaussian equation provides a good approximation to the measured PD pulse

As shown in Figure 9.8, a first order Gaussian matches the initial lobe of the current pulse quite well, with $\sigma = 0.105$ picoseconds. However, higher order Gaussian functions are able to achieve a significantly better match as can be seen by the 5th order approximation, which has an r^2 value [1] of 0.9922 with the first order approximation providing a match of $r^2 = 0.8788$. Pulse parameters were found using regressive curve-fitting in MATLAB. The 5th order Gaussian approximation has the form:

$$I(t) = I_0 e^{-t^2/2\sigma_0^2} + \ldots + I_4 e^{-t^2/2\sigma_4^2}$$

9.4 Discussion

Pulse shape is clearly an important consideration when interpreting RF as well as conventional PD measurements. Conventional systems aim to quantify apparent charge, which is related to the integral of the current pulse. Therefore if two PD pulses occur within a time period inside the measurement threshold, an artificially high value of apparent charge will be measured. However, since RF measurements respond to the rate of change of PD current rather that the integral, it would be difficult to quantify apparent charge based on this technique, irrespective of the number of pulses or the pulse shape.

[1] The coefficient of determination r^2 is the proportion of variability in a data set. If the fitted curve matches the data exactly $r^2 = 1$, if it does not match at all $r^2 = 0$.

Previous work by the author [68, 91, 92] has shown that simultaneous measurement using both conventional and RF techniques affords more information on the underlying PD pulse shape. The reported results have shown that the effects of multiple PD pulses must be taken into account not only on conventional measurements but also on RF measurement when interpreting the relationship between RF energy and IEC60270 apparent charge.

9.5 Conclusion

By measuring partial discharge current pulses directly using a high bandwidth measurement system, PD rise time can be measured and characteristics of the pulse shape can be resolved more accurately than before. Using a 13 GHz bandwidth oscilloscope, it was possible to measure a PD rise time of 35 ps for a point-plane configuration in SF_6 gas at 210 kPa; the fastest rise time measured to date. A considerable variation in the pulse shape and pulse characteristics was observed. For example, multiple pulses were seen to occur within 1 ns. These measurements will help to inform future studies of ionisation mechanisms on a very short timescale.

The effect of current pulse reflections on PD pulses measurements has been investigated for a protrusion. It was found that pulse reflections can be mitigated by shortening the needle, although in this case it was still possible to observe some oscillatory waveforms caused by pulse reflections. By applying non-linear regressive curve fitting to the measured PD pulses it was found that a higher-order Gaussian function provides a good approximation to the PD pulse. This knowledge will allow us to more accurately describe the excitation function for electromagnetic modeling of PD phenomena.

Chapter 10

The Effect of Superposition on Radiometric PD Measurement

This chapter will focus on the effect of PD current pulses on radiometric PD measurement. It has been shown in the previous chapter that high bandwidth direct measurement reveals PD current pulses produced by a point-plane configuration in SF_6 often occur in multiple bursts. This will cause the resulting IEC waveforms to become superimposed (conventional measurement systems having a response time of the order of μs). However, as has been shown in the previous chapter, multiple pulse bursts occurring within 1 ns can be produced by certain PD sources which may also cause the resulting RF waveforms to become superimposed. The effect of superposition of RF waveforms has been investigated by studying the variation in detected RF energy with respect to the time delay between PD pulses. It was found that when two partial discharges occur within a short period ($< 150ns$) the combined energy of the resulting RF pulse has the potential to vary by ± 30 % of that resulting from two equivalent PD pulses with a wider pulse spacing ($\gg 150ns$). In terms of a practical monitoring system concerned with order-of-magnitude variations, this is not considered to pose a major problem for the RF technique.

10.1 Superposition effects in RF signals

10.1.1 Simulations

Initially, superposition of RF waveforms will be investigated using some simple simulations. The shape of the time-domain RF signal excited by PD is often

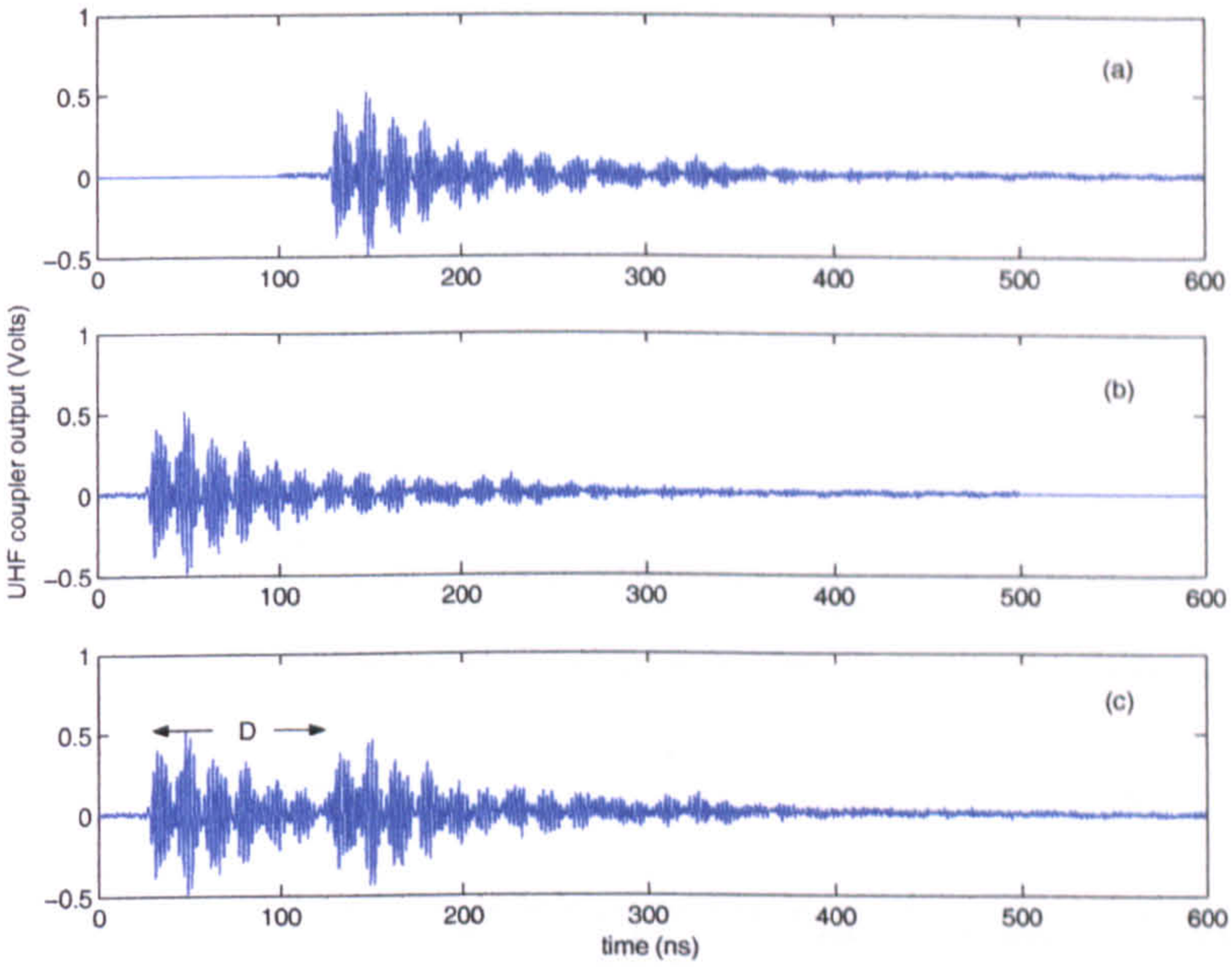

Figure 10.1: To simulate the effects of overlapping RF signals, the recorded RF signal (a) is added to a shifted version of itself (b). The resultant signal is shown in (c). This artificial RF signal would result from two PD current pulses occurring within 100 nanoseconds.

complex and is a function of the GIS or transformer dimensions, their attenuation characteristics, and the location of the PD source. It is therefore convenient to quantify the RF signal in terms of its cumulative energy U, as stated previously in Equation (3.1.3). If U is to be employed as a measure of PD severity, it would be useful to determine whether its value varies significantly when signals radiated from the PD site occur sufficiently close together so as to overlap. The term 'simulation' is used here since, in this initial investigation, RF signals are added artificially. As illustrated in Figure 10.1, the first signal is shifted by an amount D. Both signals are zero-padded to ensure that their lengths remain equal. The RF signals used in the simulation obtained by measuring high amplitude discharges produced by a floating component. The conducting component was situated between two high voltage electrodes within a large metal tank. It should be noted that due to the resonant nature of the transformer or GIS chamber inside which the partial discharge pulse occurs, the shape of each RF pulse radiated from a single discharge site will often look very similar. It is therefore valid to use similar RF signals in our simulation.

Let $U(a)$, $U(b)$, $U(a+b)$ be equal to the respective cumulative energy of

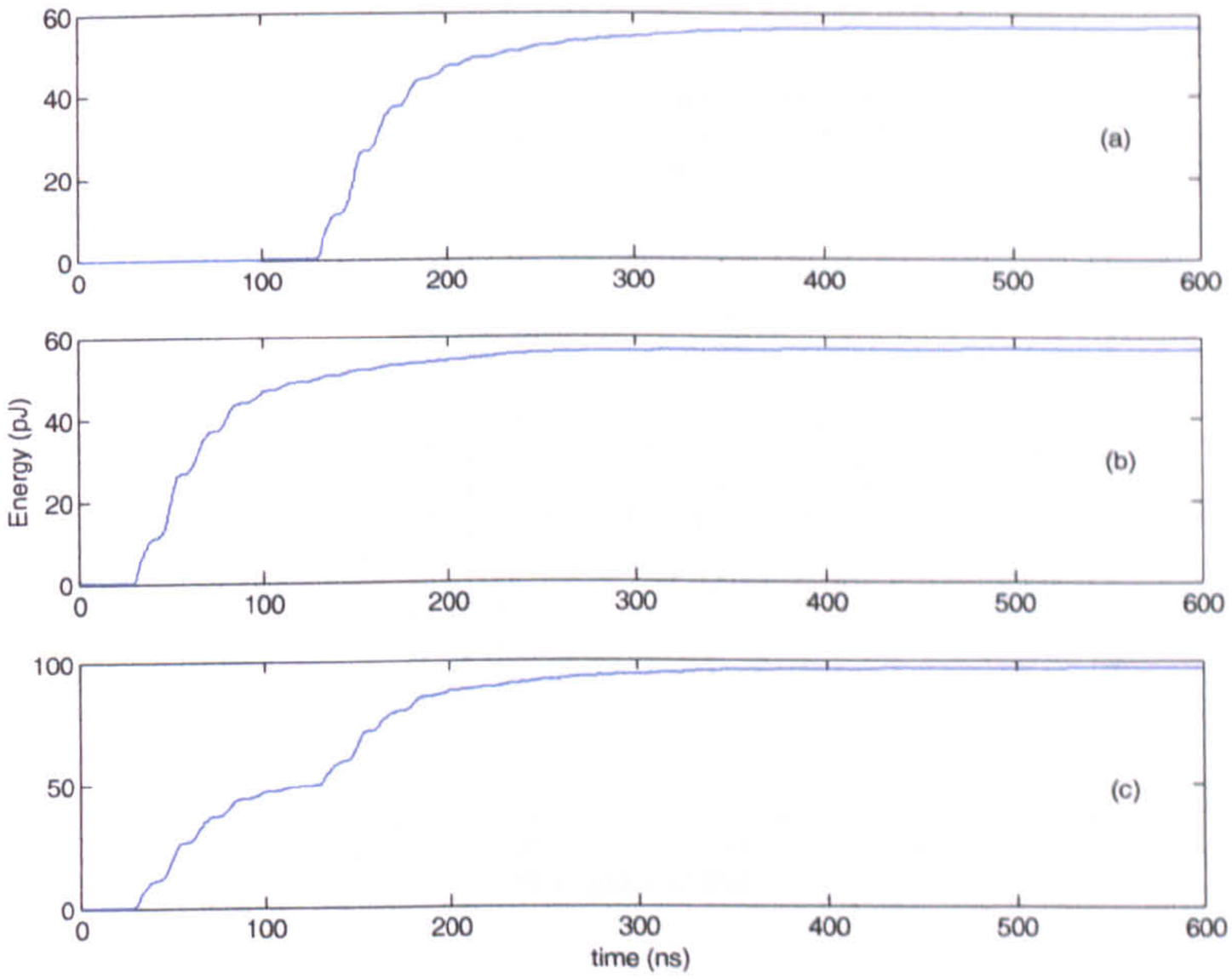

Figure 10.2: The variation of cumulative energy with time for the three RF signals shown in Figure 10.1(a), (b) and (c). The cumulative energy at a generalised data point U_i is calculated using Equation (3.1.3).

signals a, b and (a+b) in Figure 10.1. Figure 10.2 shows how the cumulative energy U of each signal increases over time. The respective cumulative energy of the single RF pulses and the double pulse are initially calculated for a single value of D, say 100 nanoseconds. For this particular case $U(a)+U(b) = 113.4\ pJ$ and $U(a+b) = 96.8\ pJ$. Clearly then, the effect of constructive and destructive interference on the measured RF energy cannot be ignored when multiple pulses are present. Expanding the simulation to take into account a wide range of time delays allows us to plot the variation in U with D. This variation is depicted in Figure 10.3 firstly, for the addition of two RF signals produced by floating component defects, secondly for two respective RF signals produced by a floating component and a void and thirdly, for two single RF pulses. The dashed line represents $U(a)+U(b)$, which is of course constant for all values of D. However, it can be seen that there is a considerable variation in $U(a+b)$ as the time separation between the two pulses increases. In the case where $D = 0$, only constructive interference is present. This is in contrast to the energy a short time later at $D = 1\ ns$, where both signals almost entirely cancel each other out. The periodic nature of the graph is a consequence of high frequency resonance within the tank as many high order TE and TM modes are set up. Due to computational

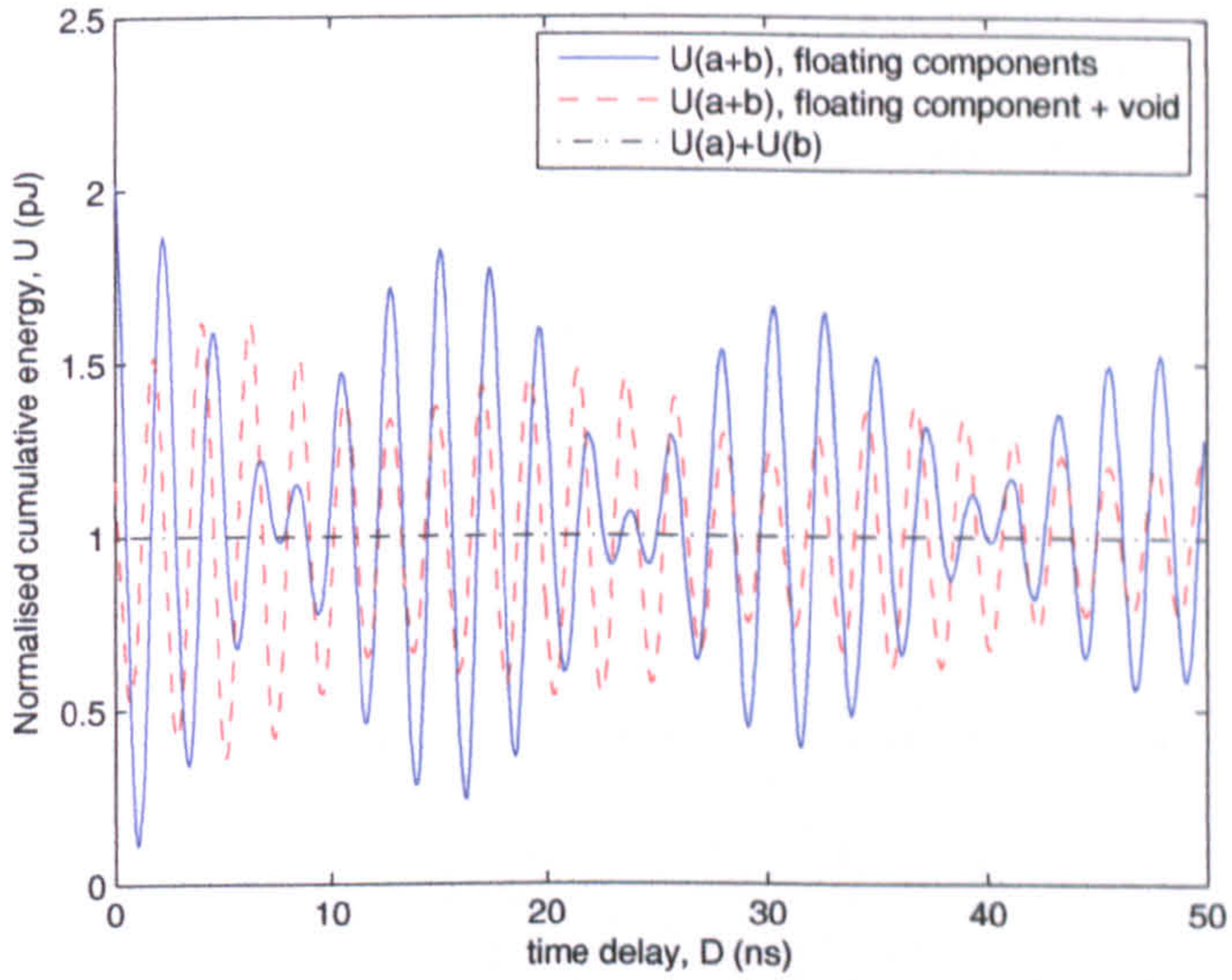

Figure 10.3: Simulated variation of cumulative energy with time separation between signals. Each point on the graph represents the total energy of a double RF pulse at a given time delay D.

limitations, the data has been analysed for values of D between 0 and 50 ns.

Simulations were also carried out on a number of PD signals measured on an 18 MVA, single phase 132/25 kV transformer as reported in [67]. Discharge activity was measured by means of three RF sensors mounted on three of the transformers hatch plates. PD activity was observed and located to a point just under one of the tap changer mechanisms. The order of arrival at the sensors was S1, S3, S2. Simulation results shown in Figure 10.4 are most relevant to measurements on electrical plant since the signals measured on the transformer are less resonant than those measured in the laboratory test chamber.

Since calculation of RF energy involves taking the square of the RF coupler voltage at a given data point, the energy would be expected to be higher for two RF signals which occur close together. Initial simulations indicate that when multiple PD pulses occur within a short period, the energy of the resultant RF signal has the potential to vary significantly from that resulting from a single PD pulse of the same shape. For the majority of cases, $U(a+b) \neq U(a)+U(b)$, however, based on observation of the RF signal alone there is no way of knowing whether the radiated signal is the result of a single PD pulse or of multiple PD pulses unless the current pulse can be measured in some way.

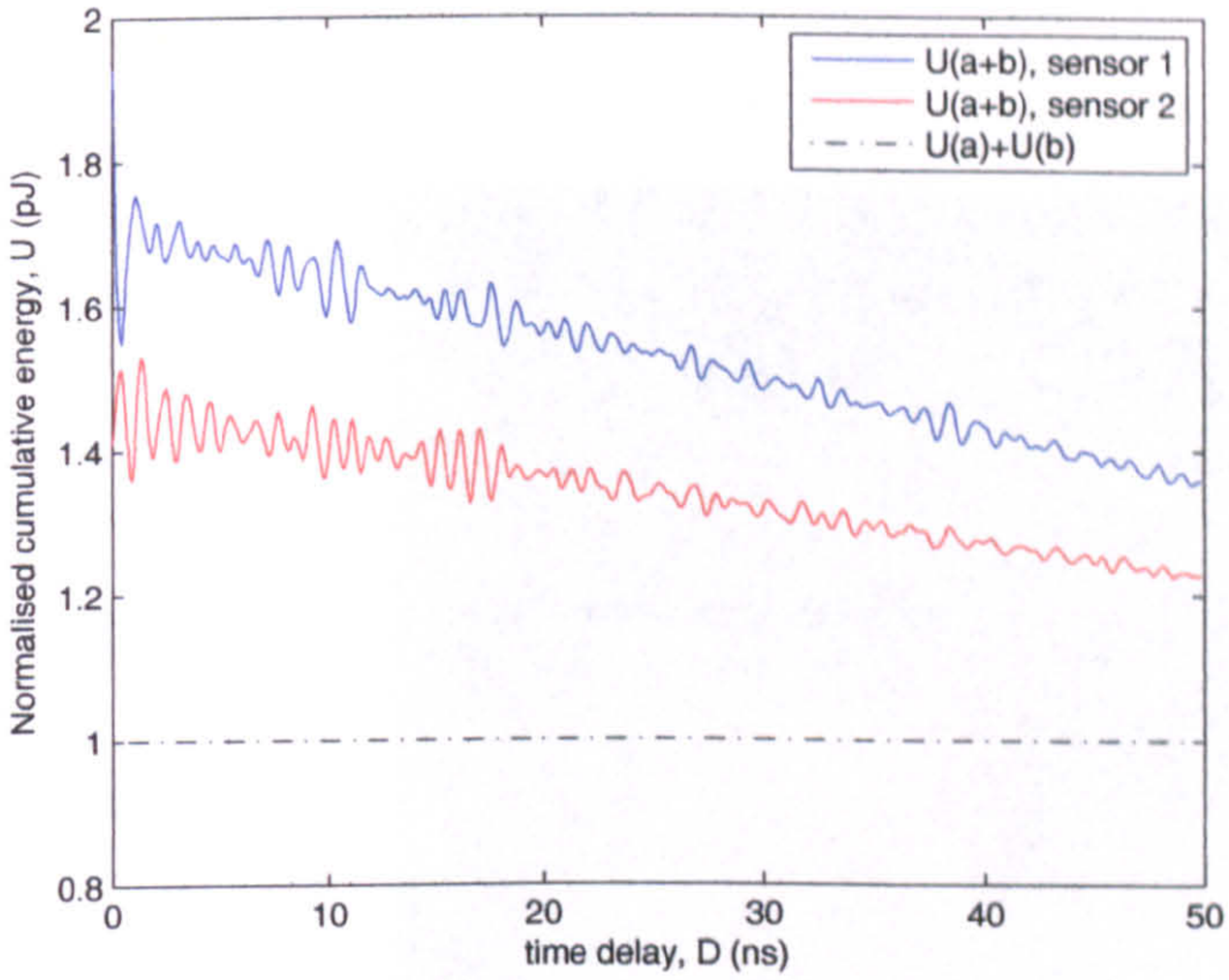

Figure 10.4: Simulated variation of cumulative energy with time separation between two signals produced by a defect inside a high voltage transformer.

10.2 Experimental investigation of superposition

The results presented in Section 9.2 indicate that many of the PD current pulses produced using a point-plane configuration occur within a very short period of time. Although simultaneous measurement of PD current and the resultant RF signal would be achievable using our arrangement, the effect of superposition on radiometric PD measurement requires two repeatable pulse sources, the spacing between which can be accurately varied. Our previous experimental arrangement is unsuitable in this regard since there is no way of ensuring repeatability of the PD pulse.

The author has previously reported on the use of a step recovery diode (SRD) for PD simulation [93]. There are analogies between the physics of SRD switching and the physical mechanism of PD. For example, in the case of PD, a material that was formerly insulating suddenly becomes conducting as ionisation takes place, often within a very small region. When the SRD switches, a small region that was conducting rapidly becomes insulating. From the point of view of radiated electromagnetic fields, the only difference between a rapid increase or decrease in current is the direction of the radiated field vector.

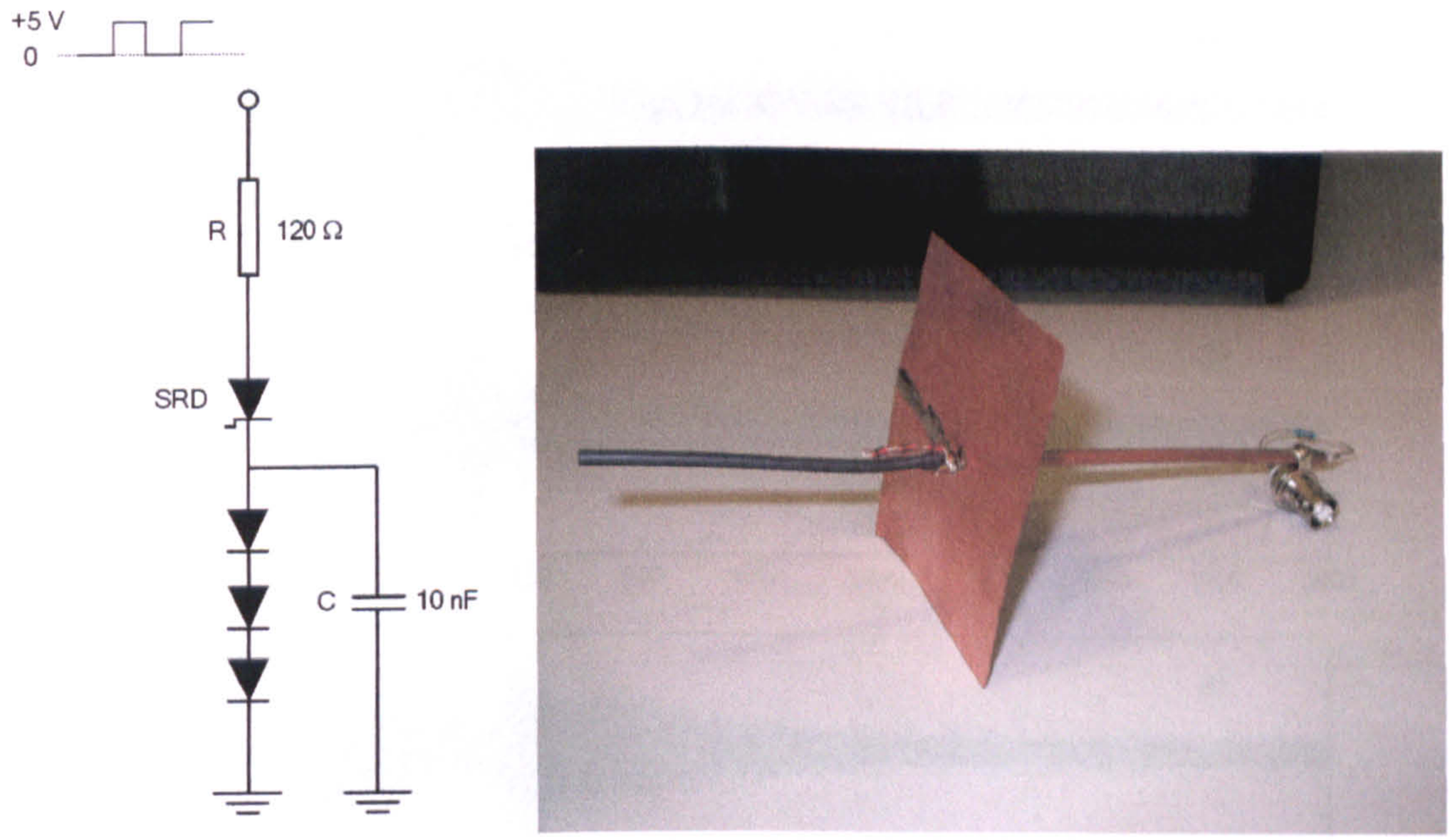

Figure 10.5: The SRD circuit produced repeatable RF pulses with similar characteristics to those caused by partial discharge. Since the oscilloscope's delayed trigger produces a TTL output voltage, three diodes are used to allow the SRD to switch from forward to reverse bias. The current-limiting resistor is chosen so as to allow a forward current of no more than 50 mA.

10.2.1 Set-up

To investigate the effect of pulse spacing, a controllable time delay between pulses is required. To fulfill this requirement, two step recovery diodes were used, each driven by a separate voltage source; the first diode by a rectangular pulse from a signal generator and the second by the external delayed trigger output on an oscilloscope. Figure 10.5 shows the SRD circuit used to produce repeatable RF pulses.

10.2.2 Measurements

Initially, single pulses produced by each of the respective SRD circuits were recorded as reference. Thereafter, double RF pulses were recorded, with the delayed trigger used to increase the delay between pulses from 16 ns to 500 ns in 4 ns increments. An RF monopole antenna was used to measure the resulting double pulses. Figure 10.6 shows three sets of double pulses produced using the step recovery diodes. Figure 10.7 shows the FFT of a typical RF pulse produced

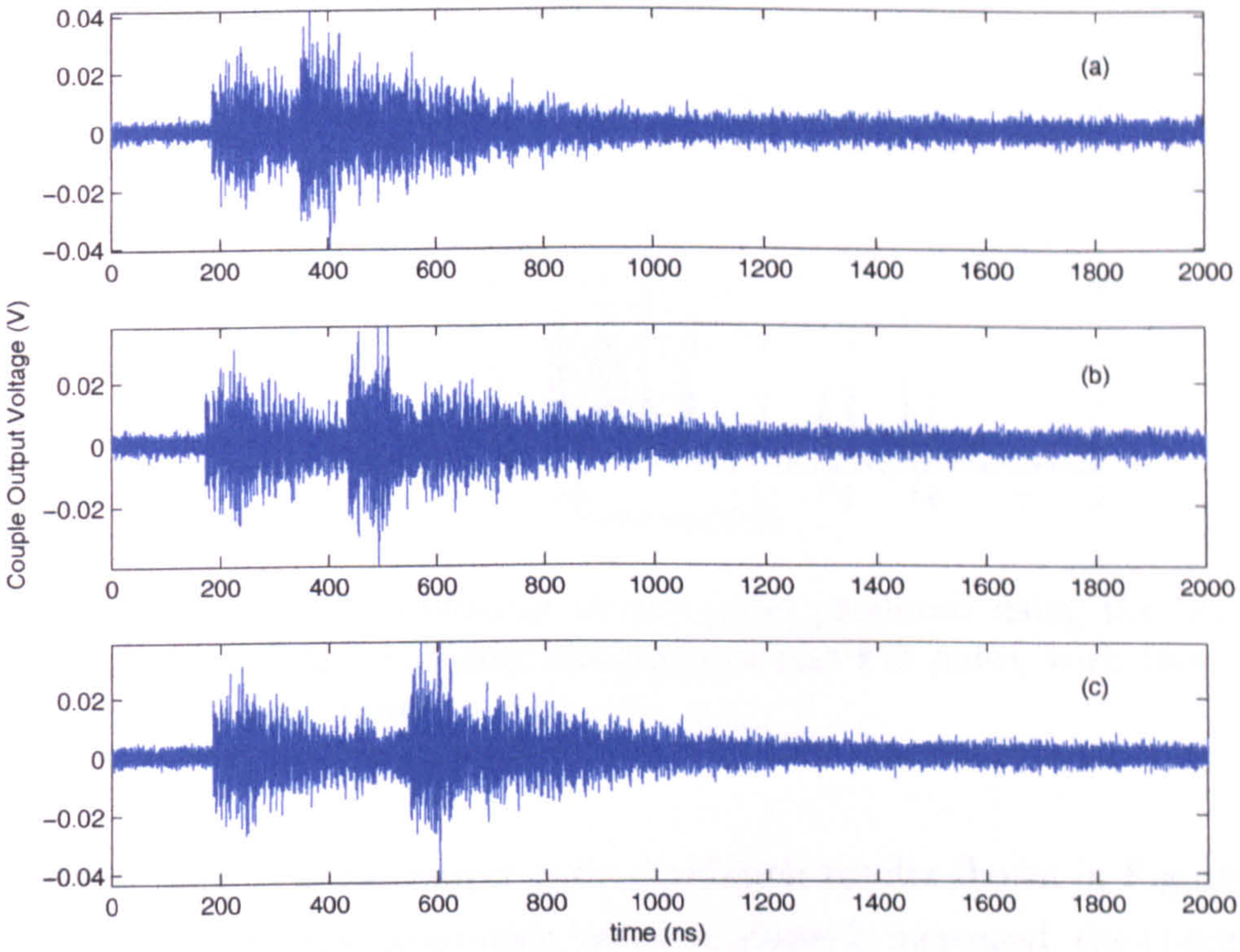

Figure 10.6: Examples of double RF pulses produced using two SRD circuits. The above graphs show double pulses with delays of (a) 100, (b) 200 and (c) 300 ns. The pulse spacing can be controlled accurately using the delayed output trigger of an oscilloscope.

using the SRD circuit. The frequency content of the signal is similar to that produced by a real PD pulse.

10.3 Results

The cumulative energy was calculated for various double RF pulses and the time delay between pulses was recorded for each case, with the results shown in Figure 10.8. For comparison, cumulative energy was also calculated for two single pulses produced by each of the respective SRD circuits and is shown in the figure as a dashed line. The envelope of the scatter plot follows approximately the same trend as that shown in Figure 10.4. In both cases, the energy of a double pulses is $\sim$ 30 per cent greater than that of two equivalent single pulses at $\Delta T = 16ns$. It is also noted that since measurements were taken inside a resonant chamber, the RF energy has the potential to fall to a level lower than that of two equivalent

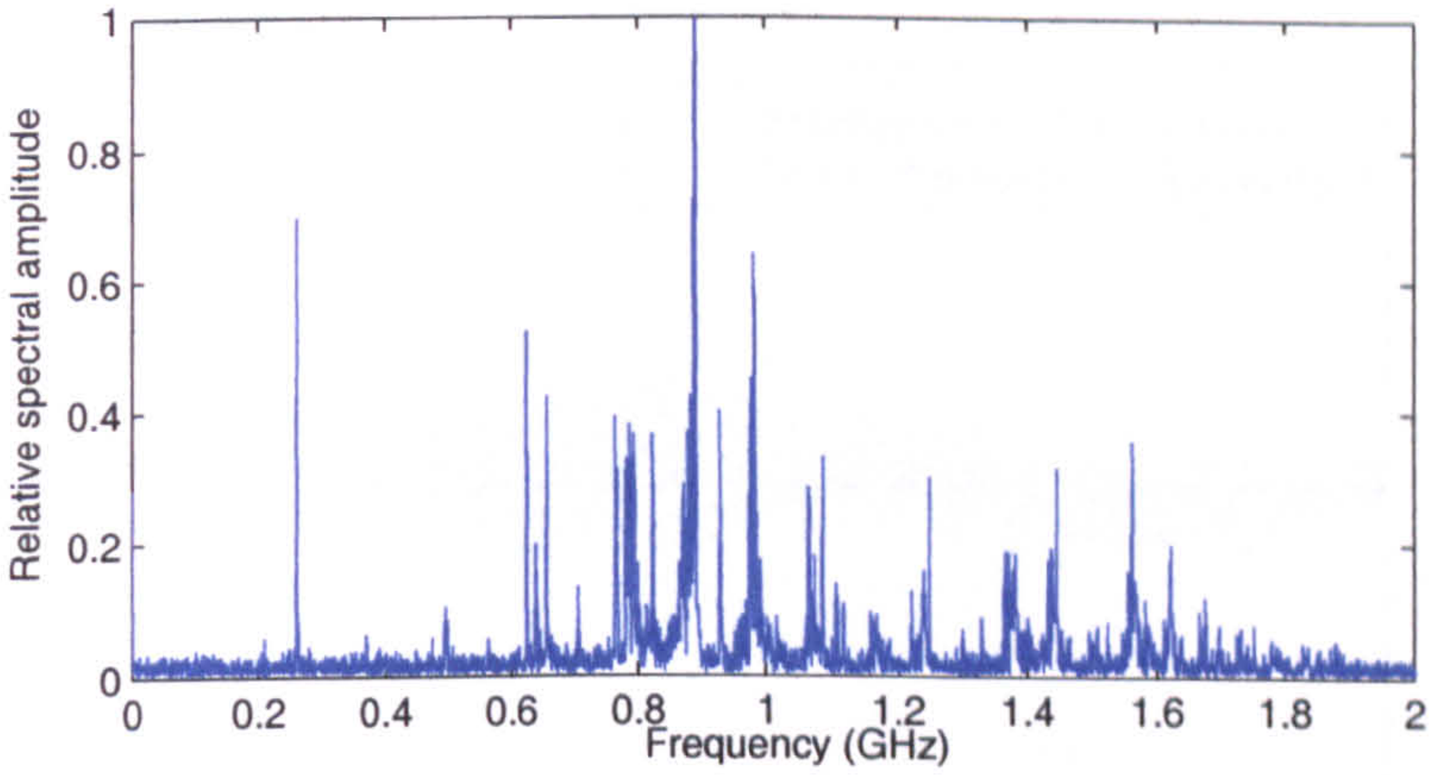

Figure 10.7: Frequency spectrum of an RF pulse produced using the SRD circuit. The signal has characteristics similar to a real PD pulse, with frequencies extending into the GHz range.

single pulses. This is in agreement with simulation results shown in Figure 10.3.

In general, as the time separation between pulses is increased, the cumulative energy decreases until the pulses are sufficiently separated so as to have no effect on each other. As regards the practical implications of this result, although a small variation in discharge energy is possible when PD pulses occur sufficiently close together, these variations are negligible in comparison with fluctuations in RF energy observed in typical laboratory or on-site measurements. The use of discharge energy U as a measurement of defect severity therefore remains valid.

10.4 Discussion

Conventional partial discharge measurement systems are unable to provide time resolved information on multiple discharge variations or events occurring within around 1μs. If two partial discharges occur within this period, then both pulses will contribute to the same cumulative apparent charge. In contrast, RF measurements are able to resolve multiple discharge events occurring within a much shorter period. From our results, it is clear that uncertainties regarding the nature of the underlying pulse are also evident in the RF method for PD measurement. In most cases, multiple PD pulses can be observed separately in the RF spectrum, however, using high bandwidth measurement, it has been shown that corona discharges in SF_6 can occur in bursts of multiple PD pulses within a period of 1 ns. In these cases it would appear that the RF signal resulting from these discharges

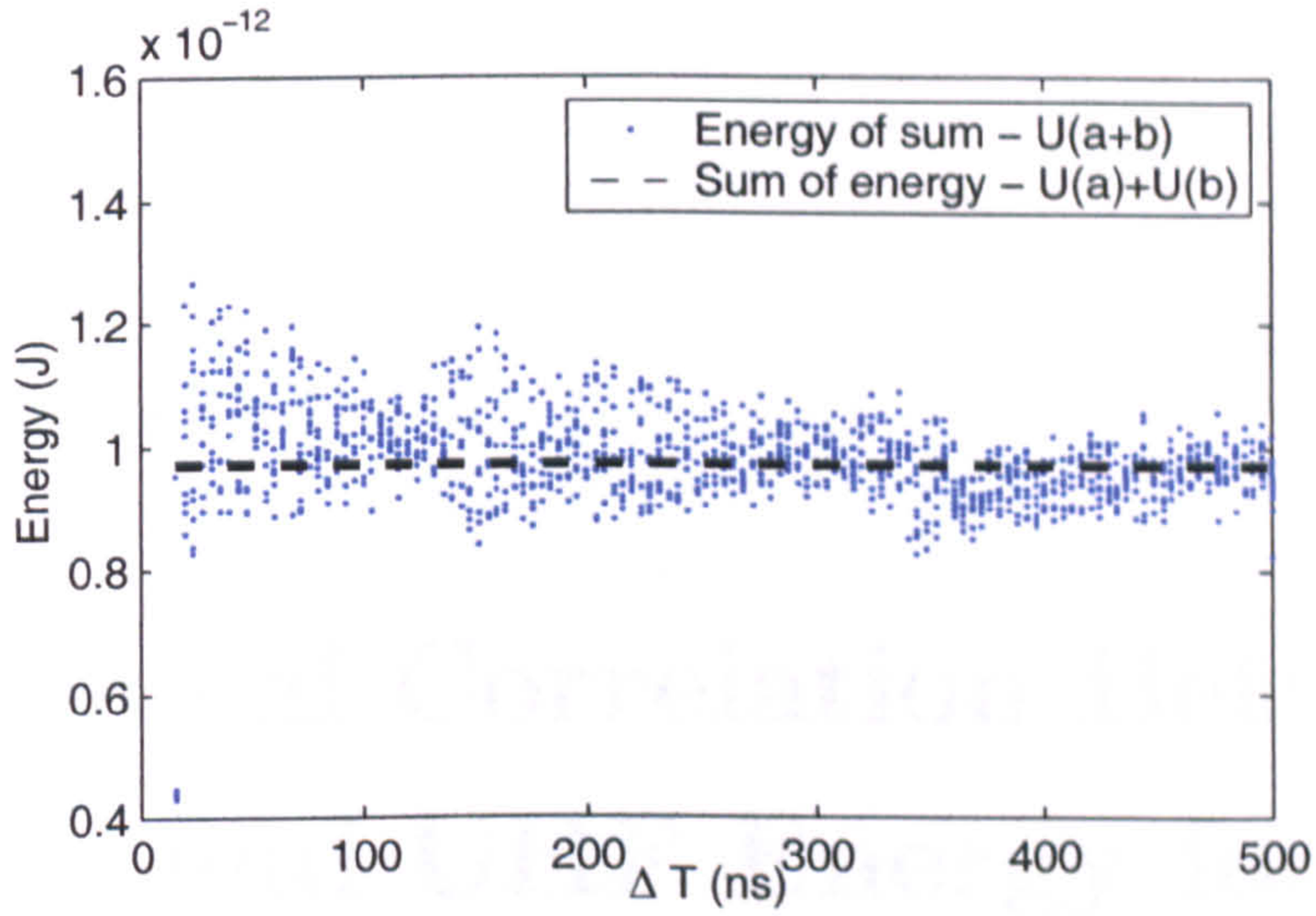

Figure 10.8: Measured variation in cumulative energy of double RF pulses with time delay. Each point on the scatter plot represents a double RF pulse.

arose from a single current pulse. It is important to remember in this regard that one of the goals of RF PD measurement is ascertain discharge severity by means of RF signal energy. When assessing physical damage by means of RF measurement the potential variation in energy with PD current pulse spacing should be considered.

10.5 Conclusion

It has been shown that the energy of the radiated signal resulting from partial discharges will show a greater variation pulse-to-pulse than that resulting from identical discharges with a wider pulse spacing. Although it is impossible to measure the current of an unknown discharge directly, the influence of pulse shape and pulse repetition on conventional as well as RF PD measurement must be considered. Although a small variation in discharge energy is possible in the case of multiple current pulses, the practical outcome is that these variations are negligible in comparison to the order-of-magnitude variations observed when measuring PD either on-site or in the laboratory. This knowledge will be useful for the future development of non-contact RF monitoring systems for detecting partial discharges in electrical plant.

Chapter 11

Theoretical Correlation Between Charge and UHF Energy for Partial Discharge Pulses using GIS Transfer Functions

To date, much experimental investigation has focused on characterising the relationship between RF energy and apparent charge for various PD source configurations. It has been found that distinct relationships exist for each defect source and that the combined measurement approach can provide insight into the underlying PD mechanisms, severity and number of defects within a sample. However, interpretation of these correlation patterns in terms of the underlying physics of the discharge has proven difficult due to the number of factors contributing to trends in the observed correlations. Therefore, in order to aid in the interpretation and understanding of combined UHF/IEC60270 measurements, an algorithm has been developed which can determine the complete response of a GIS chamber to a PD pulse of known parameters, allowing theoretical correlation graphs to be produced. Both simulated pulses, approximated using a Gaussian function, and pulses measured directly can be used as the excitation function.

11.1 Background

Attempts have been made to quantify the relationship between PD charge and the induced electromagnetic wave for discharges in GIS [94]. The cited investign-

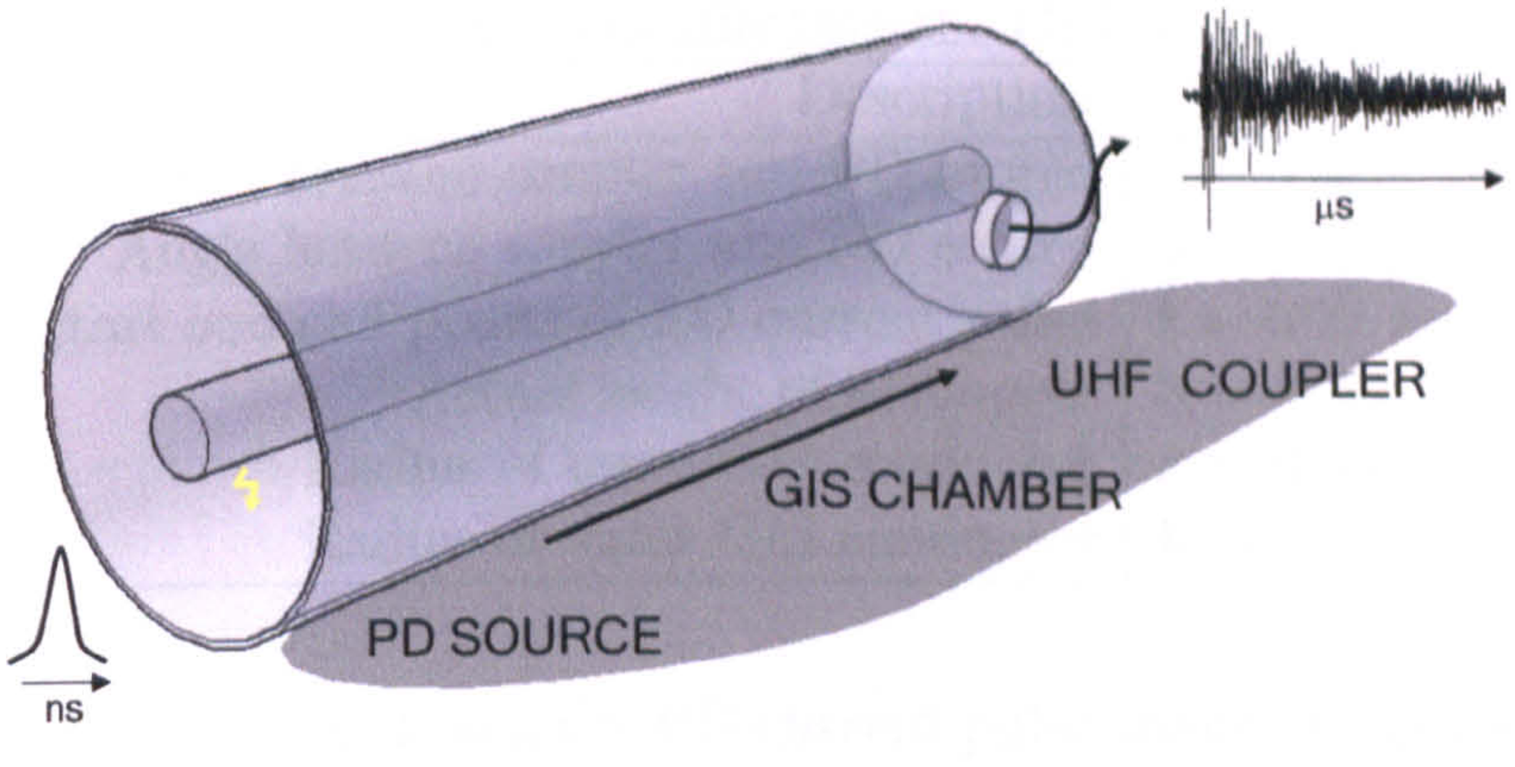

Figure 11.1: Modeling the complete response of the GIS chamber involves combining the excitation (PD current pulse), propagation (GIS chamber) and extraction (UHF coupler) transfer functions.

tion can be improved in several ways, greatly increasing the accuracy of results. These are as follows. Firstly, PD rise times used in the cited investigation are of the order of 1 ns. Recent investigations have shown that PD rise times are actually in the order of 100 ps [44]. Secondly, the authors of the cited paper use a triangular pulse as the excitation function. This approximation is invalid since sharp discontinuities will introduce higher-order frequency components into the induced electromagnetic wave. Thirdly, the UHF pulse is quantified in terms of its peak-peak amplitude. Due to the complex resonant nature of UHF pulses, the cumulative energy of the pulse is a more suitable measure as it takes into account all points on the signal by effectively taking the discreet integral of the pulse. Fourthly, the response of the GIS chamber is modeled using finite difference time domain (FDTD) techniques, however, no further details are given in the paper regarding this. Although FDTD modeling is useful, theoretical modeling is more accurate.

11.2 The GIS Transfer Function

Judd et al. [95] have modeled the complete response of a GIS chamber to a PD current pulse. The GIS response can be modeled if the excitation, propagation and extraction transfer functions can be found. This is illustrated in Fig 11.1 Parameters affecting the excitation function include the location of the PD, the

Table 11.1: List of constants affecting the GIS transfer function.

Description	Value
Distance between coupler and PD source	z = 5 m
Angle between coupler and PD source	ϕ = 0 degrees
Radial start and end points of PD current pulse	r = 0.25 m, 0.24 m
Actual height of monopole	h = 0.025 m
Radius of inner GIS conductor	a = 0.05 m
Radius of outer GIS conductor	b = 0.25 m

length of the discharge path and the PD current pulse shape. Propagation effects include time delay, reflections and attenuation. Factors affecting signal extraction include UHF field strength, coupler response and any noise or interference present. If the GIS chamber is assumed to form a coaxial waveguide then the excitation and propagation transfer functions can be obtained using the appropriate Dyadic Green's functions [96]. The excitation, propagation and extraction transfer functions are described in the following sections. Tab. 11.1 lists values of constants.

Pearson et al. [47] derive some useful equations, which can be used to calculate the frequencies of the allowable TE and TM modes excited by partial discharge within an infinitely long coaxial chamber and a coaxial cavity respectively. It is shown that by solving Maxwell's equations

$$\nabla^2 E + \omega^2 \mu \varepsilon E = 0$$

$$\nabla^2 H + \omega^2 \mu \varepsilon H = 0$$

under the relevant boundary conditions, the following expressions can be obtained.

Infinitely long coaxial chamber

TM modes are given by the characteristic equation:

$$\det \begin{vmatrix} J_n(ka) & Y_n(ka) \\ J_n(kb) & Y_n(kb) \end{vmatrix} = 0 \qquad (11.2.1)$$

where n is the number of circumferential field variations $(0, 1, 2, \ldots)$, $J_n(x)$ is the n_{th} order Bessel function of the first kind, $Y_n(x)$ is the n_{th} order Bessel function of the second kind, a and b are the respective inner and outer radii of the coaxial chamber and k is the mode constant. Each value of k is written as

k_{nm} to denote the m_{th} solution of equation (11.2.1), which has n circumferential field variations.

A similar characteristic equation is derived for TE modes:

$$\det \begin{vmatrix} \frac{\partial}{\partial r} J_n(ka) & \frac{\partial}{\partial r} Y_n(ka) \\ \frac{\partial}{\partial r} J_n(kb) & \frac{\partial}{\partial r} Y_n(kb) \end{vmatrix} = 0 \tag{11.2.2}$$

Coaxial cavity

When end plates are inserted onto the GIS chamber, it becomes a coaxial cavity. This introduces a further boundary condition, allowing a solution of the relevant Maxwell equations. The equation defining the mode constant can be rewritten to give the resonant frequency:

$$f_{nmp} = \frac{c}{2\pi} \sqrt{k_{nm}^2 + (p\pi/l)^2} \tag{11.2.3}$$

This equation gives the frequency of each mode in the cavity. The resonant frequencies for TM modes can be obtained if values of k_{nm} are taken from equation (11.2.1). Similarly, TE modes can be found if values of k_{nm} are taken from (11.2.2).

11.2.1 The Excitation Function

Firstly, the PD pulse can be simulated using a Gaussian function, as shown in Fig. 11.2 (a). Previous studies have shown that the Gaussian function provides a good approximation to the fast rising edge of a real PD pulse [44]. Although it was shown in Chapter 9 that a 5^{th} order Gaussian equation matches more accurately to a real PD pulse, the first order approximation was used for the purposes of simulation due to its simplicity. The Gaussian function is of the form

$$i(t) = I_0 e^{-t^2/2\sigma^2} \tag{11.2.4}$$

where I_0 is the peak current and σ is related to the pulse width by $\sigma = width/\sqrt{2\pi}$. Secondly, the excitation function can take the form of real current pulse data. Various PD current pulses have been measured directly using a matched-impedance point-plane test cell along with a high-bandwidth oscilloscope. One such example is shown in Fig. 11.2 (b).

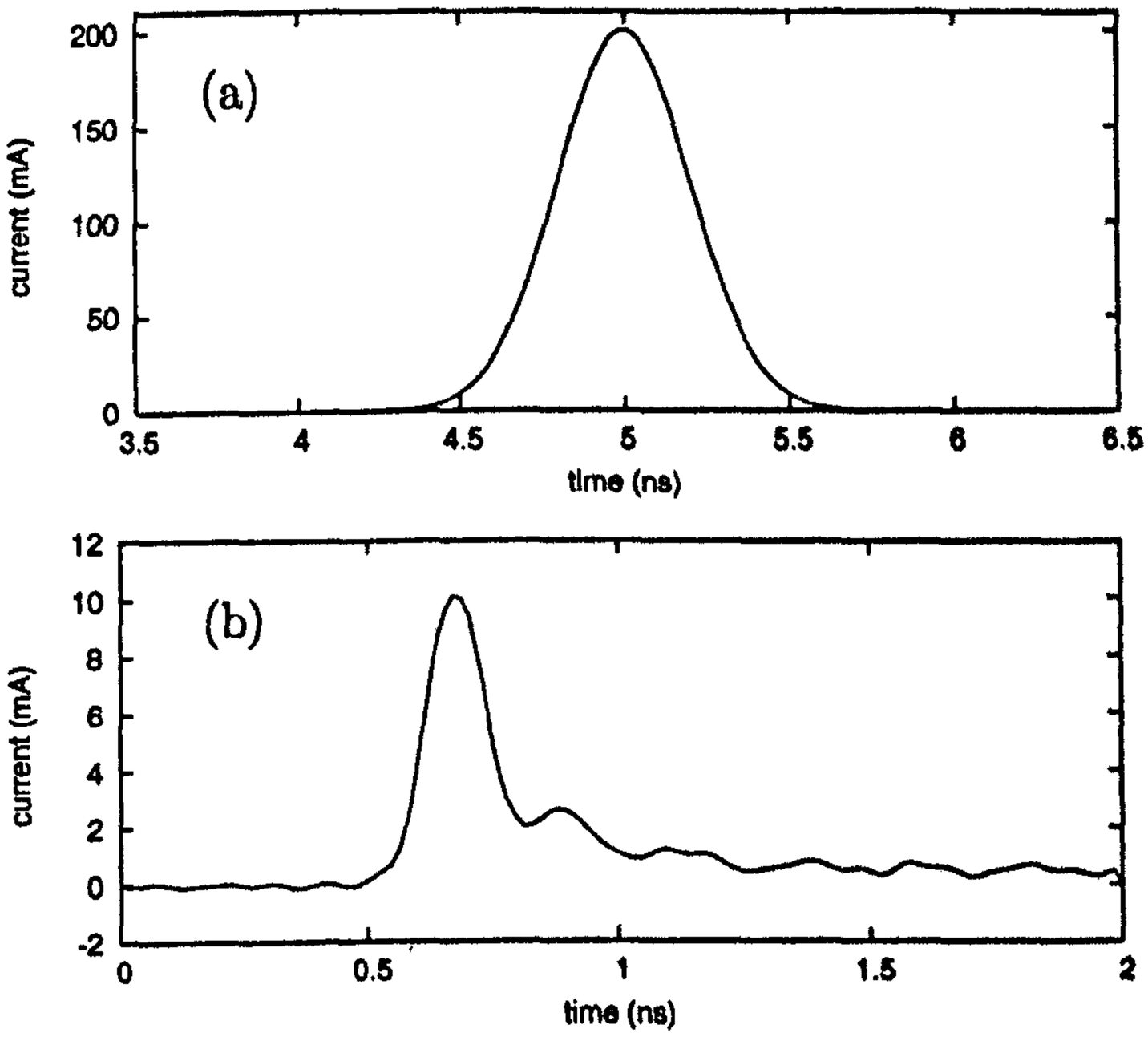

Figure 11.2: (a) Gaussian function used to simulate a PD current pulse. Pulse width = 0.5 ns. q = 100 pC. (b) PD current pulse measured directly using a 13GHz bandwidth oscilloscope and a matched-impedance test cell.

11.2.2 Green's Functions for a Coaxial Waveguide

The electric field within a waveguide excited by a current source can be expressed as

$$\vec{E}(\vec{R}) = \omega\mu_0 \iiint_V \mathbf{G}(\vec{R}|\vec{R}')\vec{J}(\vec{R}')dV' \tag{11.2.5}$$

where $\vec{E}(\vec{R})$ is the vector electric field at a remote couple location defined in cylindrical coordinates by the vector $\vec{R} = (r, \phi, z)$. $\vec{J}(\vec{R}')$ is a vector current density defined at the source location $\vec{R}' = (r', \phi', z')$. $\mathbf{G}(\vec{R}|\vec{R}')$ is the Green's dyadic for the waveguide. The TEM, TE and TM modes are considered separately and are described in detail in [95].

11.2.3 Extraction of the UHF Signal

The UHF coupler is a simple monopole antenna. The transfer function of the antenna is given in [97] as

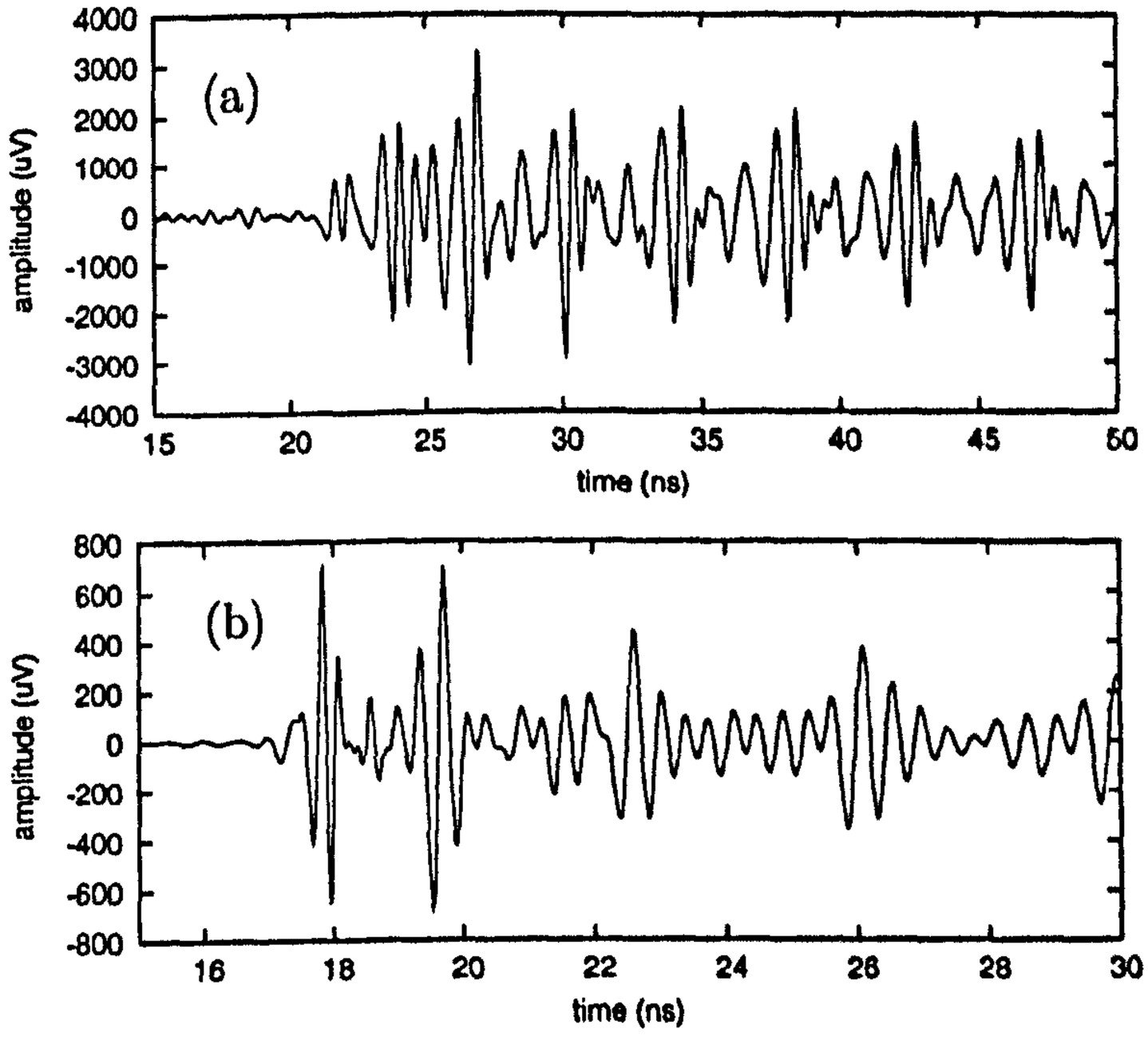

Figure 11.3: Theoretical response of the GIS model showing the UHF signal at the coupler output resulting from excitation by (a) a Gaussian current pulse, (b) a measured current pulse.

$$T_p(\omega) = \frac{V_L}{E_r} = \frac{-L_{eff} Z_L}{Z_L + Z_P} \tag{11.2.6}$$

where V_L is the output voltage, E_r is the incident electric field, L_{eff} is the effective half length and Z_p is the probe impedance. Since the load R is purely resistive and the probe is capacitive, the transfer function becomes

$$T_p(\omega) = L_{eff} \cdot \frac{1}{1 - \frac{j}{\omega C_a R}} \tag{11.2.7}$$

The effective half-length and driving point capacitance of an electrically short monopole are given in [64] in terms of its physical length and radius. Figs 11.3 shows the respective coupler outputs in response to the simulated and measured PD current pulses.

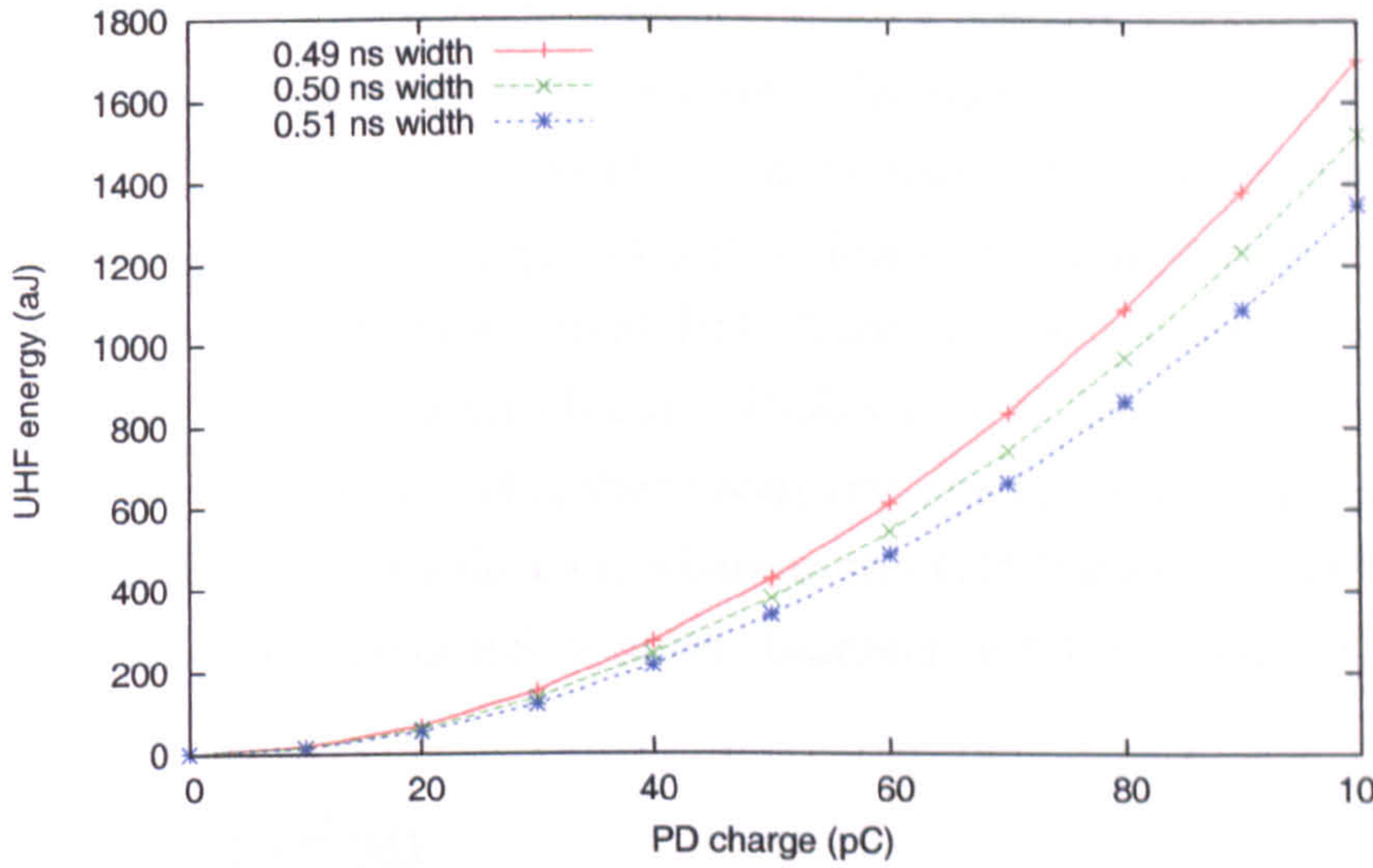

Figure 11.4: Correlation between UHF energy and PD charge for simulated PD pulses with constant pulse width.

11.3 Correlation Between Charge and UHF Energy for Simulated PD Pulses

A 100 pC Gaussian pulse with a width of 0.5 ns is shown in Fig. 11.2 (a). For a Gaussian pulse, charge is related to pulse width by $q = I_0 \cdot width$. By keeping the pulse width constant and varying the charge from 0 to 100pC in 10 pC increments, a quadratic correlation curve of the form $U = aq^2$ is produced. Shorter pulse widths lead to faster rise times and hence greater radiated energy for a given apparent charge. This is shown in Fig. 11.4.

11.4 Correlation Between Charge and UHF Energy for Measured PD Pulses

A number of positive and negative corona pulses have been measured directly using a high bandwidth system [44]. Each measured pulse has been used as the excitation function for the GIS model, allowing a correlation to be obtained between real PD charge and UHF energy for a point-plane configuration. This approach allows greater insight into the physical relationship between PD charge and UHF energy since it is not possible to quantify PD charge using conventional measurement techniques. Results are shown in Fig. 11.5 (a). Due to the polarity

of the PD source, negative corona pulses produce a positive PD charge. It should be noted that the data clusters are not caused by variations in SF_6 pressure, but are more likely to be caused by variations in factors related to the measurement system such as trigger level. Fig. 11.5 (b) shows the same correlation pattern produced from measured data. Real PD charge is approximately an order of magnitude lower than apparent charge. Differences in UHF energy levels may be partly due to differences in chamber geometry; the experimental configuration utilises a cubic chamber of side 1 m, whereas the GIS transfer function assumes a coaxial transmission line of 0.5 m outer diameter and 0.1 m inner diameter.

11.5 Discussion

The GIS model provides a useful platform for investigating the effects of PD pulse parameters on the correlation plot. The model may prove useful in the interpretation of measured PD data. For example, it will be possible to determine the variation in PD current pulse width producing an observed percentage variation in UHF energy in the correlation graph. So far, simultaneous measurement of apparent charge and UHF energy has taken place on PD sources within a cubic test chamber rather than a coaxial GIS chamber. The difference in chamber geometries may explain discrepancies in UHF energy levels between measured data and that obtained using the GIS model. Future work may therefore involve measurements on a GIS chamber having the same dimensions as that used in the model.

11.6 Conclusions

In this study, the theoretical relationship between PD charge and UHF energy is investigated for discharges occurring within a GIS chamber. The transfer function of the complete GIS chamber has been modeled theoretically. Simulated Gaussian pulses as well as measured PD current pulses have been applied as the excitation function. A quadratic relationship has been found to exist between PD charge and UHF energy for Gaussian pulses having a constant pulse width. Comparison of the correlation graph for real PD pulses applied to the GIS model and simultaneously-measured UHF and IEC data for the same point-plane source shows a similar trend. Differences in UHF energy values may be due to differences

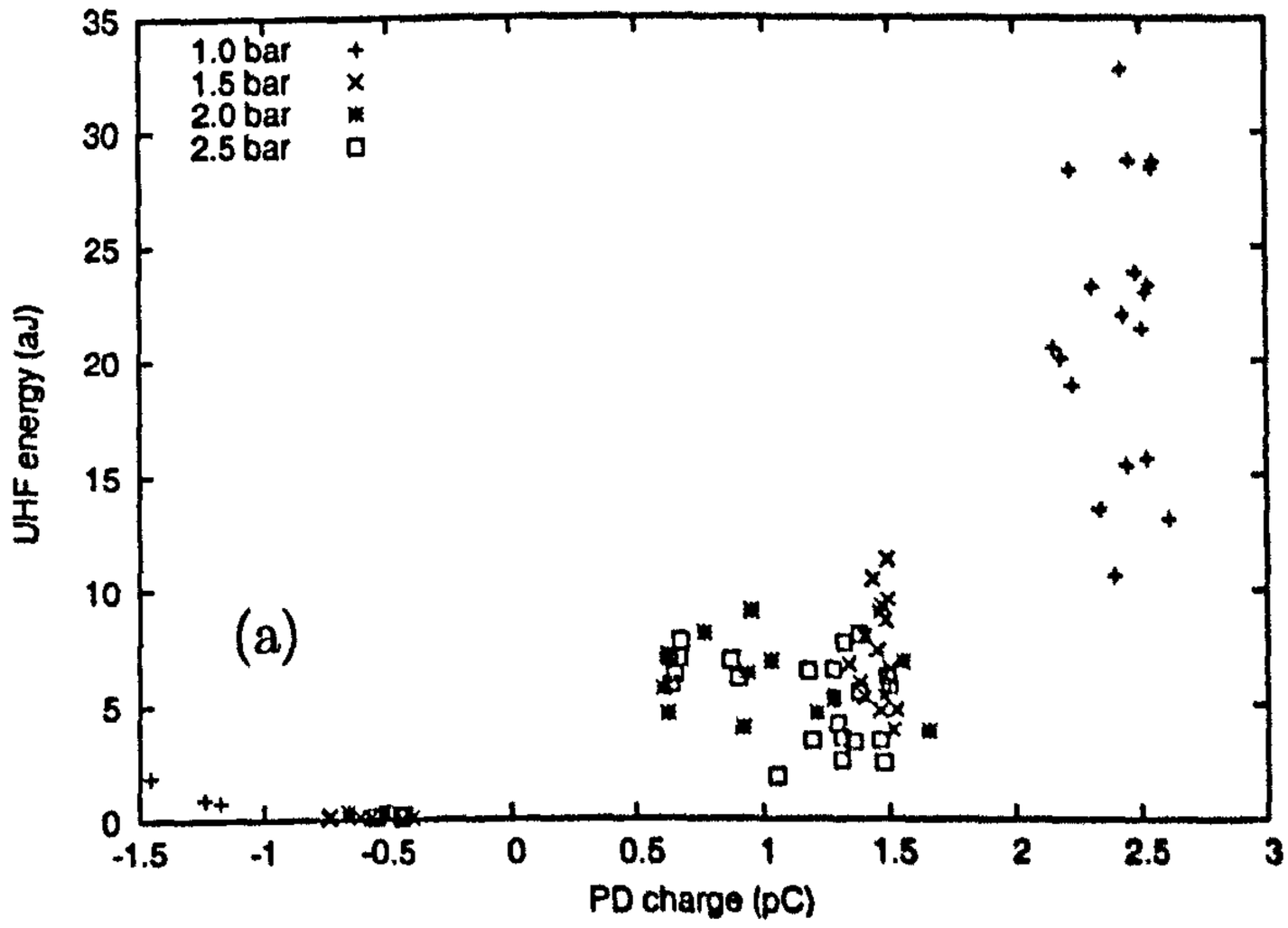

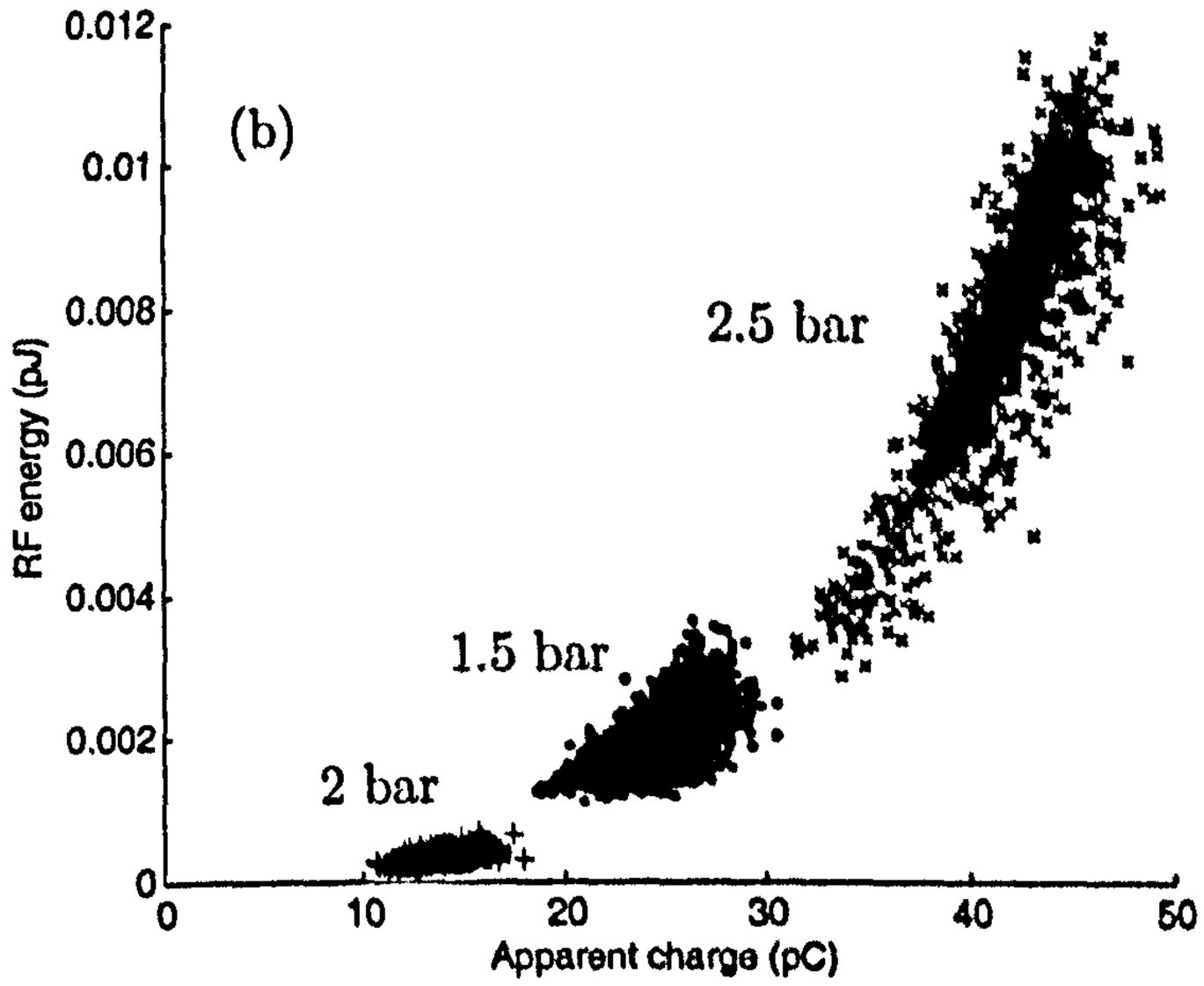

Figure 11.5: (a) Correlation between UHF energy and PD charge using measured current pulses as excitation functions for the GIS model. Current pulses were measured directly using a matched-impedance point-plane cell. 14 mm gap, 13 kV applied to the plane electrode. (b) Measured correlation between UHF energy and apparent charge. Point-plane configuration, 14 mm gap, 13 kV applied to plane electrode.

in chamber geometry. Differences between real PD charge and apparent charge are caused by attenuation effects in the measurement circuit.

Chapter 12

Discussion

In this chapter the benefits of a two-dimensional measurement system are discussed. The feasibility of deploying the system for field measurements is outlined. Finally, potential augmentations to the RF section of the IEC60270 standard are suggested based on the results of combined RF/IEC measurement.

12.1 A system for simultaneous RF and IEC PD measurement

The feasibility of combined PD measurement using RF and IEC techniques has been shown by the construction and testing of a two-dimensional measurement system. For all of the reported results, the oscilloscope was triggered on the UHF traces. This approach has several advantages, for example, the use of a combined measurement system allows the user to take advantage of the UHF technique's insusceptibility to corona interference. Triggering on the UHF signal will effectively filter out spurious signals in both UHF and IEC channels, producing a high signal-to-noise ratio. Additionally, due to the oscillatory nature of the UHF signal, UHF triggering ensures that both positive and negative IEC polarities are captured.

12.2 Correlation between RF energy and IEC apparent charge

Towards the end of this 3-year research project a few publications have arisen by other authors [51,94,98] showing the results of combined measurement using both RF and IEC techniques.

So far it has been shown that the correlation between apparent charge and UHF energy provides more information about the defect than each system does simultaneously. In some respects this is an intuitive result since the combined technique cannot give any less information than each individual technique. Due to the different responses of each system, the correlation between RF energy and apparent charge can give additional information on the shape of the underlying current pulse. This information can be interpolated from the correlation pattern. For example a free particle in oil shows a distinctive quadratic relationship between the two measurands, indicating a consistent pulse shape. In other cases, such as that of multiple voids, although it is difficult to determine the exact nature of the underlying current pulses from observation of the pattern, the appearance of multiple clusters gives an indication that multiple defects are present within the sample. It is noted that without directly measuring the PD current pulse, it is only possible to make assumptions on its shape based on the correlation pattern. In all of the patterns, a distinct upper boundary on UHF energy levels is evident for a given apparent charge, while there appears to be no well-defined limit on apparent charge for a given value of UHF energy.

One challenge relating to the appearance of multiple clusters on the correlation plots is the difficulty in distinguishing whether each cluster corresponds to a different discharge site or discharge mechanism. If sufficient spatial separation exists between discharge sites, the introduction of three additional UHF antennas will facilitate PD location using time-difference-of-arrival methods, addressing to some extent the aforementioned ambiguity. While it may be possible to identify transition to a more severe PD mechanism by the appearance of additional clusters or trend lines on the correlation diagram, more work is needed if an accurate diagnosis is to be achieved given a black box situation as, although a more severe PD mechanism will produce a new cluster on the plot, an increase in severity does not necessarily correspond to an increase in amplitude of either the UHF or IEC pulses.

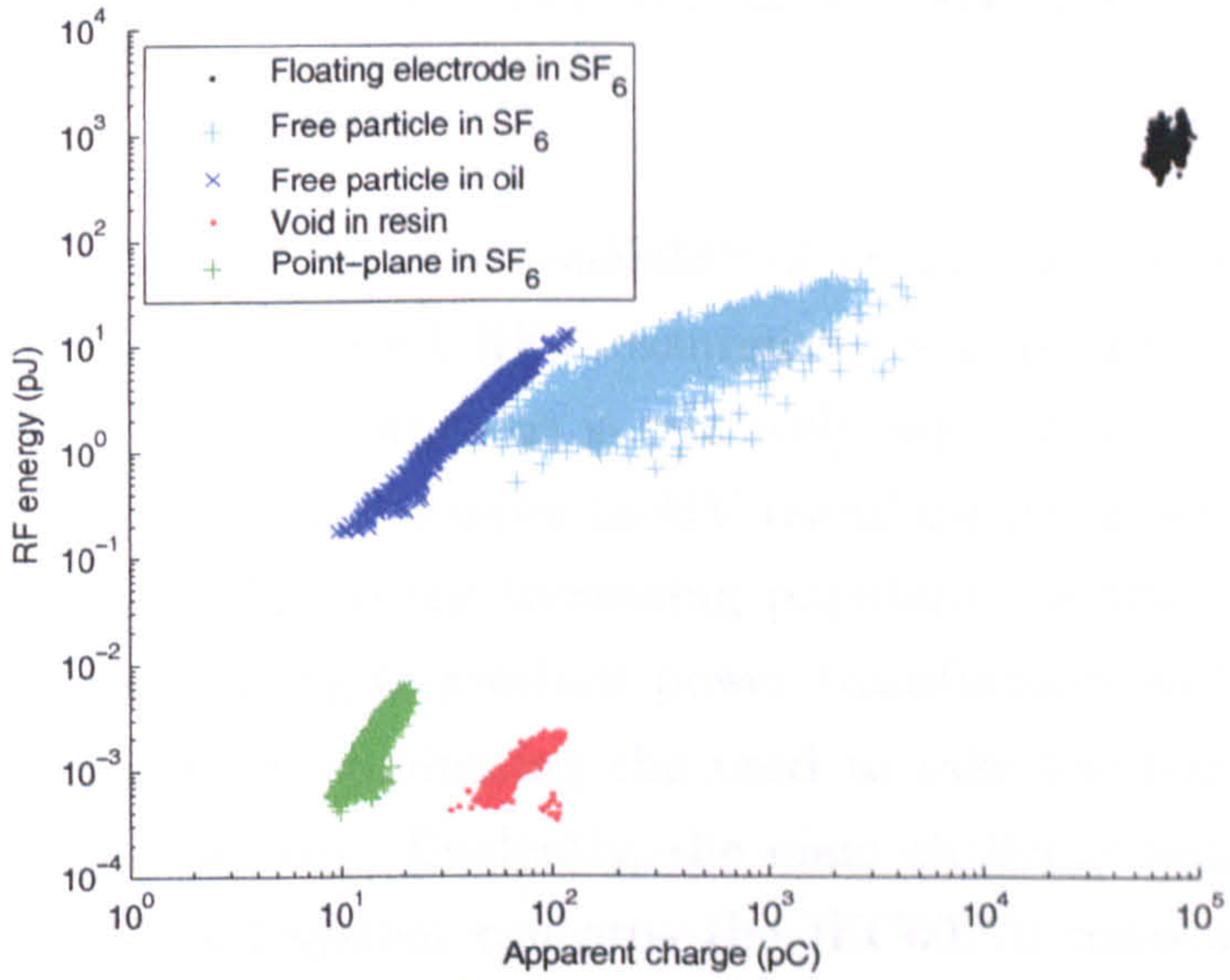

Figure 12.1: Correlation plot for all defects tested. Test conditions are as follows: Floating electrode in SF_6: 4 bar, 16 kV. Free particle in SF_6: 2 mm diameter, 3 bar, 15 kV. Free particle in oil: 3 mm diameter, 14 kV. Void in resin: 13 kV applied voltage. Point-plane in SF_6: 18 kV, 1 bar, 14 mm gap, 25 micron tip radius, tungsten tip.

It has been shown that since the order-of-magnitude relationship between the pJ and pC levels varies significantly between each PD source. This is illustrated in Figure 12.1, where the correlation plots for all defects tested under selected conditions are shown on the same graph using log scales. Due to the large variation in discharge levels, the PD sources can be clearly separated, showing that combined measurements can be used as a simple means of defect identification. Applying the pJ/pC levels measured under laboratory conditions to the identification of real defects in, for example, a power transformer is not simply a case of applying a scaling factor since the relationships are likely to be affected not only by chamber geometry but by coupler position and orientation relative to the defect. Additionally, the internal structure of a transformer tank leads to UHF pulses that are less resonant than those measured in the laboratory test chamber - a property that is likely to affect the relationship. Calibration of the IEC60270 system is also likely to be a factor affecting the application of the pJ/pC relationship to diagnosis of real plant items. For accurate calibration, current pulses would need to be injected at the point where the PD occurs which is of course impossible for an unknown discharge site.

12.3 Field-deployment of a combined measurement system

This section will briefly outline the feasibility of deploying a combined measurement system in the field. Since UHF measurement is non-contact, PD measurement on large HV insulation systems is relatively safe. It has been shown that it is possible to retro-fit UHF sensors to HV transformers as well as HVDC reactors [52, 67, 99], and due to the increasing popularity of the UHF technique, manufacturers are beginning to produce power transformers with internal UHF couplers already installed, eliminating the need to take the transformer out of service to install the sensors. Evidently, the main challenge regarding field deployment of a combined system concerns the IEC60270 measurements. Since IEC60270 is a contact measurement technique, safety becomes an important consideration. Glasgow Caledonian University (GCU) have developed an optically-isolated IEC60270 measurement system which has been used to measure PD on a 3-phase 275kV transformer [100]. The team at GCU utilised the bushing taps on each of the three phases as the test points since discharge pulses coupled effectively via the bushing capacitance. To prevent damage to the measurement system, discharge signals were transmitted via optical fibre cables. The addition of one or more UHF couplers to the GCU system would be a fairly straightforward means of producing a field-deployable combined measurement system [1]. Although, due to the limited number of channels on the oscilloscope, it would be necessary to sacrifice one or more of the IEC measurement channels and measure data on one phase only.

12.4 RF Section of the IEC60270 Standard

RF measurements are only mentioned briefly in IEC60270 in section 4.6. No recommendations are given regarding instrumentation or measurement techniques since it is not possible to quantify apparent charge using RF methods. Section 4.6 is quoted in full below.

[1] An upgraded version of the GCU IEC60270 measurement system has been developed since the publication of the cited article. At the time of writing the system has a 1mV/pC sensitivity and can be powered remotely through an optical fibre using a laser. The system has been successfully tested on a power transformer.

> **4.6 Ultra wide-band instruments for PD detection**
>
> **Partial discharges** can also be detected by oscilloscopes providing very high bandwidth or by frequency selective instruments (for example, spectrum analyzers) together with appropriate coupling devices. The aim of application is to measure and to quantify the shape of the frequency spectrum of **partial discharge** current or voltage pulses in equipment with distributed parameters, for example cables, rotating machines or gas insulated switchgear, or to provide information about the physics or origin of the discharge phenomena.
>
> No recommendations are given in this standard for either measuring methods or bandwidth/frequencies of instruments to be used in such investigations, as these methods or instruments, in general, do not directly quantify the **apparent charge** of PD current pulses.

Although the results do not conflict with the above section of the standard, they may be used to improve it. It is true that RF measurements cannot directly quantify the apparent charge of a PD current pulse, the term 'apparent charge', however, illustrates the inability of conventional measurements to quantify PD current, relying on calibration to provide an approximation to the actual charge quantity. That aside, it is possible to determine the relationship between RF energy and apparent charge for a given test configuration by applying simultaneous measurement. These are not simple linear relationships, but complex patterns which reveal details of the underlying pulse shapes. Putting aside this complexity, it is possible to calibrate the order-of-magnitude relationship between RF energy and apparent charge for a given defect, as this relationship varies significantly between PD sources.

Whether it would be reasonable to state quantatively the RF/IEC relationships acquired under laboratory conditions is doubtful, since it has been shown that these quantities vary depending on tank geometry (the size of the transformer of GIS chamber). It is more likely that a library of data giving details on the shape of the correlation pattern for a given defect will prove more useful. As will the relative order-of-magnitude variations between defects.

Chapter 13

Conclusions

This chapter will summarise the main conclusions drawn from the research activity. The feasibility of producing a combined measurement system is discussed as are the relative merits of such a system. Potential applications of the research are considered including its possible contribution towards a more widespread acceptance of the RF method as a diagnostic technique.

13.1 The measurement system

A system for simultaneously measuring partial discharge using the RF and IEC60270 techniques has been successfully constructed and tested using a range of PD sources. The system provides useful additional information which would be otherwise unavailable using either the IEC or RF techniques individually. Traces from each of the measurement systems are recorded using a high-bandwidth (3 GHz) oscilloscope and analysed in post-processing using high-level software developed using MATLAB. By plotting the energy of each RF pulse against the corresponding IEC apparent charge, it is possible to determine the relationship, or 'correlation', between the two quantities. Since both systems respond differently to the original PD current pulse, the correlation pattern can provide an insight into the shape of the PD current pulse and therefore give some information on the PD mechanism.

13.1.1 Advantages

The combined measurement system has many advantages over either of the individual techniques, for example:

1. It is possible to identify simultaneously active PD sources within a sample by the appearance of data clusters in the correlation plots corresponding to each PD source.

2. The insusceptibility of RF measurements to corona interference may be harnessed on both sets of measurements by triggering on the RF channel.

3. Plotting RF energy against apparent charge for a large number of pulses produces distinctive patterns specific to each PD source topology, allowing identification of the defect.

4. The order-of-magnitude pJ/pC relationship between the two measurements can also be used as a simple means of defect identification.

5. Unlike conventional techniques, simultaneous measurement requires no phase reference.

13.1.2 Issues

Some shortcomings also exist respecting the combined technique. Firstly, given a black box situation, it can be difficult to identify some defects which do not conform to the well-defined test samples used throughout the investigation. It could however be argued that this is still the case with any PD measurement system. Secondly, without PD location capability, it is unclear whether clusters appearing on the correlation patterns correspond to multiple PD sites or to multiple PD mechanisms. Thirdly, it has been shown that the pJ and pC levels vary depending on the test environment. Since these levels are affected by factors such as chamber volume, coupler orientation and coupler position, it is unlikely that pJ/pC relationships measured under laboratory conditions can be used as a basis for defect classification in the field. Fourthly, the identification of multiple defects by the appearance of clusters can prove difficult when cluster separation is not clearly defined or if clusters are overlapping. In these cases, clustering algorithms may be able to identify features of the correlation plots that are not immediately obvious to the observer.

13.2 PD current pulse measurement

Gaining an insight into the underlying shape of the PD current pulses is important in understanding and interpreting the relationship between RF energy and apparent charge. Direct measurement of the PD current pulse has been carried out on a matched impedance point-plane test cell in SF_6 using a 12 GHz bandwidth measurement system. It was possible to measure a PD rise time of 35 ps at 210 kPa; the fastest rise time measured to date. A considerable variation in the pulse shape and pulse characteristics was observed. For example, pulses were found to occur in multiple bursts within a period of 1 ns.

Direct measurement of PD current pulses provides valuable data that can be used to more accurately define the excitation function for analytical studies and numerical modeling of PD and associated phenomena.

13.3 Applications

13.3.1 Diagnostic monitoring

It has been shown that the combined technique has the potential to identify individual defect types such as floating electrodes, free particles and voids. Simultaneously active PD sources within an insulation sample as well as transition to a more severe PD mechanism may potentially be identified. Although conventional measurements can also be used for defect identification, they are reliant on a phase reference. Combined measurements can be applied without the requirement of a phase reference, additionally avoiding the complication of harmonic distortion of the phase resolved patterns [101].

13.3.2 Acceptance of the UHF method

Although the results presented herein may have practical significance for future on-line monitoring hardware employing a combined measurement system, of equal importance is the contribution to the general acceptance of UHF measurement as a powerful diagnostic technique. Due to the ubiquity of conventional measurement systems and the expertise gained in their use over a number of decades, the pC level has become the standard measure of PD severity. By experimentation, it has been possible to show the relationship between the pC level and the UHF energy level on the most common insulation defects. Knowledge of how these

quantities relate to each other is an important factor in gaining acceptance of the UHF technique as a safer and more practical alternative to conventional measurements.

Chapter 14

Future Work

This chapter will discuss additional avenues of research which may be pursued as a result of the findings reported in this thesis, including automatic interpretation and classification of the correlation patterns, interpretation of the underlying physical mechanisms, improvements to the simultaneous phase-resolved measurement system and methods examining the phase-resolved measurements in terms of the relationship between RF and IEC techniques.

14.1 Interpretation of the measurements given a 'black box' situation

RF/IEC correlations are fairly distinctive for each PD source topology and therefore identification of the defect by visual examination of the correlation pattern is fairly straight-forward. However, given a black-box situation, where the type and number of defects is unknown, identification becomes more challenging. As shown previously, multiple discharge sites as well as varying levels of discharge severity are manifested on the correlation graph as multiple clusters of data. Given a black box situation, determining whether different clusters are caused by multiple discharge sites or multiple discharge mechanisms can be difficult. For example, the correlation patterns for discharges produced by a small transformer on page 56 shows multiple clusters. The appearance of new clusters with increasing voltage does not necessarily indicate whether discharges are produced as a result of a more severe PD mechanism or whether the electric field has reached inception level within a new void inside the test object.

This ambiguity may be resolved by installing an array of UHF couplers rather

than the single sensor that is currently used. This would facilitate time-difference-of-arrival measurements, allowing PD location and giving a definitive identification of the number of different PD sites in the object under test.

14.2 Interpreting the correlation patterns in terms of physical mechanisms

Interpreting the physics of the PD mechanism may be possible on examination of the correlation graph, although in some cases this can be more complicated than in others. The most simple case is the quadratic relationship between RF energy and apparent charge, which can be seen in the case of a point-plane in SF_6 and a free particle in oil. It has been previously shown that this indicates a consistent PD current pulse shape [53]. Interpretation of the PD mechanism for configurations other than the point plane can be challenging since the mechanism is less well understood in these cases. One possible avenue of research which may be pursued further is to automate the GIS model discussed in Chapter 11. If a similar test environment to that used in the model is created, then it would be possible to determine the shape of the original current pulse based on the radiated energy and charge of the measured signals. Of course this analysis relies on the assumption that the original PD pulse is Gaussian in nature, which is not always the case.

A greater aid in the understanding of the underlying PD mechanisms and how they affect the correlation graph would be direct measurement of the PD current pulses. This has already been achieved in the case of the point-plane configuration, which lends itself well to this purpose. It should be possible to devise strategies for direct measurement of PD current pulses from additional test geometries, such as voids, free particles and floating electrodes.

14.3 Improving the RF section of the IEC60270 standard

The IEC60270 standard states that its contents will remain unchanged until 2008, at which point it will either be reconfirmed, withdrawn, replaced by a revised version or amended. The proposed document would not be an amendment to

the standard, since the research does not conflict with what is stated in the RF section, rather, it would be an expansion or augmentation of the standard, giving the results of recent activity toward understanding the relationship between RF and conventional PD measurement.

14.4 Automatic defect classification

Identification of the type and number of defects within a sample based on visual examination of the correlation plot is achievable in the majority of cases. Automation of this process is significantly more difficult. There are challenges to be addressed firstly when identifying the number of clusters within a correlation plot. For example, the suitability of various clustering algorithms such as fuzzy c-means clustering have been examined. Such algorithms are suitable for identifying clusters of data within a plot, but fall down when used in a black-box situation where no information is known regarding the number of clusters which should be identified or when cluster separation is less distinct. Secondly, when correlation patterns become less distinct, curve-fitting becomes a less viable approach to quantifying the relationship between the two measurements. Some means of defect identification based on the shape or envelope of the pattern is therefore required.

14.5 Phase-resolved measurements

14.5.1 The 'OR' triggering function

Chapter 7 showed PRPD patterns produced using simultaneously acquired UHF and IEC pulses. It was noted that although clear differences can be observed in the spread in discharge magnitudes between the sets of patterns, there is no noticeable variation in phase position. This is likely due to the nature in which the data is triggered. With triggering implemented on the UHF channel of the oscilloscope, both UHF and IEC pulses are captured when a UHF pulse is detected. To detect whether differences exist in phase positions while capturing the two PD measurements simultaneously, it will be necessary to implement an 'OR' triggering function. It would be possible to implement such a function using two additional oscilloscopes to trigger the respective UHF and IEC pulses. The output triggers of each additional oscilloscope could be fed into an OR gate, the

output of which would be used to trigger the main LeCroy oscilloscope externally. Although this is not the most cost-effective method, it is relatively easy to implement since the equipment is already available in the laboratory in the form of a 500 MHz Tektronix TDS3054B oscilloscope and a 3 GHz Tektronix TDS694C oscilloscope.

14.5.2 Incorporating phase-resolved information into the correlation patterns

The development of the phase-reference circuit and its use alongside the existing simultaneous measurement setup opens up new opportunities for relating correlation data to specific phase windows and quadrants. Although during the project simultaneous measurement of the RF and IEC pulses along with the phase angle has been achieved, additional analysis could be performed on the measured data which has so far not been possible due to limitations in the correlation software. A useful feature on any future software would be the ability view the correlation pattern for selected clusters of PD pulses selected on the PRPD plot.

Appendix A

List of Publications

Much of the work contained in this theses is based on the following papers, which the author has published during the course of the research:

Published conference papers

[102] A. J. Reid and M. D. Judd. Partial discharges and RF signals. In *1st UHVnet Colloqium on Condition Monitoring and Ageing of High Voltage Plant/Equipment*, Cardiff University, January 2005

[91] M. D. Judd, A. J. Reid, L. Yang, B. G. Stewart, and R. A. Fouracre. A new integrated diagnostic partial discharge monitoring strategy for HV plant items: combining UHF couplers and the IEC60270 standard. In *18th International Conference on Electricity Distribution*, Turin, Italy, June 2005

[92] A. J. Reid, L. Yang, M. D. Judd, B. G. Stewart, and R. A. Fouracre. An integrated measurement strategy for simultaneous fault identification: Combining the UHF and IEC60270 techniques. In *14th International Symposium on High Voltage Engineering*, page 394, Beijing, China, August 2005

[103] A. J. Reid and M. D. Judd. High bandwidth measurement of partial discharge pulses in SF_6. In *14th International Symposium on High Voltage Engineering*, page 348, Beijing, China, August 2005

[68] L. Yang, B. G. Stewart, A. J. Reid, M. D. Judd, and R. A. Fouracre.

Study on combining UHF techniques with the IEC60270 standard for monitoring partial discharge of HV plant. In *14th International Symposium on High Voltage Engineering*, page 347, Beijing, China, August 2005

[93] M. D. Judd, D. Gray, and A. J. Reid. Using a step recovery diode to generate repeatable pulses for partial discharge simulation. In *14th International Symposium on High Voltage Engineering*, page 595, Beijing, China, August 2005

[104] B. G. Stewart, L. Yang, M. D. Judd, A. J. Reid, and R. A. Fouracre. A simple metric for assessing the severity of partial discharge activity based on time-sequence-analysis-discharge level patterns. In *International Conference on Condition Monitoring and Diagnostics*, Changwon, Korea, April 2006

[105] A. J. Reid, M. D. Judd, B. G. Stewart, and R. A. Fouracre. Frequency distribution of RF energy from PD sources and its application in combined RF and IEC60270 measurements. In *IEEE Conference on Elcctrical Insulation and Dielectric Phenomena*, Kansas City, MO, USA, October 2006

[99] M. Judd, S. McArthur, A. Reid, V. Catterson, L. Yang, B. Jacobson, K. Svensson, and M. Gunnarsson. Investigation of radiometric partial discharge detection for use in switched HVDC testing. In *PES General Meeting*, Montreal, June 2006. IEEE

[106] A. J. Reid, M. D. Judd, B. G. Stewart, R. A. Fouracre, and S. Venkatesan. Identification of multiple defects in solid insulation using combined RF and IEC60270 PD measurement. In *9th IEEE International Conference on Solid Dielectrics*, Winchester, Hampshire, UK, July 2007

[107] S. Venkatesan, B. G. Stewart, M. D. Judd, A. J. Reid, and R. A. Fouracre. Analysis of PD in voids using correlation plots of RF radiated energy and apparent charge. In *9th IEEE International Conference on Solid Dielectrics*, Winchester, Hampshire, UK, July 2007

[108] D. Templeton, R. Brinzer, J. S. Pearson, A. J. Reid, and M. D. Judd. Sensitivity testing of a UHF power transformer monitoring system. In *15th International Symposium on High Voltage Engineering*, Ljubljana, Slovenia, August

2007

[109] A. J. Reid, M. D. Judd, B. G. Stewart, R. A. Fouracre, and S. Venkatesan. Correlation between RF energy and IEC60270 apparent charge for selected partial discharge source geometries. In *15th International Symposium on High Voltage Engineering*, Ljubljana, Slovenia, August 2007

[110] A. J. Reid and M. D. Judd. A novel self-powered condition monitoring sensor for harsh environments - feasibility study. In *15th International Symposium on High Voltage Engineering*, Ljubljana, Slovenia, August 2007

[111] B. G. Stewart, A. J. Reid, M. D. Judd, and R. A. Fouracre. UHF and IEC60270 correlation analysis of radiated frequency band measurements on resin insulation void samples. In *Electrical Insulation Conference and Electrical Manufacturing Expo*, Nashville, TN, USA, October 2007

[112] B. G. Stewart, M. D. Judd, A. J. Reid, and R. A. Fouracre. Suggestions to augment the IEC60270 partial discharge standard in relation to radiated electromagnetic energy. In *Electrical Insulation Conference and Electrical Manufacturing Expo*, Nashville, TN, USA, October 2007

Published journal papers

[44] A. J. Reid, M. D. Judd, B. G. Stewart, and R. A. Fouracre. Partial discharge current pulses in SF_6 and the effect of superposition of their radiometric measurement. *Journal of Physics D: Applied Physics*, 39:4161–4177, September 2006

[113] B. G. Stewart, L. Yang, M. D. Judd, A. J. Reid, and R. A. Fouracre. A simple metric for assessing the severity of partial discharge activity based ion time-sequence-analysis-discharge level patterns. *Trans. Electrical and Electronic Materials*, 7(6):313–318, Dec 2006

[114] R. Sarathi, A. J. Reid, and M. D. Judd. Partial discharge study in transformer oil due to particle movement under dc voltage using uhf technique. *Electric Power Systems Research (Elsevier)*, 2007

Journal papers in preparation

[115] A. J. Reid, M. D. Judd, B. G. Stewart, D. M. Hepburn, and R. A. Fouracre. Identification of simultaneously active partial discharge sources using combined RF and IEC60270 measurement. *Journal of Physics D: Applied Physics*

[116] A. J. Reid, M. D. Judd, B. G. Stewart, and R. A. Fouracre. Combined RF and IEC60270 partial discharge measurement on selected PD source geometries. *IEEE Trans. Power Delivery*

Appendix B

Phase Reference Circuit

This appendix describes the circuit used to obtain a phase reference signal for simultaneous phase-resolved PD measurement. The circuit produces a ramp output voltage that is proportional to the phase position of the reference wave in order to overcome any ambiguity in phase position when feeding the reference sinusoid directly into the oscilloscope.

The mains input feeds a PSU that powers the circuit electronics. There is also a small transformer that gives a few volts AC synchronised to the mains input so that internal triggering can be selected if there is no phase reference available from the HV circuit. If there is a phase reference, the toggle switch can be set to trigger from the external input socket (BNC). A zero crossing detector triggers on the positive zero crossings of the power frequency. Its output resets the counter to zero. A monostable detects pulses present on the zero crossing detector output and pulses an LED, which will glow only when zero crossings are being detected. Note that the reset pulse to the counter should not be longer than one clock cycle (20 microseconds). The counter should count nearly its full range in one cycle (20 ms). With 10 bits (0 - 1023 count), this would require 51.2kHz clock. To avoid the risk of ever exceeding the max count should the power freq. drift below 50Hz, a 50 kHz clock was used. The output is a triangular wave where V is proportional to phase angle coming out of the BNC output. A small capacitor across the output helps to smooth the staircase, but does not seriously degrade the flyback when the counter gets reset.

Appendix B

Phase Reference Circuit

This appendix describes the circuit used to obtain a phase reference signal for simultaneous phase-resolved PD measurement. The circuit produces a ramp output voltage that is proportional to the phase position of the reference wave in order to overcome any ambiguity in phase position when feeding the reference sinusoid directly into the oscilloscope.

The mains input feeds a PSU that powers the circuit electronics. There is also a small transformer that gives a few volts AC synchronised to the mains input so that internal triggering can be selected if there is no phase reference available from the HV circuit. If there is a phase reference, the toggle switch can be set to trigger from the external input socket (BNC). A zero crossing detector triggers on the positive zero crossings of the power frequency. Its output resets the counter to zero. A monostable detects pulses present on the zero crossing detector output and pulses an LED, which will glow only when zero crossings are being detected. Note that the reset pulse to the counter should not be longer than one clock cycle (20 microseconds). The counter should count nearly its full range in one cycle (20 ms). With 10 bits (0 - 1023 count), this would require 51.2kHz clock. To avoid the risk of ever exceeding the max count should the power freq. drift below 50Hz, a 50 kHz clock was used. The output is a triangular wave where V is proportional to phase angle coming out of the BNC output. A small capacitor across the output helps to smooth the staircase, but does not seriously degrade the flyback when the counter gets reset.

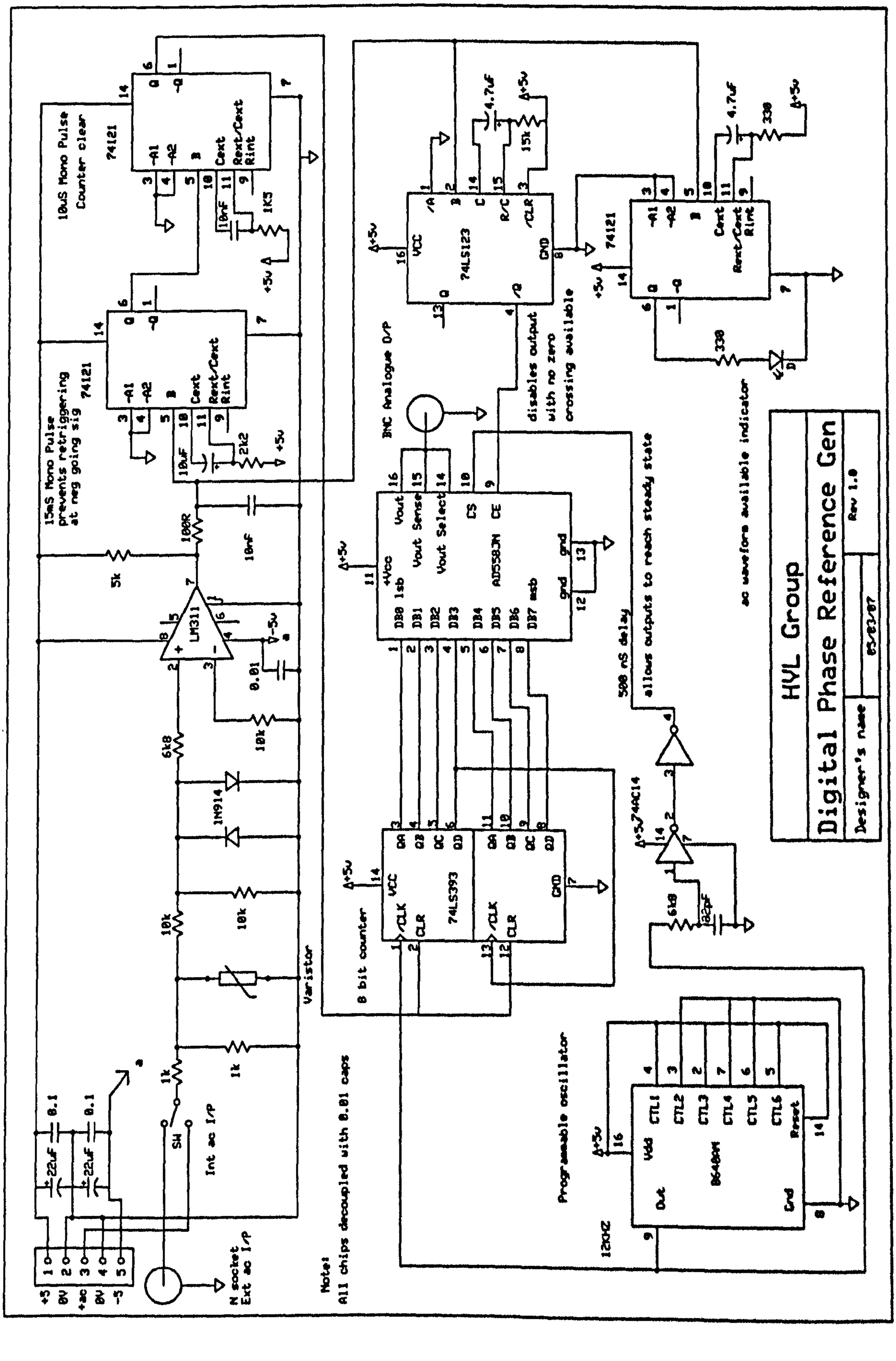

Figure B.1: Digital phase reference circuit.

Bibliography

[1] P. Lorin. Extend the lifetime of your transformer by using computer modeling. *IEE Power Engineer Magazine*, pages 18–21, April/May 2005.

[2] M. D. Judd, G. P. Cleary, and S. Meijer. Testing UHF partial discharge detection on a laboratory based power transformer. In *Proc. 13th International Symposium on High Voltage Engineering*, Delft, August 2003.

[3] *IEC International Standard 60270. High Voltage Test Techniques - Partial Discharge Measurements.* International Electrotechnical Commission (IEC), Geneva, Switzerland, 3rd edition, 2000.

[4] G. C. Lichtenberg. *Novi Commentarii Societatis Regiae Scientiarium Gottingae*, 8:168–180, 1777.

[5] F. H. Krueger. *Partial Discharge Detection In High Voltage Equipment.* Butterworth-Heinemann, 1989.

[6] F. Paschen. *Weid. Ann*, 37:69–96, 1889.

[7] D. Chang, T. S. Sudaschan, and J. E. Thompson. Analysis of electric stress distribution of cavities embedded within dielectric structures. *IEEE Transactions on Electrical Insulation*, 21(2), 1986.

[8] S. A. Boggs. Electromagnetic techniques for fault and partial discharge location in gas-insulated cables and substations. *IEEE Transactions on Power Apparatus and Systems*, PAS-101(7):1935–1941, July 1982.

[9] F. Romain, V. Cooray, and V. Scuka. Corona from floating electrodes. *Journal of Electrostatics*, 37:67–78, 1996.

[10] H. Günther. *Hochspannungstechnik*, page 72. Teubner, Stuttgart, 1981.

[11] N. Fujimoto and G. L. Ford. Results of recent GIS fault survey. In *IERE Workshop on Gas Insulated Substations*, Toronto, September 1990.

[12] D. Kopejtkova, T. Molony, S. Kobayashi, and I. M. Welch. A twenty-five year review of experience with gas–insulated substations, CIGRE Paper 23-101 1992.

[13] E. Kuffel, W. S. Zaengl, and J. Kuffel. *High Voltage Engineering: Fundamentals.* Butterworth-Heinemann, 2nd edition edition, 2000.

[14] R. Patsch and F. Berton. The role of space charges in PD-processes. In *Proceedings of International Symposium on Electrical Insulating Materials*, pages 21–24, Himeji, Japan, 2001.

[15] R. Altenburger, C. Heitz, and J. Timmer. Analysis of phase-resolved partial discharge patterns of voids based on a stochastic process approach. *Journal of Applied Physics*, 35:1149—1163, May 2002.

[16] H. Schering. Brüke für verlustmessungen. *Tätigkeitsbericht der Physikalisch-Technischen Reichsanstalt*, 1919.

[17] A. Kelen. Studies on partial discharges on solid dielectrics - a contribution to the discharge resistance testing of insulating materials. Electrical engineering series, Acta Polytechnica Scandinavia, 1967.

[18] R. Bartnikas. Discharge rate and energy loss in helium at low frequencies. *Arch. für Elektrotechn.*, 52:348–359, 1969.

[19] R. Bartnikas and E. I. McMahon. *Engineering Dielectrics*, volume 1. ASTM special technical publication 669, Philadelphia, 1979.

[20] P. Degn. *Partial Disscharges in Solid Dielectrics.* PhD thesis, Technical University of Denmark, Lyngby, 1971.

[21] J. C. Devins. The physics of partial discharges in solid dielectrics. *IEEE Transactions on Electrical Insulation*, 19:475–495, 1984.

[22] T. Tanaka. Internal partial discharges and material degredation. *IEEE Transactions on Electrical Insulation*, 21:899–905, 1986.

[23] O. E. Ibrahim and O. Farish. Negative-point-breakdown and prebreakdown coron processes in SF6 and SF6/N2 mixtures. In *6th International Conference on Gas Discharges*, pages 161–164, Edinburgh, 1980.

[24] A. B. Borishade. The development of electrical discharges in simulated tree channels. *IEEE Transactions on Electrical Insulation*, 12:348–354, 1977.

[25] L. Niemeyer, B. Fruth, and H. Kugel. Phase resolved partial discharge measurements in particle contaminated SF6 insulation. In *6th International Symposium on Gaseous Dielectrics*, pages 579–585, Knoxville, TE, 1991.

[26] C. Heuser and G. Pietsch. Prebreakdown phenomena between glass-glass and glass-metal electrodes. In *6th International Conference on Gas Discharges*, pages 98–101, Edinburgh, 1980.

[27] I. Gallimberti, G. Marchesi, and R. Turri. Corona formation and propogation in weekly and strongly attaching gases. In *8th International Conference on Gas Discharges*, pages 587–594, Oxford.

[28] W. Y. Gu, C. Laurent, and C. Mayoux. Characteristics of discharges inside simulated tree channels under impulse voltage. *Journal of Physics D: Applied Physics*, 19:2197–2204, 1986.

[29] P. H. F. Morsahuis and F. H. Kreuger. Transition from streamer to townsend mechanisms in dielectric voids. *Journal of Physics D: Applied Physics*, 23:1562–1568, 1990.

[30] J. S. Pearson, O. Farish, B. F. Hampton, M. D. Judd, D. Templeton, B. M. Pryor, and I. M. Welch. Partial discharge diagnostics for gas insulated substations. *IEEE Transaction on Electrical Engineering*, 2(5):893–905, October 1995.

[31] A. Haddad and D. Warne, editors. *Advances in High Voltage Engineering*. The Institution of Electrical Engineers, London, 2004.

[32] I. J. Kemp. Partial discharge plant-monitoring technology: present and future developments. *IEE Trans. Sci, Meas, Tech.*, 142(1):4–10, Jan 1995.

[33] R. Baumgartner, B. Fruth, W. Lanz, and K. Pettersson. Partial discharge. x. PD in gas-insulated substations - measurement and practical considerations. *IEEE Electrical Insulation Magazine*, 8(1):16–27, Jan/Feb 1992.

[34] T. Waters and D. Morgan. On-line DGA during controlled energization of a 1000MVA autotransformer exhibiting partial discharge. In *EPRI Substation Equipment Diagnostics Conference X*, 2002.

[35] G. L. Martin. The hydran - a system for the detection and monitoring offailure conditions in power transformers. In *IEE Colloquium on Monitors and Condition Assessment Equipment*, pages 3/1–3/5, Leatherhead, Surrey, UK, Dec 1996.

[36] Kelman services (promotional brochure). www.kelman.co.uk, Lisburn. UK.

[37] *Mineral Oil-Impregnated Electrical Equipment in Service - Guide to the Interpretation of Dissolved and Free Gas Analysis.* International Electrotechnical Commission (IEC), Geneva, Switzerland, 2nd edition, 1999.

[38] L. E. Lundgaard. Partial discharge - part XIV: Acoustic partial discharge detection - practical application. *IEEE Electrical Insulation Magazine*, 8(5):34–43, Sep/Oct 1992.

[39] M. Lindner, S. Elstein, P. Linder, and J. M. Topaz. Datlight corona discharge imager. In *Procedings of International Symposium on High Voltage Engineering*, volume 4, pages 349–352, London, 1999.

[40] A. Pedersen, G. C. Crichton, and I. W. McAllister. The functional relation between partial discharges and induced charge. *IEEE Transactions on Dielectrics and Electrical Insulation*, 2(4):535–543, August 1995.

[41] A. Pedersen, G. C. Crichton, and I. W. McAllister. The theory and measurement of partial discharge transients. *IEEE Trans. Electrical Insulation*, 26(3):487–497, June 1991.

[42] A. Pedersen, G. C. Crichton, and I. W. McAllister. Partial discharge detection: theoretical and practical aspects. *IEE Proc.-Sci. Meas. Technol.*, 142(1):29–36, January 1995.

[43] I. W. McAllister. Electrical field theory and the fallacy of void capacitance. *IEEE Trans. Electrical Insulation*, 26(3):459–459, June 1991.

[44] A. J. Reid, M. D. Judd, B. G. Stewart, and R. A. Fouracre. Partial discharge current pulses in SF_6 and the effect of superposition of their radio-

metric measurement. *Journal of Physics D: Applied Physics*, 39:4161–4177, September 2006.

[45] A. Schwaiger. Über die entladungsvorgänge auf isolatoren. *Rosenthal-Mitt. H.*, 6, 1925.

[46] B. F. Hampton and R. J. Meats. Diagnostic measurements at UHF in gas insulated substations. *IEE Proc.-C: Generation, Transmission and Distribution*, 135(2):137–144, March 1988.

[47] J. S. Pearson, B. F. Hampton, and A. G. Sellars. A continuous UHF monitor for gas insulated substations. *IEEE Transaction on Electrical Engineering*, 26(3):469–478, June 1991.

[48] M. D. Judd, G. P. Cleary, and C. J. Bennoch. Applying UHF partial discharge detection to power transformers. *IEEE Power Eng. Rev.*, 22(8):57–59, 2002.

[49] M. D. Judd, G. P. Cleary, C. J. Bennoch, J. S. Pearson, and T. Breckenridge. Power transformer monitoring using UHF sensors: site trials. In *IEEE International Symposium on Electrical Insulation*, pages 145–149, Boston, MA, USA, April 2002.

[50] M. Judd, L. Yang, C. Bennoch, I. Hunter, and T. Breckenridge. Condition monitoring of power transformers using UHF partial discharge sensors: Operating principals and site testing. In *Procedings of Euro Tech Conference*, Manchester, November 2003.

[51] T. Hoshino, H. Koyama, S. Maruyama, and M. Hanai. Comparison of sensitivity between UHF method and IEC 60270 for onsite calibration in various GIS. *IEEE Trans. Power Delivery*, 21(4):1948–1953, Oct 2006.

[52] M. D. Judd, L. Yang, and I. Hunter. Partial discharge monitoring for power transformers using UHF sensors part 1: Sensors and signal interpretation. *IEEE Electrical Insulation Magazine*, 21(2):5–14, March/April 2005.

[53] G. P. Cleary and M. D. Judd. UHF and current pulse measurements of partial discharge activity in mineral oil. *IEE Proc. Science, Measurement and Technology*, pages 47–54, March 2006.

[54] CIGRE WG 15-03. Diagnostic methods for GIS insulating systems, CIGRE Paper 15/23-01 1992.

[55] M. D. Judd, O. Farish, S. G. Pearson, and B. F. Hampton. Dielectric windows for UHF partial discharge detection. *IEEE Transactions on Dielectrics and Electrical Insulation*, 8(6):953–958, December 2001.

[56] N. Kock, B. Coric, and R. Pietsch. UHF PD detection in gas-insulated switchgear–suitability and sensitivity of the UHF methon in comparison with the IEC 270 method. *IEEE Electrical Insulation Magazine*, 12(6):20–26, November/December 1996.

[57] K. Raja, F. Devaux, and S. Lelaidier. Recognition of discharge sources using UHF PD signatures. *IEEE Electrical Insulation Magazine*, 18(5):8–14, September - October 2002.

[58] R. Kurrer and K. Feser. The application of ultra-high-frequency partial dischage measurements to gas-insulated substations. *IEEE Transactions on Power Delivery*, 13(3):777–782, July 1998.

[59] M. D. Judd, O. Farish, and B. F. Hampton. Broadband couplers for UHF detection of partial discharge ingas-insulated substations. *IEE Proc. Sci. Meas. Tech.*, 142(3):237–243, May 1995.

[60] M. D. Judd, O. Farisha, J. S. Pearson, and B. F. Hampton. Dielectric windows for UHF partial discharge detection. *IEEE Trans. Dielectrics and Electrical Insulation*, 8(6):953–958, Dec 2001.

[61] M. D. Judd, O. Farish, and P. F. Coventry. UHF couplers for GIS - sensitivity and specification. In *Proc. 10th Int. Symp. on High Voltage Engineering*, volume 6, Montreal, Aug 1997.

[62] M. Judd and O. Farish. A pulsed GTEM system for UHF sensor calibration. *IEEE Transactions on Instrumentation and Measurement*, 47(4):875–880, August 1998.

[63] M. D. Judd. Transient calibration of electric field sensors. *IEE Proc. Science, Measurement and Technology*, 146(3):113–116, May 1999.

[64] J. P. Karst, C. Groh, and H. Garbe. Calculable field generation using tem cells applied to the calibration of a novel e-field probe. *IEEE Transactions on Electromagnetic Compatability*, 44(1):59–71, February 2002.

[65] A. Ambardar. *Analog and Digital Signal Processing.* Brooks-Cole, 2nd edition edition, 1999.

[66] *IEEE Standard for Calibration of Electromagnetic Field Sensors and Probes, Excluding Antennas, from 9 kHz to 40 GHz.* 345 East 47th St., New York, USA, 1996.

[67] M. D. Judd, L. Yang, and I. Hunter. Partial discharge monitoring for power transformers using uhf sensors part 2: Field experience. *IEEE Electrical Insulation Magazine*, 21(3):5–13, May/June 2005.

[68] L. Yang, B. G. Stewart, A. J. Reid, M. D. Judd, and R. A. Fouracre. Study on combining UHF techniques with the IEC60270 standard for monitoring partial discharge of HV plant. In *14th International Symposium on High Voltage Engineering*, page 347, Beijing, China, August 2005.

[69] L. Yang and M. D. Judd. Propagation characteristics of uhf signals in transformers for locating partial discharge sources. In *Proc. 13th Int. Symp. on High Voltage Engineering*, Delft, August 2003.

[70] R. A. Jongen, P. Morshuis, S. Meijer, and J. J. Smit. Identification of partial discharge defects in transformer oil. In *IEEE Conference on Electrical Insulation and Dielectric Phenomena (CEIDP)*, pages 565–568, Nashville, Tennessee, USA, Oct 2005.

[71] S. Meijer. *Partial Discharge Diagnosis of High-Voltage Gas-Insulated Systems.* PhD thesis, Technische Universiteit Delft, November 2001.

[72] L. Yang and M. Judd. Recognising multiple discharge sources in power transformers by wavelet analysis of UHF signals. *IEE Proc. Science, Measurement and Technology*, 150(3):119–127, May 2003.

[73] R. Morrow. Theory of positive corona in SF6 due to a voltage impulse. *IEEE Transactions on Plasma Science*, 19(2):86–94, April 1991.

[74] R. Morrow. The theory of positive glow corona. *J. Phys. D: Appl. Phys.*, 30(22):3099–3114, November 1997.

[75] R. Morrow. Theory of electrical corona in SF6. *Nuclear Instruments and Methods in Physics Research Section A*, 382(1):57–65, November 1996.

[76] M. D. Judd and O. Farish. FDTD simulation of UHF signals in GIS. In *Proc. 10th Int. Symp. on High Voltage Engineering*, volume 6, Montreal, august 1997.

[77] M. D. Judd. Using finite difference time domain techniques to model electrical discharge phenomena. In *IEEE Conference on Electrical Insulation and Dielectric Phenomena*, pages 518–521, Victoria, Canada, October 2000.

[78] D. Pommerenke and S. Sakaguchi. Application of maxwell solvers to PD propagation. I. concepts and codes. *IEEE Electrical Insulation Magazine*, 18(5):15–21, September/October 2002.

[79] K. Wang, D. Pommerenke, Ra. Chundru, T. Van Doren, J. L. Drewniak, and A. Shashindranath. Numerical modeling of electrostatic discharge generators. *IEEE Transactions on Electromagnetic Compatibility*, 45(2):258–271, May 2003.

[80] M. Pompili, C. Mazzetti, and R. Bartnikas. PD pulse burst characteristics of transformer oils. *IEEE Transactions on Power Delivery*, 21(2):689-698, April 2006.

[81] A. G. Sellars, O. Farish, and M. M. Peterson. UHF detection of leader discharges in SF6. *IEEE Transactions on Dielectrics and Electrical Insulation*, 2(1):143–154, June 1995.

[82] M. D. Judd and O. Farish. High bandwidth measurement of partial discharge current pulses. In *Conf. Record of IEEE International Symposium on Electrical Insulation*, volume 2, pages 436–439, Arlington, Virginia, USA, 1998.

[83] G. Wanninger. Discharge currents of free moving particles in GIS. In *10th International Symposium on High Voltage Engineering*, volume 2: Dielectrics and Insulation, pages 219–222, Montreal, Quebec, Canada, August 1997.

[84] G. Wanninger. *Ultrahochfrequente Teilentladungssignale in gasisolierten Schaltanlagen (GIS)*. PhD thesis, Technische Universität München, May 1998.

[85] H. Okubo, M. Yoshida, T. Takahashi, and T. Hoshino. Partial discharge measurement in a long distance gas insulated transmission line (GIL). *IEEE Transactions on Power Delivery*, 13(3):683–690, July 1998.

[86] H. Okubo, N. Hayakawa, and A. Matsushita. The relationship between partial discharge current pulse waveforms and physical mechanisms. *IEEE Electrical Insulation Magazine*, 18(3):38–45, May/June 2002.

[87] T. S. Saad, editor. *The Microwave Engineering Handbook and Buyers Guide*. William Bazzy, 2nd edition, 1963.

[88] P. J. Mohr and B. N. Taylor. CODATA recommended values of the fundamental physical constants:1998. *Rev. Mod. Phys.*, 72(2):351–495, April 2000.

[89] M. D. Judd, O. Farish, and B. F. Hampton. Modelling partial discharge excitation of UHF signals in waveguide structures using Green's functions. *IEE Proc. Science, Measurement and Technology*, 143(1):63–70, January 1996.

[90] N. Ari and W. Blumer. Transient electromagnetic fields due to switching operations in electric power systems. *IEEE Transactions on Electromagnetic Compatibility*, 29(3):233–237, August 1987.

[91] M. D. Judd, A. J. Reid, L. Yang, B. G. Stewart, and R. A. Fouracre. A new integrated diagnostic partial discharge monitoring strategy for HV plant items: combining UHF couplers and the IEC60270 standard. In *18th International Conference on Electricity Distribution*, Turin, Italy, June 2005.

[92] A. J. Reid, L. Yang, M. D. Judd, B. G. Stewart, and R. A. Fouracre. An integrated measurement strategy for simultaneous fault identification: Combining the UHF and IEC60270 techniques. In *14th International Symposium on High Voltage Engineering*, page 394, Beijing, China, August 2005.

[93] M. D. Judd, D. Gray, and A. J. Reid. Using a step recovery diode to generate repeatable pulses for partial discharge simulation. In *14th International Symposium on High Voltage Engineering*, page 595, Beijing, China, August 2005.

[94] S. Ohtsuka, T. Teshima, S. Matsumoto, and M. Hikita. Relationship between PD-induced electromagnetic wave measured with UHF method and charge quantity obtained by PD current waveform in model GIS. In *IEEE Conference on Electrical Insulation and Dielectric Phenomena*, pages 615–618, Kansas City, Missouri, USA, October 2006.

[95] M. D. Judd, O. Farish, and B. F. Hampton. The excitation of UHF signals by partial discharges in gis. *IEEE Transactions on Dielectrics and Electrical Insulation*, 3(2):213–228, April 1996.

[96] C. Tai. *Dyadic Green's functions in electromagnetic theory.* IEEE Press, 2nd edition, 1994.

[97] H. J. Schmitt, C. W. Harrison, and C. S. Williams. Calculated and experimental response of thin cylindrical antennas to pulse excitation. *IEEE Trans. Antennas and Propagation*, 14(2):120–127, 1966.

[98] T. Hoshino, S. Maruyama, K. Nojima, and M. Hanai. A unique sensitivity verification combined with real-time partial-discharge identification method. *IEEE Transactions on Power Delivery*, 20(3):1890–1896, July 2005.

[99] M. Judd, S. McArthur, A. Reid, V. Catterson, L. Yang, B. Jacobson, K. Svensson, and M. Gunnarsson. Investigation of radiometric partial discharge detection for use in switched HVDC testing. In *PES General Meeting*, Montreal, June 2006. IEEE.

[100] I. J. Kemp, A. Nesbitt, B. G. Stewart, and C. Zhou. On-line electrical measurement of partial discharge activity from a 400/275kV transformer. In *EPRI Substation Diagnostics Conference*, New Orleans, USA, February 2003.

[101] R. Candela, I. Romano, and P. Romano. Influence on pd parameters due to distorted voltage. In *IEEE Conference on Electrical Insulation and Dielectric Phenomena*, pages 593–596, Albuquerque, NM, USA, Oct 2003.

[102] A. J. Reid and M. D. Judd. Partial discharges and RF signals. In *1st UHVnet Colloqium on Condition Monitoring and Ageing of High Voltage Plant/Equipment*, Cardiff University, January 2005.

[103] A. J. Reid and M. D. Judd. High bandwidth measurement of partial discharge pulses in SF_6. In *14th International Symposium on High Voltage Engineering*, page 348, Beijing, China, August 2005.

[104] B. G. Stewart, L. Yang, M. D. Judd, A. J. Reid, and R. A. Fouracre. A simple metric for assessing the severity of partial discharge activity based on time-sequence-analysis-discharge level patterns. In *International Conference on Condition Monitoring and Diagnostics*, Changwon, Korea, April 2006.

[105] A. J. Reid, M. D. Judd, B. G. Stewart, and R. A. Fouracre. Frequency distribution of RF energy from PD sources and its application in combined RF and IEC60270 measurements. In *IEEE Conference on Electrical Insulation and Dielectric Phenomena*, Kansas City, MO, USA, October 2006.

[106] A. J. Reid, M. D. Judd, B. G. Stewart, R. A. Fouracre, and S. Venkatesan. Identification of multiple defects in solid insulation using combined RF and IEC60270 PD measurement. In *9th IEEE International Conference on Solid Dielectrics*, Winchester, Hampshire, UK, July 2007.

[107] S. Venkatesan, B. G. Stewart, M. D. Judd, A. J. Reid, and R. A. Fouracre. Analysis of PD in voids using correlation plots of RF radiated energy and apparent charge. In *9th IEEE International Conference on Solid Dielectrics*, Winchester, Hampshire, UK, July 2007.

[108] D. Templeton, R. Brinzer, J. S. Pearson, A. J. Reid, and M. D. Judd. Sensitivity testing of a UHF power transformer monitoring system. In *15th International Symposium on High Voltage Engineering*, Ljubljana, Slovenia, August 2007.

[109] A. J. Reid, M. D. Judd, B. G. Stewart, R. A. Fouracre, and S. Venkatesan. Correlation between RF energy and IEC60270 apparent charge for selected partial discharge source geometries. In *15th International Symposium on High Voltage Engineering*, Ljubljana, Slovenia, August 2007.

[110] A. J. Reid and M. D. Judd. A novel self-powered condition monitoring sensor for harsh environments - feasibility study. In *15th International Symposium on High Voltage Engineering*, Ljubljana, Slovenia, August 2007.

[111] B. G. Stewart, A. J. Reid, M. D. Judd, and R. A. Fouracre. UHF and IEC60270 correlation analysis of radiated frequency band measurements on resin insulation void samples. In *Electrical Insulation Conference and Electrical Manufacturing Expo*, Nashville, TN, USA, October 2007.

[112] B. G. Stewart, M. D. Judd, A. J. Reid, and R. A. Fouracre. Suggestions to augment the IEC60270 partial discharge standard in relation to radiated electromagnetic energy. In *Electrical Insulation Conference and Electrical Manufacturing Expo*, Nashville, TN, USA, October 2007.

[113] B. G. Stewart, L. Yang, M. D. Judd, A. J. Reid, and R. A. Fouracre. A simple metric for assessing the severity of partial discharge activity based ion time-sequence-analysis-discharge level patterns. *Trans. Electrical and Electronic Materials*, 7(6):313–318, Dec 2006.

[114] R. Sarathi, A. J. Reid, and M. D. Judd. Partial discharge study in transformer oil due to particle movement under dc voltage using uhf technique. *Electric Power Systems Research (Elsevier)*, 2007.

[115] A. J. Reid, M. D. Judd, B. G. Stewart, D. M. Hepburn, and R. A. Fouracre. Identification of simultaneously active partial discharge sources using combined RF and IEC60270 measurement. *Journal of Physics D: Applied Physics.*

[116] A. J. Reid, M. D. Judd, B. G. Stewart, and R. A. Fouracre. Combined RF and IEC60270 partial discharge measurement on selected PD source geometries. *IEEE Trans. Power Delivery.*